Summer 2020

Measurement of Inclusive Fiducial and Differential Cross Sections in the H → ZZ∗ → 4l Decay Channel in p-p Collisions at 13 TeV with the Full ATLAS Run 2 Dataset

Madalyn McKay
Southern Methodist University, mckaym@smu.edu

MEASUREMENT OF INCLUSIVE FIDUCIAL AND DIFFERENTIAL CROSS SECTIONS IN THE $H \to ZZ^* \to 4\ell$ DECAY CHANNEL IN P-P COLLISIONS AT 13 TEV WITH THE FULL ATLAS RUN 2 DATASET

Approved by:

Dr. Ryszard Stroynowski
Professor of Physics

Dr. Jodi Cooley-Sekula
Associate Professor of Physics

Dr. Pavel Nadolsky
Associate Professor of Physics

Dr. RD Schaffer
Professor of Physics

MEASUREMENT OF INCLUSIVE FIDUCIAL AND DIFFERENTIAL CROSS SECTIONS IN THE $H \to ZZ^* \to 4\ell$ DECAY CHANNEL IN P-P COLLISIONS AT 13 TEV WITH THE FULL ATLAS RUN 2 DATASET

A Dissertation Presented to the Graduate Faculty of the

Dedman College

Southern Methodist University

in

Partial Fulfillment of the Requirements

for the degree of

Doctor of Philosophy

with a

Major in Physics

by

Madalyn McKay

B.S., Physics, Carnegie Mellon University
M.S., Physics, Southern Methodist University

August 4, 2020

Acknowledgments

The work in this thesis represents upwards of six years of my life and would not have been possible without the support of a number of people who I want to thank here.

The first person is my advisor, Ryszard Stroynowski, who has been an unwavering supporter, teacher, and source of guidance. I feel incredibly lucky to have come to SMU and have had you as an advisor.

Next I would like to thank my thesis committee, Jodi Cooley-Sekula, Pavel Nadolsky, and RD Schaffer, for helping me progress through the program, helping me improve my thesis, and participating in my defense with interesting questions and discussion.

I also want to thank the SMU ATLAS group in general. Thank you to my fellow grad students who I studied with, learned with, and grew as a researcher with. Thank you to the postdoctoral researchers who were both mentors and friends, and thank you to the professors who led our group and provided guidance and mentorship as well.

I need to thank the analysis team, including Haider, Andrea, Laurelle, Antonio, Roberto, Bianca, Gaetano, and RD. As Haider put it - I hope they don't ask us to, but if we had to do it over, there's no one else I'd rather do this analysis with.

Thank you also to the ATLAS Liquid Argon operations and online software groups. These groups were the first that I joined when I moved out to CERN and they really felt like a family at times more than a collaboration. I will forever remember the LAr-BQs, Bois Joly dinners, and amazing colleagues and friends I made in the world of LAr.

I want to thank the amazing group of friends I met during my stay at CERN, including Adriana, Hannah, Graham, Sun, Birgit, Billy, Elodie, and my beer-brewing crew, in addition to my LAr and analysis friends. And Tal especially. Thank you for everything.

Finally, I want to thank my friends 'back home' and my family for their support and encouragement. I couldn't have done this without you.

McKay, Madalyn

B.S., Physics, Carnegie Mellon University
M.S., Physics, Southern Methodist University

Measurement of Inclusive Fiducial and Differential
Cross Sections in the $H \to ZZ^* \to 4\ell$ Decay Channel in p-p Collisions
at 13 TeV with the Full ATLAS Run 2 Dataset

Advisor: Dr. Ryszard Stroynowski

Doctor of Philosophy degree conferred August 4, 2020

Dissertation completed April 22, 2020

The Higgs boson inclusive and differential fiducial cross sections are measured in the $H \to ZZ^* \to 4\ell$, decay channel, where $\ell = e, \mu$. The measurements are performed using proton−proton collision data from the Large Hadron Collider produced at a center-of-mass energy of 13 TeV. The data was recorded by the ATLAS detector between 2015 and 2018 and corresponds to an integrated luminosity of 139 fb^{-1}. Differential fiducial cross sections are measured for a set of observables that are sensitive to the production and decay of the Higgs boson. All measured cross sections are found to be in agreement with the Standard Model within the measured uncertainties. Finally, several results are used to constrain anomalous interactions between the Higgs boson and other Standard Model particles.

TABLE OF CONTENTS

LIST OF FIGURES

LIST OF TABLES

To my mom.

CHAPTER 1

Introduction

There are many distinct scientific fields in which researchers try to better understand and describe the world we live in. The topics of study range from the smallest scales imaginable to those that span the universe; however, one thing these various fields all have in common is the cyclical nature of discovery and revolution. In 1964, American philosopher Thomas Kuhn published *The Structure of Scientific Revolutions* [1], in which he provides a framework for analyzing trends in major scientific revolutions throughout history.

Kuhn posits that these trends comprise the stages through which scientific revolutions begin, follow through, and then return to periods of "normal science". The framework is as follows: prior to a scientific revolution, scientists engage in research "firmly based upon one or more past scientific achievements ... supplying the foundation for further practice" [1]. During these periods of normal science, anomalies exist that cannot be explained within the current paradigm. As these anomalies are investigated, new thinking beyond the current paradigm takes place, which Kuhn refers to as "pre-revolutionary thinking". Eventually, a discovery is made and a new paradigm replaces the old one. This is the scientific revolution, and the cycle repeats.

This cycle is apparent in the history of many fields, particularly in physics. The Copernican Revolution, occurring in the early 1500s, was the revolution in which Nicolaus Copernicus' heliocentric model replaced Ptolemy's geocentric model as a new paradigm in which scholars understood and continued to research planetary motion.

The quantum revolution can be considered in the same framework. At the beginning of the 20th century, there was a period of normal science in which physics was believed to be complete, and research focused on precise determination of known constants. Classical

physics built upon Newtonian principles desribed everything from kinematics to electricity and magnetism, and the paradigm in which scientists worked was rooted in these principles. Anomalies existed, such as Newton's concept of absolute space and time, gravity's unexplained action from a distance, and the strange corpuscular view of light. While the classical theory worked extremely well in describing everyday phenomena, these anomalies became hard to ignore, and competing theories came into favor. Newton's theory of corpuscular light was unexplainable and was challenged by Young's wave theory of light, and later discarded in favor of Maxwell's single theory of electromagnetism, which built upon Young's theory. More problems arose, and pre-revolutionary thinking as defined by Kuhn began to take place, eventually giving way to a new paradigm.

The field of particle physics has been in a period of normal science for the past few decades. The Standard Model of Particle Physics, completed in its current form in 1964 with the theoretical prediction of the Higgs boson [2] [3] [4], is the current paradigm in which scientists in this field conduct research. Prediction after prediction made by the Standard Model has been observed, with the last missing piece, a Higgs-like scalar boson, finally being observed at the Large Hadron Collider (LHC) in 2012 [5] [6]. However, there are many anomalies that the Standard Model fails to explain. There is no description of dark matter and no quantum description of gravity. The Standard Model provides no reason for the matter-antimatter asymmetry that we observe in the world around us. Despite being an incredibly well-verified theory, it is incomplete.

And so we have entered a period of pre-revolutionary thinking. Theories beyond the Standard Model are abundant and a large amount of research is focused towards either finding new particles desribed by one of these theories, or making precision measurements of known Standard Model particles in search of hints of new physics beyond our currently accepted paradigm.

The two experiments at which the Higgs-like boson was discovered, ATLAS and CMS, continue to be at the forefront of this exploration. Unprecedented in size and scope, these experiments are highly collaborative and would not be possible without the support and

expertise of over 3000 scientists who work on each experiment, as well as thousands more engineers, technicians, and staff who help keep the LHC running. The size and complexity of the experiments at the LHC preclude solitary work. The research for this thesis was done using data collected by the ATLAS experiment, where, as a member of the ATLAS collaboration, I worked on both detector operations and physics analysis. In both aspects, I was a part of smaller collaboration groups within the larger ATLAS collaboration. I will highlight my specific contributions as they are discussed in this thesis; however the full content respresents the work of many.

The focus of my analysis work within ATLAS (and the focus of this thesis) is a set of precision measurements of the Higgs boson - a likely candidate for hints of new physics that could spark a revolution in the field of particle physics. These are specifically measurements of the fiducial and differential cross sections of the Higgs in the decay channel to two Z bosons that then decay to four leptons. The structure of this thesis is as follows:

In Chapter 2, I will give a brief overview of our current paradigm, the Standard Model of Particle Physics. I will begin with a short, qualitative description of the Standard Model particles and interactions before approaching it from a mathematical standpoint. Important concepts related to symmetries in physics and the mathematics we use to describe them will be given, followed by a quick review of the quantum theories of electrodynamics, electroweak theory, and chromodynamics. This will be followed by the introduction of spontaneous symmetric breaking, the Higgs Mechanism, and electroweak symmetry breaking. I will end with a return to an experimental point of view. I will discuss Higgs production at hadron colliders, and finally provide motivation for performing cross section measurements.

Chapter 3, is devoted to descriptions of the LHC and the ATLAS detector, with extra detail given to the Liquid Argon (LAr) calorimeter, where I contributed to operations and data-taking efforts.

In Chapter 4, I will talk about the various physics objects that are detected in the ATLAS experiment, and desribe how they are identified and how their properties are measured.

In Chapter 5 I begin to dive into the specifics of my analysis. In this chapter, I will discuss how we select Higgs boson candidates in the four lepton decay channel. I will describe the various backgrounds that compete with our desired data, and how their effects are mitigated and controlled. I will also introduce Monte Carlo simulations used for modeling what we expect to see in the data given various theoretical predictions. I contributed to work that is included in this chapter.

Next, I will discuss the details of the cross section measurements in Chapter 6. I will define the fiducial phase space in which the measurements are made. I will define the fiducial cross sections that are measured as well as the observables with respect to which the differential cross sections are measured, and provide motivations for the measurements. This and all following chapters contain work that I contributed to significantly.

In Chapter 7, the statistical methods used to extract the cross sections. Deconvolution of detector effects on the measurements will be described, with a discussion on various unfolding methods and how these fit into the statistical treatment. The systematic uncertainties that are considered are presented, along with their effects on the measured quantities.

In Chapter 8, results of the measurements are given along with comparisons to theoretical predictions. Various interpretations of these results in theories beyond the Standard Model are presented following in Chapter 9.

Finally in Chapter 10, I will conclude the thesis.

As alluded to previously, I was lucky enough to be able to participate in every aspect of this analysis. I contributed to data-taking efforts through my work with the ATLAS LAr calorimeter online software and operations group. I was a member of the team of people working on the event selection code that is used to select $H \to ZZ^* \to 4\ell$ events from the ATLAS dataset. I studied the unfolding method and its potential biases, studied and reduced several systematic uncertainties, and implemented these updates to the statistical framework used to extract the cross section results. I ran this code, extracting the cross sections and producing the final results plots provided in Chapter 8. In addition, I collaborated with theorists from the theory community to obtain alternate predictions with which to compare

our final measurements. I am grateful to the incredible group of people I worked with on this analysis, and am very proud of our results.

CHAPTER 2

Theory and motivation

Following the Quantum Revolution, several theories were developed that together form the current paradigm in which particle physics is understood - the Standard Model of particle physics. Various theories and experiments led to the understanding of fundamental particles and the forces through which they interact in terms of a quantum field theory - where particles are considered field operators that operate on a vacuum, either creating an excitation, or annihilating one.

Paul Dirac proposed the first theory of quantum electrodynamics (QED) in the 1920s [7]. This was followed by the proposal of the weak theory in 1933 by Enrico Fermi [8]. In 1968, Weinberg, Glashow, and Salam described the two theories as manifestations of a single unified, electroweak (EW) theory [9] [10] [11]. Concurrently, the theory of quantum chromodynamics (QCD) was developed in the 1960s [12] [13], and with the introduction of the Higgs mechanism and the accompanying theoretical prediction of the Higgs boson in 1964 [4] [2] [3], the theory of the Standard Model was complete.

In the first section of this chapter, a quick summary of the Standard Model (SM) will be given. The particles and their interactions described by the SM will be described qualitatively.

This will serve as context in which to place the following overview of the mathematical basis of the SM. A discussion of symmetries, transformations, and conserved quantities will be presented - these are the keys to understanding the SM. Next, the symmetry considerations that can be used to derive QED are presented, from which analogies are drawn to QCD and then electroweak theory. Electroweak symmetry breaking is presented along with the Higgs mechanism. References [14], [15], [16], and [17] were used heavily for this section.

Once the theoretical framework is established, we will return to a discussion of the SM from an experimental point of view.

2.1. The Standard Model

2.1.1. Summary of the Standard Model particles

The goal of particle physics can be described as an attempt to observe the most fundamental particles that make up our universe and formulate a predictive, self-contained mathematical framework to describe their properties and interactions. The mathematical framework accepted today, introduced previously as the Standard Model (SM) of particle physics, describes our current best understanding of the fundamental particles that make up the world around us. These particles appear structureless at the highest energies probed so far.

The particles of the SM can be organized into categories based on their properties. Most generally, one can introduce two classes of particles based on a quantum mechanical degree of freedom, spin. Fermions are particles with half-integer spin that form everyday matter. All elementary fermions in the SM have spin $\frac{1}{2}$. Bosons, the force carriers of the SM, have integer spin. Fermions interact with each other via exchanges of either real or virtual bosons, each of which is associated with a force group in the SM that acts on a specific quantum degree of freedom, or charge. This will be discussed further in Sections 2.1.3.1- 2.1.3.3.

There are three groups of spin-1 bosons predicted by the SM and discovered experimentally. First is the massless photon, γ, which mediates the electromagnetic force between electrically charged particles. The massive weak vector bosons, W^+, W^-, and Z^0, mediate the weak force, which acts on the weak isospin quantum degree of freedom. Fermions carry weak isospin charges of $\pm\frac{1}{2}$ while the weak vector bosons carry weak isospin charges of +1, -1, and 0, respectively. As mentioned previously, the electromagnetic and weak forces are unified in the SM and manifest as a single electroweak force. Finally there are the eight massless gluons, which act on the color quantum degree of freedom, of which there are three

values denoted red - R, green - G, and blue - B. The Higgs boson, which has spin 0, provides a mechanism through which the massive bosons acquire their mass. Fermions also acquire mass through interactions with the Higgs boson. These mechanisms of mass generation will be discussed in further detail in Section 2.1.4.

Fermions are classified as either leptons or quarks, based on which force groups of the SM they interact with. Leptons are spin-$\frac{1}{2}$ particles that interact only in the electroweak sector of the SM.

There are three lepton "generations", roughly ordered by increasing mass of the leptons in each generation. Each generation contains a charged lepton and a neutral lepton neutrino. The charged leptons are (in order of generation) the electron, e, the muon, μ, and the tau, τ. The neutrinos are the electron neutrino, ν_e, the muon neutrino, ν_μ, and the tau neutrino, ν_τ. The masses of the leptons are provided in Figure 2.1, while the neutrinos are predicted by the SM to have zero mass. However, experimental evidence of non-zero neutrino masses adds to the issues with the SM.

Only the left-handed components of the Dirac spinors used to represent the leptons participate in weak interactions. These left-handed fields are doublets of SU(2), which will be discussed in 2.1.3.3, while the right-handed fields are singlets. The general fields are given below:

$$\psi_L = P_L\psi = \frac{1}{2}(1-\gamma^5)\psi \qquad\qquad \psi_R = P_R\psi = \frac{1}{2}(1+\gamma^5)\psi\,, \tag{2.1}$$

where $P_L = \frac{1}{2}(1-\gamma^5)$ and $P_R = \frac{1}{2}(1+\gamma^5)$ are the left- and right-handed projection operators, respectively. The left-handed leptonic fields that transform as $\mathrm{SU}(2)_L$ doublets are given below, along with the third component their weak isospin (t_3) and hypercharge (t):

$$t = -1 \qquad t_3 = \begin{matrix} +\frac{1}{2} \\ -\frac{1}{2} \end{matrix} \qquad \begin{pmatrix} \nu_e \\ e^- \end{pmatrix} \qquad \begin{pmatrix} \nu_\mu \\ \mu^- \end{pmatrix} \qquad \begin{pmatrix} \nu_\tau \\ \tau^- \end{pmatrix} \tag{2.2}$$

The electric charge is defined as $Q = t_3 + \frac{t}{2}$.

The second type of elementary fermions, quarks, are spin-$\frac{1}{2}$ particles that interact not only via the electroweak force, but also in the SU(3) sector of the SM, via the strong force, which will be described quantitatively in 2.1.3.2.

Under electroweak interactions, quarks also transform as SU(2) doublets. The quark $SU(2)_L$ doublets are listed below, also with the third component of their weak isospin (t_3) and hypercharge (t):

$$t = \frac{1}{3} \qquad t_3 = \begin{matrix} +\frac{1}{2} \\ -\frac{1}{2} \end{matrix} \qquad \begin{pmatrix} u \\ d \end{pmatrix} \qquad \begin{pmatrix} c \\ s \end{pmatrix} \qquad \begin{pmatrix} t \\ b \end{pmatrix} . \tag{2.3}$$

The interactions of the quarks via the strong force involve the exhange of color charge. The color charge is confined, meaning only color singlet states are physically observed [18]. Quarks (and gluons) are therefore not observed as free particles, but rather in bound states called hadrons, which are colorless.

The elementary particles described here, along with the gauge boson force carriers with which they interact, are summarized in Figure 2.1. The mass of each particle is given, as is its spin, electric charge, and color charge (if applicable).

The graviton is a spin-2 boson that is not described by the SM. It is a proposed mediator of the gravitational force.The absence of gravity from the SM, the pattern of three generations of fermions with three different mass scales, as well as other unanswered puzzles will be discussed in Section 2.3, after a mathematical approach to the SM is provided.

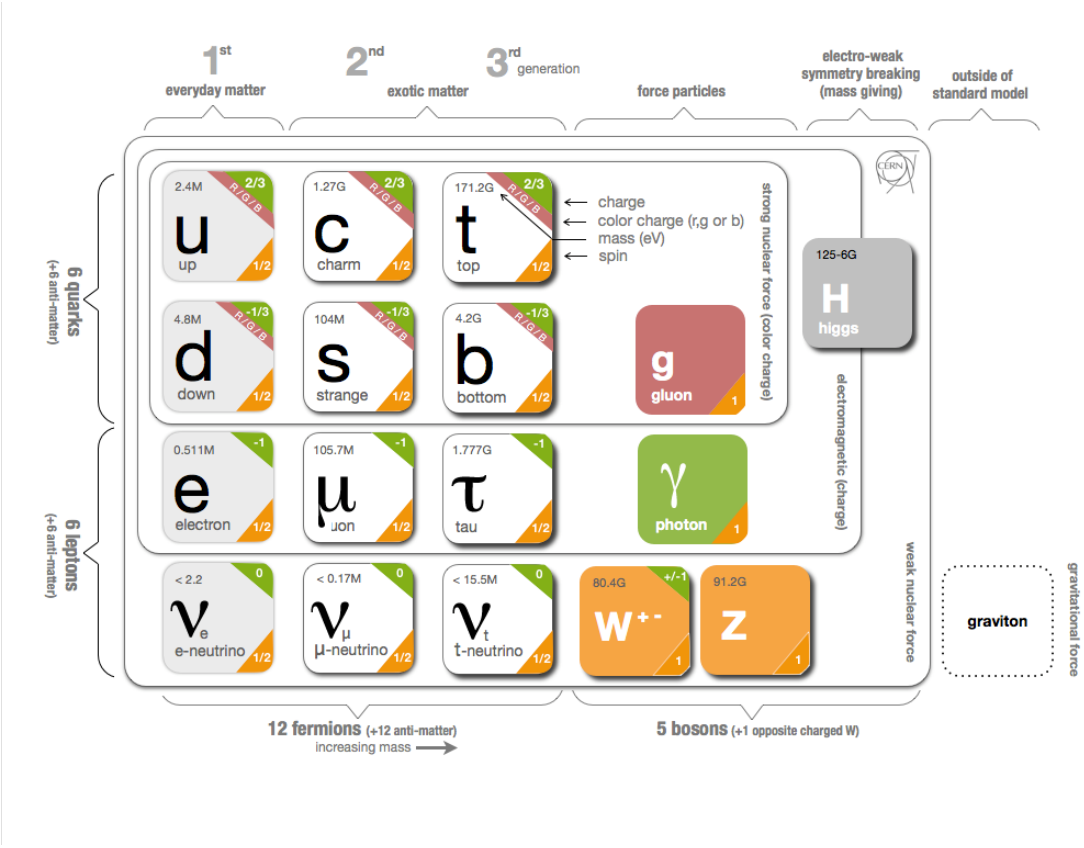

Figure 2.1. Infographic describing Standard Model particles [19].

2.1.2. Transformations and conserved quantities

Throughout the history of physics, symmetries have been directly related to the laws used to describe physical phenomena around us. In a famous example in 1687, Isaac Newton published *Principia* in which his first law, conservation of momentum, is a consequence of the symmetry of translational invariance in space. Though symmetries such as this were apparent, they did not drive the theory in any deliberate way [20].

In the 1800s however, symmetries began to be studied on their own, and group theory was developed as a mathematical study. In 1844, Augustin Cauchy studied groups of properties of permutations, with the symmetric group S_N becoming known as the group of permutations of fixed number of N elements. In 1878, the abstract concept of "groups" was formulated by Arthur Cayley, and between 1886 and 1904, Larmor, Lorentz, and Poincaré introduced transformations that comprise what is now known as the Lorentz group [21]. Again, manifestations of symmetries under this group are apparent in Maxwell's equations governing electromagnetism - for example, where transformations under the Lorentz group leave the equations invariant. However, the equations were formulated without dedicated consideration of the symmetry.

Finally, in 1918, Emmy Noether provided a theorem showing a general connection between symmetries and conserved quantities [22]. This theorem - Noether's Theorem - coupled with the mathematical tools of group theory and the calculus of variations, allowed for a reversal of the role of symmetry in the approach to describing physical phenomena.

2.1.2.1. Noether's Theorem

Noether's theorem allows for the exploration of the quantities that are conserved when a system is transformed under a given symmetry.

Consider a Lagrangian, $\mathcal{L} = L(q, \dot{q}) = T(q, \dot{q}) - V(q)$. Here, T is the total kinetic energy of the system in consideration, V is the total potential energy, and q and $\dot{q}$ are the generalized coordinates and momenta, respectively. Noether's Theorem states that continuous symmetries in the action lead to conserved quantities. If the infinitesimal transformation

$q \to q + \epsilon\delta q$ is made, it can be found that $\mathcal{L}$ transforms as [14]:

$$L \to L + \frac{d}{dt}(\frac{\partial}{\partial \dot{q}}\epsilon\delta q)\,, \tag{2.4}$$

where

$$j \equiv \frac{\partial}{\partial \dot{q}}\delta q \tag{2.5}$$

is the Noether current. If δq is 0 under a certain group transformation, the Lagrangian is invariant under the corresponding group and the Noether current is conserved.

2.1.2.2. Gauge Transformations

Another crucial topic to consider in the discussion of field theories is that of gauge transformations. A gauge transformation is one in which the components of a field are transformed under some local symmetry such that the Lagrangian remains invariant.

Beginning with a general transformation example, if an arbitrary electromagnetic (EM) potential, A^μ, is transformed as:

$$A^\mu \to A'^\mu = A^\mu + \partial^\mu \chi\,, \tag{2.6}$$

the EM field-strength tensor becomes[1] :

$$F'^{\mu\nu} = \partial^\mu A'^\nu - \partial^\nu A'^\mu = \partial^\mu(A^\nu + \partial^\nu\chi) - \partial^\nu(A^\mu + \partial^\mu\chi) = \partial^\mu A^\nu + \partial^\nu A^\mu = F^{\mu\nu}\,. \tag{2.7}$$

Thus, it remains the same. Such transformations are called global transformations, as the field is changed in the same way at all points in space-time. Another important global symmetry occurs when a field is invariant under phase shifts: $\psi = e^{i\alpha}\psi$.

Local transformations and local symmetries, on the other hand, vary in spacetime. In the previous example of the phase shift, $\alpha = \alpha(x^\mu)$ is now a function of x^μ instead of a constant. Taking a global symmetry and making it local is called gauging the symmetry.

[1]Recall, the μ and ν indices are space-time indices.

2.1.2.3. Lie Groups

Lie groups are powerful mathematical tools through which symmetries and their accompanying conserved quantities can be understood. Several important groups for the purposes of this thesis are introduced in the following [14]:

- Generalized orthogonal group, O: the group of generalized rotations.
- Special orthogonal group, SO: the subgroup of orthogonal group with $\det\|\mathrm{R}\| = 1$. SO(n) = group of all n×n special orthogonal matrices. SO(1, 3) is the Lorentz group.
- Unitary group, U: the set of all n×n invertible matrices that preserves $\bar{\mathrm{r}}^{\dagger} \cdot \bar{\mathrm{r}}$ for all vectors, $\bar{\mathrm{r}}$, in complex space.
- Special unitary group, SU: the set of all unitary matrices with $\det\|\mathrm{R}\| = 1$. SU(n) = group of all n×n special unitary matrices.

The number of generators of each group is the dimension of the group. The commutation relations between generators X_i and X_j:

$$[X_i, X_j] = i f_{ijk} X_k \tag{2.8}$$

form the Lie algebra of the group, where f_{ijk} are the structure constants of the group.

Whereas SO(1, 3) is the previously mentioned Lorentz group, which describes rotations through spacetime and has the angular momentum operators as generators[2], SU(2) is a complex cover group for O(3) that allows for interger or half integer spin. One can show that the generators of SU(2) can be linearly combined to form raising and lowering operators of a field theory. There are $2j + 1$ states for a general representation of SU(2).

- When $j = \frac{1}{2}$ the generators are found to be the Pauli spin matrices, and we have a representation for quantum mechanical spin, for a spin-$\frac{1}{2}$ particle.
- When $j = 1$ we find the generators for the quantum mechanical spin of a spin-1 particle

[2]The 3 in SO(3) refers to the dimension of the group.

2.1.3. QED, QCD, and the beginnings of EW Theory

2.1.3.1. QED

Following the historical evolution of the SM briefly given previously, one can begin with QED, which arises from quantization of Maxwell's theory of electromagnetism. It was shown previously in Equation 2.7 that the electromagnetic field strength tensor is invariant under global U(1) transformations - here this global symmetry is reduced to a local symmetry. We begin with the Dirac Lagrangian which describes a spin-$\frac{1}{2}$ particle:

$$\mathcal{L}_D = \bar{\psi}(i\gamma^\mu \partial_\mu - m)\psi \,, \tag{2.9}$$

which follows from the Dirac equation:

$$(\gamma^\mu \partial_\mu + im)\psi = 0 \,. \tag{2.10}$$

Here, the fermion, with mass m, is described by the spinor field ψ, and the γ^μ are the Dirac matrices. The Dirac Lagrangian is symmetric under the global U(1) transformation $\psi \to e^{i\alpha}\psi$, where α is some constant parameter of the transformation. The conserved current is $j^\mu = \bar{\psi}\gamma^\mu\psi$ [16].

To gauge the symmetry, we require instead invariance under the local U(1) transformation $\psi \to e^{i\alpha(x^\mu)}\psi$. Letting $x^\mu = x$ for convenience, the Lagrangian transforms as:

$$\mathcal{L}_D \to \bar{\psi}e^{-i\alpha(x)}(i\gamma^\mu - m)e^{i\alpha(x)}\psi = \bar{\psi}(i\gamma^\mu\partial_\mu - \gamma^\mu\partial_\mu\alpha(x) - m)\psi \,. \tag{2.11}$$

However, because α is now dependent on x, the second term no longer vanishes, and so the Lagrangian is not invariant under the local U(1) transformation. In order to restore invariance under this transformation, one can define a gauge field A_μ which transforms as $A_\mu \to A_\mu - \frac{1}{q}\partial_\mu\alpha(x)$ under the local U(1) transformation. We then define a covariant

derivative in terms of this field: $D_\mu \equiv \partial_\mu + iqA_\mu$. $\mathcal{L}$ then becomes:

$$\mathcal{L}_D = \bar{\psi}(i\gamma^\mu D_\mu - m)\psi = \bar{\psi}(i\gamma^\mu[\partial_\mu + iqA_\mu] - m)\psi\,. \tag{2.12}$$

Under the local U(1) transformation, we have:

$$\mathcal{L}_D \to \bar{\psi}e^{-i\alpha(x)}(i\gamma^\mu[\partial_\mu + iqA_\mu] - m)e^{i\alpha(x)}\psi = \bar{\psi}(i\gamma^\mu[\partial_\mu + iqA_\mu] - m)\psi\,. \tag{2.13}$$

Thus, the Lagrangian is now invariant under a local U(1) transformation, with the same conserved current as before. This demand of local U(1) invariance required the addition of a gauge field, A_μ, which appears in the covariant derivative. This gauge field is associated with the gauge boson that mediates the force of the U(1) sector of the SM. This is the electromagnetic force, and the gauge boson that emerges in the theory after gauging the U(1) symmetry is the photon [16].

In general, for some arbitrary Lie group SU(n), transformations can be expressed in the form:

$$\psi \to \psi' = U\psi = e^{ig\theta^\alpha(x)T^\alpha}\psi\,, \tag{2.14}$$

where U is an arbitrary element of the group. Again, x^μ has been written as x for convenience. The θ^α's are the $n^2 - 1$ elements of the group, while the T^α's are the generator matrices, and g is a dimensionless coupling constant. Each continuous symmetry under which a Lagrangian is invariant is represented by a Lie group. When a global symmetry is made to be a local symmetry, gauge fields arise and their corresponding force-mediating particles - gauge Bosons - enter the theory. Each of these force carriers is associated with a generator matrix of its associated Lie group. The U(1) group gives rise to the photon (or A^μ, as shown previously), SU(2) to the weak vector bosons, and SU(3) to the gluons. The latter two cases will be described in the following sections. The historical evolution of the theories will not be followed, and the SU(3) symmetry will be discussed first.

2.1.3.2. QCD

Quantum chromodynamics, or QCD, is the theory that describes the strong force which governs interactions between quarks, spin-$\frac{1}{2}$ particles, and gluons, spin-1 particles that mediate the strong force.

We begin, as in the case of QED, with the Dirac spinor Lagrangian. In this case we consider a particular quark flavor, q. The full Lagrangian should be a sum over q, but here a single quark flavor is considered for simplicity[3]:

$$\mathcal{L}_{Dq} = \bar{\psi}(i\gamma^\mu \partial_\mu - m_q)\psi \,. \tag{2.15}$$

As there are three charges associated with QCD interactions - the three color quantum degrees of freedom - we now look at the invariance under global SU(3) transformations:

$$\psi \to \psi' = U\psi = e^{i\sum_a \Theta^a(x)\frac{\lambda^a}{2}}\psi \,, \tag{2.16}$$

where a runs from one to eight as the SU(3) group has eight generators[4]: $\frac{\lambda^a}{2}$, which are the 3×3 Gell-Mann matrices [16]. The Θ^a are parameters of the transformation, which are constants in the global case and dependent on x in the local case. For simplicity the sum over the generators of the group will be omitted moving forward.

Requiring the global symmetry to be a local symmetry, one can define a covariant derivative such that the Lagrangian remains invariant under local SU(3) transformations:

$$D^\mu \equiv \partial^\mu + ig_s A_a^\mu \frac{\lambda^a}{2} \,, \tag{2.17}$$

where A_a^μ, the eight scalar gluon potentials, transform as: $A^\mu \to U(A^\mu + \frac{i}{g_s}\partial^\mu)U^\dagger$. Here g_s is the strong coupling constant, related to α_s via $\alpha_s = \frac{g_s^2}{4\pi}$, a is the color index, and U is the SU(3) transformation defined in Equation 2.16.

[3]The mass of the quark represented by the field ψ is m_q, while the γ^μ are again the Dirac matrices.

[4]Recall: the number of generators of an SU(n) group is $n^2 - 1$.

Because of the requirement of local SU(3) invariance, we end up with eight gauge bosons, associated with the eight generators of the SU(3) group. These gauge bosons are the gluons that were mentioned before. Gluons transfer color charge, also introduced previously, allowing for QCD interactions between quarks.

The interaction term in the QCD Lagrangian is[5]:

$$\mathcal{L}_{int} = -g_s \bar{\psi}_j A_a^\mu \frac{\lambda_{ij}^a}{2} \gamma_\mu \psi_i \,. \tag{2.18}$$

Because gluons can transfer energy and momentum as well as color charge, an additional kinematic term is needed in the Lagrangian, which can be written down analogously to that of the field strength tensor from electromagnetism:

$$\mathcal{L}_{int'} = -\frac{1}{4} F_a^{\mu\nu} F_{\mu\nu}^a \,, \tag{2.19}$$

where $F_a^{\mu\nu} = \partial^\mu A_a^\nu - \partial^\nu A_a^\mu - g_s[A_a^\mu, A_a^\nu]$ is invariant under the local SU(3) transformation given above. This is the gluon field strength tensor.

The last term in this second interaction term gives rise to three- and four-gluon self-interaction terms. The full QCD Lagrangian can therefore be written as:

$$\mathcal{L}_{QCD} = \mathcal{L}_{int} + \mathcal{L}_{int'} \,. \tag{2.20}$$

While the formalism looks similar between QED and QCD, the force structure is dramatically different. Because of the gluon self-interactions, the strong coupling constant decreases with energy, leading to phenomena such as asymptotic freedom, wherein at very high energies and small distances, interquark forces become small. Such behavior is not observed in the other sectors of the SM.

[5]Reminder: A_a^μ are the gluon potentials, where a is the color index in the adjoint representation of the SU(3) group which runs from 1 to 8, and μ is a summation index. λ_{ij}^a are the 3×3 Gell-Man matrices, where i and j are color indices in the fundamental representation of the SU(3) group, and run from 1 to 3. The γ_μ parameters are the Dirac matrices. The ψ_i fields are the quark fields in the fundamental representation of SU(3), and g is the strong coupling constant.

2.1.3.3. SU(2) and the beginnings of Electroweak Theory

Electroweak theory can be obtained through an analogous group-theoretical approach, where instead of imposing local U(1) or SU(3) symmetry, SU(2) symmetry is imposed, requiring that the Lagrangian be invariant under the SU(2) transformation[6]

$$\psi_L \to e^{i\alpha\cdot\tau/2}\psi_L\,, \tag{2.21}$$

which is made local by allowing α to depend on x.

As the partial derivative acts on $\alpha(x)$, the Lagrangian is no longer invariant under local SU(2) symmetry, and a covariant derivative must be defined to restore the symmetry. It can be shown that the suitable choice is given by [16]:

$$D^\mu \equiv \partial^\mu + \frac{ig}{2}\tau\cdot W^\mu(x)\,. \tag{2.22}$$

Here, $W^\mu(x)$ are three independent gauge fields[7], and $\tau\cdot W^\mu(x)$ is the 2×2 matrix:

$$\begin{pmatrix} W_3^\mu & W_1^\mu - iW_2^\mu \\ W_1^\mu + iW_2^\mu & -W_3^\mu \end{pmatrix}. \tag{2.23}$$

Thus, requiring local SU(2) symmetry results in a theory that includes interactions between spinors and three gauge fields, the $W^\mu(x)$. This is suggestive of the weak interactions, which are mediated by the three gauge bosons, the W^+, W^-, and Z, introduced in Section 2.1.1. However, there is an inconsistency in that the W and Z bosons are known to have nonzero mass due to the short range of the weak interaction. At the same time, the explicit addition of a mass term for the W^μ would violate the local SU(2) gauge invariance. This dilemma is solved via electroweak symmetry breaking and the Higgs mechanism, which are discussed in the following sections.

[6] The τ's are the three Pauli matrices.

[7] Again, there are three fields because the number of generators of the SU(2) group is $n^2 - 1 = 2^2 - 1 = 3$

2.1.4. Spontaneous symmetry breaking and the Higgs mechanism

The concept of spontaneous symmetry breaking is a crucial part of the Standard Model [2] [3] [4], and will be explained as follows. As a first example, consider a massless, scalar boson described by a complex, scalar field ϕ, where:

$$\phi = \frac{1}{\sqrt{2}}(\phi_1 - i\phi_2)\,, \qquad \text{and} \qquad \phi^\dagger = \frac{1}{\sqrt{2}}(\phi_1 + i\phi_2)\,, \tag{2.24}$$

with a Lagrangian that is invariant under global U(1) transformations:

$$\mathcal{L} = \partial^\mu \phi^\dagger \partial_\mu \phi - V(\phi)\,, \qquad \text{where} \qquad V(\phi) = \frac{1}{4}\lambda(\phi^\dagger\phi)^2 + \mu^2\phi\phi^\dagger\,. \tag{2.25}$$

Here, λ quantifies the self-coupling strength of the scalar field, ϕ, while μ defines the mass. The requirement of a stable ground state, necessitates that $\lambda > 0$, in order for the energy to be bounded from below [16]. There are no similar constraints on μ. If we choose $\mu^2 > 0$, it can be seen that the ground state of the system - the vacuum - is reached when $\phi = \phi_0$, where ϕ_0 is the minimum of the classical version of the potential. If we instead set $\mu^2 < 0$, so that the classical minimum is no longer at $\phi = \phi_0$, we end up with a symmetry breaking potential:

$$V(\phi) = \frac{1}{4}\lambda(\phi^\dagger\phi)^2 - \mu^2\phi\phi^\dagger\,. \tag{2.26}$$

The symmetry of the Lagrangian under global U(1) transformation is preserved. However, we now have an unstable maximum which occurs at:

$$\phi_1^2 + \phi_2^2 = \frac{4\mu^2}{\lambda} \equiv v^2\,. \tag{2.27}$$

This equivalently occurs for $|\phi| = \frac{v}{\sqrt{2}}$, which can be expressed in polar coordinates as:

$$\phi(x) = \frac{\rho(x)}{\sqrt{2}} e^{i\theta(x)/v}\,. \tag{2.28}$$

It can be seen that there now exists an infinite number of vacua in the theory, all lying along the circle at $\rho = v$, for any value of θ. The value v is the vacuum expectation value, or vev. The modified potential can be visualized as shown in Figure 2.2, represented here in only two dimensions.

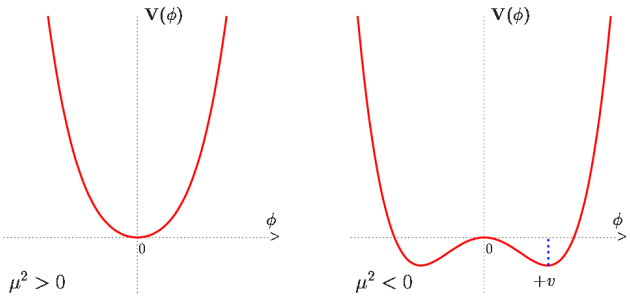

Figure 2.2. Diagrams representing the potentials in Equations 2.25 (left) and 2.26 (right) in two dimensions. Here, μ is the mass parameter, and v is the vacuum expectation value [23].

As particles are expressed in a quantum field theory as oscillations about the vacuum state, to get a stable theory one must expand fields about points along the stable minimum. As the minimum is infinitely degenerate, the "true" ground state must be chosen by hand, thus breaking the U(1) symmetry. If we choose $\rho = v$ and $\theta = 0$, our field expansion about the vacuum expectation value, v, becomes:

$$\phi(x) = \frac{1}{\sqrt{2}}(v + h(x))e^{i\theta(x)/v}\,, \tag{2.29}$$

with Lagrangian (ignoring higher order terms):

$$\mathcal{L} = \partial^\mu h \partial_\mu h - \mu^2 h^2 + \frac{1}{2}\partial_\mu \Theta \partial^\mu \Theta + \frac{\mu^2}{\lambda} + \dots\,. \tag{2.30}$$

The Lagrangian describes a field, h, that oscillates in the "radial" $\hat{\rho}$ direction in Figure 2.2 and is associated with a mass $\sqrt{2}\mu$. It also describes a field, Θ, whose oscillations are directed in and out of the page in Figure 2.2. The Θ field is not associated with any mass, and is known as a Goldstone mode. Goldstone modes are massless particles that appear when a

continuous symmetry is spontaneously broken, as stated by Goldstone's theorem [24]. The breaking of the rotational U(1) symmetry by the selection of a particular ground state leads to the appearance of the massless Goldstone bosons in the theory. Meanwhile, the mode in the direction orthogonal to the degenerate ground state in field space (the h field) aqcuires a mass.

Again, this example of a global U(1) symmetry can be extended to the case of a local $\mathrm{SU}(2)_L \times \mathrm{U}(1)_Y$ symmetry[8]. We begin first with a Lagrangian which is invariant under global $\mathrm{SU}(2)_L$ and $\mathrm{U}(1)_Y$ transformations:

$$\mathcal{L} = \partial^\mu \phi^\dagger \partial_\mu \phi + \mu^2 \phi^\dagger \phi - \frac{\lambda}{4}(\phi^\dagger \phi)^2 \,. \tag{2.31}$$

As discussed in previous sections, the requirement of local gauge invariance necessitates the introduction of three $\mathrm{SU}(2)_L$ gauge fields, the $W_i^\mu(x)$ triplet, and one $\mathrm{U}(1)_Y$ gauge field, $B^\mu(x)$, used to define a covariant derivative [16]:

$$D^\mu = \partial^\mu + \frac{ig}{2}\bar{\tau} \cdot \bar{W}_i^\mu + \frac{ig'}{2} B^\mu \,, \qquad \text{where} \qquad i = 1, 2, 3 \,. \tag{2.32}$$

Anticipating symmetry breaking and the appearance of the Higgs field, we act on an $\mathrm{SU}(2)_L$ scalar doublet field,

$$\phi = \frac{1}{\sqrt{2}} \begin{pmatrix} \phi_1 + i\phi_2 \\ \\ \phi_3 + i\phi_4 \end{pmatrix} \,, \tag{2.33}$$

and the Lagrangian becomes:

$$\mathcal{L} = (D^\mu \phi)^\dagger (D_\mu \phi) + \mu^2 \phi^\dagger \phi - \frac{\lambda}{4}(\phi^\dagger \phi)^2 - \frac{1}{4}\bar{F}_{\mu\nu}\bar{F}^{\mu\nu} - \frac{1}{4} G_{\mu\nu} G^{\mu\nu} \,, \tag{2.34}$$

[8]Where L denotes the left-handed field components and Y denotes hypercharge, as introduced in Section 2.1.1. In this case, $\mathrm{SU}(2)_L$ transformations only involve the left-handed components of fermion fields, and the couplings are based on weak isospin charge. Meanwhile, $\mathrm{U}(1)_Y$ transformations involve both field components and couples via weak hypercharge, Y.

where

$$\bar{F}^{\mu\nu} = \partial^\mu \bar{W}_i^\nu - \partial^\nu \bar{W}_i^\mu - g\bar{W}_i^\mu \times \bar{W}_i^\nu \tag{2.35}$$

$$G^{\mu\nu} = \partial^\mu \bar{B}^\nu - \partial^\nu \bar{B}^\mu \,. \tag{2.36}$$

These are the field strength tensors of the forces associated with three $\mathrm{SU}(2)_L$ gauge fields and one $\mathrm{U}(1)_Y$ gauge field. It is now necessary to choose by hand the non-zero vacuum expectation value. The appropriate choice was proposed by Weinberg in 1967 to be [9]:

$$< 0|\phi|0 >= \begin{pmatrix} 0 \\ \\ \frac{v}{\sqrt{2}} \end{pmatrix} , \qquad \text{where} \qquad \frac{v}{\sqrt{2}} = \frac{\sqrt{2}\mu}{\sqrt{\lambda}} \,, \tag{2.37}$$

which leads to a theory with three massive gauge bosons and one massless gauge boson, and a symmetry breaking of $\mathrm{SU}(2)_L \times \mathrm{U}(1)_Y \rightarrow \mathrm{SU}(2)_L \times \mathrm{U}(1)_{EM}$. Experimental evidence requires that the photon is massless[9]. At the same time, Goldstone's theory states that massless bosons are associated with the symmetry that is left unbroken by the vacuum state. Therefore, the photon is expected to be associated with this symmetry that is left unbroken, while the weak vector bosons, which are known to be massive, should be associated with the symmetry that is no longer preserved. The unbroken symmetry is the $\mathrm{U}(1)_{EM}$ symmetry combined with the third component of $\mathrm{SU}(2)_L$ weak isospin. Before symmetry breaking, there exist four massless spin 1 fields with two polarizations. After symmetry breaking, the Goldstone bosons become the longitudinal components of the massive vector bosons. If we now consider oscillations about the vacuum state:

$$\phi = \begin{pmatrix} 0 \\ \\ \frac{1}{2}(v + H(x)) \end{pmatrix} , \tag{2.38}$$

[9]As one example, we know that due to the range of the EM interaction, the EM force carrier must be massless.

this expansion can be substituted into the Lagrangian. Keeping only second order terms in the fields, we find [16]:

$$\begin{aligned}\mathcal{L} = \frac{1}{2}\partial_\mu H \partial^\mu H - \mu^2 H^2 - \frac{1}{4}(\partial_\mu W_{1\nu} - \partial_\nu W_{1\mu})(\partial^\mu W^{1\nu} - \partial^\nu W^{1\mu}) + \frac{1}{8}g^2 v^2 W_{1\mu} W_1^\mu \\ -\frac{1}{4}(\partial_\mu W_{2\nu} - \partial_\nu W_{2\mu})(\partial^\mu W^{2\nu} - \partial^\nu W^{2\mu}) + \frac{1}{8}g^2 v^2 W_{2\mu} W_2^\mu \\ -\frac{1}{4}(\partial_\mu W_{3\nu} - \partial_\nu W_{3\mu})(\partial^\mu W^{3\nu} - \partial^\nu W^{3\mu}) - \frac{1}{4}G_{\mu\nu}G^{\mu\nu} \\ +\frac{1}{8}v^2(gW_{3\mu} - g'B_\mu)(gW_3^\mu - g'B^\mu)\,. \end{aligned} \tag{2.39}$$

Here we have three distinct massive fields, the H, W_1, and W_2 that appear in the first two lines. There are also two other fields, the W_3 and B that appear in the last two lines that have mass and are mixed. The W_3 and B fields can be unmixed by rotating into a different representation in field space. To do this, the weak mixing angle θ_W is introduced, defined as:

$$\cos(\theta_W) = \frac{g}{\sqrt{g^2 + g'^2}} \qquad \sin(\theta_W) = \frac{g'}{\sqrt{g^2 + g'^2}}\,. \tag{2.40}$$

Here, g and g' are couplings to the W and B fields as seen in Equation 2.39. Now, we can define two new bosons as Euler rotations in field space of the B^μ and W_3^μ fields:

$$Z^\mu = \cos(\theta_W)W_3^\mu - \sin(\theta_W)B^\mu \qquad A^\mu = \cos(\theta_W)W_3^\mu + \sin(\theta_W)B^\mu\,. \tag{2.41}$$

Thus the Lagrangian given by Equation 2.39 can be expressed as [16]:

$$\begin{aligned}\mathcal{L} = \frac{1}{2}\partial_\mu H \partial^\mu H - \mu^2 H^2 - \frac{1}{4}(\partial_\mu W_{1\nu} - \partial_\nu W_{1\mu})(\partial^\mu W^{1\nu} - \partial^\nu W^{1\mu}) + \frac{1}{8}g^2 v^2 W_{1\mu} W_1^\mu \\ -\frac{1}{4}(\partial_\mu W_{2\nu} - \partial_\nu W_{2\mu})(\partial^\mu W^{2\nu} - \partial^\nu W^{2\mu}) + \frac{1}{8}g^2 v^2 W_{2\mu} W_2^\mu \\ -\frac{1}{4}(\partial_\mu Z_\nu - \partial_\nu Z_\mu)(\partial^\mu Z^\nu - \partial^\nu Z^\mu) \\ +\frac{1}{8}v^2(g^2 + g'^2)Z_\mu Z^\mu - \frac{1}{4}F_{\mu\nu}F^{\mu\nu}\,. \end{aligned} \tag{2.42}$$

The first two terms in first line of Equation 2.42 describe the Higgs field - a scalar field with mass $\sqrt{2}\mu$. The remaining terms in the first line and the second line describe the W^+ and W^- bosons, which have mass of $\frac{gv}{2}$ at the tree level. The fourth and fifth lines of Equation 2.42 describe the neutral Z^0 boson, which has a mass of $\frac{v}{2}\sqrt{g^2+g'^2} = \frac{M_W}{\cos(\theta_W)}$ at the tree level. The last line also describes the photon, which is massless, exactly as expected.

Finally, we have a complete description of the Higgs sector. There are no couplings of the Higgs field to fermions included as these terms would violate gauge invariance; fermions instead acquire mass via Yukawa couplings to the Higgs field [25], where the mass of the particle is proportional to the strength with which it couples to the Higgs field.

2.2. Higgs at the LHC

Higgs bosons are produced via proton-proton (p-p) collisions at the LHC; however, the probability of producing a Higgs is relatively low. In collider physics, probabilities of particular interactions occuring during inelastic scattering are discussed in terms of cross sections, σ, which are quoted in units of barns (b), where 1 b = 10^{-28}m^2. This unit of measure originates from the rate at which neutrons in nuclear reactors hit Uranium-235 targets - a cross section of roughly 1 b.

At proton colliders such as the LHC, colliding proton beams can pass through each other, with only elastic collisions occurring between protons or partons (quarks and gluons inside the proton). However, we are more interested in inelastic collisions between partons, when new particles will emerge from the interaction point, with rates proportional to the cross sections for various interactions. These are known as hard scatter events.

The process with the highest cross section in p-p collisions is the process in which two partons are produced in the hard scattering and emerge from the collision point with high momentum. The interaction strength between the emerging partons increases as they separate, to the point that it becomes energetically favorable to produce color singlet hadrons. This process, known as fragmentation, leads to a cascading effect ending in highly collimated showers of particles known as jets.

This QCD activity is a signature feature of p-p colliders, and many measurements can be used to test predictions of the parton distribution functions (PDFs) of the colliding protons, as well as the accuracy of QCD predictions. However, high levels of QCD activity can also lead to large backgrounds referred to as "QCD backgrounds" in the physics signatures of interest. To highlight the large QCD activity, an illustration of a proton-proton collision simulated from Monte Carlo is given in Figure 2.3.

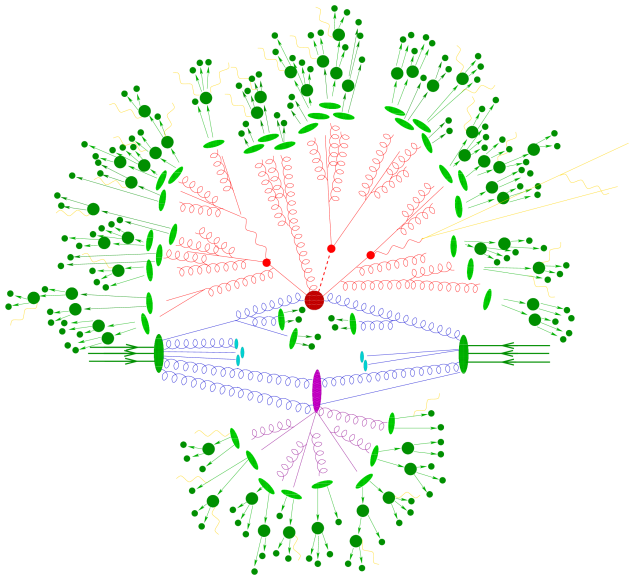

Figure 2.3. Graphic visualization of Monte Carlo simulation of a proton-proton collision. Here, the green ovals coming in from the left and right are the colliding protons. The red blobs indicates the hard scattering interaction, which produces the physics objects of interest. The particles coming out of the red blob represent Bremsstrahlung. The purple oval represents a secondary hard scattering event, and light green ovals surrounding the red and purple represent transitions from partons to hadrons, which may then decay (dark green circles). Finally, soft photon radiation is represented by the yellow lines [26].

As mentioned previously, this QCD activity can lead to large backgrounds obscuring other physics signatures of interest. Contrasted with the rate of production of jets at hadron colliders (at the LHC with center of mass energy of 13 TeV, this is roughly 10^7 pb), Higgs production has a relatively low cross section of roughly 60 pb [27].

Higgs bosons can be produced through various production modes. The most common modes at the LHC are shown in the Feynman diagrams below. In Figure 2.4, the two most dominant production modes at the LHC are shown. The Feynman diagram for gluon-gluon fusion (ggH), which accounts for 87% of Higgs events, is given in Figure 2.4(a), while the diagram for vector boson fusion (VBF), which accounts for 6.8%, is given in Figure 2.4(b). Following, in Figure 2.5, are the two vector boson associated production modes (VH), in which the Higgs is produced along with a W boson or along with a Z boson (WH or ZH). These account for 4% of Higgs events. Finally in Figure 2.6, the Feynman diagram corresponding to Higgs production along with a top quark pair (ttH) is shown. This production mode accounts for less than 1% of events in which a Higgs is produced. Higgs production along with a bottom quark pair (bbH) has a similar production rate as ttH, however its signature is difficult to distinguish from ggH production where gluon radiation leads to two or more jets. Furthermore, the jets from bbH production tend to be in the forward region, outside of the detectable phase space, making it difficult to observe. Other production modes are more rare and will not be discussed here.

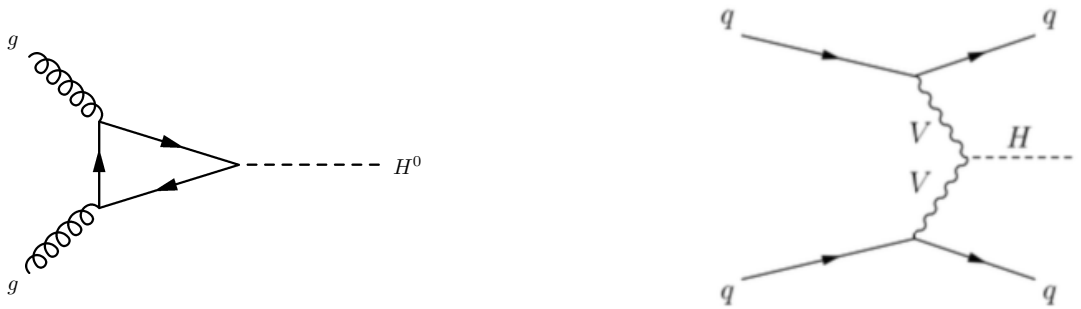

(a) ggH (b) VBF

Figure 2.4. Feynman diagrams representing Higgs production via gluon-gluon fusion, ggH and vector boson fusion, VBF [28].

With a predicted lifetime of 1.6×10^{-22} seconds, corresponding to a witdth of 4.2 MeV [29], the Higgs boson predicted by the SM cannot be observed on its own and instead must be

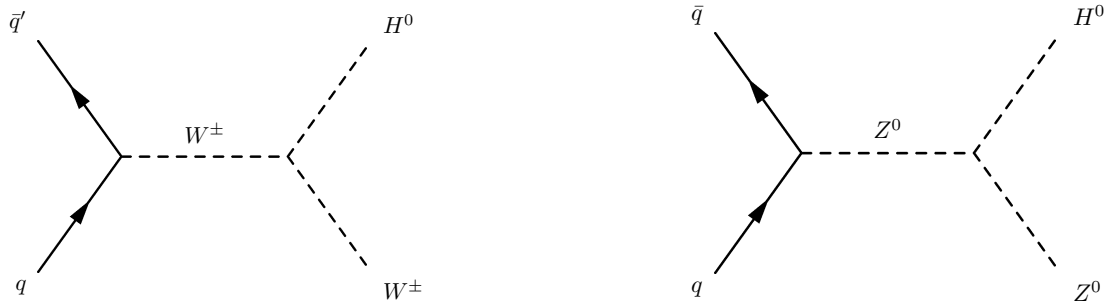

(a) WH (b) ZH

Figure 2.5. Feynman diagrams representing Higgs production via associated production with a W boson, WH, and association with a Z boson, ZH. Both are sometimes referred to as Higgsstrahlung [28].

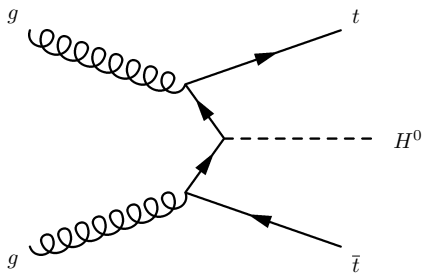

Figure 2.6. Feynman diagram representing Higgs production in association with a top quark pair, ttH [28].

studied via its decay products. At its observed mass of about 125 GeV, its decay rates are given in Table 2.1.

While the Higgs has the highest probability of decaying to a pair of b-quarks, it is a difficult channel in which to measure Higgs properties. The b-quarks are observed as jets which leave energy deposits in a calorimeter and can therefore be difficult to discriminate against the QCD background. The number of events in which a Higgs is produced and decays to b-quarks has a cross section on the order of 10^5 times smaller than that of total di-jet prodcution from QCD [27]. The Higgs decays to a pair of Z bosons much less frequently; however, the final reconstructed physics objects that are observed in the detector are the

Decay Mode	BR	Error %	
H$\to b\bar{b}$	5.77×10^{-1}	+3.21	-3.27
H$\to WW$	2.15×10^{-1}	+4.26	-4.20
H$\to gg$	8.57×10^{-2}	+10.22	-9.98
H$\to \tau\tau$	6.32×10^{-2}	+5.71	-5.67
H$\to c\bar{c}$	2.91×10^{-2}	+12.17	-12.21
H$\to ZZ$	2.64×10^{-2}	+4.28	-4.21
H$\to \gamma\gamma$	2.28×10^{-3}	+4.98	-4.89
H$\to Z\gamma$	1.54×10^{-3}	+9.01	-8.83
H$\to \mu\mu$	2.19×10^{-4}	+6.01	-5.86

Table 2.1. Branching ratios (BRs) for a Higgs with mass 125 GeV, with theoretical uncertainties [30]. The dependence of the BRs on the Higgs mass within the experimental uncertainties on the mass is below experimental precision.

objects to which the Z bosons decay. While these can be leptons, quarks, or neutrinos, the focus of this thesis is on the decay to leptons - specifically electrons and muons. Furthermore, precise knowledge of the Z mass at roughly 91 GeV [31] along with the invariant mass of the four lepton system can be used to constrain events with Higgs production against events with nonresonant two Z production. Because of this, and because leptons (excluding taus) have a very clean signature in detectors at the LHC, the Higgs to ZZ to four lepton channel is considered to be a "golden channel" for making precision measurements. This is the channel in which the measurements presented in this thesis are made.

2.3. Motivating Cross Section Measurements

The Standard Model (SM) has held up extremely well to experimental testing so far, yet there are many questions that have been left unanswered. Some of these are: Why is the mass of the Higgs boson 125 GeV? Why is there such a disparity between the scales of the fundamental forces? Is there a cause of the pattern we see in the grouping into generations of fermions based on mass? We currently have no explanation to these questions. Furthermore, the SM does not give a complete picture of interactions in nature. Gravity is not included

nor is any description of dark matter. All of these open questions and missing pieces indicate that the SM does not give us the full picture.

With pre-revolutionary thinking aimed at filling these gaping holes in the theory, we have seen the emergence of a multitude of models Beyond the SM (BSM theories). Many of these BSM theories predict new particles above the scale at which we are able to probe at current particle colliders. Even though we cannot detect these particles directly, if they are massive and acquire mass via the Higgs mechanism, their existence would modify the Higgs couplings to other, observable, particles. In this way, the Higgs serves as a useful tool for probing the existence of physics beyond the Standard Model.

This approach to searching for BSM physics motivates precision measurements of Higgs properties. Many of these precision measurements are sensitive to BSM effects and we can search for BSM physics without directly searching for new particles [32]. In addition, because these measurements are made within the fiducial volume of the detector - that is, within the detectable phase space - they are as model-independent as possible, which allows for comparisons with predictions from various models and ensures longevity of the results.

In this thesis, differential cross section measurements are made with respect to variables that probe the kinematics of the Higgs candidate and its decay products - for example probing spin and CP properties via angular relations between decay products. A more specific example is the measurement of $\frac{d\sigma}{dp_{\mathrm{T}}^{H}}$, the differential cross section with respect to Higgs transverse momentum, p_T^H. The treatement of top and bottom quark masses in the calculation of the ggH production cross section can lead to an order 10% difference in the differential transverse momentum cross section. Measuring this spectrum precisely provides a good test of our existing SM calculations. Furthermore, anomalous couplings to the Higgs and/or the existence of heavy BSM particles that could run in the loop in Figure 2.4(a) would modify this spectrum, causing devations from the SM prediciton.

Measurements are also presented in this thesis which allow us to study the nature of jet activity in Higgs events. Differential cross section measurements such as $\frac{d\sigma}{dN_{jets}}$, the differential cross section with respect to the jet multiplicity in an event in which a Higgs

is produced, can provide information on how well QCD activity is modeled. They are also sensitive to different Higgs production modes. The $p_{\mathrm{T}}^{\mathrm{lead.jet}}$ distribution, or $\frac{d\sigma}{dp_{\mathrm{T}}^{\mathrm{lead.jet}}}$, is sensitive to theoretical modeling of high p_T quark and gluon emission.

The ultimate aim for the analysis presented in this thesis is a set of model-independent measurements that are sensitive as probes of possible deviations from the Standard Model. Differential cross sections have helped push our understanding of physics further in the past, and they continue to be key components in the sets of measurements that probe potential BSM signatures.

CHAPTER 3

The ATLAS experiment at the LHC

The European Organization for Nuclear Research (CERN) was established in 1954, and has since been home to many physics experiments pushing the energy frontier in search of new physics, including the highest energy collider to date, the Large Hadron Collider (LHC). The LHC is a large ring, 27 kilometers in circumference, that lies 100-200 meters beneath the French-Swiss border, just west of Geneva. It is the largest particle accelerator in the world, accelerating protons to nearly the speed of light and colliding them at center-of-mass energies of up to 13 TeV. These collisions take place at four different points around the ring (so called "interaction points") where data is recorded and analyzed by four independent experiments: ALICE, LHCb, CMS, and ATLAS. Of the four detectors, ATLAS (A Toroidal LHC AparatuS) and CMS (Compact Muon Solenoid) are two general-purpose detectors. This means that while ALICE and LHCb were designed with the intent of studying specific physics properties (physics in heavy ion collisions and flavor physics, respectively), ATLAS and CMS were designed for a broad physics program aimed at discovery of new phenomena. This program ranges from the study of known physics processes, to the search for expected but still unobserved physics signatures (e.g. signatures of the Higgs boson[1]), to the search for signs of BSM physics. In this chapter, relevant information about the LHC, ATLAS, and the different subsystems within the two will be provided.

3.1. The LHC

[1]The Higgs had not yet been observed when the detectors were being designed. They were designed with the hope of finding the Higgs as well as supersymmetry. Only one of these came to fruition..

The LHC began operation in September 2008. Though the LHC occasionally collides heavy ions, its main focus is proton-proton collisions. Protons are supplied from hydrogen gas subjected to an electric field of 90 kV that breaks down the gas into protons and electrons. The protons are then accelerated by the LINAC2, a linar accelerator that uses radio-frequency (RF) cavities to accelerate the protons to an energy of 50 MeV. At this point, the protons enter the proton synchrotron booster, where four vertically stacked synchrotron rings are available to accelerate the protons further (up to 1.4 GeV in 1.2 seconds) before they are injected in bunches into the proton synchrotron, or PS. The proton synchrotron accelerates the protons up to 24 GeV, then injects them into the super proton synchrotron (SPS), the second largest machine in CERN's accelerator complex. Here they are accelerated up to 450 GeV before finally being injected into the LHC. When injected into the LHC, the protons are in bunches with a typical intensity of 1.5×10^{11} protons per bunch. They reach an energy of 6.5 TeV, for a center of mass energy of 13 TeV at the four collision points [33]. This center of mass energy was reached in 2016.

The operation of the LHC so far has been broken up into two segments - Run 1, which includes data taken between 2009 and 2013, and saw the discovery of the Higgs boson, and Run 2, which includes data taken between 2015 and 2018. The material in this thesis uses only data from the LHC Run 2, which operated at a center of mass energy of 13 TeV. The following description of the LHC operation parameters as well as ATLAS and its various subsystems reflect the status at the end of Run 2, before the Phase I upgrades and the start of Run 3.

3.1.0.1. Luminosity at the LHC

The number of events per second that occur at an interaction point is given by the cross section for such an event, σ_{event}, multiplied by the instantaneous luminosity provided by the LHC, L:

$$\frac{N_{event}}{s} = L\sigma_{event}\,. \tag{3.1}$$

The instantaneous luminosity, typically quoted in units of $\mathrm{cm}^{-2}\mathrm{s}^{-1}$, is a measure of how many collisions per second are possible, given the parameters of the proton beams provided by the LHC to the different interaction points. The instantaneous luminosity is given by the equation [34]:

$$L = \frac{N_b^2 n_b f_{rev} \gamma_r}{4\pi \epsilon_n \beta^*} F \,. \tag{3.2}$$

Here, N_b is the average number of particles per bunch, n_b is the number of bunches, and f_{rev} is the frequency of revolution of the bunches. For the nominal LHC operation in Run 2, these numbers were 1.5×10^{11} protons per bunch, 2556 bunches (with 25 ns spacing between the time of collision of consecutive bunches), and a rate of 40MHz [35]. The relativistic gamma - γ_r, transverse emittance - ϵ_n, and beta star - β^*, together quantify the spread of the beam in the transverse plane and give a measure of how localized it is. In Run 2 these had values of $\gamma_r = 7461$, $\epsilon_n \approx 2\mu m$, and $\beta^* \approx 25 - 30$ cm. Finally the geometric reduction factor, F, is a function of the crossing angle of the beams (θ_c) as well as the bunch length (σ_Z). This factor takes into account that while the bunches can be treated as gaussian ellipsoids, they have a much larger spread in the z-direction than in the radial direction. Furthermore, they don't cross head on, but rather at an angle. The crossing angle in ATLAS during Run 2 varied between 120 and 150 μrad, while the RMS bunch length was 7.55 cm, leading to an average value for F of 0.836 [34] [35].

The total integrated luminosity, $L_{int} = \int L dt$, delivered to ATLAS from the LHC in Run 2 is shown in Figure 3.1 below, represented in green, while the integrated luminosity read out by the ATLAS detector is shown in yellow. Of the recorded data, the total amount usable for physics is shown in blue.

Another important quantity that will be discussed in following chapters is pileup, μ. Pileup refers to multiple inelastic collisions that occur during one bunch crossing. With the high luminosities reached at LHC during Run 2, pileup collisions also reached record numbers, with up to 80 interactions per bunch crossing occurring at the maximum, and an average of 33.7 interactions per bunch crossing during the full Run 2 operation period. The

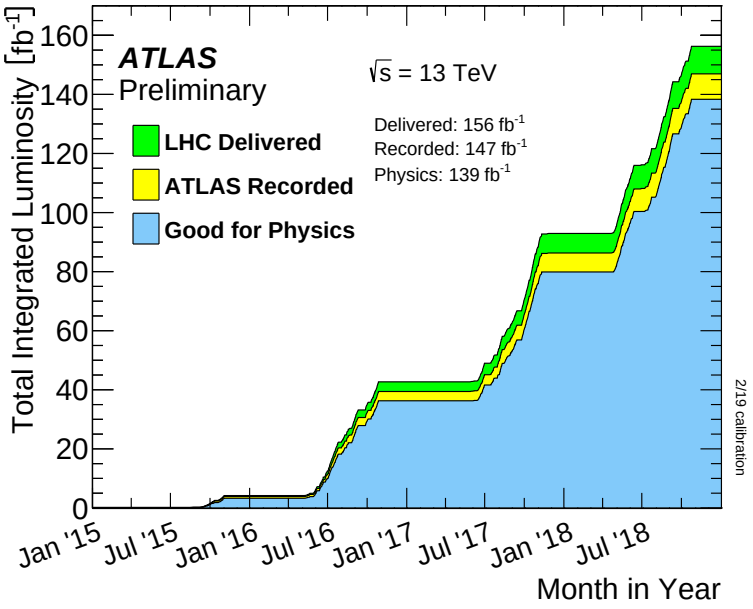

Figure 3.1. Integrated luminosity delievered by LHC (green), recorded by ATLAS (yellow), and deemed good to use for analyses (blue) during Run 2 [36].

recorded luminosity as a function of μ can be seen in Figure 3.2, with the distribution per year shown as well as the average pileup (average number of interactions per bunch crossing) per year.

These large values of pileup cause unique challenges with implications for detector design that will be discussed in the following sections.

3.2. The ATLAS detector

The ATLAS detector (often referred to as simply "ATLAS") is one of two general-purpose detectors built to detect, record, and reconstruct particles that are created in collisions at the LHC. It is roughly 45 m long and 25 m high, located in a cavern 100 m below the LHC Point 1, where the ATLAS control room is located. An illustration of the detector is shown in Figure 3.3.

The ATLAS detector is made up of various subdetectors organized concentrically around the beam pipe, with collisions taking place at the midpoint. Together, the subdetectors

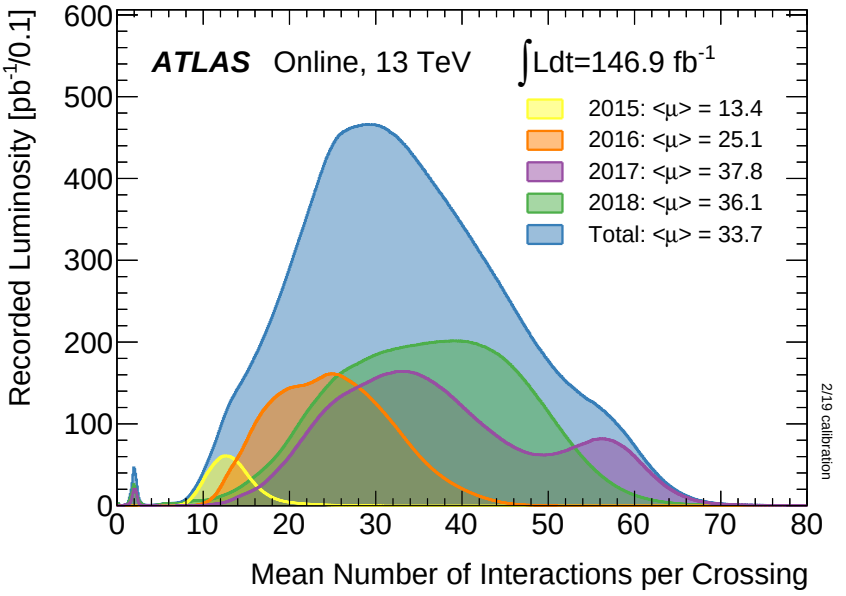

Figure 3.2. Luminosity as a function of the number of interactions per bunch crossing (pileup, or μ) during each year of the LHC Run 2. The total distribution is shown in blue. The average number of interactions per bunch crossing, $< \mu >$, is provided for each year separately and for all four years combined [36].

are designed to identify particles emerging from collisions and measure their charge, energy, momentum, and other properties. Combined, the information from all subdetector systems provides a description of a collision event, with each system providing specific parts of this full description.

The first subdetector system that a particle encounters when emerging from the collision point is the inner tracking system, often referred to as the inner detectors. Housed inside a solenoid magnet, the tracking system is designed to measure the momentum of charged particles while at the same time keeping the energy deposited by the particles in the system to a minimum. Once outside the tracker, all known particles except for muons and neutrinos will deposit their energy in the calorimeters, which surround the tracking system. Finally, the muon tracker system, aided by toroidal magnets that bend the trajectories of the muons,

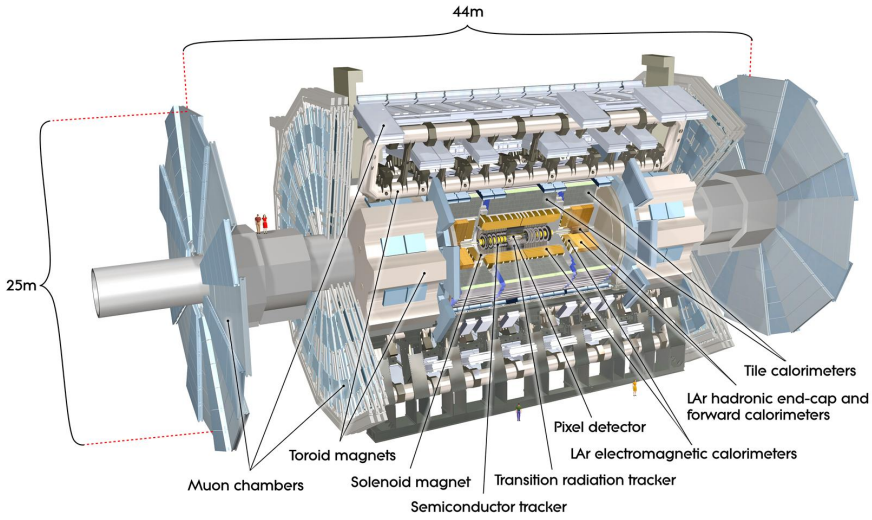

Figure 3.3. Illustration of ATLAS detector with human for scale [37].

identifies muons that have passed through the tracking and calorimeter systems and measures their momenta.

The goal in designing the ATLAS detector was to have the highest coverage possible around the collision point as well as to maximize the energy and momentum resolution of all physics objects originating from it. The details of each subdetector and how they contribute to achieving this high level of performance will be provided in the following sections, after a short description of the ATLAS coordinate system.

3.2.0.1. ATLAS Coordinate System

Preceeding a description of the ATLAS subsystems, a definition of the coordinate system is necessary. ATLAS uses a right-handed coordinate system depicted in Figure 3.4. The x-axis points towards the center of the LHC, the y-axis points upward, and the z-axis runs along the beam pipe. The origin of the axes is set at the interaction point. The half of the detector that is east of the interaction point is known as the "A side", while the western half is known as the "C side". While these descriptors are not used for physics analyses, they are useful when describing the detector subsystems.

In physics analyses, a cylindrical coordinate system is typically used. The azimuthal angle, ϕ, is the angle around the beam axis, while the polar angle, θ, is measured from the beam axis [38].

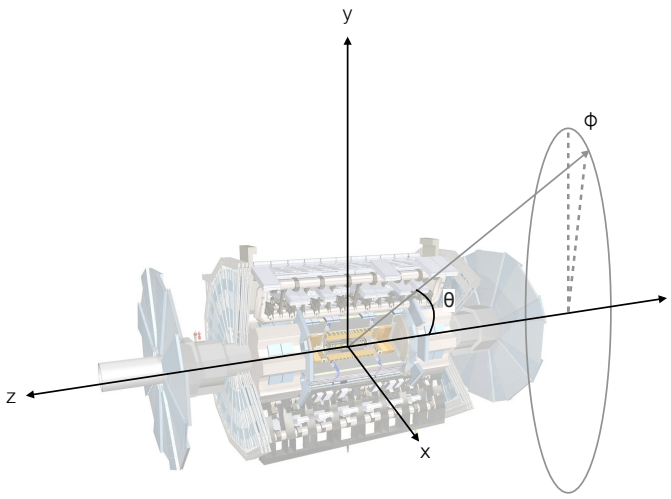

Figure 3.4. Coordinate system used in the ATLAS experiment.

Two commonly used angles in particle physics are the rapidity, y, and pseudorapidity, η. The rapidity is defined as:

$$y = \frac{1}{2}\ln(\frac{E + p_z}{E - p_z})\,, \tag{3.3}$$

where E is the energy of the physics object in consideration and p_z is its momentum in the direction of the beamline. The pseudorapidity is defined as:

$$\eta = -\ln(\tan(\frac{\theta}{2}))\,. \tag{3.4}$$

Collisions at the LHC take place in a highly relativistic regime. Rapidity is a useful angle to use when discussing collision products due to the invariance of differences in rapidities

between two objects under Lorentz boosts along the beam direction. For highly energetic particles, pseudorapidity can be a more useful angle due to the relative ease of calculation compared to rapidity; however for highly relativistic particles, the two are almost identical.

The transverse momentum, or p_T, of an object is its momentum in the x-y plane, transverse to the beamline. It is defined by $p_T = p \sin\theta$. The distance between two reconstructed physics objects is typically referred to in the pseudorapidity-azimuthal angle space using:

$$\Delta R = \sqrt{\Delta\eta^2 + \Delta\phi^2}\,. \tag{3.5}$$

3.2.1. Inner detectors

There are three distinct detectors that make up inner tracking detector subsystem in ATLAS. They sit inside a 2 T central solenoid magnet that bends the trajectory of charged particles. The magnetic field will bend a charged particle's trajectory according to the classical force law $\bar{F} = q\bar{v} \times \bar{B} = m\frac{v^2}{r}$, where q is the charge of the particle, $\bar{v}$ is the particle's velocity, $\bar{B}$ is the strength and direction of the magnetic field, m is the mass of the particle, and r is the radius of the bent trajectory. "Hits" refer to signals in the sensors of the detector that arise when a particle passes through. When hits occur in several parts of the inner detector, one can construct a fit of the curved trajectory, and thus determine the momentum and charge of the particle that passed through. This will be discussed in detail in Chapter 4, where the reconstruction of physics objects is explained.

Due to the high luminosity and high pileup, there can be thousands of tracks in the inner detectors during bunch crossings. To handle such high track densities, these detectors were designed to have high granularity and excellent charged particle momentum and vertex resolution. In the following sections, a description of the inner detectors, illustrated in Figure 3.5 is given.

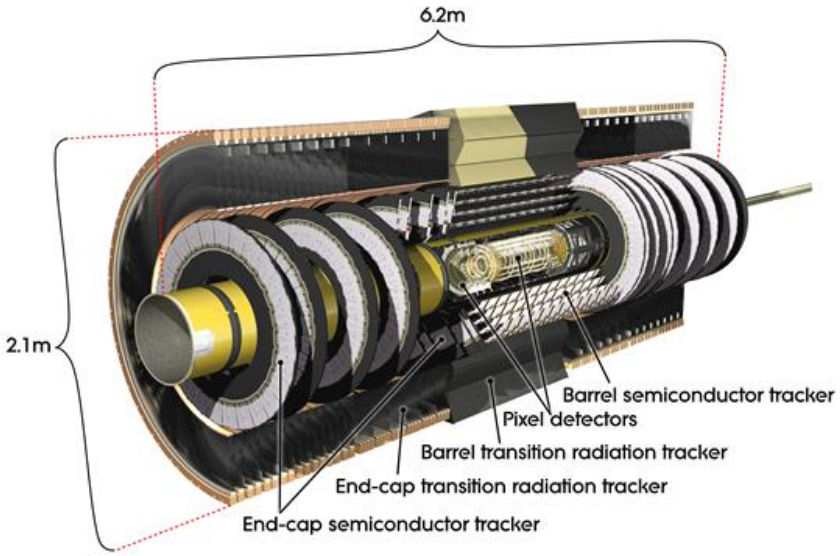

Figure 3.5. Illustration of ATLAS inner detector system [37].

3.2.1.1. Pixel Detector

The detector closest to the beampipe is the pixel detector. The pixel detector is made up of 1744 silicon pixel modules with over 80 million read-out channels. The modules are divided into three concentric cylindrical 'barrel' layers, which cover the more central region in $|\eta|$, as well as one endcap on each side of the barrel, each comprised of three disks. Each module is made up of 250 μm n-on-n silicon sensors divided into 47232 pixels, each with an average size of 50×400 μm^2 [39]. These hybrid pixel modules are each connected to a readout chip connected via bump bonding. As a charged particle traverses a sensor, it ionizes the material, creating electron hole pairs that drift in an applied electric field and induce a current on the pixel electrode. Each module has a resolution of 10 μm in r-ϕ and 115 μm in z. In total the pixel detector has full ϕ coverage and pseudorapitity coverage between $0 < |\eta| < 2.5$.

An innermost fourth barrel layer, the insertable b-layer (IBL), was installed in May 2014 during the long shutdown after the LHC Run 1 in order to reduce the distance from the interaction point (IP) to the first tracking layer during Run 2. The IBL is comprised of 280

silicon pixel modules supported by 14 carbon fiber staves. It surrounds the beam pipe with a mean radius of 33 mm from the axis, allowing for better determination of secondary vertices of long-lived particles [40].

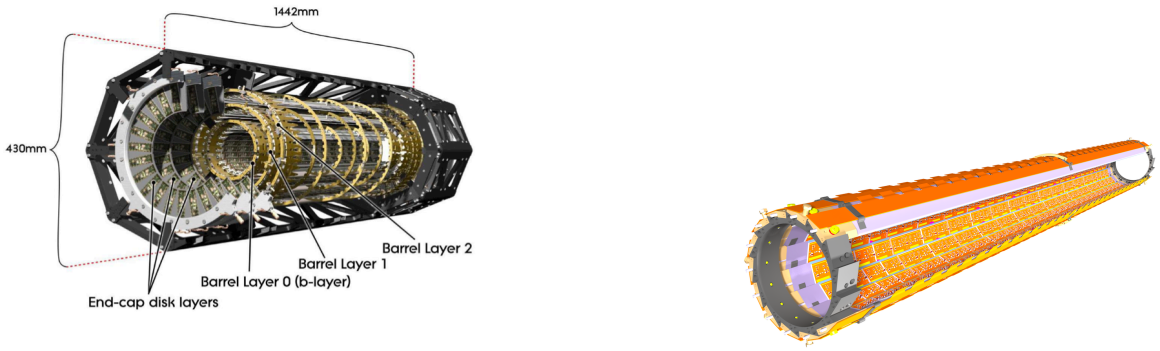

(a) Pixel Run 1

(b) IBL

Figure 3.6. Schematic drawings of the ATLAS Pixel detector as of Run 1 [41], and the Insertable B-Layer (IBL) inserted concentrically within the Pixel detector for Run 2 [42].

3.2.1.2. Semiconductor Tracker

Moving radially outwards, the semiconductor tracker (SCT) surrounds the pixel detector, extending from a radial distance of 299 mm from the beampipe out to 560 mm. It is comprised of 4088 p-on-n silicon strip detector modules. Of these 4088 modules, 2112 are in four concentric barrel layers, while 988 are in two encaps, each comprised of nine disks. Each of the modules is two-sided, with four rectangular silicon strip sensors. In contrast to the pixel detector, which uses silicon pixels as the basic detecting unit where each pixel is read out and thus provides a true 3D spacepoint, the SCT's silicon microstrips only provide measurements in one coordinate. The modules are two-sided, with the strips on one side oriented at a small angle with respect to those on the other, allowing for a 2D measurement. Strips are read out every 80 μm, which leads to a resolution of 17 μm in each layer, in r-ϕ, and a resolution of 580 μm in the z direction [41]. The modules are mounted to supports in an angular fashion such that they provide hermitic coverage in ϕ, and allow for eight strip measurements to be provided for particles originating at the interaction point [43].

3.2.1.3. Transition Radiation Tracker

The transition radiation tracker (TRT) is the final component of the ATLAS inner detector system. Extending radially from 554 mm to 1082 mm from the beampipe, it consists of wound Kapton drift tubes 4 mm in diameter that are reinforced with thin carbon fibers. Inside the tubes are gold-plated tungsten wires, 31 μm in diameter, that are grounded, while the tubes are kept at -1.5 kV. The tubes are filled with a gas mixture of Xe, CO_2, and O_2. When a charged particle passes through the TRT, this gas mixture is ionized and free elctrons drift to the wire where the signal is read out. The barrel region, covering $|\eta| < 1$, contains 52544 of these tubes placed parallel to the beamline, each 1.5 m long and read out at both ends. In the end cap region, the tubes are 0.4 m long and are oriented radially outward and read out at the outer ends. Here they cover $1 < |\eta| < 2$.

The TRT is filled with polymer fibers between the tubes in the barrel region and foils in the endcap region. This creates, in addition to the ionization signal inside the tubes,

transition radiation that occurs when a relativistc charged particle traverses the material boundary. This radiation is logarithmically dependent on the relativistic factor, $\gamma = \frac{E}{m}$, which aides in particle identification. Examples can be seen in Figures 3.7(a) and 3.7(b), where the γ factor is used to distinguish muons tracks from electron tracks and pion tracks from electron tracks, respectively. Thus, the TRT provides complimentary information to the SCT and pixel detectors. While it has a worse intrinsic spatial resolution of 120 μm, it benefits from a larger number of hits per particle track, which is typically around 30. Furthermore its radial distance from the interaction point provides a larger lever arm, allowing for more precise momentum determination [44].

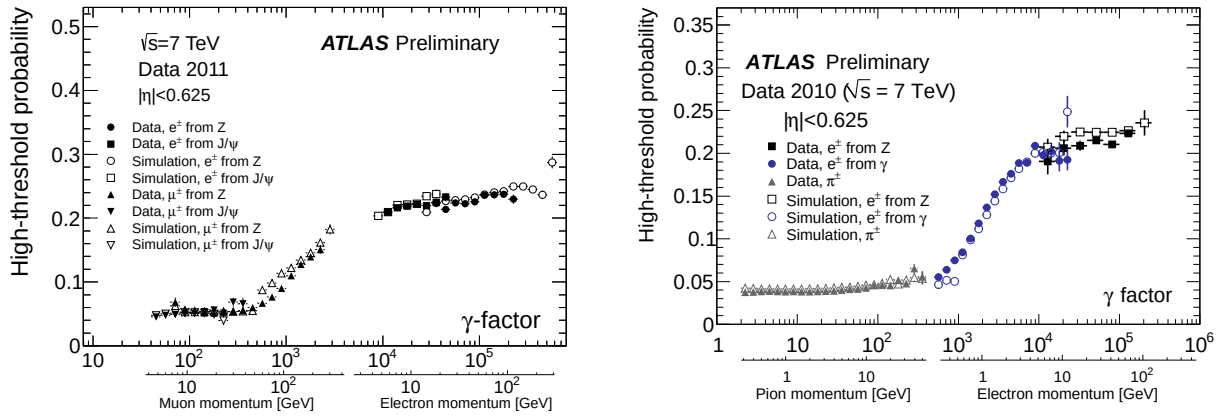

Figure 3.7. Examples of turn-on curves for the relativistic γ factor measured in the TRT barrel region which can be used to discriminate between muon and electron tracks (left) and pion and electron tracks (right). In both plots, solid points represent data while open points represent simulation. In Figure 3.7(a), circles correspond to electrons from the decays of Z bosons, squares correspond to electrons from the decays of J/ψs, while triangles and upside-down triangles correspond to muons from each of the two sources, respectively. In Figure 3.7(b), squares and circles correspond to electrons from the decays of Z bosons and photon conversions, respectively, while triangles correspond to pions [45].

3.2.2. Calorimeters

Particles that pass through the inner detectors will next encounter the calorimeters, which measure deposited energy. There are two types of calorimeters in ATLAS - electromagnetic (EM), which occupy the central barrel region, and hadronic, which cover the forward region as well as the barrel region surrounding the EM calorimeters. They were designed such that particles such as electrons and photons deposit the entirety of their energy in the EM calorimeter, while hadrons and the jets originating from them leave deposits in the EM calorimeters and are stopped in the hadronic calorimeters, where they deposit the remainder of their energy. In order to avoid punch-through from particles like electrons into the hadronic calorimeter layers, or from jets into the muon system, the calorimeter layers were designed with specific radiation and interaction length requirements.

The calorimeters in ATLAS are broken up into two distinct subsystems - the Liquid Argon (LAr) calorimeters, which have both EM and hadronic partitions, and the Tile calorimeter, which is fully hadronic. The details of these two subsystems are provided in the following sections.

3.2.3. LAr calorimeter

The ATLAS Liquid Argon Calorimeter system (LAr) is composed of a set of electromagnetic and hadronic sampling calorimeters that aim to measure the energies of particles that have passed through the tracking layers. Liquid argon was chosen as the active material due to its long radiation length, linearity, and radiation hardness. Several different absorbing materials and several different detector geometries are used in the different LAr subdetectors in order to meet the requirements of the different physics processes of interest expected over the η range covered by the calorimeter as well as to handle expected levels of particle fluence.

LAr is made up of two electromagnetic barrel calorimeters (EMB) that provide coverage in the region $0 < |\eta| < 1.475$. These have an accordion-shaped structure that provides full coverage in ϕ, and use lead as the absorbing material. In addition to the full ϕ coverage, the accordion shape has a bending angle that decreases as a function of distance from the

beampipe, which allows for constant gap thickness and provides a good uniformity of response, around 0.7% [46]. Copper electrodes are held in place between the lead absorbing plates by honeycomb spacers, and a voltage ranging from around 300 to 2000 V, dependant on the $|\eta|$ region, is applied across the gaps that are filled with the liquid argon. A cross section can be seen in Figure 3.8(a), while Figure 3.8(b) illustrates the four sampling layers in an EMB module.

The presampling layer provides information closer to the interaction point before EM showers have developed laterally. The fine granularity of the first targets π^0 detection, while the second sampling layer contains most of the energy of the shower. Finally, the third layer catches the tails of the showers from electrons and photons and provides important shower shape information for particles that carry on to the hadronic calorimeter. The granularity of the cells in η and ϕ are provided in Figure 3.8(b) as well, along with the radiation lengths in each of the four layers.

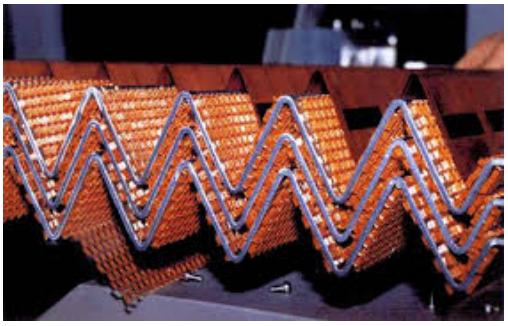

(a) LAr EMB cross section

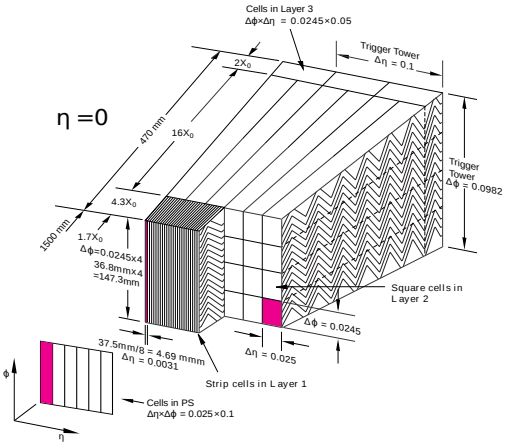

(b) Illustration of EMB sampling layers

Figure 3.8. Cross section of the LAr electromagnetic barrel (EMB) calorimeter in which the accordion geometry is apparent [47] and illustration of sampling layers in the EMB [48]. Honeycomb spaces hold copper electrodes in place between the lead absorber plates. The gaps between are filled with liquid argon as the active material.

Between $1.4 < |\eta| < 3.2$ are the electromagnetic end cap calorimeters (EMEC). These are composed of an inner and outer wheel, both of which are formed from azimuthal sections with

accordion geometry where the fold again varies with respsect to the radius. Lead absorbers and liquid argon are used in the EMEC, similarly to the EMB.

In the foward region of detector are the hadronic end caps (HEC) and forward calorimeters (FCAL), which cover the regions $1.5 < |\eta| < 3.2$ and $3.2 < |\eta| < 4.9$, respectively. These employ slightly different geometries than the previous two. The HEC wheels are constructed from copper plates with 8.5 mm gaps in which electrodes made of carbon-loaded kapton are placed. These wheels are composed of 32 azimuthal modules, and are housed in the endcap cryostats [49].

Finally, the FCAL is composed of three wheel-shaped modules on each side - one EM module and two hadronic modules. In the EM case, the modules consist of an absorbing bulk material into which copper electrode tubes are inserted. Tugsten electrodes are used in the case of the hadronic modules. Anode rods, with diameters slightly less than those of the electrode tubes and made of the same material as the absorber, are housed inside the tubes. They are positioned concentrically via plastic fibers wound around them in a helix, such that very thin gaps are formed between the anode and cathode. The narrowness of the gaps prevents ion build up in this forward region that receives high particle fluxes. The gap is filled with LAr as the active medium [47].

The granularity in each of the different sampling layers, depicted in the barrel region in Figure 3.8(b), is provided in Table 3.1 in different η regions. The granularity of information sent to the Level 1 Trigger, discussed in Section 3.2.6 is also provided, as are the number of readout channels in each η region.

The energy resolution of calorimeters is determined by:

$$\frac{\sigma_E}{E} = \frac{a}{\sqrt{E}} \oplus \frac{b}{E} \oplus c\,. \tag{3.6}$$

In defining the resolution, a is a stochastic term, which cannot be modeled and is dependent on the number of sampling layers and the fraction of energy seen in the lead versus LAr layers [46]. It is often referred to as the sampling term. In the ATLAS LAr calorimeter is it 11%. The second term, b, is the systematic term, determined from calibrations and

LAr Calorimeter Granularity					
$\|\eta\|$ range	0 to 1.4	1.4 to 1.8	1.8 to 2.0	2.0 to 2.5	2.5 to 3.2
Presampler	0.025×0.1	0.025×0.1	-	-	-
Sampling 1 (Front)	0.003×0.1	0.003×0.1	0.004×0.1	0.006×0.1	0.1×0.1
Sampling 2 (Middle)	0.025×0.025	0.025×0.025	0.025×0.025	0.025×0.025	0.1×0.1
Sampling 3 (Back)	0.025×0.025	0.025×0.025	0.025×0.025	0.025×0.025	-
Trigger	0.1×0.1	0.1×0.1	0.1×0.1	0.1×0.1	0.2×0.2
Readout Channels	110,208	25,600	12,288	24,064	1792

Table 3.1. Granularity in different $|\eta|$ regions for each sampling layer of the LAr calorimeter, as well as the granularity of information sent to the Level 1 Trigger. In addition, the number of readout channels in each $|\eta|$ region is provided [49].

referred to as the noise term, as it driven by electronic noise and pileup. Finally, c is the constant term, which is 1.2%, 1.8%, 3.3%, and 2.5% in EMB, EMEC outer wheel, EMEC inner wheel, and FCAL, respectively [50]. It has contributions from many sources, including the absorber and gap thickness and cross-talk between channels.

The first term dominates at low energy. To prevent it from being too high, the presampling layer of the calorimeter also serves to correct for energy losses in dead material before the rest of the calorimeter.

3.2.3.1. Measuring energy

When an electromagnetically interacting particle passes through the lead absorbers, it creates a shower of particles via photon conversions and/or Bremsstrahlung. These showers traverse the gaps filled with liquid argon, ionizing it along the tracks. An applied high voltage between the gaps causes the electrons and ions to drift, inducing an electrical signal which is read out via the read-out electronics.

The first steps in the read-out system are carried out by the front end electronics, housed in Front End Crates (FECs) that are mounted concentrically around the calorimeter. Each

crate houses 28 Front End Boards (FEBs) that perform the first set of readout operations, Tower Builder Boards (TBBs), a controller board, and a calibration board.

The FEBs recieve the signals from the calorimeter cells and amplify and shape them. The ionization current signal has a triangular shape versus time; however these signals are shaped and contracted as a first step in the read-out process in order to mitigate the effects of interactions that may overlap in time. This occurs when, while the signal currents from one interaction are still being collected on the electrodes, another interaction has already occured and induced more showers in the calorimeter. This is done by a preamplifier and CR-RC^2 shaping filter on the FEBs, and the signals are then stored in a switched capacitor array while awaiting a decision on whether or not the event will be stored. More information on this decision, made by the trigger system, will be given in Section 3.2.6.

Meanwhile, coarser granularity information is provided to the trigger system by the TBBs, which perfom analog sums of the calorimeter signals from the different sampling layers in a trigger tower, which is formed by goups of cells covering $\Delta\eta \times \Delta\phi = 0.1 \times 0.1$.

If the event passes the level 1 trigger criteria, the full calorimeter granularity signals are digitized by a 12 bit analog-to-digital converter (ADC) on the FEBs and transmitted opitcally to the back-end electronics.

3.2.3.2. Calibration system

The energy deposited in a calorimeter cell is calculated by:

$$E_{cell} = F_{\mu A \to MeV} F_{DAC \to \mu A} \frac{M_{calib}}{M_{phys}} \sum_{i=1}^{M_{ramps}} R_i [\sum_{j=1}^{N_{samples}} a_j (s_j - p)]^i \,. \tag{3.7}$$

The terms are described below. Those that are determined from calibration are denoted, with the description of the calibration types provided following.

- $F_{\mu A \to MeV}$ - conversion between ionization current in μA and cell energy in MeV. This value is obtained from test beam studies.

- $F_{DAC \to \mu A}$ - conversion between digital to analog converter (DAC) signal input from calibration boards to μA. This value comes from the calibration boards.
- $\frac{M_{calib}}{M_{phys}}$ - pulse shape comparison between physics and calibration signals, determined from delay calibration runs.
- R - conversion factor between ADC and DAC, determined from ramp calibration runs.
- $N_{samples}$ - number of samples
- a_j - optimal filtering coefficients
- s_j - pulse samples
- p - pedestals, determined from pedestal calibrations.

During calibrations, a known pulse signal is injected and read out via the normal data readout path. There are three types of calibrations designed to measure the various terms needed for calculating the energy of an unknown signal pulse from data. These are:

- Ramps - injected input current (DAC) values are scanned and analog signals are read out
- Delays - cells are pulsed several times with a known DAC value with delays between calibration pulses, allowing for the reconstruction of the full calibration curve
- Pedestals - no signal is injected and the FEBs read out electronic noise

My work in the LAr online software group was focused on development and maintenenace of code for the calibration infrastructure. More details of my work are provided in Appendix A. My work related to the operations of LAr is described in Appendix B. Though they are not the focus of this thesis, my activities described in these appendices comprised a large part of my work during my graduate studies.

3.2.4. Tile calorimeter

The tile calorimeter, located concentrically outside of the LAr calorimeter, is a hadronic sampling calorimeter that measures the energy of hadrons. Objects such as hadrons, τ's, and jets will have deposited some of their energy in the EM calorimeters, and the remainder will be deposited in the hadronic calorimeter. When traversing the hadronic calorimeter, these particles interact with the nuclei in the steel absorbers, creating secondary particles which undergo further inelastic collisions. This leads to a cascade of energy through sequential decays of the secondary and further resulting particles. Interspersed between the absorbers are plastic scintillators which, when traversed by these ionizing particles, produce UV scintillation light. This light is collected by wavelength shifting fibers and transmitted to a PMT, after which point it is read out.

These layers of absorber/scintillator are the basis of the tile calorimeter modules. These modules are wedge-shaped in the azimuthal direction, as depicted in Figure 3.9, and comprised of alternating layers of 5 mm thick steel plates with 4 mm spacing in which scintillating polystyrene tiles were inserted. The tile calorimeter consists of a 5.8 m long central barrel region and two extended barrels, each 2.6 m long, and covers the region $|\eta|< 1.7$. These extend from an inner radius of 2.28 m to an outer radius of 4.25 m. Each of the four cylindrical components is made of 64 of the wedge-shaped modules.

In total, the tile calorimeter has about 5,000 cells, each covering $\Delta\eta \times \Delta\phi$ of 0.1×0.1 in most of the segments. This corresponds to roughly 10,000 readout channels.

3.2.5. Muon system

ATLAS was designed such that the momentum of muon tracks could be measured in two independent systems. The first is the inner tracking system, described in Section 3.2.1. The second is the Muon Spectrometer (MS), or muon tracking system. The goals of the muon tracking system are to identify and reconstruct muon tracks with a high momentum

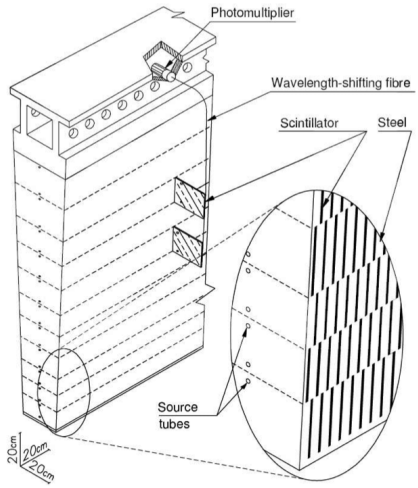

Figure 3.9. Illustration of one module of the Tile calorimeter. Each module is wedge-shaped, covering 0.1 radians in ϕ [51].

resolution of 3% over a wide range of track momenta and 10% at $p_T = 1$ TeV [2]. Full phase space coverage is needed, up to $|\eta| \leq 3$. Finally, the ability to trigger on event topologies with single or multiple muons with high efficiency and quickly, within the period between bunch crossings, is critical. The design choices that satisfy these requirements are detailed in the following subsections.

In order to bend the trajectories of the muon tracks, ATLAS uses a second magnet system comprised of three large superconducting toroid magnets. In the barrel region covering $|\eta| < 1.4$, a large barrel toroid magnet consisting of eight coils outside of the tile calorimeter provides the magnetic field. In the region $1.4 < |\eta| < 2.7$, two endcap magnets sit inside the ends of the barrel toroid. In the transition region between the two, trajectories are bent by a combination of the fields. Throughout, the field lines are mostly perpendicular to the muon trajectories, thus bending muon tracks in the transverse plane, and the field has an average value of 4 T. Furthermore, the radial distance between the interaction point and the muon system allows for maximal profit of the toroidal magnet system due to the large lever arm.

[2]This was important in targeting a key Higgs discovery channel, $H \to ZZ \to \mu\mu\mu\mu$, as well as searching for physics beyond the Standard Model.

To reach the MS, a muon must have greater than around 3 GeV in p_T due to energy loss in the calorimeters.

The muon detection system itself is comprised of chambers arranged in layers called stations. These chambers belong to four distinct subsystems - two that provide precision measurements of the muon tracks, and two that provide fast identification for the triggering system. The two precision measurement systems are the Monitored Drift Tubes (MDTs) and the Cathode Strip Chambers (CSCs). The two triggering systems are the Resistive Plate Chambers (RPCs) and the Thin Gap Chambers (TGCs). An illustration of the muon system in the y-z plane is shown in Figure 3.10(a), while a second perspective from the x-y plane is shown in Figure 3.10(b). The toroidal magnets are depicted in both illustrations. Descriptions of the four types of chambers used in the muon system follow.

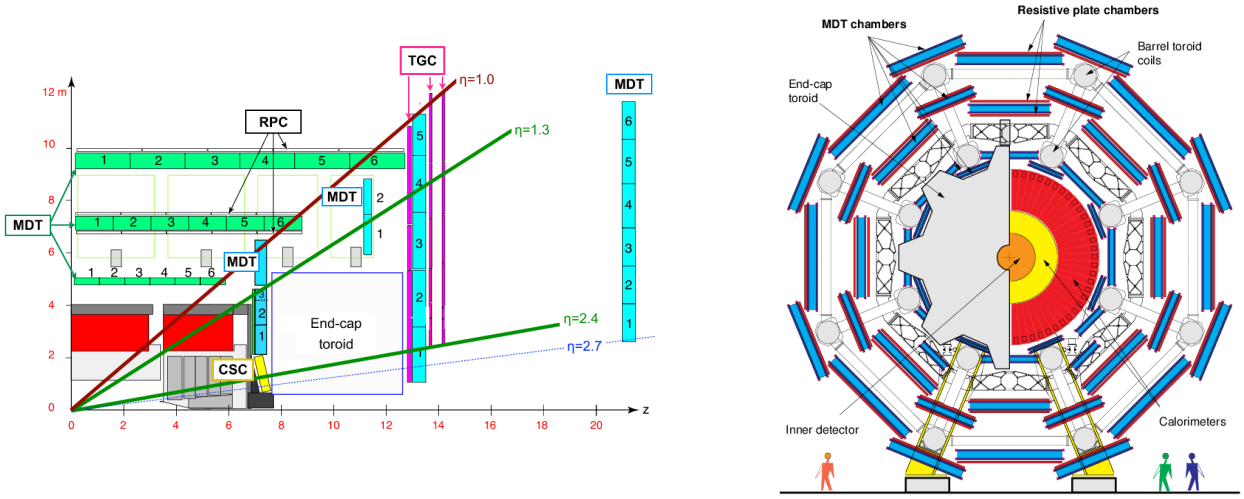

(a) Muon System in ATLAS

(b) Muon System Cross Section

Figure 3.10. Schematic illustrations of the muon system in the y-z plane [52], and in the x-y plane [53]. The barrel and encap toroids are also indicated.

3.2.5.1. Monitored Drift Tubes

The MDTs are arranged in three concentric cylindrical layers about the beampipe in the barrel region. In the transition and endcap regions, they are installed vertically. In all,

they cover a region of $|\eta|< 2.7$. The smallest functional element of one chamber is a drift tube. These tubes are hollow aluminum cylinders, 30 mm in diameter, with a central wire of gold-plated tungsten-rhenium that is 50 μm in diameter. The central wire is kept at 3270 V, and the chambers are arranged such that the wires are perpendicular to the magnetic field. Each tube is filled with a gas mixture of 91% Ar, 4% N_2, and 5% CH_4. When a muon passes through a tube, it ionizes the gas mixture, and a drift current is collected on the wire. The maximum drift time is 480 ns.

Each chamber is formed by assembling these drift tubes on a support frame in typically six parallel layers with three layers per side, though some chambers have four layers per side. They are rectangular, each covering an area of 2×10 m^2. There are a total of 1,154 MDT chambers in the muon system, with roughly 370,000 readout channels [54].

When a muon passes through through the full muon system in the barrel region, six coordinates can typically be determined per MDT chamber. To determine the momentum, the coordinates measured by three chambers are usually compared. Because of this, and because the track measurements depend on the known relationship between drift time and distance in the tubes, both the relative chamber positions and the wire positions must be known with high precision. Optical systems are built into the chambers to monitor deformations. Meanwhile, the wire position is determied by the two anchor points and the gravitational sag, in the case of the horizontally oriented chambers, which can typically be controlled to within 10 μm with a support structure in the middle of the tube [54].

The spatial resolution as a function of the distance of a muon track from the wire within a drift tube is provided in Figure 3.11. A single tube has a lower limit on the spatial resolution of roughly 80μm. When combining all layers within a chamber, this resolution limit improves to 35μm.

3.2.5.2. Cathode Strip Chambers

The CSCs form the second group of precision chambers that also use timing information to determine the position of muon track hits. They are mulitwire proportional chambers that

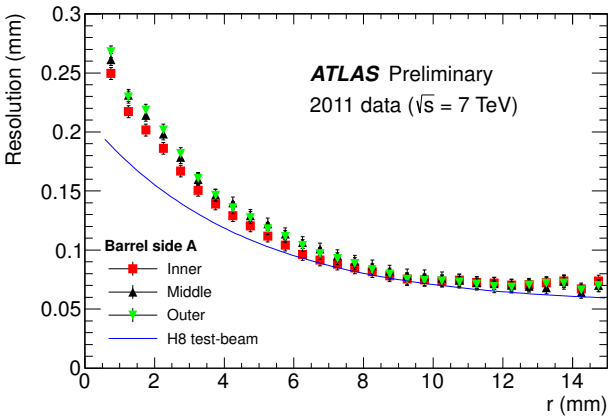

Figure 3.11. Spatial resolution as a function of the distance, r, of a muon track from the wire within a drift tube measured separately for Inner (red squares), Middle (black triangles), and Outer (green triangles) MDT chambers of the Muon Spectrometer Barrel side A [55].

are used in the forward region, covering $|\eta|>$ 2.0 in place of the MDTs, due to their lower sensitivity to high particle fluxes. The two planar cathodes of a single unit are constructed from copper-clad laminates on Nomex honeycomb panels. Nomex is a lightweight yet sturdy polymer, chosen in part to reduce multiple scattering. The cathodes strips for the precision coordinate measurement are segmented and aligned perpendicular to the anode wires. The anode wires are tungsten-rhenium wires 30 μm in diameter, and are kept at a potential of 2600 V. The cathode readout pitch is 5.08 mm, equal to the cathode spacing, while the anode wire pitch is 2.54 mm, equal to the cathode-anode spacing.

The gas mixture is 30% Ar, 50% CO_2, and 20% CF_4. With an electron drift time of less than 30 ns, the RMS timing resolution of the CSCs is roughly 7 ns.

There are 32 CSC chambers in the muon system, corresponding to 67,000 readout channels [54].

3.2.5.3. Resistive Plate Chambers

The RPCs are the trigger chambers that cover the barrel region. There are three stations, as depicted in Firgure 3.10(a), each with two detector layers. Low p_T muon triggers recquire

coincidence hits in the two innermost RPC layers and high p_T triggers which require an additional coincidence hit in the outer RPC layer. The low p_T thresholds are between 4 and 10 GeV, while the high p_T thresholds are between 11 and 20 GeV [56]. The full triggering system in ATLAS will be discussed in more detail in Section 3.2.6.

A signle RPC unit consists of two parallel resistive plastic plates, 2 mm thick. The outside surfaces of these plates are coated with thin graphite paint layers connected to a voltage supply. On the inside, the two plates are kept 2 mm apart by polycarbonate insulating spacers. This gas gap is sealed by a polycarbonate frame and filled with 97% tetrafluoroethane ($C_2H_2F_4$) and 3% isobutane (C_4H_{10}), chosen for its non-flammable property and low operating voltage. This allows for operation at a high rate, satisfying the fast trigger requirements.

An electric field of 4.5 kV/mm is applied across the gas gap, where primary ionization electrons are amplified via avalanches, resulting in typical pulses of 0.5 pC. Metal strips on both sides of the plates read out the signals. These are separated from the graphite layers by insulating films. The readout strips are aligned parallel to the MDT wires, as well as perpendicular, in order to provide a second coordinate measurement that is used in offline reconstruction.

One RPC chamber is formed by two detector layers with four such readout strip panels. There are 596 RPC chambers in the muon system, with 355,000 total readout channels. The timing resolution is 1.5 ns [54]. RPC performance plots illustrating reconstructed hit times in η 3.12(a) and ϕ 3.12(b) strips of a single RPC readout panel are provided in Figure 3.12.

3.2.5.4. Thin Gap Chambers

The TGCs are the second group of trigger chambers that cover the more forward region from $1.05 < |\eta| < 2.4$. They again measure hit time and are designed similarly to the CSCs, with the main difference being that the anode wire pitch of 1.8 mm is larger than the anode-cathode distance. The plates forming the structure of the basic TGC unit are G-10 plates on which graphite cathodes are deposited. The gas gap is 2.8 mm wide, the anode wires are

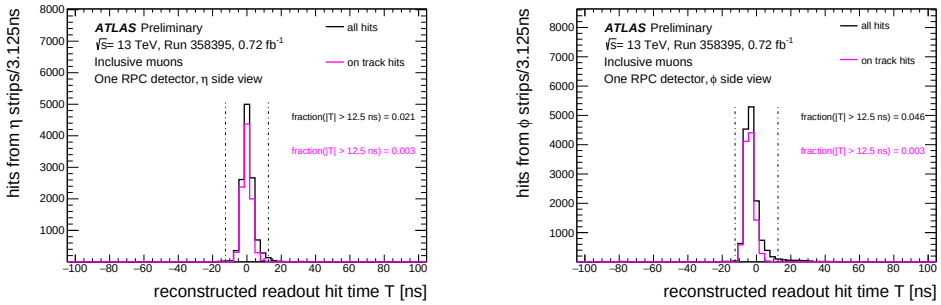

(a) Hit time in η strips

(b) Hit time in ϕ strips

Figure 3.12. Reconstructed hit times measured in η 3.12(a) and ϕ 3.12(b) strips of a single RPC readout panel. The black distribution indicates timing of all recorded hits, while the magenta distribution includes only hits that are within 33 mm of the extrapolated muon track position. The fraction of of hits considered to be out of time, denoted fraction($|T| >$ 12.5 ns) is provided [57].

50 μm in diameter, and the operating voltage is 3.1 kV. The gas used is a mixture of 55% CO_2 and 45% n-C_5H_{12}.

The readout strips are aligned perpendicular to the MDT wires, while the anode wires are parallel to the MDT wires. The electric field configuration and small wire distance yield short drift times and thus good timing resolution.

There are 192 TGC chambers, where a chamber is formed from either two or three of the basic unit sandwiched together with 20 mm thick paper honeycomb panels separating the layers. In all the TGCs have 320,000 anode readout channels and 120,000 strip readout channels.

3.2.6. Trigger

With a bunch crossing rate of 40 MHz and an average of 33 interactions per bunch crossing in the LHC Run 2, an event trigger is necessary in ATLAS in order to select events that are potentially interesting in terms of the physics goals of the experiment and discard those that are likely uninteresting. The concept of a trigger allows for a predetermination of basic event topologies that can be used to select such interesting events, thus decreasing the

event readout rate to one that the readout electronics can cope with, as well as decreasing the sheer amount of data that is stored to disk.

In ATLAS, there are two trigger levels. The first is the Level 1 (L1) trigger, which is hardware-based and uses reduced granularity information from limited sections of the detector to reduce the readout rate from 40 MHz to 100 kHz with a latency of 2.5 μs. The L1 Trigger system is composed of the Level 1 Calorimeter (L1Calo), Level 1 Topological (L1Topo), and Level 1 Muon (L1Muon) systems, which feed information to the Central Trigger Processor (CTP).

The L1Calo system receives analog trigger tower signals from the calorimeters with a granularity of $\Delta\eta \times \Delta\phi$ of 0.1×0.1, roughly 16 times lower than the full granularity used in analyses, and digitizes them in the pre-processor modules (PPMs). The information is then sent to the Cluster Processors (CPs), which look for localized clusters that can be identified as electron, photon, or τ candidates. Concurrently, the information is sent to the Jet Energy Processors, which find groups of trigger towers that have summed transverse energies larger than a pre-defined threshold around local 2×2 trigger tower maximum cores, which are identified as jet candidates. These coarse trigger object candidates are sent from both types of processors to the L1Topo system, which uses topological algorithms to compute global quantities such as missing transverse energy (E_T^{miss}), as well as perform selections based on kinematic relations between the trigger objects. Finally, the L1Muon system uses spatial and temporal coincidence patterns of hits in the RPCs and TGCs of the muon system to define physics object candidates.

The information from all systems is then sent to the CTP, which makes the ultimate trigger decision, and, if an event is selected, sends the Level 1 Accept (L1A) signal to the front end readout electronics of all ATLAS subdetector systems.

Once an L1A has been sent, full granularity information is sent to the High Level Trigger (HLT), which is a software-based trigger that runs on CPUs in a counting room off of the cavern that houses the detector. Here, regions of interest defined around physics obejects sent from the L1 Trigger are processed using the higher-granularity calorimeter information

as well as precision muon spectrometer measurements and tracking information from the inner detectors. Global event topologies are considered as well. In all, the HLT reduces the rate further from 100 kHz to an average of around 1 kHz, after which data is stored to disk [58].

CHAPTER 4

Object ID and reconstruction

Once data has been stored to disk, experiments are faced with the task of taking raw signals from the detector and reconstructing physics objects that can be used in statistical analyses. These objects must be associated with the correct bunch crossing and interaction and have well defined properties such as energy and momentum. This chapter describes the process of reconstructing track and vertex objects first, which are then built upon in the descriptions of the reconstruction of electrons, muons, and finally jets. Objects such as photons and taus, which are not used in the analysis that this thesis focuses on, will not be discussed.

4.1. Tracks and vertices

In any physics analysis, it is imperative to determine whether or not the reconstructed physics objects in consideration originated from the same interaction. The final state particles in the analysis considered in this thesis are electrons and muons, which, because of their non-zero electric charges, are expected to leave signals in the inner detector system, allowing for reconstruction of their tracks.

The main goal of tracking is to determine the trajectory of a particle such that its initial momentum and point of primary origin can be determined. Using tracking information, one can discern whether multiple particles originated from the same origin, or primary vertex.

In tracking, the trajectories of the particles are not directly measured; rather, electrical signals called hits arise in the detector at discrete points as a particle passes through. These points are made into a track by the use of pattern recognition to find track candidates, after which point statistical fits are used to determine the track parameters.

The step of track finding in ATLAS begins with the determination of 3-point track seeds in the silicon detectors, either the pixel detector or the SCT. Starting at the seeds and moving away from the interaction point, hits are added using a combinatorial Kalman filter [59], which is a recursive algorithm that estimates state parameters based on a combination of earlier measurements and the currrent measurement. The seed is extended out to the TRT, after which point it is considered a track candidate. This is known as the inside-out algorithm sequence, and is the baseline algorithm used in ATLAS for reconstruction of tracks from primary particles. Primary particles are defined as either particles that have a mean lifetime of less than 3×10^{-11} s that are produced in the primary interaction, or particles that originate from the decay of particles with shorter lifetimes that are produced in the primary interaction [60]. The track reconstruction efficiency is measured from simulation as the fraction of primary particles with $p_T > 400$ MeV and $|\eta| < 2.5$ that are matched to a reconstructed track.

Once reconstructed tracks from the primary particles are formed, the primary vertex of the interaction is reconstructed using an iterative vertex-finding algorithm. Vertex seeds are selected from the positions of the reconstructed tracks extrapolated to the z-axis along the beamline. An iterative χ^2 fit is performed using each seed along with nearby tracks. Tracks that are more than 7σ away from the vertex in consideration are used to seed a new vertices. The process is repeated until no new vertices are found, and vertices containing only one track are removed. The reconstructed vertices are then matched to interactions by summing weights given to each track assigned to the vertex, where the weight is a measure of compatibility based on the χ^2 fit. An interaction, consisting of reconstructed tracks and a vertex, is considered successfully reconstructed if the sum of the weights of each track associated with the vertex is over 50% of the sum of all track weights in the interaction [60].

Finally, important parameters that aide in reconstruction of physics objects as well as event selection are determined. Two examples of these are the track impact parameter, d_0 and longitudinal impact parameter, z_0. These are defined as the distance of closest approach

of a reconstructed track to the primary vertex, and the projection of this distance onto the z-axis, respectively. They are shown geometrically in Figure 4.1 below.

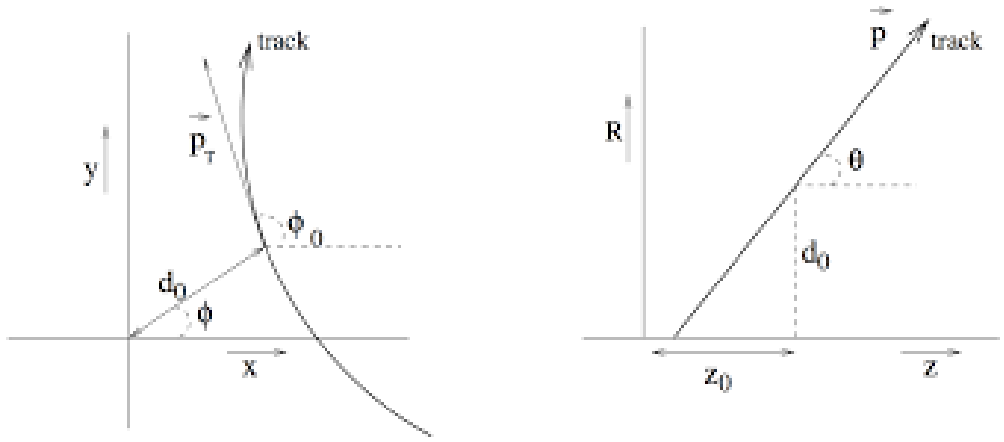

Figure 4.1. Impact parameter, d_0, and longitudinal impact parameter, z_0, of a track with respect to the primary vertex [61].

4.2. Electrons

The process of taking raw information from the ATLAS detector and arriving at a physics object that has been identified as an electron with a measured and calibrated energy can be broken down into a series of steps. These steps are cluster reconstruction, track reconstruction, track-cluster matching, and identification, and are described in the following subsections. Isolation requirements will be described in Section 5.3.

4.2.0.1. Algorithm Overview

Electrons traversing the ATLAS detector will pass through the inner detectors, interacting with the material and hits before depositing their energy in the electromagnetic calorimeter. An illustration of this trajectory is provided in Figure 4.2.

Because of their low mass, electrons lose significant amounts of energy via bremsstrahlung when traversing detector material. These radiated photons can convert into electron-positron pairs, which then interact with the material, leading to collimated clusters of energy in the

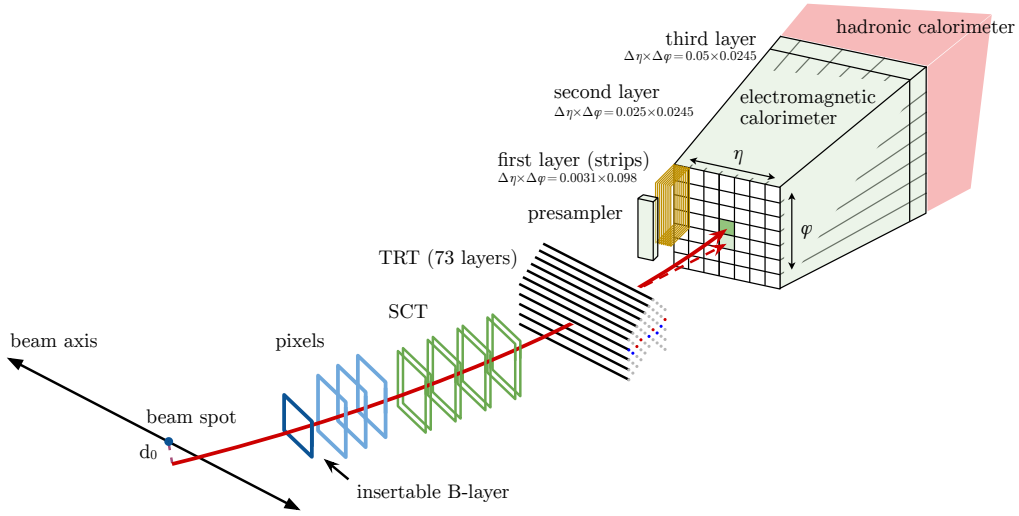

Figure 4.2. Illustration of the trajectory of an electron, represented by the solid red line, through various components of the ATLAS detector. The dashed red line represents the trajectory of a photon, radiated during interaction between the primary electron and the TRT material [62].

EM calorimeter. The deposition of these localized clusters is a fundamental characteristic of electron signatures, along with charged particle tracks in the inner detector, and close matching between these tracks and EM clusters in $\eta \times \phi$ space.

Electron identification and reconstruction in ATLAS is based on identification of tracks in the inner detector as well as clusters of energy deposits in the calorimeter. Two types of clusters are reconstructed. The first are 'topo-clusters', which are groups of cells with energy deposits in the EM and hadronic calorimeter. The second are 'superclusters', which are variable-sized clusters that expand upon the topo-clusters in order to improve recovery of energy lost to bremsstrahlung. Tracks are matched to each type of cluster and refitted at different stages. The general procedure is as follows [63]:

- Topo-clusters are reconstructed
- Tracks losely matched to topo-clusters are refit
- Track-matched topo-clusters are used to seed superclusters

- Secondary clusters are added to account for energy loss
- Calibrations and corrections are applied to superclusters
- Tracks are matched to electron superclusters
- Energies are recalibrated and discriminating variables are calculated

The clustering and track-related steps are explained in more detail in the following sections.

4.2.0.2. Calorimeter Cluster Reconstruction

Electron cluster reconstruction begins with the formation of so-called 'proto-clusters' in the EM and hadronic calorimeters. A noise threshold is applied to select cells that have a cell energy of at least 4 times that of the cell noise, including noise from both pileup and electronics. Cells satisfying this requirement are used as seeds, to which neighboring cells are added if they have an energy-to-noise ratio of at least 2. Each of these cells acts as a seed for the next iteration. As the final step, a last layer of nearest-neighboring cells is added to form the final proto-cluster candidates. These are the topo-clusters. Tracks are matched as described in the following section.

After track matching, topo-clusters are sorted in order of decreasing E_T. All are required to have $E_T > 1$ GeV and to be matched to a track with at least 4 hits in the silicon detectors in order to be an electron supercluster seed. For each seed cluster, satellite clusters are identified if they fall within $\Delta\eta \times \Delta\phi = 0.0175 \times 0.125$ of the seed cluster barycenter, or within $\Delta\eta \times \Delta\phi = 0.125 \times 0.3$ if they share a best-matched track with the seed cluster. For electrons, these tend to be secondary EM showers from the same initial particle. The seed clusters with the addition of the satellites make up the superclusters.

In a final step, calorimeter cells are assigned to a given supercluster. With the exception of the transition region between η of 1.4 and 1.6 where the energy measured in the hadronic calorimeter is also added, only cells from the presample and first three layers of the LAr calorimeter are considered.

4.2.0.3. Track Reconstruction and Matching

In addition to cluster candidates, tracks in the inner detector must be identified. This reconstruction process is described in Section 4.1. Track candidates are required to be loosely matched to clusters in the EM calorimeter. A loose matching is described in terms of the separation of the center of the cluster's energy spread and the position of the track when extrapolated from the perigee, the point of closest approach to the interaction point, to the second EM layer.

Qualitatively, a loose matching satisfies the requirement of $|\eta_{cluster} - \eta_{track}| < 0.05$, and one of the following:

$$-0.02 < \Delta\phi < 0.05 \qquad \text{where} \qquad \Delta\phi = -q \times (\phi_{cluster} - \phi_{track})\,, \tag{4.1}$$

or

$$-0.10 < \Delta\phi_{res} < 0.05\,, \tag{4.2}$$

where $\Delta\phi_{res}$ is defined similarly to ϕ, with the momentum of the track scaled to match the energy of the cluster. Here the variable q is charge [62].

The final step in reconstructing electron candidates is matching seed clusters from the calorimeter to track candidates. A matching similar to the loose matching defined above is performed, with a slightly stricter requirement on the $\Delta\phi$ between the tracks and clusters of $-0.10 < \Delta\phi < 0.05$. If several tracks satisfy this new matching requirement to a seed cluster, the candidate track is selected by considering the distance in η and ϕ betwen the extrapolated tracks and the cluster center in the second EM layer, the number of silicon hits, and the number of hits in the innermost silicon layer. For example, if a candidate has no pixel hits and can be matched to a secondary vertex, it is likely a photon conversion and is thus discarded.

After the superclusters are formed and calibrated, the final matching between tracks and superclusters is performed, similarly to the method used to match tracks with topo-clusters.

4.2.0.4. Identification

The signal of interest in electron identification consists of prompt electrons, which refer to electrons that are produced in the hard scatter event, or electrons that come from the decays of heavy, short-lived particles such as Z bosons. The challenge in electron identification is descriminating this signal from the background of non-prompt or fake electrons. These are electrons produced from photon conversions or in the decays of hadrons containing heavy-flavor quarks, or even jets that fake electron signatures.

Once reconstructed electron candidates have been formed, they are categorized as prompt electrons using a likelihood identification that aims to separate this signal from the background. The likelihood identification relies on a series of discriminating variables that are sensitive to prompt electron signatures. These variables make use of information from the tracking and calorimeter systems, such as shower shape variables and variables that relate positions of the cluster in different EM layers to the track position.

The use of a likelihood identification has several benefits over a simple cut-based approach, where an electron candidate must pass a series of selection criteria. It allows for candidates to be classified as electrons even though they may fail the requirement of a single discriminant variable, thus raising the signal efficiency. Furthermore a likelihood approach can benefit from the inclusion of discriminating variables that may have similar distributions between background and signal, in which case a cut-based method would suffer from a loss in efficiency.

The likelihood discriminant is defined in terms of the signal likelihood, L_S, and the background likelihood, L_B, as:

$$d_L^{'} = -\frac{1}{15}\ln(\frac{1}{d_L} - 1) \qquad \text{where} \qquad d_L = \frac{L_S}{L_S + L_B}\,. \tag{4.3}$$

The likelihoods themselves are built from the products of n probability distribution functions, P, determined from simulation. They are:

$$L_S(\bar{x}) = \prod_{i=1}^{n} P_{S,i}(x_i) \qquad\qquad L_B(\bar{x}) = \prod_{i=1}^{n} P_{B,i}(x_i)\,, \tag{4.4}$$

where $\bar{x}$ is a vector of the discriminating variables. Operating points are then defined based on thresholds set for the $d_L^{'}$ discriminant. Physics analyses can use these operating points to define the electrons based on their physics needs - from a requirement of higher signal acceptance to a preference for better background at the cost of lowering signal efficiency. These operating points are, in order of the threshold set for the $d_L^{'}$ discriminant: VeryLoose, Loose, Medium, and Tight. The efficiencies for prompt electrons with an E_T of 40 GeV for each of the last three working points are 93%, 88%, and 80%, respectively [62]. The analysis described in this thesis uses Loose Likelihood quality electrons, as will be discussed in Section 5.3.

4.2.0.5. Efficiency Corrections

Imperfections exist in the detection and reconstuction of all physics objects. To account for these, efficiency corrections are applied when using these physics objects in an analysis. The corrections are determined using a 'tag-and-probe' method in $J/\psi \to ee$ and $Z \to ee$ events in data and simulation.

The tag-and-probe method uses well-known, di-object resonances to measure efficiencies. A resonant pair of objects, in this case electrons, is reconstructed with one object passing the Tight identification requirements, known as the 'tag', and the other passing looser selection requirements, known as the 'probe'. The probe is defined in terms of the efficiency that is being measured. The invariant mass lineshape for a tag object and a passing probe is fit using a background + signal model, as is the lineshape for a tag object and a probe that fails the selection. The efficiency is defined as the ratio of signal yields of the tag object and passing probe case to the total.

The electron identification (ID) efficiencies for these three working points are shown in Figure 4.3, as a function of E_T in Figure 4.3(a) and as a function of η for $E_T > 15$ GeV in Figure 4.3(b). The efficiencies were determined in $Z \to ee$ events from 2017 data with an integrated luminosity of $43.8 fb^{-1}$.

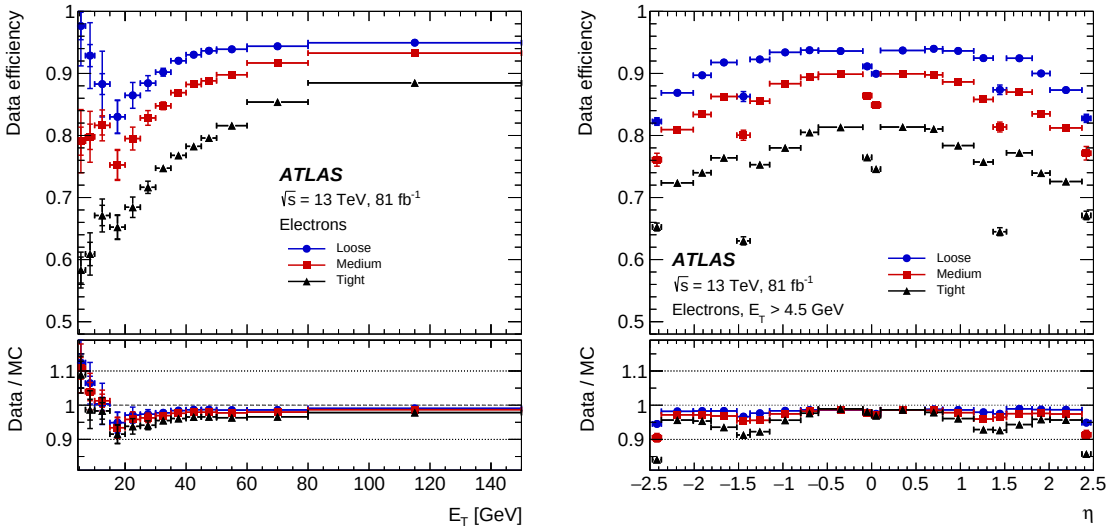

(a) Electron ID Efficiency vs. E_T

(b) Electron ID Efficiency vs. η

Figure 4.3. Electron identification efficiency as a function of E_T (integrated over the full η range) and as function η (for $E_T > 15$ GeV). Efficiencies were measured in $Z \to ee$ events and evaluated based on a likelihood approach for three operating points: Loose (blue), Medium (red), and Tight (black) [61].

4.3. Muons

Muons are formed using information from the inner detectors, the muon system (MS), and occasionally the EM calorimeter. In the first steps, tracks are reconstructed in both the inner detector, as discussed in Section 4.1, and in the MS separately. This tracking information is then combined to form muon candidates. The MS reconstruction and combination steps will be discussed here, followed by muon identification and efficiency corrections.

4.3.0.1. Muon Reconstruction and Track Matching

Reconstruction in the MS is based on the formation of objects called 'segments', which are hit patterns in the different chambers of the MS. MS track candidates are formed by fitting hits from segments in different layers. Segments in the middle layers are taken as seeds, which are then extended to the outer layers. Cuts are performed based on the number of hits in the segments and the quality of fits to the hit positions, and finally segments are matched together based on matching orientation and proximity to form track candidates.

A global χ^2 is then used to fit the hits in the track candidates. If the track χ^2 from the fit is too high, the culprit hits are iteratively removed until the χ^2 is below the cut threshold.

Following this algorithm, four categories of muons are defined. They are:

- **Combined (CB) muons**: A track in the inner detector and a track in the MS can be combined and refit globally using hits from both.
- **Segment-tagged (ST) muons**: A track in the inner detector can be extrapolated to the MS and matched with at least one segment in the MDTs or CSCs. ST muons typically have low p_T or fall into regions of lower acceptance in the MS.
- **Calorimeter-tagged (CT) muons**: A track in the inner detector can be matched to an energy deposit in the calorimeter with properties consistent with a minimum-ionizing particle. CT muons have the lowest purity of the four types; however, they can be used to recover acceptance losses in MS gaps that allow for services such as cabling.
- **Extrapolated (ME) muons**: A track in the MS can be extrapolated back to the interaction point with loose compatibility. This MS track is required to traverse at least two chamber layers in the barrel region, or at least three in the forward region. ME muons are used to extend acceptance in the region $2.5 < |\eta| < 2.7$, where there is no coverage from the inner detector, and thus they do not require an inner detector track. They can, however, be fit with extra hits in the pixel detectors, if such hits are present, as the acceptance of the pixel detector is larger than that of the SCT.

4.3.0.2. Muon Identification

The main background for muons comes from pion and kaon decays. In-flight decays in the inner detector are characterized a kink-like topology in the reconstructed track with a poor fit quality and poor matching between the momentum measured in the inner detector and in the MS. These background characteristics can be used to separate out the desired muon signal that comes from the hard scatter event or from decays of heavy resonances from the unwanted background.

There are four muon identification categories available: Loose, Medium, Tight, and High-p_T. These categories are based on different cuts meant to separate signal from background and achieve different levels of reconstruction efficiency, purity, and levels of systematic uncertainties. The first three are inclusive, meaning Tight muons are also classified as Medium and Loose, while Medium muons are also classified as Loose, and Loose muons have the most relaxed requirements. The analysis presented in this thesis uses Loose requirements, which broaden slightly the Medium requirements, so only these two categorizations will be discussed here.

- **Medium muons**: The Medium identification requirements use only CB and ME tracks. The CB tracks are required to have at least three hits in at least two MDT layers. In the region where $|\eta|< 0.1$, tracks with at least one MDT layer hit and fewer than two MDT holes are allowed [1]. While ME tracks are allowed in the Medium categorization, the analysis presented in this thesis requires muons to fall within $|\eta|< 2.5$, thus cutting out all ME muons. Thus, the ME requirements will not be discussed.

- **Loose muons**: The Loose requirements were optimized specifically for the identification of muons coming from the decays of Z bosons from a Higgs decay. They maximize the reconstruction efficiency and require good quality tracks. All muon types are allowed, with CB and ME tracks satisfying the Medium requirements and CT and ST muons restricted to $|\eta|< 2.5$.

[1] A hole is defined as an absence of a hit where one is expected, within a series of other hits.

4.3.0.3. Muon Efficiency Corrections

As in the case of electron reconstruction, efficiency corrections must be applied to account for imperfections in the muon reconstruction and identification process. The tag-and-probe method is utilized again, this time using $Z \rightarrow \mu\mu$ events for the high p_T regime and $J/\psi \rightarrow \mu\mu$ events for low p_T.

In the case of $Z \rightarrow \mu\mu$ events, the tag muon is required to have a p_T greater than 24 GeV and satisfy both the Loose and Medium identification requirements. In the case of ID probe tracks or CT probe muons, stricter requirements are applied to reduce background contamination. If a reconstructed muon is found within a cone of size $\Delta R = 0.05$ around the probe track, it is considered successful.

In the case of $J/\psi \rightarrow \mu\mu$ events, tag probe pairs are required to have an invariant mass between 2.7 and 3.5 GeV. Each must have a p_T greater than 5 GeV, and the tag muon must be a Medium muon that triggered the event. If after satisfying further background suppression cuts on Δz_0 and their distance in the $\eta - \phi$ plane, a probe is considered successful is a muon is reconstructed within a cone of size $\Delta R = 0.05$ around the probe.

After fitting the signal and background in each case and subtracting off the background contribution, the efficiency is determined as the ratio of the successfully reconstructed events divided by the total. In Figure 4.4 below, plots of the muon reconstruction efficiency as a function of p_T and η can be seen for both data and simulation, calculated using $Z \rightarrow \mu\mu$ events.

4.4. Jets

The analysis presented in this thesis aims to reconstruct Higgs events where the Higgs decays to a final state of four leptons, through its decay to two Z bosons. The reconstruction of the main ingredients for reconstructing the Higgs in this channel - muons and electrons - have been covered; however, the jet activity accompanying the Higgs in such events is also interesting, and measurements related to this activity are provided in addition to measure-

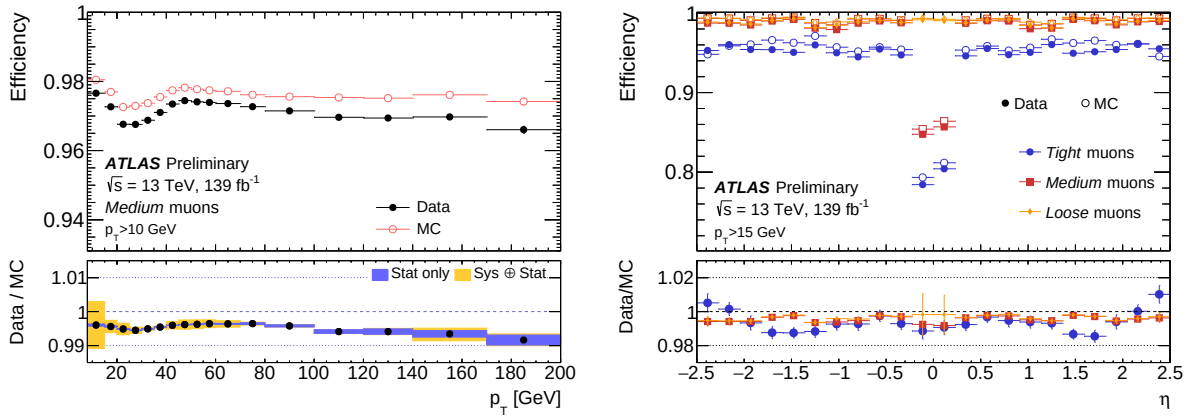

(a) Muon Reconstruction Efficiency vs. p_T

(b) Muon Reconstruction Efficiency vs. η

Figure 4.4. Muon reconstruction efficiency as a function of p_T (integrated over the full η range) and as function η (for $p_T > 15$ GeV). Efficiencies in Figure 4.4(a) were measured in $Z \to \mu\mu$ events in data (black) and in simulation (red), using the Medium muon requirements. In Figure 4.4(b), efficiencies are shown for Tight, Medium, and Loose muons in blue, red, and yellow, respectively. Open circles represent results obtained from simulation, while filled dots represent efficiencies from data [64].

ments of the kinematics of the Higgs decay products. Thus, the final reconstructed physics objects needed are jets.

4.4.0.1. Jet Algorithms

Jets pose a more difficult problem for reconstruction than electrons and muons. While electrons and muons are well-defined physics objects with well-defined properties, jets are not. At the theoretical level of consideration, jets are single partons emitted as QCD radiation. At the experimental level, jets, as mentioned in Section 2.2, are collimated showers of particles resulting from hadronization of quarks or gluons. Finally, what can actually be measured in the detector are signals left by the final state particles resulting from this hadronization and further radiated particles, including tracks in the inner detector system and groups of signals clustered in the calorimeters.

The end goal in jet reconstruction is to group these collimated signals together into a single, distinct object with well-defined properties that can be called a jet. Multiple algorithms for performing these clusterings exist. The one widely used by the ATLAS Collaboration is a sequential recombination algorithm called the Anti-k$_T$ algorithm [65].

In this algorithm, a distance parameter, $d_{i,j}$, between a particle, i, and a particle, j, is defined as:

$$d_{i,j} = min(p_{T,i}^{-2}, p_{T,j}^{-2})\frac{\Delta R_{i,j}^2}{R^2} \qquad \text{where} \qquad \Delta R_{i,j}^2 = (y_i - y_j)^2 + (\phi_i - \phi_j)^2\,, \tag{4.5}$$

and $p_{T,i}$ and $p_{T,j}$ are the transverse momenta of particles i and j, repectively.

Here, R is a radius parameter that defines the size of the jet. For jets in this thesis reconstructed using the Anti-k$_T$ algorithm, R is set to 0.4. These are denoted 'AntiKt4' jets. For all input objects in the event, $d_{i,j}$ is calculated and compared to $\frac{1}{p_{T,i}^2}$. If $d_{i,j}$ is less than $\frac{1}{p_{T,i}^2}$, the two objects i and j are recombined into a single object. If $\frac{1}{p_{T,i}^2}$ is greater, object i is considered to be a jet and removed from the list of objects under consideration. This is done until there are no objects left. Following the Anti-k$_T$ algorithm, clustering grows around hard cores, leading to cone-shaped jets with regular boundaries.

The two different jet 'types' used in the remainder of this thesis are differentiated by the inputs that are provided to the Anti-k$_T$ algorithm. The first jet type, 'AntiKt4EMTopo' jets, provide topo-clusters as inputs to the algorithm. These are topologically grouped clusters of calorimeter cells that have been noise-suppressed. Topo-clusters are formed by identifying seed cells in the calorimeter that have energy greater than four times the average noise expected for that given cell, σ. Here noise includes contributions from pileup as well as electronic noise, though pileup typically dominates, especially in conditions with high instantaneous luminosity. For each seed cell, all cells adjacent to it in all directions that have an every of at least 2σ are grouped together. This is repeated until no such adjacent cells are left, at which point one more layer of cells is grouped. Each of these groupings is a topo-cluster [66].

The use of topo-clusters, which use only calorimeter information, has a few drawbacks. For softer particles, those with lower transverse momentum, the energy deposited in the calorimeter often fails the threshold for topo-cluster seeding. As an example, roughly 25% of 1 GeV pions will fail the threshold [66]. In addition, at low energy, the inner tracking system in ATLAS has better resolution than the calorimeter, and in all cases provides better vertexing allowing for association with the primary vertex. Finally, tracking allows for rejection of pileup contamination to the jet energy and momentum measurements.

Thus, a second type of jet that uses information from both the calorimeters and the inner detectors is defined. These jets are denoted here as 'AntiKt4EMPFlow' jets. They use topo-clusters as well as tracks from the inner detectors as inputs to a second jet algorithm, the particle flow algorithm, which uses a cell-based energy subtraction to remove overlaps between the tracks and the topo-clusters. This new ensemble of overlap-removed particle flow objects is then used as the input to the Anti-k$_T$ algorithm. The particle flow algorithm is as folllows:

First, tracks from the inner detectors that have $|\eta| < 2.5$, $p_T > 0.5$ GeV, and at least 9 hits in the Silicon detector with no holes are selected. Tracks with $p_T > 40$ GeV are excluded due to isolation requirements. The tracks are matched to topo-clusters in the calorimeter by extrapolating to the second EM layer and requiring proximity to a topo-cluster in η and ϕ. The average energy expected to be deposited in the calorimeter by a particle associated to the track is calculated by:

$$< E_{exp} >= p_T^{track} < \frac{E_{cluster}^{ref}}{p_{track}^{ref}} > \ . \tag{4.6}$$

Here, p_T^{track} is the transverse momentum of the track in consideration, while the ratio of $E_{cluster}^{ref}$ to p_{track}^{ref} is the ratio of reference clusters of energy deposited particles that left reference tracks with a given p_T, calculated from simulation.

The probability that the particle deposited energy in more than one topo-cluster is evaluated, and more topo-clusters are added to the system if it is deemed necessary to recover

the full shower energy. The expected energy is then recalculated, and subtracted cell-by-cell from the system of topo-clusters under consideration.

This procedure is followed for all tracks associated with the primary vertex in order of decsending p_T. The remaining ensemble of particle flow objects, comprised of topo-clusters and inner detector tracks, are then provided as inputs to the Anti-k$_T$ algorithm for jet reconstruction [66].

Finally, reconstructed jets are calibrated to the proper energy scale using a combination of correction factors derived from simulation and *in situ* [67].

4.4.0.2. Flavor Tagging

In addition to reconstructing jets, it is often useful to identify whether or not a jet originated from hadronization of a heavy flavor quark. This process, known as *b*-tagging, uses distinct properties of b-quarks to create likelihood working points that can be used for jet classification.

Jets initiated by b-quarks, or b-jets, are characterized by a vertex that is displaced with respect to the primary vertex, due to measurable distances typically travelled by long-lived heavy flavor hadrons. The decay products usually have a relatively large transverse momentum with respect to the jet axis, and due to the branching ratio for semileptonic decays of heavy hadrons, the decay products often include soft leptons.

All of these characteristics can be used to define discriminating quantities that are used either in an multivariate (MVA) combination or to train a recurrent neural network, whose output is used to define operating points based on identification efficiencies with various thresholds. In Figure 4.5 the b-jet identification efficiencies for the 70% working point derived using AntiKt4EMTopo jets are provided.

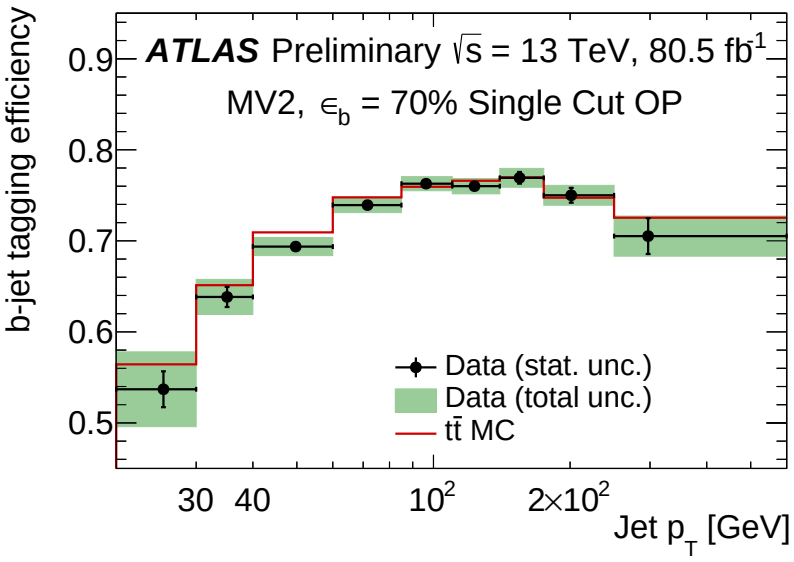

(a) b-tagging Efficiency vs. p_T

Figure 4.5. Efficiency of b-tagging for the 70% operating point using a multivariate likelihood-based approach (MV2) and AntiKt4EMTopo jets as a function of jet p_T. Black dots are efficiencies mesured in data while the red line represents efficiencies in simulated $t\bar{t}$ events [68].

CHAPTER 5

$H \to ZZ^* \to 4\ell$ decay channel overview

The focus of this thesis is the measurement of inclusive fiducial and diferential cross sections of the Higgs boson in the $ZZ^* \to 4\ell$ decay channel. In this chapter, an overiew of the foundations of the analysis is provided. This begins with the dataset used, described in Section 5.1, and the signal and background simulations, described in Section 5.2.

Signal here refers to events in which a Higgs boson is produced, which then decays to two Z bosons. One of the Z bosons is produced on-shell, i.e. within the Z boson mass resolution of the Z boson mass peak, while the other is produced off-shell, at a lower invariant mass. The Z bosons then each decay to two leptons (where leptons will henceforth refer to only electrons or muons). Background refers to events in which a Higgs is not produced, but has a final state that mimics that of the signal. These include, for example, $qq \to ZZ$ production, $t\bar{t}$ production where four leptons are in the final state, and production of a Z boson where jets in the event are mistaken for leptons.

In Section 5.3, the process by which signal events are selected and Higgs candidates are reconstructed is provided, with consideration given to how each selection 'cut', or requirement, either reduces a particular background or enhances the experimental resolution. While the backgrounds can be reduced significantly by the kinematic cuts used in the event selection, some background events will always be selected. Thus, accurate estimation of this contamination is essential. The data-driven background estimations are described in Section 5.4, which concludes the chapter.

5.1. Dataset

The analysis presented in this thesis uses the full ATLAS Run 2 dataset, consisting of proton-proton collision data at $\sqrt{s} = 13$ TeV, collected between 2015 and 2018. The total integrated luminosity delivered by the LHC, collected by ATLAS, and deemed good for use in physics analyses was provided in Figure 3.1 of Chapter 3, while the average pileup, or averge number of interactions per bunch crossing, was shown in Figure 3.2. In Table 5.1 below, the data taking conditions in each year are summarized. The total integrated luminosity, after

ATLAS Run 2 Data Taking Conditions					
Year	Total Integrated Luminosity $[fb^{-1}]$	Peak Instantaneous Luminosity $[\text{cm}^{-2}\text{s}^{-1}]$	Average Pileup $< \mu >$	Peak Pileup	ATLAS Data Taking Efficiency
2015	3.86	5.0×10^{33}	13.6	40.5	92.0%
2016	35.6	13.7×10^{33}	24.9	51.1	92.4%
2017	46.9	20.9×10^{33}	37.8	80.0	93.6%
2018	62.2	21.4×10^{33}	37.0	90.0	95.7%

Table 5.1. Summary of the ATLAS data taking conditions during each of the four years that comprise the LHC Run 2.

applying data quality requirements, is 139 fb^{-1}. These data quality requirements reject data taken during periods when parts of the ATLAS detector were not operating properly. The resulting data taking efficiency for Run 2 is 91% [36].

5.2. Signal and background simulation

Monte Carlo (MC) event generators are commonly used in analyses to compare observed distributions in data with theoretical expectations. These event generators are code frameworks developed by theorists and represent many years of work by various groups to provide the best possible descriptions of different processes. As such, the tools summarized in this section were chosen as they provide the best possible theoretical description of the pro-

cesses under consideration; however, the work done in developing these tools and carrying out the necessary calculations comes from the theory community. Furthermore, though the best available predictions are used, there is still some discrepancy between prediction and data, as calculations are carried out at finite orders. This leads to theoretical systematic uncertainties, which will be discussed further in Section 7.3.

Signal and background process events are generated assuming some model - in this case, the Standard Model. These are interfaced with parton shower programs that simulate evolution of jets, then run through a simulation of the detector using GEANT4 [69]. The resulting simulated detector signals are then used to reconstruct events, keeping the same possible biases and efficiency effects of reconstruction as in real data. Signal processes considered here are the gluon-gluon fusion production mode, ggF, vector boson fusion, VBF, associated Higgs production with a vector boson, WH or ZH (together denoted VH), along with a few rarer modes including bbH, ttH, $tHjb$, and tWH (with the last two denoted together as tH).

The ggF, VBF, VH, and ttH processes are modelled using the POWHEG-BOX v2 MC event generator [70–76]. For all except ggF, the PDF4LHC next-to-leading-order (NLO) set of parton distribution functions (PDFs) are used. In the case of ggF, the PDF4LHC next-to-next-to-leading-order (NNLO) set is used [77].

The ggF Higgs boson production uses the POWHEG method for merging the NLO Higgs + jet cross section with the parton shower and the MiNLO method [78] to simultaneously achieve NLO accuracy for inclusive Higgs boson production. In a second step, a reweighting procedure (NNLOPS) [79] is applied using the HNNLO program [80, 81] to achieve NNLO accuracy in the strong coupling constant α_s.

The matrix elements of the VBF, VH and ttH production modes are calculated up to NLO in QCD. For VH production, the MiNLO method is used to merge 0- and 1-jet events [76, 78]. The $gg \to ZH$ contribution is modelled at leading order (LO) in QCD.

Higgs production in association with a pair of bottom quarks, bbH, is simulated at NLO with MadGraph5_aMC@NLO v2.3.3 [82]. The CT10 NLO PDF set is used [83].

Production in association with a single top quark, tH, is simulated at NLO with MadGraph5_aMC@NLO v2.6.0, using the NNPDF30 PDF set [84].

The generator PYTHIA 8 with the AZNLO parameter set is used for the $H \to ZZ^* \to 4\ell$ decay as well as for the parton shower modelling for all production modes except ttH. In the case of ttH, the A14 tune [85] is used. PYTHIA 8 is interfaced to EvtGen v1.2.0 [86] for simulation of the bottom and charm hadron decays. All signal samples are simulated for a Higgs boson mass $m_H = 125$ GeV.

Final results are presented with additional predictions of the ggF cross sections for comparison. One comparison that is provided for all variables was generated with MadGraph5_aMC@NLO, which is accurate at NLO in QCD for zero, one, and two additional partons merged with the FxFx merging scheme [87], with top and bottom mass effects taken into account [88–90].

A second alternate prediction evaluated using NNLOJET is provided for Higgs plus one or two jet distributions [91–93]. For a subset of these distributions, comparisons calcuated using RadISH, which provides resummation at N^{3}LL+NNLO [94–98], and MATRIX for the fixed-order part of the calculation [99, 100] are provided.

For four of the variables sensitive to the modelling of the Higgs decay, alternate predictions using Hto4l and PROPHECY4F are provided. The latter includes the full NLO electroweak corrections to Higgs boson decay into four charged leptons [101–109].

Predictions for the production cross sections and decay branching ratios of the Higgs as well as the associated uncertainties are taken from Refs. [32, 84, 110–116]. The orders of the calculations for the predictions and the predictions themselves are summarized in Table **??**. PROPHECY4F [103, 105] is used for the prediction of the branching ratio for the $H \to ZZ^* \to 4\ell$ decay with $m_H = 125$ GeV, predicted to be 0.0124% [101, 113]. As mentioned previously, it includes the full NLO QCD and EW corrections as well as interference effects between identical final-state fermions, which leads to expected branching ratios for the same flavor final states, $4e$ and 4μ, to be roughly 10% higher than those of the opposite flavor final states, $2e2\mu$ and $2\mu2e$.

Production process		σ [pb]
ggF	$(gg \to H)$	48.6 ± 2.4
VBF	$(qq' \to Hqq')$	3.78 ± 0.08
WH	$(q\bar{q}' \to WH)$	1.373 ± 0.028
ZH	$(q\bar{q}/gg \to ZH)$	0.88 ± 0.04
ttH	$(q\bar{q}/gg \to t\bar{t}H)$	0.51 ± 0.05
bbH	$\left(q\bar{q}/gg \to b\bar{b}H\right)$	0.49 ± 0.12
tH	$(q\bar{q}/gg \to tH)$	0.09 ± 0.01
Decay process		$\mathcal{B}$ [$\cdot 10^{-4}$]
$H \to ZZ^*$		262 ± 6
$H \to ZZ^* \to 4\ell$		1.240 ± 0.027

Table 5.2. The predicted SM Higgs boson production cross sections (σ) for ggF, VBF and five associated production modes in pp collisions for $m_H = 125$ GeV at $\sqrt{s} = 13$ TeV [77, 84, 101, 103, 105, 110–135]. The quoted uncertainties correspond to the total theoretical systematic uncertainties calculated by adding in quadrature the uncertainties due to missing higher-order corrections and PDF+α_s. The decay branching ratios ($\mathcal{B}$) with the associated uncertainty for $H \to ZZ^*$and $H \to ZZ^* \to 4\ell$, with $\ell = e, \mu$, are also given.

Modeling of the various backgrounds are described following. The data-driven estimation methods for these backgrounds are described in Section 5.4.

The ZZ^* background has contributions from quark-antiquark annihilation and gluon-initiated processes. Both are modelled using SHERPA 2.2.2 [136–138]. The former is modelled with NLO accuracy in α_s for 0-, and 1-jet final states and LO accuracy for 2- and 3-jet final states. The latter is modelled at LO for 0- and 1-jet final states. For quark-initiated processes, the ME+PS@NLO prescription is used to merge with SHERPA parton shower. NLO EW corrections are included as a function of the ZZ^* invariant mass. This process is also modelled using POWHEG-BOX v2 interfaced to PYTHIA 8 for parton shower and hadronization, with EVTGEN for the simulation of $B-$ and $C-$hadron decays, as well as MADGRAPH5 with FXFX merging at NLO for 0- and 1-jet final states. These secondary simulations are used for evaluation of modelling uncertainties described in Section 7.3. The gluon-induced simulation has higher order QCD effects for the $gg \to ZZ^*$ continuum production calculated for massless quark loops [139–141] in the heavy m_t approximation [142]. Finally, it is scaled by a K-factor of 1.7±1.0, derived from the ratio of the higher-order and the leading-order cross section predictions.

POWHEG-BOX v2 interfaced to PYTHIA 8 is used to model the WZ background. These are interfaced to EVTGEN v1.2.0 for the simulation of $B-$ and $C-$hadron decays. SHERPA 2.2.2 is used to model triboson backgrounds with four or more prompt leptons, including ZZZ, WZZ, and WWZ. MADGRAPH5_AMC@NLO interfaced to PYTHIA 8 is used to simulate $t\bar{t}+Z$ events where both top quarks decay semi-leptonically and the Z boson decays leptonically. Here the total cross section is normalized to the cross section prediction including the two dominant terms at both LO and NLO in a mixed perturbative expansion in the QCD and EW couplings [132]. Smaller contributions from processes including tWZ, $t\bar{t}W^+W^-$, $t\bar{t}t$, $t\bar{t}t\bar{t}$ and tZ are simulated with MADGRAPH5_AMC@NLO interfaced to PYTHIA 8.

Events with jets produced alogn with Z bosons ($Z+$jets) are modelled using SHERPA 2.2.1, with matrix elements calculated for up to two partons at NLO and four at LO using

COMIX [137] and OPENLOOPS [138]. These are merged with the SHERPA parton shower [143] using the ME+PS@NLO prescription [144]. The NNPDF3.0 NNLO PDF set is used.

POWHEG-BOX v2 interfaced to PYTHIA 8 is used to model the $t\bar{t}$ background. EVTGEN v1.2.0 is used for heavy flavoured hadron decays. The A14 parameter set [85, 145] is used.

Finally, as mentioned previously, the GEANT4 framework [69] is used to pass all generated events through the ATLAS detector simulation [146]. Events are reconstructed in the same way as actual collision data to model detector and reconstruction effects. Pileup is included and modelled by overlaying simulated inelastic pp events generated with PYTHIA 8.186 [147] using the NNPDF2.3LO set of PDFs [148] and the A3 tune [149] over the original event. These overlayed events are weighted to the average number of interactions per bunch crossing, $\langle\mu\rangle$, from data, where $\langle\mu\rangle$ is rescaled by a factor of 1.03 ± 0.07 to improve the agreement between data and simulation in the visible inelastic pp cross section [150].

5.3. Event selection

From data passing the quality requirements discussed in Section 5.1, Higgs candidate events are selected using a combination of single-lepton, dilepton, and trilepton triggers, with a trigger efficiency of over 98%. From events passing these triggers, all are required to have at least one vertex with two associated tracks in the ID with transverse momentum $p_T > 500$ GeV.

Following these initial requirements are stages of selection cuts, summarized in Table 5.3. The objective of the event selection process is to have collections of events from data and simulation where every event contains a Higgs boson candidate, formed from the combination of reconstructed muon and/or electron pairs. The event selection process targets high resolution and efficiency, and aims to minimize the probability of contamination from various background sources by making specific cuts targeting these sources. These cuts can be grouped several stages, which are described below.

For every event, reconstructed physics objects, as described in Chapter 4, are first considered. Selection cuts are balanced between being tight enough to cut out unwanted background, while remaining loose enough to maintain a high selection efficiency.

5.3.1. Object-level selection

Object selection begins with physics objects reconstructed as described in Chapter 4, including electrons, muons, and jets.

Electrons, as discussed previously, are reconstructed using energy clusters in the EM calorimeter matched to tracks in the ID. The loose likelihood identification discriminant is used, which corresponds to a reconstruction and identification efficiency of around 95%. Electrons used in the analysis are required to have $|\eta|< 2.47$, chosen to match the acceptance of the ID, and $E_T > 7$ GeV, chosen to discriminate against backgrounds with objects such as photons and jets that fake electrons.

Muons are built using fully reconstructed tracks from the MS and the ID, within the coverage of the ID, from $0.1 < |\eta|< 2.5$. In the central detector region where the MS has reduced coverage, $|\eta|< 0.1$, muons are reconstructed using ID tracks and are identified using either an energy deposit in the calorimeter that is consistent with a minimum ionizing particle (calorimeter-tagged muons), or hits in the MS (segment-tagged muons). In the forward region between $2.5 < |\eta|< 2.7$, only the MS is used for muon reconstruction (standalone muons). All muons are required to satisfy $p_T > 5$ GeV, except for calorimeter-tagged muons, which must satisfy $p_T > 15$ GeV. As in the case of electrons, these cuts are also informed by the detector acceptance.

To ensure that all leptons originate from the primary vertex, both muons and electrons are subjected to longitudinal impact parameter requirements of $|z_0 \sin(\theta)| < 0.5$ mm. An additional impact parameter requirement of $|d_0| < 1$ mm is imposed on muons to reject those originating from cosmic rays. If electron and muon candidates are reconstructed using the same detector information, the muon is rejected if it is a calorimeter-tagged muon; otherwise, the electron is rejected. Again, the preference is towards higher-quality physics objects.

Physics Objects	
Vertex	
At least one collision vertex with at least two associated track	
Primary vertex	
Vertex with the largest p_T sum	
Electrons	
Loose Likelihood quality electrons with hit in innermost layer, $E_T > 7$ GeV and $\|\eta\| < 2.47$	
Interaction point constraint: $\|z_0 \cdot \sin\theta\| < 0.5$ mm (if ID track is available)	
Muons	
Loose identification with $p_T > 5$ GeV and $\|\eta\| < 2.7$	
Calo-tagged muons with $p_T > 15$ GeV and $\|\eta\| < 0.1$, segment-tagged muons with $\|\eta\| < 0.1$	
Stand-alone and silicon-associated forward restricted to the $2.5 < \|\eta\| < 2.7$ region	
Combined, stand-alone (with ID hits if available) and segment-tagged muons with $p_T > 5$ GeV	
Interaction point constraint: $\|d_0\| < 1$ mm and $\|z_0 \cdot \sin\theta\| < 0.5$ mm (if ID track is available)	
Jets	
anti-k_T jets, formed using Particle Flow inputs, that satisfy $p_T > 30$ GeV and $\|\eta\| < 4.5$	
b-tagging	
Previously selected jets with $\|\eta\| < 2.5$ passing the continuous `MV2_c10` algorithm	
overlap removal	
Jets within $\Delta R < 0.2$ of an electron or $\Delta R < 0.1$ of a muon are removed	
Event Selection	
Quadruplet Selection	- Require at least one quadruplet of leptons consisting of two pairs of same-flavour opposite-sign leptons fulfilling the following requirements: - p_T thresholds for three leading leptons in the quadruplet: 20, 15 and 10 GeV - Maximum one calo-tagged, stand-alone, or silicon-associated forward muon per quadruplet - Leading di-lepton mass requirement: $50 < m_{12} < 106$ GeV - Sub-leading di-lepton mass requirement: $m_{\text{threshold}} < m_{34} < 115$ GeV - $\Delta R(\ell, \ell') > 0.10$ for all leptons in the quadruplet - Remove quadruplet if alternative same-flavour opposite-sign di-lepton gives $m_{\ell\ell} < 5$ GeV - Keep all quadruplets passing the above selection
Isolation	- Contribution from the other leptons of the quadruplet is subtracted - FixedCutPFlowLoose WP for all leptons
Impact Parameter Significance	- Apply impact parameter significance cut to all leptons of the quadruplet - For electrons: $d_0/\sigma_{d_0} < 5$ - For muons: $d_0/\sigma_{d_0} < 3$
Vertex Selection	- Require a common vertex for the leptons: - $\chi^2/\text{ndof} < 5$ for 4μ and < 9 for other decay channels
Best Quadruplet	- If more than one quadruplet has been selected, choose the quadruplet with highest Higgs decay ME according to channel: 4μ, $2e2\mu$, $2\mu2e$ and $4e$

Table 5.3. Summary of the event, physics object, and Higgs candidate selection requirements. The masses of two lepton pairs are denoted as m_{12} and m_{34}. d_0 is the impact parameter and z_0 is the longitudinal impact parameter, as defined in Section 4.1.

Jets are reconstructed using the anti-k_T algorithm with a radius parameter $R = 0.4$. Inputs to the algorithm are formed from matching energy clusters in the calorimeters to tracks reconstructed in the ID using the Particle Flow algorithm, as discussed in Section 4.4.0.1. Reconstructed jets are corrected for calorimeter response, noise threshold and contributions from pile-up, and are required to have $p_T > 30$ GeV and $|\eta| < 4.5$. This aims to reject jets originating from pileup interactions. In order to identify jets originating from b-quarks, the MV2c10 b-tagging algorithm is used to assign a b-tagging weight to jets with $|\eta| < 2.5$.If a jet overlaps geometrically with a reconstructed muon or electron within a cone of radius R = 0.2, the jet is removed.

5.3.2. Higgs candidate selection

Once all physics objects in an event are defined, same-flavor opposite-sign (SFOS) leptons passing the selection requirements are paired and used to form Higgs candidates. The SFOS pair with invariant mass m_{12} closest to the Z boson mass is labeled as the leading pair. The other pair is the subleading pair. All combinations of two SFOS lepton pairs are combined to form a set of Higgs candidates for a single event. The selection proceeds in parallel for all final state (4μ, 2e2μ, 2μ2e, 4e).

The three leading leptons of each Higgs candidate must satisfy $p_T(E_T) > 20, 15, 10$ GeV. No more than one calorimeter-tagged or stand-alone muon is allowed per Higgs candidate, to prevent degradation of the momentum resolution. The leading di-lepton pair must have an invariant mass between 50 and 106 GeV. The subleading di-lepton pair must fall between $m_{threshold}$ and 115 GeV, where $m_{threshold}$ is set to 12 GeV for $m_{4\ell} < 140$ GeV, rises linearly to 50 GeV at $m_{4\ell} = 190$ GeV, and remains at 50 GeV for all higher $m_{4\ell}$ mass points.

Higgs candidates with SFOS pairs passing the di-lepton mass cuts must satisfy a distance cut of $\Delta R(\ell, \ell') > 0.10$ for all leptons in the quadruplet to prevent overlap. Here, ℓ and ℓ' denote alternate flavor leptons. Finally, to eliminate contributions from $J/\psi \to \ell\ell$ decays, Higgs candidates in the same-flavor decay channels, $4e$ and 4μ, are removed if alternate opposite-charge lepton pairings have a mass $m_{\ell\ell} < 5$ GeV.

From Higgs candidates passing these cuts, all electrons (muons) must pass a transverse impact parameter significance cut of $|d_0|/\sigma(d_0) < 5(3)$ to suppress the background from heavy-flavor hadrons. Additional backgrounds from $Z+$jets and $t\bar{t}$ are reduced by imposing track-based and calorimeter-based isolation criteria on each lepton, as well as a cut requiring the leptons to originate from the same vertex. A vertex fit using the ID tracks of the leptons is performed, with a requirement that the χ^2/N_{dof} value be < 6 in the 4μ channel and < 9 in all other channels, accounting for the worse resolution of electron track reconstruction. This maintains a signal efficiency of 99.5% while rejecting between 20 and 30% of backgrounds from $Z+$jets and $t\bar{t}$.

At the end of the selection, multiple Higgs candidates may remain. A first choice of the final candidate is made based on the decay channel and the mass of the leading lepton pair. If multiple candidates in the same decay channel remain, the one with the leading lepton pair closest to the Z boson mass is kept. If there is more than one candidate from different decay channels, the candidate from the decay channel with the highest efficiency is kept, where the signal selection efficiencies are 31%, 21%, 17%, and 16%, in the 4μ, $2e2\mu$, $2\mu2e$, and $4e$ channels, respectively. Finally, after this choice is made, if there is a fifth lepton in the event satisfying $p_T > 12$ GeV that passes all of the lepton identification and isolation requirements, the best possible Higgs candidate is chosen using a matrix element-based method. The matrix element for each Higgs candidate is calculated at LO using MadGraph5_aMC@NLO, and the candidate with the highest matrix element is selected. This improves the probability of selecting the correct Higgs candidate in cases where the extra lepton comes from the decay of a vector boson or top quark in VH-leptonic or ttH production.

Once a single Higgs candidate has been selected for a given event, the four-lepton mass resolution is improved by accounting for final state radiation (FSR) in the decays of the Z bosons. FSR photons have a spectrum of dN/dE_γ and can be categorized into two groups. The first is collinear, or near FSR, in which the $\eta - \phi$ separation between the photon and the lepton, $\Delta R_{\ell\gamma}$ is less than 0.15 and the photon has a transverse energy satisfying E_T^γ > 1.5 GeV. The second is non-collinear, or far FSR, where $\Delta R_{\ell\gamma} > 0.15$ and E_T^γ 10 GeV.

Only one FSR photon is added per Higgs candidate, and the preference is given to collinear FSR photons. In this case, a the photon four momentum is added to that of the muons of the leading Z boson if $m_{Z_1} < 89$ GeV. In the case of non-collinear FSR, the photon four momentum is added to the four momentum of leptons or muons from either Z candidate. In both cases, selection cuts are applied on properties of the FSR photons such as the fraction of energy deposited in different layers of the calorimeter and the distance between the photon and the lepton from the Higgs decay in order to remove backgrounds from sources like ionization of the lepton itself. In the case that more than one candidate FSR photon is found, the one with the highest E_T is selected. If after inclusion of the FSR photon a Z boson mass is greater than 100 GeV, the FSR photon is removed.

Finally, Higgs boson candidates within the $m_{4\ell}$ range between 105 and 160 GeV are used for the analysis.

5.4. Background estimation

There are several main backgrounds to the $H \to 4\ell$ signal. These are processes which either have four leptons in the final state that come from processes other than the decay of a Higgs boson, or processes that do not have four leptons in the final state, but some other object, such as a jet, is mistaken for one or more leptons. All background contributions are estimated in a data-driven way, wherever possbile. This provides the most accurate estimation achievable and allows for the reduction of systematic uncertainties associated with the use of theoretical predictions. These data-driven methods will be described in the following sections, beginning with the second type of background sources just mentioned, referred to as the 'reducible background'.

Smaller background contributions from processes including tWZ, $t\bar{t}WW$, $t\bar{t}t$, $t\bar{t}t\bar{t}$ and tZ, denoted together as tXX, are estimated purely from simulation described in Section 5.2. These contribute to less than 1% of events in the signal region.

5.4.1. Reducible background

The reducible background, denoted as such due to the large reduction possible with kinematic cuts, has contributions from events where a Z boson is present along with jets, referred to as $Z+$jets, as well as from $t\bar{t}$ and WZ production. Here, simluation is less robust than using data in determining selection efficiencies of these background events, and often comes with large theoretical uncertainties. To combat this, the reducible background yields are estimated using the general data-driven procedure: Control regions are first designed by relaxing or inverting selection and isolation requirements detailed in Section 5.3 in order to enhance contributions from various background processes. In these control regions (CRs), the background compositions and shapes from each contribution are studied, and higher statistics allow for better comparisons between data and simulation compared to the Higgs signal region (SR), where by design these backgrounds have lower yields. Once normalizations of the background contributions are obtained in the various control regions, transfer factors are used to extrapolate to the signal region.

Because the Higgs is formed from two reconstructed Z bosons where one Z is on-shell and the other is off-shell, the mass constraint cannot be used for the off-shell Z boson. This causes the dominant contribution to the reducible background to depend on the flavor of the subleading lepton pair from the off-shell Z boson decay. Consequently, the background yields are estimated for $Z+\mu\mu$ and $Z+ee$ separately. The methods are described in detail in the following two subsections.

5.4.1.1. $Z+\mu\mu$

The dominant background contribution to Higgs events where the subleading Z boson is reconstructed from two muons comes from events where one Z boson is present accompanied by leptons from semi-leptonic decays of heavy flavor hadrons. Such events are referred to as Z+HF (where the HF denotes heavy flavor). This background is augmented slightly by events where the accompanying leptons come from in-flight decays of pions or kaons from light-flavor jets. These are denoted Z+LF (where LF indicates light flavor). Together, these

contributions make up the $Z+$jets components of the reducible background. There are also smaller contributions from $t\bar{t}$ and WZ production.

We define four control regions, each designed to enhance one of the background topologies, defined by relaxing or inverting components of the selection criteria defined in Section 5.3. They are designed to be orthogonal to the signal region and to each other, meaning no event can be present in more than one control region, and there is no event overlap between the signal region and the control regions. They were also chosen to have little to no contamination from ZZ^*, as this background is estimated separately. The control regions are defined as:

- *Inverted* d_0 - enhanced in Z+HF and $t\bar{t}$. This control region is created by applying the standard selection to the leading dilepton, while inverting the d_0 significance for at least one lepton in the pair, and not applying isolation requirements. This enhances Z+HF over Z+LF, as Z+HF events are characterized by a large d_0 significance. The vertex cut is not applied during quadruplet selection.

- $e\mu + \mu\mu$ - enhanced in $t\bar{t}$. This control region is constructed by requiring different flavor leptons to form the leading Z boson. Because both leptons of a Z must be of the same flavor, this excludes contributions from Z bosons, creating a region with clean $t\bar{t}$ contibutions. All other selection cuts are standard for the leading Z boson, while the subleading dilepton pair is not subjected to the d_0 significance cut or isolation requirements. These leptons can have the same or opposite charge. The vertex cut is again not applied.

- *Inverted isolation* - enhanced in Z+LF. In this control region, the standard selection is applied to the leading dilepton pair, while the subleading pair is required to have at least one lepton failing isolation requirements. The preservation of the d_0 significance cut enhances Z+LF contribution over Z+HF.

- *Same sign* - The last control region has contibutions from all background sources. It is formed by applying the standard selection to the leading dilepton pair, removing the d_0 significance cut and isolation requirements from the subleading dilepton pair, and requiring the subleading pair to have the same sign.

In all cases, the standard four-lepton combination selections are applied, and a single combination is chosen per event. In addition, a fifth control region is defined in order to validate the normalization after the estimation is performed. It is not orthogonal to the control regions or the signal region, and is not used in the fit. It is referred to as the *Relax* control region, and is formed by removing the isolation and d_0 significance requirements on the subleading lepton pair. The standard quad selection is then applied, without the vertex cut.

The background estimation proceeds as follows: in each control region, shapes for each background contribution are taken from simulation. The data is fit simultaneously in each control region to these shapes in order to extract a yield normalization. The fit is a simultaneous, unbinned maximum likelihood of the mass of the leading dilepton pair, m_{12}, as it is resonant in $Z+$jets distributions and non-resonant in $t\bar{t}$, thus providing good separation between the two. The validity of the estimations is checked in the Relax control region, and then the yield is extrapolated to the signal region using transfer factors.

The probability distribution functions (PDFs) in each control region is expressed in terms of the number of events in the Relax control region as follows:

$$\mathcal{F}_{CR} = \sum N_i \cdot f_{i,CR} \cdot \mathcal{M}_{i,CR}\,, \tag{5.1}$$

where i is an index representing each of the various background components considered. f_i is the ratio of background component i in the control region over its contribution in the Relax control region. This is originally taken from MC as an initial starting point and constrained during the fit to data to be within $\pm 3\sigma$ of this value. N_i is the fitted parameter of interest, the number of background events. Finally, $\mathcal{M}_i$ is the shape model.

The shape models are analytic functions used to describe the m_{12} distribution of each background type in each control region. The $t\bar{t}$ m_{12} shape is described by a second order Chebyshev polynomial in all control regions. Meanwhile, in the inverted isolation, inverted d_0, and same sign control regions, the Z+HF and Z+LF resonant shapes are described by a Breit-Wigner (BW) convolved with a Crystal Ball function (CB). In the $e\mu + \mu\mu$ control

region, as the leading dilepton cannot originate from a Z but instead comes from random opposite flavor leptons in the event, it has a non-resonant m_{12} distribution which is described by a first order polynomial.

Contibutions from WZ and ZZ^* events in the background control regions are very small. The shape is similar to that of $Z+$jets, as the leading Z boson is a true Z and not another object faking one; however there exists a tail in the distribution. This contibution is modeled as

$$f \cdot G(m_{12}) + (1-f) \cdot F(m_{12}) \,, \tag{5.2}$$

where G is a Gaussian, F is a CB-BW convolution, and f is the ratio of events with $m_{12} < 75$ GeV to events with $m_{12} > 75$ GeV, essentially giving the ratio of the tail to the peak. The normalization is estimated from MC and accounts for ttV and VVV contributions as well.

Results from the fit to data are compared to MC in Figure 5.1, shown in the validation region in Figure 5.2. The yield results of the fit along with transfer factors and final yields in the signal region are provided in Table 5.4, with the yields per channel in the signal region provided in Table 5.5.

4μ+$2e2\mu$ - Full Run2 data			
type	data fit	extrapolation factor [%]	signal region yield
$t\bar{t}$	3074 ± 45	0.24 ± 0.02	$7.38 \pm 0.11 \pm 0.71$
Z+jets (HF)	2862 ± 110	0.43 ± 0.04	$12.39 \pm 0.48 \pm 1.11$
Z+jets (LF)	277 ± 63	1.08 ± 0.11	$2.98 \pm 0.68 \pm 0.30$
Z+jets (HF+LF)	3287 ± 72		$14.23 \pm 0.31 \pm 1.27$
WZ	MC-based estimation		4.53 ± 0.52

Table 5.4. Final $\ell\ell + \mu\mu$ background estimates in the relaxed region for each of the contributing background components, corresponding to the full m_{4l} range between 105 and 160 GeV. The second column shows the extrapolation factors to the signal region along with the corresponding statistical uncertainties. The last column shows the estimates for the signal region yields with both statistical and systematic uncertainties [151].

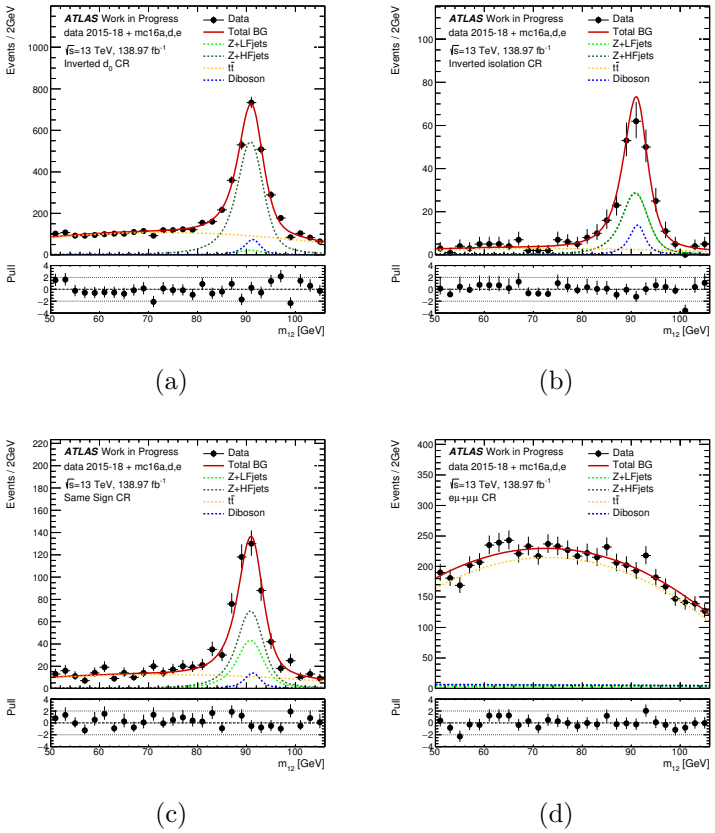

Figure 5.1. Distributions of m_{12} for the full Run2 data compared to the modelled background components in the (a) inverted-d_0, (b) inverted isolation, (c) same-sign and (d) $e\mu$+$\mu\mu$ control regions. The lower panels show the fit pulls [151].

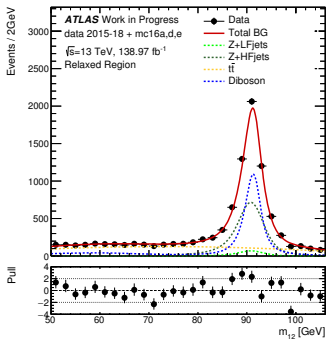

Figure 5.2. Distributions of m_{12} compared to the background yields, estimated by the fit, in the Relax validation region [151].

type	4μ	$2e2\mu$
$t\bar{t}$	$2.02 \pm 0.01 \pm 0.23$	$5.36 \pm 0.08 \pm 0.50$
Z+HF	$6.93 \pm 0.31 \pm 0.60$	$5.46 \pm 0.26 \pm 0.48$
Z+LF	$1.72 \pm 0.30 \pm 0.17$	$1.26 \pm 0.36 \pm 0.12$
WZ	2.10 ± 0.29	2.43 ± 0.33

Table 5.5. Final estimates in the signal region − corresponding to the full m_{4l} range between 105 and 160 GeV− for the $t\bar{t}$, Z+HF and Z+LF background components in each channel with both statistical and systematic uncertainties shown, as well as the WZ contribution which is shown with its total uncertainty. These yields account for roughly 4.7% of expected events in the full $m_{4\ell}$ range, and roughly 1.5% of exepected events in the signal region with $m_{4\ell}$ between 115 and 130 GeV [151].

5.4.1.2. $Z + ee$

The second group of contributions to the reducible background are $Z + ee$ events, in which the subleading Z boson decays to two electrons. The dominant sources of these events are:

- events in which a Z boson is produced along with a light-flavor jet that deposits energy in the EM calorimeter, where these energy deposits fake an electron, denoted as f,
- events in which one electron is from the semi-leptonic decay of a heavy quark, denoted as q,
- and events in which one or more electron comes from a photon conversion or from final state radiation, denoted as γ.

f, q, and γ will be used throughout the rest of this section to refer to these types of events. To estimate these contributions, a method similar to that used in the $Z + \mu\mu$ reducible background estimation is employed. A control region (CR) that is orthogonal to the signal region (SR) is defined, the various background components are estimated in this control region using a fit to data. The yield estimates are then extrapolated to the signal region using transfer factors.

The control region defined to estimate the $Z + ee$ component contributions is known as the '$3\ell + X$' control region. It is formed by performing the standard set of selections on the first three leading leptons in p_T, and relaxing the identification and selection criteria on the lower p_T electron of the subleading lepton pair, known as the 'X'. Both leptons from the subleading lepton pair are required to have the same sign, reducing contamination from ZZ^* and ensuring orthogonality with the signal region. The X candidates are subjected to cuts on the number of total silicon hits, the number of inner pixel hits, and the d_0 significance cut, and the vertex cut is applied to the final quadruplets.

In the $3\ell + X$ control region, a template fit on the number of inner pixel hits observable, $n_{InnerPix}$, is performed. This variable corresponds to the number of hits in the IBL, and provides good discrimination between γ's with respect to f and q. As photons convert in the

detector material after the inner pixel layers, γ's have $n_{InnerPix} = 0$. In the case that there is a dead region in the IBL where the hits are expected, the number of hits in the second innermost layer is used instead.

The templates used in the fit are taken from simulation in a separate control region, $Z + X$. This region is selected in data using single- and di-electron triggers, forming Z candidates, and using the same X selection as is used in the $3\ell + X$ control region. The region is then enriched in either γ or f events by requiring $n_{InnerPix} = 0$ or $n_{InnerPix} > 0$, respectively. The templates are extracted from simulation in this region, while scale factors are determined from data/simulation comparison. Finally, transfer factors to be used in extrapolating yields to the signal region are determined by comparing yields in the control region to yields in the signal region, in simulation.

The templates used are $n_{InnerPix}$ distributions, with the same template used for f and q, as they have almost indentical $n_{InnerPix}$ distributions. The fit to data is done with the $4e$ and $2\mu 2e$ decay channels combined. The *sPlot* method [152] is used to obtain the contributions from each background source in the fit. For each event, the method determines a covariance-weighted quantity equal to the probability the the X object is an f or a γ. The full distribution for each contribution, shown in Figure 5.3 below, is obtained by summing these weights.

The final estimates in the signal region are obtained separately for the f and γ contributions, with the function:

$$N_{\mathrm{SR}} = \sum_i s_i \sum_j \varepsilon_{ij} \cdot N^{ij}_{\mathrm{sPlot}} \,, \tag{5.3}$$

where i is an index over p_T bins, j is an index over N_{jets} bins, ϵ is the efficiency for a given background component, estimated as a funciton of p_T and N_{jets} in the $Z + X$ control region, and s is the p_T efficiency scale factor, also estimated in the $Z + X$ control region. Finally, N_{sPlot} is the sum of probability weights for the given background contribution.

The final yield results in the signal region for the three background contributions in the two decays channels, $4e$ and $2\mu 2e$, are provided in Table ??.

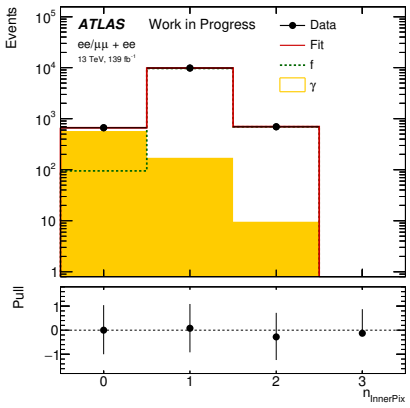

(a)

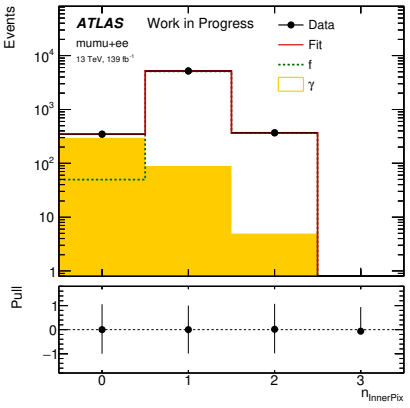

(b)

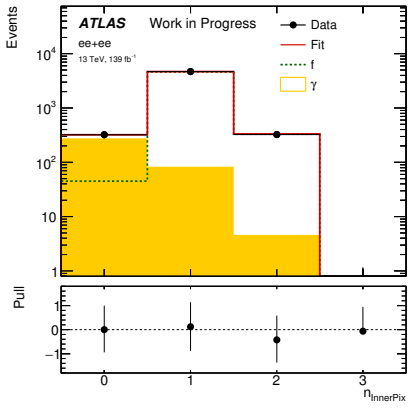

(c)

Figure 5.3. Events in the 3ℓ+X control region from data (black) compared to results of the fit to $n_{InnerPix}$, for the combined $2\mu 2e$ and $4e$ channels (a), and for the separate $2\mu 2e$ (b) and $4e$ (c) channels, using the full Run 2 dataset. The lower panel in each plot shows the fit pulls. The fit components modeling f and γ contributions separately are also shown [151].

	Full Run 2	
type	$4e$	$2\mu 2e$
f	$7.06 \pm 0.38 \pm 1.10$	$7.73 \pm 0.40 \pm 1.23$
γ	$2.01 \pm 0.50 \pm 0.40$	$2.17 \pm 0.53 \pm 0.44$
q	4.33 ± 1.30	7.77 ± 2.33

Table 5.6. Electron reducible background event number estimates in the signal region broken down by channel, $4e$ vs. $2\mu 2e$, and contribution, f, γ, and q. These background sources constitute roughly 1.5% of the total event yield in the signal region, with $m_{4\ell}$ between 115 and 130 GeV, and rougly 4.7% of events in the extended $m_{4\ell}$ window between 105 and 160 GeV [151].

5.4.2. Non-resonant background

The largest source of background in $H \to 4\ell$ events is from prompt leptons resulting from from the decays of non-resonant ZZ^* pairs that come from either $q\bar{q}$ annihilation or gluon-gluon fusion. This background is constrained in a data-driven way, though using a slightly different approach compared to the reducible background estimations. The shape of the background is taken entirely from simulation, normalized to yields obtained in the $m_{4\ell}$ sidebands.

These sidebands are defined as the $m_{4\ell}$ regions between 105 and 115 GeV, and 130 and 160 GeV, shown by the shaded bands in 5.4. The sideband between 130 and 160 GeV is further split into two regions, between 115 and 130 GeV, to be constrained during the fit to the m4l spectrum in data by using a common normalization factor. Estimations from the sideband regions allow the normalization in the signal region, between 115 and 130 GeV, to be constrained during the fit to the $m_{4\ell}$ spectrum in data by using a common normalization factor. The fit and signal extraction methods will be discussed in more detail in Section 7.2.

The ZZ^* contribution is estimated separately in each bin of each differential observable. In phase space regions where the ZZ^* contribution in the $m_{4\ell}$ side bands is too low to provide a reliable estimation of the contribution in the signal region of a particular bin, the estimation is performed for several differential bins simultaneously, and the relative normalization in each bin is determined using simulation.

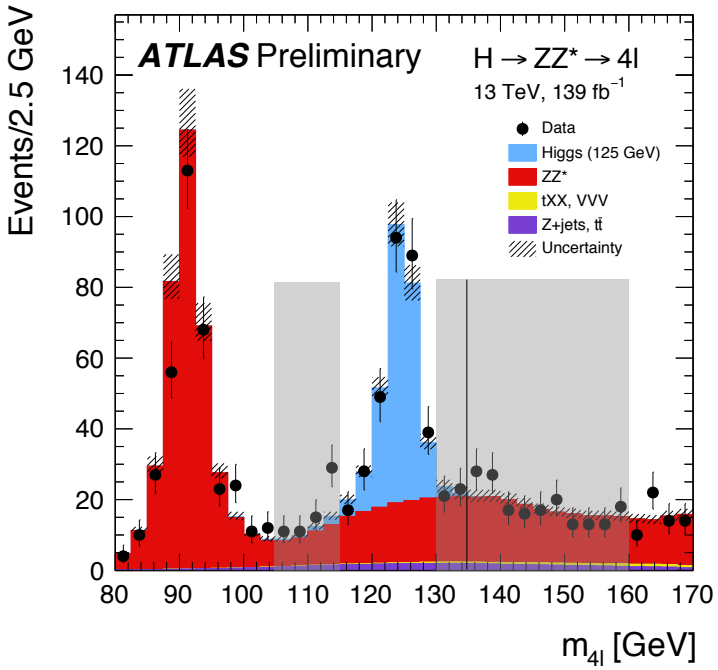

(a)

Figure 5.4. $m_{4\ell}$ distribution with the sidebands between 105 and 115 GeV, 130 and 135 GeV, and 135 and 160 GeV depicted by the shaded bands.

CHAPTER 6

Fiducial phase space and unfolded observables

In this thesis, measurements of the fiducial and differential cross sections of the Higgs boson in the ZZ^* to four lepton decay channel are presented. In an ideal world with a perfect detector and many signal events, one could obtain a smooth probability distribution function for these differential cross sections as a function of any observable that probes aspects of the Higgs boson production or decay. In reality, due to finite detector resolution and a limited number of signal events, binned histograms are typically used to measure the rate of events in bin of a particular observable. Furthermore, these measurements are made inside of what is known as the fiducial phase space region, which corresponds closely to the phase space region in which the ATLAS detector can identify particles and measure their properties.

In Section 6.1 of this chapter, the fiducial phase space is defined and motivated. The observables with respect to which the cross sections are measured are then defined in Sections 6.2 and 6.3. The differential observables are motivated following their definitons, and the chapter closes with a discussion on the binning choices for these observables.

The term 'unfolded' refers to the correction of detector efficiency effects, and will be expanded upon in Chapter 7.

6.1. Fiducial definitions

In order to avoid extrapolation outside of the phase space covered by the ATLAS detector, the fiducial and differential cross section measurements are made within the fiducial phase space that corresponds to the active region of the detector. This ensures minimal model dependence of the measurements, which lowers theoretical uncertainties and allows for easier interpretation of results in various theoretical frameworks.

As mentioned previously, the fiducial phase space refers to the phase space region in which the ATLAS detector - and analysis selection cuts - can identify particles from an interaction. As an example, the coverage of the inner detector ends at $|\eta| = 2.5$, so charged particles such as electrons and muons produced with $|\eta| > 2.5$ fall outside of the fiducial acceptance of the inner detector. The reconstruction-level, or 'reco', particle selection further cuts on the $|\eta|$ of electrons, requiring them to have $|\eta| < 2.47$. Thus, electrons with $|\eta| > 2.47$ fall outside the fiducial region of the analysis selection.

As discussed in Section 5.2, Monte Carlo (MC) events are passed through a simulation of the ATLAS detector in order to model detector effects. A second set of MC events are generated in which the 'truth-level', or 'particle-level', information is kept. These truth events are not passed through a simulation of the detector, and thus simulate the underlying 'truth' distributions, with Standard Model assumptions built in. Two sets of events are kept - one in which all generated events are accepted, and one in which all generated events are passed through a fiducial selection designed to match the reconstructed-level selection as closely as possible. These are referred to as 'truth' and 'fiducial' events, respectively. Furthermore, for each of these two types of events, both born- and dressed-level information is stored. Born-level leptons refer to leptons prior to QED radiation emission. Dressed leptons refer to those after QED radiation emission, where the MC record is used to account for the radiation emitted, as in the case of the FSR recovery described in Section 5.3.2.

The fiducial definitions of physics objects are provided below, and the fiducial selection of these objects is summarized in Table 6.1.

- **Electrons.** *Dressed* electrons (e) are required to have $p_T^e > 5\,\text{GeV}$, $|\eta^e| < 2.7$, chosen to match the inner detector acceptance, and are required to originate from Z and W decays (not from hadron decays).

- **Muons.** Muons (μ) are required to have $p_T^\mu > 5\,\text{GeV}$, $|\eta^\mu| < 2.7$. Similarly to electrons, they are required to originate from Z and W decays.

- **Jets.** Particle-level jets (j) are reconstructed using all stable particles, excluding those originating from the Higgs and leptonic vector boson decays. Stable particles

are clustered using the anti-k_t algorithm [65] with radius parameter $R = 0.4$. Each jet is required to have $p_T(\mathrm{j}) > 30\,\mathrm{GeV}$ and $|y(j)| < 4.4$ and must not be within $\Delta R < 0.1$ of any truth electron or muon as selected above. b-jets are tagged within the kinematic range $p_{T,j} > 30$ GeV and $\eta_j < 2.5$. A fiducial jet is labelled as a b-jet if there is a b-hadron within a cone around the jet axis of radius $\Delta R = 0.3$ with a transverse momentum greater than 5 GeV.

- **Higgs candidate.** The Higgs candidate is composed of two pairs of same flavor opposite sign (SFOS) truth leptons. The lepton flavor can be different between the two pairs, but is the same for the two leptons in each pair. The leading pair is defined as the SFOS lepton pair with invariant mass closest to the nominal Z mass ($m_Z = 91$ GeV), and the sub-leading pair is defined as the remaining SFOS lepton pair with invariant mass second closest to the m_Z. In cases where multiple Higgs candidates can be formed, the best candidate is selected using a matrix element based method, as is done in the reco selection, detailed in Section 5.3.2.

Lepton defintion	
Muons: $p_T^\mu > 5\,\mathrm{GeV}$, $\lvert\eta^\mu\rvert < 2.7$	Electrons: $p_T^e > 5\,\mathrm{GeV}$, $\lvert\eta^e\rvert < 2.7$
Pairing	
Leading pair:	SFOS lepton pair with smallest $\lvert m_Z - m_{\ell\ell}\rvert$
Sub-leading pair:	Remaining SFOS lepton pair with smallest $\lvert m_Z - m_{\ell\ell}\rvert$
Event selection	
Lepton kinematics:	Leading lepton $p_T > 20$, 15, 10 GeV
Mass requirements:	$50 < m_{12} < 106\,\mathrm{GeV}$; $12 < m_{34} < 115\,\mathrm{GeV}$
Lepton separation:	$\Delta R_{\ell_i\ell_j} > 0.1$ for all leptons
Jet/Lepton separation:	$\Delta R_{\ell_i jet} > 0.1$ between jets and leptons (else jet is vetoed)
J/ψ veto:	$m_{\ell_i\ell_j} > 5\,\mathrm{GeV}$ for all SFOS lepton pairs
Mass window:	$105 < m_{4\ell} < 160\,\mathrm{GeV}$

Table 6.1. Fiducial event selection requirements for the $H \to 4\ell$ fiducial region.

6.1.1. Detector Acceptance

The acceptance, $\mathcal{A}$, of the ATLAS detector refers to the fiducial phase space defined previously, and is defined in terms of the number of particles passing the particle-level, or

fiducial-level event selection criteria, N_{fid}, divided by the total number of particles generated, N_{tot}:

$$\mathcal{A} = \frac{N_{\text{fid}}}{N_{\text{tot}}} \,. \tag{6.1}$$

The acceptance describes the fraction of total events in the generated phase space that pass the selection criteria. These values are taken purely from MC, and are evaluated for each bin of each unfolded variable as well as for the inclusive fiducial observables, where the categories correspond to the different final states, 4μ, $4e$, $2e2\mu$, $2\mu2e$. As τ leptons are not included in the reco event selection, they are also filtered out in the event generation and are thus not included in N_{tot}.

With the $H \to 4\ell$ branching ratio of $BR = (1.25 \pm 0.03) \times 10^{-4}$ [30], the total cross section, σ^{tot}, can be calculated

$$\sigma^{tot} = \frac{N_{\text{s}}}{\mathcal{A} \times \mathcal{C} \times BR \times \mathcal{L}_{\text{int}}} \,, \tag{6.2}$$

where N_{s} is the number of observed signal events, $\mathcal{L}_{\text{int}}$ is the integrated luminosity, $\mathcal{C}$ is a detector efficiency factor that will be discussed in following sections, and $\mathcal{A}$ is the detector acceptance.

The acceptance factor, $\mathcal{A}$, cannot be measured directly from data, as by definition the non-fiducial events and objects cannot be detected. Instead it must be estimated using simulation, which introduces a model dependence.

In order to factorize this model dependence, as discussed at the beginning of the current chapter, the fiducial cross section is measured instead, and is defined as:

$$\sigma^{fid} = \sigma^{tot} \times \mathcal{A} \times BR = \frac{N_{\text{s}}}{\mathcal{C} \times \mathcal{L}_{\text{int}}} \,. \tag{6.3}$$

6.2. Fiducial cross sections

The fiducial cross sections are measured in bins of several parameters of interest, or POIs. These are defined as:

- Cross sections in four categories corresponding to the four final states, or decay channels, of the Higgs decay, 4μ, $4e$, $2\mu 2e$, and $2e2\mu$, denoted as $chan, i$:

$$\mathrm{POI}_{chan,i} = [\sigma_{tot} \times BR(H \to 4\ell_i) \times A_i] \tag{6.4}$$

- Cross sections in the same flavor, 4μ and $4e$, decay channels (denoted $2\ell 2\ell$), and the opposite flavor, $2\mu 2e$ and $2e2\mu$, channels (denoted $2\ell 2\ell'$):

$$\mathrm{POI}_{2\ell 2\ell} = \sigma_{tot}[BR(H \to 4\mu) \times A_{4\mu} + BR(H \to 4e) \times A_{4e}] \tag{6.5}$$

$$\mathrm{POI}_{2\ell 2\ell'} = \sigma_{tot}[BR(H \to 2\mu 2e) \times A_{2\mu 2e} + BR(H \to 2e2\mu) \times A_{2e2\mu}] \tag{6.6}$$

  These are sensitive to final state interference effects that, under SM assumptions, should lead to a roughly 10% difference in cross section between the two decay modes.

- The sum of the cross sections across all four decay channels:

$$\mathrm{POI}_{sum} = \sum_{i=1}^{4} \sigma_{tot} \times BR(H \to 4\ell_i) \times A_i] \tag{6.7}$$

- The statistical combination of the cross sections across all four decay channels, assuming Standard Model branching fractions:

$$\mathrm{POI}_{comb} = [\sigma_{tot} \times BR(H \to 4\ell_i) \times \bar{A}] \tag{6.8}$$

- The total cross section extrapolated to the full phase space:

$$\mathrm{POI}_{tot} = \sigma_{tot} \tag{6.9}$$

6.3. Differential cross sections

Differential cross sections of the Higgs boson are measured with respect to observables that probe aspects of both its production and decay. These are measured within the fiducial phase space defined in Section 6.1. These observables, or variables, are grouped into those that probe the kinematics of the Higgs boson and its decay products, those that probe the jet activity in events where a Higgs boson is present, and differential observables that probe relationships between multiple parameters of the decay and event topology.

The kinematics of selected Higgs candidates are studied by measuring differential cross sections in bins of the transverse momentum, p_{T}^{H}, and rapidity, $|y_H|$ of the Higgs bosons, reconstructed as the transverse momentum and the rapidity of the four lepton system, $p_{\mathrm{T}}^{4\ell}$ and $|y_{4\ell}|$, respectively. The kinematics of the decay are studied by measuring cross sections in bins of the invariant mass of the leading and subleading dilepton pairs, m_{12} and m_{34}, as well as five decay angles between the decay products. These angles are labeled $\cos\theta_1$, $\cos\theta_2$, $\cos\theta^*$, ϕ, and ϕ_1, and are depicted in Figure 6.1. Their definitions are provided in Table ?? and in Ref. [153].

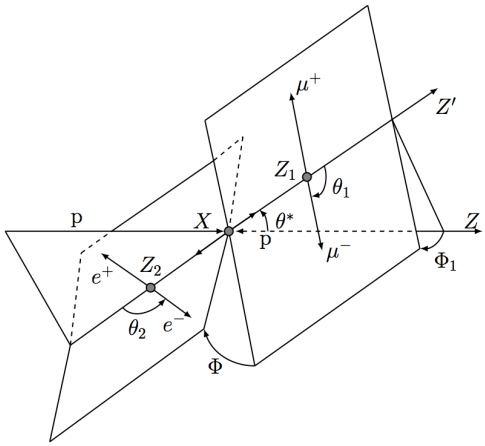

Figure 6.1. Diagram of decay angles for the $H \to 4\ell$ decay [153].

The observables that probe jet activity in events where a Higgs candidate is selected include the jet multiplicity, N_{jets}, and the number of b-tagged jets, $N_{b-\mathrm{jets}}$, where b-tagging

is performed as described in Section 4.4.0.2. Differential cross sections in bins of the transverse momentum of the leading and subleading jets, ordered in p_T and labeled as $p_{\mathrm{T}}^{\mathrm{lead.jet}}$ and $p_{\mathrm{T}}^{\mathrm{sublead.jet}}$, are measured. In addition, in events with at least two jets that pass the reconstruction and selection requirements, the dijet invariant mass, m_{jj}, distance in η between the two jets, $\Delta\eta_{\mathrm{jj}}$, and distance in ϕ between the two jets, $\Delta\phi_{\mathrm{jj}}$, are studied [1].

A summary of all the variables and their descriptions is provided in Table **??**, including the double differential variables. In the following section, motivations for each variable are provided. Following, the binning choices are discussed.

6.3.1. Variables and motivation

The measured observables probe both the Higgs boson production and decay, and either further our understanding of SM predictions, or are sensitive to BSM effects.

One of the observables most sensitive to BSM effects is the Higgs boson transverse momentum, p_{T}^{H}, measured as the transverse momentum of the four lepton system, $p_{\mathrm{T}}^{4\ell}$. The main production mode of the Higgs boson at the LHC is gluon-gluon fusion, where the Higgs boson production is mediated by a virtual quark loop, making the $p_{\mathrm{T}}^{4\ell}$ system sensitive to anomalous SM couplings or potential BSM particles that could run in the loop. In addition, when gluon-gluon fusion events with jet production are considered, the cross section depends on double logarithms of $p_{T,H}^{2}$. This dependence comes from interference between quark- and top-mediated contributions, and increases sensitivity to modifications of SM Yukawa couplings [154]. The rapidity of the Higgs boson, measured as the rapidity of the four lepton system, is sensitive to the parton distribution functions of the colliding protons.

The invariant mass of the leading and subleading lepton pairs, m_{12} and m_{34}, are sensitive to higher order electroweak corrections to the decay of the Higgs boson, as is the double

[1] where

$$\Delta\phi_{jj} = \begin{cases} \phi_{j1} - \phi_{j2}, & \text{if } \eta_{j1} > \eta_{j2} \\ \phi_{j2} - \phi_{j1}, & \text{if } \eta_{j2} > \eta_{j1} \\ \Delta\phi_{jj} + 2\pi, & \text{if } \Delta\phi_{jj} < 0 \end{cases} \tag{6.10}$$

differential distribution m_{12} vs. m_{34} and the angular variable, ϕ. In addition, m_{12} vs. m_{34} can be used to probe potential BSM contact interactions between a Higgs boson, intermediate Z bosons, and charged leptons in the Pseudo-Observables framework [155], as will be described in Section 9.1. Particular BSM scenarios that could modify this distribution include, but are not limited to, a heavy Z' or some additional heavy exotic intermediate states in the $H \to ZZ^* \to 4\ell$ decay that might couple to SM fermions non-universally. These variables are also sensitive to final state interference in the SM Higgs boson decay.

The angular variables of the Higgs boson decay are sensitive to the Higgs boson spin and parity, as well as final state interference and EW corrections. The jet-related variables probe the production mechanism of the Higgs boson as well as QCD radiation effects. In the case of the jet multiplicity, N_{jets}, the various production mechanisms are probed, as is the theoretical modelling of high p_T quark and gluon emission. The invariant mass of the two leading jets in p_T is also sensitive to the Higgs boson production mechanism, and the angular distance between the two jets in the transverse plane, $\Delta\phi_{\text{jj}}$, is sensitive to the spin and parity of the Higgs boson.

6.3.2. Binning definitions

The number of bins and the bin widths in the histogram for each observable are chosen based on several criteria. The first consideration is in targeting specific physics phenomena. For example in the invariant mass spectrum of the on-shell Z boson, m_{12}, the last bin is chosen to fully contain the on-shell Z mass. Other distributions, such as the jet multiplicity, N_{jets}, have trivial integer binning. To detect any potential deviations in the measured cross sections with respect to the SM expectations, enough events must be present in any given bin to have a significant result. Thus, the expected significance in each bin is required to be at least two sigma, where the expected significance is evaluated as:

$$\sigma = S/\sqrt{S+B}\,. \tag{6.11}$$

Here, S is the number of expected signal events and B is the number of expected background events, evaluated using simulation. Finally, a statistical error of less than 30% in each bin is targeted, while aiming for minimal migration of events between bins. In practice this means avoiding bin sizes that are too small compared to the detector resolution.

Two examples are provided below. In Figure 6.2, migration matrices for $p_{\mathrm{T}}^{4\ell}$ and $p_{\mathrm{T}}^{\mathrm{lead.jet}}$ are provided. These are defined as the percentage of reco events in a bin that are truth matched to a truth event passing the selection cuts in the same bin, where the matching is done using the MC truth record. In Figures 6.3 and 6.4, the optimized binning choices for these two variables are presented. In the figures are the expected Higgs boson signal, and non-resonant and reducible background distributions in blue, red, and purple, respectively, in the $m_{4\ell}$ range between 115 and 130 GeV. The accompanying tables provide the expected yields from each of these contributions, as well as the values of the various parameters used to optimize the binning, including the expected signal to background ratio, S/B, and expected significance defined above, σ. All numbers here are evaluated using simulation.

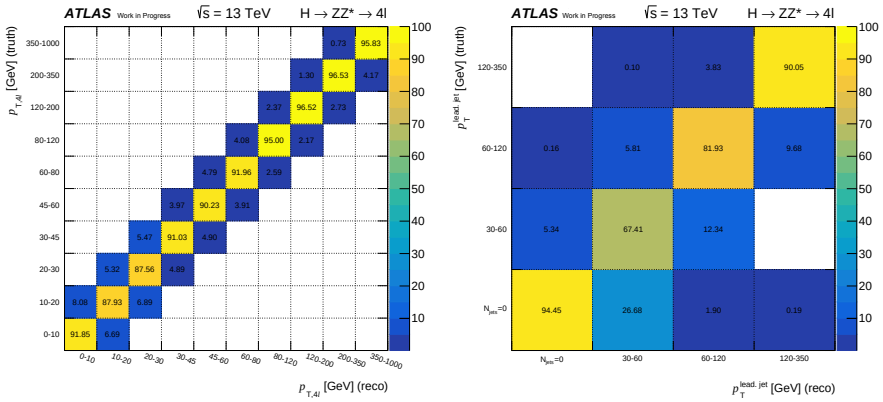

(a) (b)

Figure 6.2. Migration matrices for (a) the transverse momentum of the four lepton system, $p_{\mathrm{T}}^{4\ell}$, and (b) the transverse momentum of the leading jet in p_T, $p_{\mathrm{T}}^{\mathrm{lead.jet}}$. Bins were chosen in part to minimize migration between bins, thus maximizing the diagonal elements of the migration matrices.

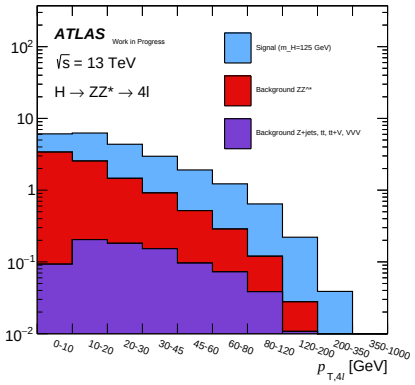

Bin	Signal	ZZ	Z+jets/$t\bar{t}$	$t\bar{t}V + VVV$	S/B	σ
0	27.0235	32.9515	0.914851	0.012977	0.79764	3.46277
1	37.1481	23.3602	1.8742	0.17073	1.46223	4.6969
2	29.0326	12.7772	1.67783	0.134918	1.98991	4.39573
3	30.8208	11.4044	2.00797	0.285118	2.2501	4.61928
4	20.9074	6.3264	1.16166	0.280699	2.69122	3.90427
5	18.7467	4.28082	1.09504	0.357664	3.26966	3.78893
6	20.9191	3.25155	0.932359	0.604984	4.36825	4.1258
7	15.4381	1.36092	0.484672	0.373598	6.95666	3.67394
8	5.42963	0.257735	0.0305352	0.0970319	14.0919	2.25163
9	0.766708	0.0321707	0.00609747	0.00624656	17.2237	0.851256

Figure 6.3. Distribution and binning choice for p_T: for each bin, signal and background yields are reported for $115 < m_{4\ell} < 130$ GeV together with S/B and expected significance values. A SM Higgs with $m_H = 125\,\text{GeV}$ has been assumed.

Higgs boson kinematic-related variables	
p_{T}^{H}, $\lvert y_{4\ell}\rvert$	Transverse momentum and rapidity of the four-lepton system
m_{12}, m_{34}	Invariant mass of the leading and subleading lepton pair
$\lvert\cos\theta^{*}\rvert$	Magnitude of the cosine of the decay angle of the leading lepton pair in the four-lepton rest frame with respect to the beam axis
$\cos\theta_1$, $\cos\theta_2$	Production angles of the anti-leptons from the two Z bosons [153]
ϕ, ϕ_1	Two azimuthal angles between the three planes constructed from the Z-bosons and leptons in the Higgs boson rest frame
Jet-related variables	
N_{jets}, $N_{b\text{-jets}}$	Jet and b-jet multiplicity
$p_T^{\text{lead. jet}}$, $p_T^{\text{sublead. jet}}$	Transverse momentum of the leading and sub-leading jets, for events with at least one and two jets, respectively
m_{jj}, $\lvert\Delta\eta_{jj}\rvert$, $\Delta\phi_{jj}$	Invariant mass, difference in pseudorapidity, and signed difference in ϕ of the leading and sub-leading jets for events with at least two jets
Higgs boson and jet-related variables	
$p_{T4\ell j}$, $m_{4\ell j}$	Transverse momentum and invariant mass of the four-lepton system and leading jet, for events with at least one jet
$p_{T4\ell jj}$, $m_{4\ell jj}$	Transverse momentum and invariant mass of the four-lepton system and leading and sub-leading jets, for events with at least two jets
Double differential variables	
m_{12} vs. m_{34}	Invariant mass of the leading vs. the sub-leading lepton pair
$p_{T4\ell}$ vs. N_{jets}	Transverse momentum of the four-lepton system vs. jet multiplicity
$p_{T4\ell}$ vs. $p_T^{\text{lead. jet}}$	Transverse momentum of the four-lepton system vs. transverse momentum of the leading jet
$p_{T4\ell}$ vs. $\lvert y_{4\ell}\rvert$	Transverse momentum vs. rapidity of the four-lepton system
$p_{T4\ell}$ vs. $p_{T4\ell j}$	Transverse momentum of the four-lepton system vs. transverse momentum of the four-lepton system and leading jet
$p_{T4\ell j}$ vs. $m_{4\ell j}$	Transverse momentum of the four lepton system and leading jet vs. invariant mass of the four lepton system and leading jet
$p_T^{\text{lead. jet}}$ vs. $p_T^{\text{sublead. jet}}$	Transverse momentum of the leading vs. sub-leading jet

Table 6.2. Definitions of observables for which differential cross sections are measured.

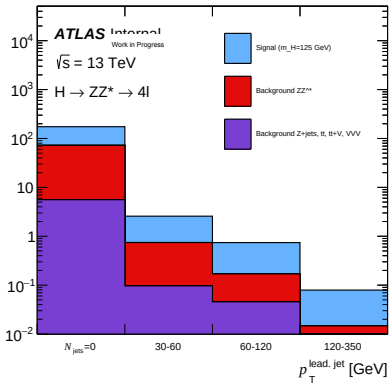

Bin	Signal	ZZ	Z+jets/$t\bar{t}$	$t\bar{t}V + VVV$	S/B	σ
0	101.618	66.9087	5.46547	0.128423	1.40157	7.70096
1	54.922	19.4096	2.44741	0.449629	2.46213	6.24967
2	34.2932	7.45239	1.7065	1.02394	3.36775	5.14215
3	14.8431	2.12081	0.565845	0.685229	4.40203	3.47785

Figure 6.4. Distribution and binning choice for $p_T^{\text{lead. jet}}$: for each bin, signal and background yields are reported for $115 < m_{4\ell} < 130$ GeV together with S/B and expected significance values. A SM Higgs with $m_H = 125\,\text{GeV}$ has been assumed.

Variable	Bin Edges	N_{bins}	ZZ Sidebands Bin Edges	$N_{ZZ\ \text{bins}}$
p_T	0, 10, 20, 30, 45, 60, 80, 120, 200, 350, 1000 GeV	11	0, 10, 20, 30, 60, 1000	5
m_{12}	50, 73, 64, 85, 106 GeV	4	50, 73, 85, 106	3
m_{34}	12, 20, 24, 28, 32, 40, 55, 65 GeV	7	12, 24, 32, 65	3
$\|y\|$	0.0, 0.15, 0.3, 0.45, 0.6, 0.75, 0.9, 1.2, 1.6, 2.0, 2.5	10	0.0, 0.15, 0.3, 0.45, 0.6, 0.75, 1.2, 2.5	7
$\|cos(\theta^*)\|$	0, 0.125, 0.25, 0.375, 0.5, 0.625, 0.75, 0.875, 1.0	8	0, 0.25, 0.5, 0.75, 1.0	4
$cos(\theta_1)$	-1.0, -0.75, -0.50, -0.25, 0.0, 0.25, 0.50, 0.75, 1.0	8	-1.0, -0.5, 0.0, 0.5, 1.0	4
$cos(\theta_2)$	-1.0, -0.75, -0.50, -0.25, 0.0, 0.25, 0.50, 0.75, 1.0	8	-1.0, -0.5, 0.0, 0.5, 1.0	4
ϕ	$-\pi, -\frac{3\pi}{4}, -\frac{2\pi}{4}, -\frac{\pi}{4}, 0, \frac{\pi}{4}, \frac{2\pi}{4}, \frac{3\pi}{4}, \pi$	8	$-\pi, -\frac{2\pi}{4}, 0, \frac{2\pi}{4}, \pi$	4
ϕ_1	$-\pi, -\frac{3\pi}{4}, -\frac{2\pi}{4}, -\frac{\pi}{4}, 0, \frac{\pi}{4}, \frac{2\pi}{4}, \frac{3\pi}{4}, \pi$	8	$-\pi, -\frac{2\pi}{4}, 0, \frac{2\pi}{4}, \pi$	4

Table 6.3. Binning chosen for Higgs kinematic variables of interest.

Variable	Bin Edges	N_{bins}	ZZ Sidebands Bin Edges	$N_{ZZ\ \text{bins}}$
N_{jets}	0, 1, 2, $\geq$3	5	0, 1, $\geq$2	3
$N_{b-\text{jets}}$	0 jets, 0 b-jets, $\geq$1 b-jets	2	0 jets, $\geq$ 0 b-jets	1
$p_T^{\text{lead. jet}}$	N_{jets}=0, 30, 60, 120, 350 GeV	4	N_{jets}=0, 30, 60, 120, 350	4
$p_T^{\text{sublead. jet}}$	N_{jets}=0, 30, 60, 120, 350 GeV	4	$N_{\text{jets}} < 2$, 30, 60, 350	4
m_{jj}	$N_{\text{jets}} < 2$, 0, 120, 450, 3000 GeV	4	$N_{\text{jets}} < 2$, 0, 120, 3000	3
$\Delta\eta_{jj}$	$N_{\text{jets}} < 2$, 0, 1, 2.5, 9	4	$N_{\text{jets}} < 2$, 0, 1, 9	3
$\Delta\phi_{jj}$	$N_{\text{jets}} < 2$, 0, $\frac{1}{2}\pi$, π, $\frac{3}{2}\pi$, 2π	5	$N_{\text{jets}} < 2$, 0, π, 2π	3

Table 6.4. Binning chosen for jet variables of interest.

Variable	Bin Edges		N_{bins}
$p_{T,4\ell}$ vs. N_{jets}	$N_{\text{jets}} = 0$	$p_{T,4\ell}$ {0, 15, 30, 120, 350}	
	$N_{\text{jets}} = 1$	$p_{T,4\ell}$ {0, 60, 80, 120, 350}	12
	$N_{\text{jets}} = 2$	$p_{T,4\ell}$ {0, 120, 350}	
	$N_{\text{jets}} \geq 3$	$p_{T,4\ell}$ {0, 120, 350}	
m_{12} vs. m_{34}	$m_{12} < 82$	$m_{34} < 32$	
	$m_{12} < 74$	$m_{34} > 32$	
	$m_{12} > 74$	$m_{34} > 32$	5
	$m_{12} > 82$	$24 < m_{34} < 32$	
	$m_{12} > 82$	$m_{34} < 24$	
$p_{T,4\ell}$ vs. $\lvert y \rvert$	$0.0 < \lvert y \rvert < 0.5$	$p_{T,4\ell}$ {0, 45, 120, 350}	
	$0.5 < \lvert y \rvert < 1.0$	$p_{T,4\ell}$ {0, 45, 120, 350}	12
	$1.0 < \lvert y \rvert < 1.5$	$p_{T,4\ell}$ {0, 45, 120, 350}	
	$1.5 < \lvert y \rvert < 2.5$	$p_{T,4\ell}$ {0, 45, 120, 350}	
$p_{T,4\ell}$ vs. $p_{T,\text{lead.jet}}$	$N_{\text{jets}} = 0$		
	$30 < p_{T,\text{lead.jet}} < 60$	$p_{T,4\ell}$ {0, 80, 350}	7
	$60 < p_{T,\text{lead.jet}} < 120$	$p_{T,4\ell}$ {0, 120, 350}	
	$120 < p_{T,\text{lead.jet}} < 350$	$p_{T,4\ell}$ {0, 120, 350}	
$p_{T,4\ell}$ vs. $p_{T,4\ell,j}$	$N_{\text{jets}} = 0$		
	$0 < p_{T,4\ell,j} < 60$	$p_{T,4\ell}$ {0, 120, 350}	5
	$60 < p_{T,4\ell,j} < 350$	$p_{T,4\ell}$ {0, 120, 350}	
$p_{T,4\ell,j}$ vs. $m_{4\ell,j}$	$120 < m_{4\ell,j} < 220$	$0 < p_{T,4\ell,j} < 350$	
	$220 < m_{4\ell,j} < 350$	$p_{T,4\ell,j}$ {0, 60, 350}	4
	$350 < m_{4\ell,j} < 2000$	$0 < p_{T,4\ell,j} < 350$	
$p_T^{\text{lead. jet}}$ vs. $p_T^{\text{sublead. jet}}$	$N_{\text{jets}} = 0$		
	$p_T^{\text{lead. jet}}$ {30, 60, 350}	$N_{\text{jets}} = 1$	
	$30 < p_T^{\text{lead. jet}} < 60$	$30 < p_T^{\text{sublead. jet}} < 60$	6
	$60 < p_T^{\text{lead. jet}} < 350$	$30 < p_T^{\text{sublead. jet}} < 60$	
	$60 < p_T^{\text{lead. jet}} < 350$	$60 < p_T^{\text{sublead. jet}} < 350$	

Table 6.5. Binning choices for the double differential variables.

CHAPTER 7

Unfolding and statistical treatment

With all of the observables defined, the background estimation in place, and the event selection performed, the final step in measuring the targeted cross sections is peforming the statistical analysis. In this chapter, the unfolding method, used to deconvolve detector effects from the measurement, is discussed, followed by the statistical treatment, and finally the systematic uncertainties considered.

7.1. Unfolding

The binned histograms used to describe the rate of an observable, y, in some number of bins, M, have a 'true' distribution given by a set of M expectation values, μ_i. The probability of measuring y in a bin i is given by

$$p_i = \frac{\mu_i}{\mu_{tot}}, \qquad \text{where} \qquad \mu_{tot} = \sum_{i=0}^{M} \mu_i \,. \tag{7.1}$$

The goal of unfolding is to obtain estimators, μ, for each of the M parameters, or bins, or for the probabilities for each bin [156]. At the heart of unfolding is the fact that each observation has a true value, y, which is not necessarily the same as the measured value, x. The two are related by a convolution described by what is known as the detector response matrix, $R_{i,j}$:

$$\nu_i = \sum_{j}^{M} R_{i,n}\mu_j \,, \tag{7.2}$$

where $\bar{\nu} = (\nu_i ... \nu_M)$ are the numbers of expected events in each of the M bins in the observable x, and $\bar{\mu} = (\mu_i ... \mu_M)$ are the expectation values for the histogram of y, or the 'true' distribution.

The detector response matrix encompasses the smearing and resolution effects of an imperfect detector, and the process of unfolding seeks to correct for these effects as well as correct for the the transformation of measured observables. As an example, when measuring the Higgs boson cross section as a function of its transverse momentum, the quantity actually measured in the ATLAS detector is not the true transverse momentum of the Higgs, but rather the transverse momentum of the four lepton system. Furthermore, due to the finite resolution of the detector and realistic imperfections in the reconstruction procedure, this quantity will not necessarily correspond to the same true value as the original Higgs transverse momentum. Unfolding seeks to deconvolve these effects and provide a result as close to the true distribution as possible.

Unfolding is not always strictly necessary. In order to compare measured cross sections with predictions from a particular theory, one could in principle modify the predictions, $\bar{\mu}$, convolving them with detector effects and then directly compare to the measured results. This method is simple from an experimental point of view; however, it comes at the cost of the longevity of the results - this prevents measurements from being compared with results from other hypothetical future experiments that will have different detectors. It also requires that the response matrices for each distribution remain available. In the case that a new theory or version of a theory is developed which one wants to compare to the results, these must again be convolved with the detector effects, moving the burden of analysis onto the theory side. In this analysis, unfolding is done in order to avoid these two points, and ensure that the results maintain longevity and are easy to compare and interpret in any theoretical framework without the need for the response matrices.

The next two sections introduce two unfolding methods - bin-by-bin correction factor unfolding and detector response matrix unfolding. Aspects of each are discussed and the choice of the baseline unfolding method, detector response matrix unfolding, is motivated.

7.1.1. Correction Factors

Detector correction factors are multiplicative factors used in unfolding that essentially describe the efficiency with which an observable is reconstructed. In the inclusive fiducial cross section measurements, they are evaluated per final state, while in the differential cross section measurements they are evaluated in each bin of a distribution. Denoting these various observables as bins, i, the correction factor in a particular bin, $\mathcal{C}_i$ is defined as:

$$\mathcal{C}_i = \frac{N_i^{\text{reco}}}{N_i^{\text{fid}}}\,, \tag{7.3}$$

where N_i^{reco} is the number of events reconstructed in bin i and N_i^{fid} is the number of events that pass the fiducial selection in the same bin. As in the case of the acceptance factors, the correction factors are evaluated using simulation. Also similarly to the acceptance factors, this reliance on simulation introduces a bias. This bias is only zero if the model of the simulation used to evaluate the factors is correct, which of course is unknown before the measurement. As might be expected, this bias tends to pull the estimators towards the predictions used for evaluation, which can hinder testing of the model. This bias can be quantified as [156]:

$$< \delta\mu_i >= s_i \times ((\frac{\mu_i}{s_i})_{\text{Model}} - (\frac{\mu_i}{s_i})_{\text{Truth}})\,, \tag{7.4}$$

where μ_i is again the number of true events, s_i is the number of reconstructed signal events, and $< \delta\mu_i >$ is the average bias in the i-th bin. Although the fact that the difference between the model and the truth is not known *a priori* makes it difficult to estimate the bias, it can be shown that the bias is proportional to the off-diagonal terms of the response matrix [156]:

$$< \delta\mu_i >= s_i \times \sum_{i \neq j} R_{ij}^{-1}((\frac{s_j}{s_i})_{\text{Model}} - (\frac{s_j}{s_i})_{\text{Truth}}). \tag{7.5}$$

Therefore, in distributions where the response matrix is largely diagonal, which as will be described in the next section implies a small amount of migration between bins, one can

expect small biases from the correction factor unfolding method. However in distributions where events migrate more between bins, a larger bias might be expected.

7.1.2. Detector Response Matrix

The detector response matrix, $R_{i,j}$, is defined as the number of reconstructed events in a bin, i, that can be matched to a truth event in bin j, normalized to the number of truth events in bin j. In the plots shown in this thesis:

- Y-axis = x_{truth} and X-axis = x_{reco};
- for each truth bin the reco quantity is reported;

The response matrix encodes information about the detector response in a given binning scheme of some observable. They are evaluated using simulation, considering all Higgs production modes together with standard model assumptions regarding the production mode composition. When normalized to unity along each reconstructed bin, the matrix gives the probability for an event with a given true value of the observable to be categorized in each of the reconstructed bins. In the case where the reconstructed bins have not been normalized to the total number of truth events in that bin, the matrix is referred to as the migration matrix. In this case, the migrations of reconstructed events can be visualized directly. While the bin-by-bin correction factors work well for variables with small migration between bins - as mentioned in the previous section, this implies a smaller expected bias - they do not take into account correlations in the migrations between bins. Detector response matrices can take these correlations into account. Two response matrices are shown in Figure 7.1 below as examples - one for the p_T of the four lepton system, $p_{\text{T}}^{4\ell}$, and one for the distribution of the jet multiplicity in events with a Higgs boson, N_{jets}:

While response matrices should represent the acceptance and efficiency of the detector only, the kinematics of various production modes can cause events to fall in and out of the fiducial volume and thus change the response matrix when constructed using simulation from one production mode versus another. For example VBF events are characterized by

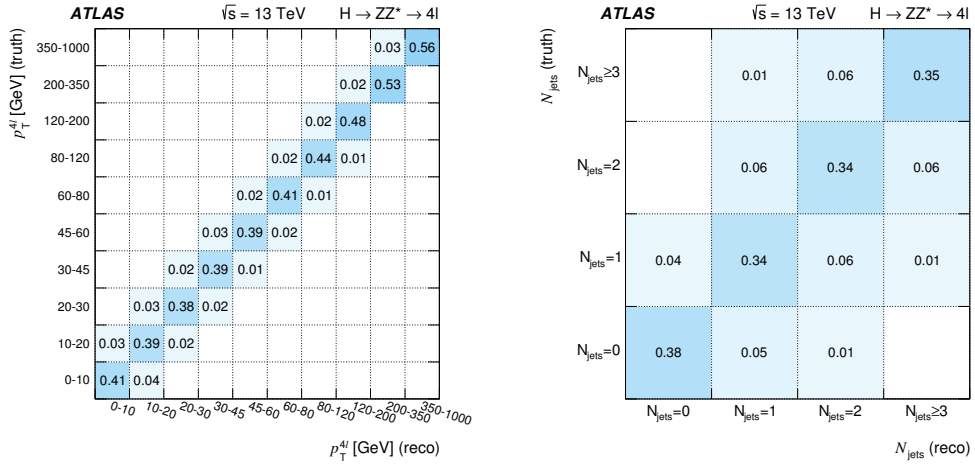

(a) $p_{\mathrm{T}}^{4\ell}$ (b) N_{jets}

Figure 7.1. Response matrices for two of the differential variables.

two forward jets well separated in rapidity. Jets from these events that occur close to the rapidity boundary of the fiducial volume may be reconstructed outside this fiducial volume, thus causing migrations of events out of a particular N_{jets} bin and into a lower bin in jet multiplicity. A production mode such as ggF which typically does not have very forward jets will not have the same migrations, thus assumptions about the composition of production modes may change the topology of the response matrix slightly. Because of this, there is a possibility of introducing a bias when using matrix inversion to unfold. Shown in Appendix C are several tests done by the author to estimate the size of any bias introduced by the matrix unfolding method.

Another concern in matrix unfolding is the possible amplification of small fluctuations in the data. This is a concern when the matrix is ill-conditioned. An ill-conditioned matrix is characterized by a large condition number, which is defined as the ratio between the maximum and minimum singular values of the matrix. Condition numbers close to 1 are considered well-conditioned. The matrices for a few of the variables considered in this thesis, which defined and motivated in Section 6.3.1, all have condition numbers less than 2.5, as

shown in Table 7.1. Thus they are well-conditioned and will not be largely affected by small fluctuations, assuming appropriate binning choices, chosen as described in Section 6.3.2.

Variable	Condition number
$p_{\mathrm{T}}^{4\ell}$	1.636
N_{jets}	1.82
$p_{\mathrm{T}}^{\mathrm{lead.jet}}$	1.6
$p_{\mathrm{T}}^{\mathrm{sublead.jet}}$	1.609
$p_{\mathrm{T}}^{4\ell}$ vs. N_{jets}	2.46

Table 7.1. Condition numbers for a few of the differential variables considered in this thesis. Condition numbers close to 1 indicate well-conditioned matrices, which may be inverted without having catestrophically large variances due to fluctuations in data.

Because of the larger bias associated with the bin-by-bin correction factors and increased model dependency, the detector response matrix unfolding method is used as the baseline.

7.2. Signal Extraction

All of the ingredients necessary for building the statistical model used to extract the cross sections have now been defined. The signal selection has been discussed in Chapter 5, along with the background estimation methods. In Section 7.1 the methods used for correcting for detector smearing effects in an attempt to return as close as possible to the 'true' value of an observable were presented. In Chapter 6 the observables were defined and the binning choices were motivated. The statistical method used to extract the cross sections is as follows.

A binned template fit is performed, in which the $m_{4\ell}$ distribution in each bin of a given differential distribution is fit to extract the number of signal events. The probability distribution functions (PDFs [1]) used for this signal are generated using simulation with $m_H = 125.0\,\mathrm{GeV}$. Furthermore, each bin is assumed to follow a Poissonian model for observing a certain num-

[1]Not to be confused with the other PDFs - parton distribution functions.

ber of events, n, with some number $n_{\mathrm{s}} + n_{\mathrm{b}}$ expected signal plus background in the mass window between 105 and 160 GeV. The extended Poisson Likelihood functional is given by [157]:

$$\begin{aligned} L\left(m_{4\ell} \,|\, n_{\mathrm{s}}, n_{\mathrm{b}}\right) = \frac{\left(n_{\mathrm{s}} + n_{\mathrm{b}}\right)^{n}}{n!} e^{-\left(n_{\mathrm{s}}+n_{\mathrm{b}}\right)} P\left(m_{4\ell} \,|\, n_{\mathrm{s}} + n_{\mathrm{b}}\right) \times \\ \prod_{i=1}^{N} P_{\mathrm{bkg}}\left(b_i \,\middle|\, \hat{b}_i\right) \times P_{\mathrm{eff}}\left(\varepsilon \,|\, \hat{\varepsilon}\right) \times P_{\mathcal{L}_{\mathrm{int}}}\left(\mathcal{L}_{\mathrm{int}} \,\middle|\, \hat{\mathcal{L}_{\mathrm{int}}}\right). \end{aligned} \tag{7.6}$$

where n_{s} and n_{b} are the total number of signal and background events, respectively, $\varepsilon = \sum_{i=0}^{n} \mathcal{A} \times \varepsilon_i$ is the acceptance times signal efficiency across the n bins, and $\mathcal{L}_{\mathrm{int}}$ is the integrated luminosity. The term $\prod_{i=1}^{N} P_{\mathrm{bkg}}\left(b_i \,\middle|\, \hat{b}_i\right)$ describes the added backgrounds and nuisance parameters, or systematic uncertainties, which will be described in the following section.

The modelling of the signal and the various backgrounds can be expressed as:

$$\begin{aligned} P\left(m_{4\ell} \,|\, n_{\mathrm{s}} + n_{\mathrm{b}}\right) &= P_{\mathrm{s}}\left(m_{4\ell} \,|\, n_{\mathrm{s}} + n_{\mathrm{b}}\right) + P_{\mathrm{b}}\left(m_{4\ell} \,|\, n_{\mathrm{s}} + n_{\mathrm{b}}\right) \\ &= \frac{n_{\mathrm{s}}}{n_{\mathrm{s}} + n_{\mathrm{b}}} F_{\mathrm{s}}\left(m_{4\ell} \,|\, n_{\mathrm{s}}\right) + \frac{n_{\mathrm{b}}}{n_{\mathrm{s}} + n_{\mathrm{b}}} \sum_{i=1}^{N} F_{\mathrm{b}}^{i}\left(m_{4\ell} \,\middle|\, n_{\mathrm{b}}^{i}\right), \end{aligned} \tag{7.7}$$

where $F_{\mathrm{s}}\left(m_{4\ell} \,|\, n_{\mathrm{s}}\right)$ and $F_{\mathrm{b}}^{i}\left(m_{4\ell} \,|\, n_{\mathrm{b}}^{i}\right)$ are the probabilities for the signal and the i-th background, respectively. The sum runs from 1 to N, where N is the number of distinctly considered background contributions, described in Section 5.4.

From Equation 7.6, a profile likelihood ratio, $\Lambda\left(m_{4\ell} \,\middle|\, \sigma^{\mathrm{fid}}\right)$, is build. Here, the cross-section is the parameter of interest, while n_{b}, ε, and $\mathcal{L}_{\mathrm{int}}$ are considered as nuisance parameters. The profile likelihood ratio is given by:

$$\Lambda\left(m_{4\ell} \,\middle|\, \sigma^{\mathrm{fid}}\right) = \frac{L\left(m_{4\ell} \,\middle|\, \sigma^{\mathrm{fid}}, \hat{\hat{N}}_{\mathrm{b}}, \hat{\hat{\varepsilon}}\left(\vec{\theta}\right), \hat{\hat{\mathcal{L}_{\mathrm{int}}}}\right)}{L\left(m_{4\ell} \,\middle|\, \hat{\sigma^{\mathrm{fid}}}, \hat{N}_{b}, \hat{\varepsilon}\left(\vec{\theta}\right), \hat{\mathcal{L}_{\mathrm{int}}}\right)}. \tag{7.8}$$

For some parameter x considered in the likelihood ratio, ($x \equiv N_{\mathrm{b}}, \varepsilon, \mathcal{L}_{\mathrm{int}}$), the numerator gives the conditional likelihood estimator of x. This is the value of x, $\hat{\hat{x}}$, that maximizes the likelihood function for a given σ^{fid}. The denominator denotes the maximized, or unconditional, likelihood estimator.

The profile likelihood ratio is evaluated using the RooFit/RooStats framework [158,159]. In bins where no measurement is made, the likelihood ratio is also used to determine upper limits on the cross-section within a 68% confidence level interval. The assumption is made that the statistical observable $-2\ln\Lambda$ behaves as a χ^2 distribution with one degree of freedom (*asymptotic approximation*).

p-values are used to quantify compatibility between observed measurements and expectation. These values are determined based on the difference between $-2\ln\Lambda$ at the best fit value of the parameter of interest and $-2\ln\Lambda$ obtained when the parameter of interest is fixed to the theoretical prediction. While systematic uncertainties, as described in Section 7.3, are included on the measurements, theoretical uncertainties on the predictions are not included in the p-value calculations.

7.3. Systematics

Several sources of uncertainty affect the measurements presented in this thesis. The largest source of uncertainty is the statistical uncertainty from the limited dataset. All other sources are referred to as systematic uncertainties. These are further categorized into two groups: experimental and theoretical systematic uncertainties. Experimental uncertainties arise from aspects of the measurements related to the detector, such as lepton and jet reconstruction, identification, and trigger efficiencies, as well as effects of calibrating these reconstructed objects, including energy and momentum scale and resolution. The uncertainty on the luminosity is included as well. Theoretical uncertainties include uncertainties from theoretical modeling of signal and background processes.

In the cross section measurements, these affect determination of the efficiency and acceptance, as well as the estimation of background yields in the signal region. In the following

sections, the two categories will be discussed in more detail, and the size of the impacts of the uncertainties on the final results will be provided.

7.3.1. Experimental uncertainties

The uncertainty on the integrated luminosity is 1.7%, as derived from a preliminary calibration of the luminosity scale using $x-y$ beam-separation scans as described in Ref. [160]. This uncertainty primarily effects the normalization of the signal and background simulation, in cases where the background estimates are not constrained by data sidebands.

Uncertainties on lepton reconstruction, isolation, and identification efficiencies as well as the energy and momentum scale and resolution are determined using large samples of $J/\psi \to \ell\ell$ and $Z \to \ell\ell$ events in data, as touched upon in Chapter 4 and described in detail in Ref. [151]. The electron (muon) reconstruction, isolation, and identification efficiency uncertainties have impacts of around 1.0-2.0% ($< 1.0\%$). The uncertainty on isolation efficiencies have a smaller impact of approximately 1%. Lepton energy and momentum scale and resolution uncertainties have negligible impacts on the final results.

The jet-related uncertainties, driven by the jet energy scale and resolution (which is between 1 and 3%), are only relevant for the jet-related differential cross section measurements. Here, their impact is typically between 3 and 5%. The uncertainty on the performance of the b-tagging algorithm, relevant for the differential cross section measurement in bins of b-tagged jet multiplicity, is on the order of a few percent over most of the jet p_T range [161].

Three sources of uncertainty are considered for the data-driven measurements of the reducible background contributions. These are statistical uncertainties, overall systematic uncertainties for the $\ell\ell + \mu\mu$ and $\ell\ell + ee$ estimates, and a shape systematic which varies with each differential variable. Impacts from these sources of uncertainty range from less than 1% to a maximum of around 3%. The inclusive reducible background estimate has a relatively small statistical uncertainty of 3%, which has minimal impact on the cross section measurements. Concerning the systematic uncertainties, uncertainties are assigned on the scale factors used to extrapolate background yields from control regions to the signal

region. These uncertainties are derived from comparing lepton efficiencies between data and simulation in the control regions. The differential distributions have an additional shape uncertainty arising from varying the relative components of the background contributions, derived separately for $\ell\ell + \mu\mu$ and $\ell\ell + ee$ [151].

7.3.2. Theoretical uncertainties

Theoretical uncertainties arise in the measurement due to uncertainties and imprecisions in the calculations involved in the signal and background modelling. As discussed in Section 5.2, theoretical modelling has several components, and each component introduces sources of uncertainty. References for all MC programs are provided in Section 5.2.

The impact of the choice of parton distribution function and the associated uncertainties are estimated using the PDF4LHC_NLO_30 Hessian PDF set eigenvector variations, as prescribed in the PDF4LHC recommendations [77].

The QCD scale uncertainties for production modes other than ggF and VBF are estimated by varying the renormalization and factorization scales by a factor of two up and down, inclusively. The configuration with the largest relative difference between the nominal configuration and the varied is selected as the uncertainty. This is done in each bin of each observable.

For the ggF process, QCD scale uncertainties from the renormalization and factorization scales, as well as resummation scales and migrations between different jet multiplicity phase space bins are taken into account [122, 162–165]. In addition, QCD scale variation impacts on the p_T spectrum of the Higgs boson as well as the uncertainty of the p_T distribution in the 0-jet bin are included. The effects due to ggF prediction uncertainties in different jet multiplicity bins as well as the migrations between these bins are large sources of theoretical uncertainty. These are handled according to the approach prescribed in Ref. [166]. Finally, the impact of the treatment of the top quark mass in the ggF loop on the predicted p_T distribution is accounted for by comparing the infinite mass treatment to predictions including finite-mass calculations.

For the VBF production mode, the uncertainties from neglecting higher orders in QCD are parameterized using the treatement defined in Ref. [167]. The jet multiplicity, Higgs boson p_T, Higgs boson and leading dijet system p_T, and invariant mass of the two leading jets are used to parameterize migration effects that contribute to these uncertainties.

Uncertainties related to the parton showering modelling and underlying event affect the acceptances in cross section measurements. These are estimated by comparing the acceptance calculated when using the parton showering algorithm from PYTHIA 8 to that of HERWIG 7. In addition, as the PYTHIA 8 algorithm with the AZNLO parameter set is used as the default, additional uncertainties are estimated using the AZNLO tune eigenvector variations.

In the case of the total cross section, where the measurement is extrapolated to the full phase space, an additional uncertainty of 2.2% related to the $H \to ZZ^*$ branching ratio is included on the measurement [103].

In Section 5.4.2, the non-resonant ZZ^* background estimation is described. Because the estimation is data-driven, most of the theoretical uncertainties on these auxiliary measurements vanish, except in the cases where the estimation is performed in several differential bins simultaneously. In such cases, because simulation is used in determining the relative contribution in each bin, theoretical uncertainties must be accounted for. Uncertainties due to missing higher-order terms in QCD are estimated by varying the QCD factorization and renormalization scales up and down by a factor of two. MC replicas of the NNPDF 3.0 PDF set are used to estimate the impact of the PDF uncertainty. Combined with uncertainties due to the shower modelling of the ZZ^* process, the impact is less than 2% for all of the fiducial differential cross section measurements. An additional source of uncertainty is applied to account for the use of SHERPA in determining the $m_{4\ell}$ shape. The $m_{4\ell}$ shape predicted by SHERPA is compared with that predicted by POWHEG and MADGRAPH5_aMC@NLO. In each $m_{4\ell}$ bin, the largest difference between the prediction from SHERPA and the two alternate predictions is used, and the systematic considered is the interpolation between the two shapes.

Finally, as discussed in Section 7.1, uncertainties on the production mode composition affect the response matrix determination while the method of unfolding introduces uncertainties on the bias. To determine the uncertainty introduced by assumptions on the production mode composition, the various production mode cross sections are varied within their measured uncertainties, taken from [168], leading to an impact of less than 1% on the final measurements. To estimate the bias uncertainty, the unfolded cross section from simulation is compared to the expected cross section obtained when varying the underlying true cross sections of the simulated dataset. In distributions with largely diagonal response matrices, such as $p_{\mathrm{T}}^{4\ell}$, the impact of this uncertainty is typically negligible; however in distributions with larger migrations, such as N_{jets}, the impact can be on the order of 10%.

7.3.3. Summary of impact of systematics

The impacts of the systematics discussed in the previous two sections are detailed in Table 7.2 and Figure 7.2. In Table 7.2, the uncertainties are presented as fractional uncertainties for the inclusive fiducial and total cross sections and ranges of systematics for the differential observables where the impacts vary across bins. The uncertainties are shown grouped into nine categories. The first two correspond to the statistical uncertainty and the total systematic uncertainty. The follow categories break down the total systematic uncertainty into the uncertainty due to the luminosity, lepton reconstruction and calibration uncertainties, jet reconstruction and calibration uncertainties, uncertainties on the tXX, VVV, and reducible background estimations, theoretical uncertainties on the non-resonant ZZ^* background estimation, uncertainties on theoretical modeling of the signal including PDF choice, QCD scale, and shower modelling, and finally, uncertainties related to the production mode composition and unfolding bias which affect the response matrices.

In Figure 7.2, the rankings of specific uncertainties, which are treated as nuisance parameters (NPs) in the statistical fit, are provided for a single bin of two of the differential observables, $p_{\mathrm{T}}^{4\ell}$ and $p_{\mathrm{T}}^{\mathrm{lead.jet}}$. The NPs are ranked in descending order according to their impact on the fitted value of the parameter of interest, σ. In order to determine the impact

Observable	Stat.	Syst.	Dominant systematic components [%]						
	unc. [%]	unc. [%]	Lumi.	e/μ	Jets	Other Bkg.	ZZ^* Th.	Sig. Th.	Comp.
σ_{comb}	9	3	1.7	2	< 0.5	< 0.5	1.0	1.5	< 0.5
$\sigma_{4\mu}$	15	4	1.7	3	< 0.5	< 0.5	1.5	1.0	< 0.5
σ_{4e}	26	8	1.7	7	< 0.5	< 0.5	1.5	1.5	< 0.5
$\sigma_{2\mu 2e}$	20	7	1.7	5	< 0.5	< 0.5	2	1.5	< 0.5
$\sigma_{2e2\mu}$	15	3	1.7	2	< 0.5	< 0.5	1	1.5	< 0.5
$\mathrm{d}\sigma \,/\, \mathrm{d}p_{\mathrm{T}}^{H}$	20–46	2–8	1.7	1–3	1–2	< 0.5	1–6	1–2	< 1
$\mathrm{d}\sigma \,/\, \mathrm{d}m_{12}$	12–42	3–6	1.7	2–3	< 1	< 0.5	1–2	1–2	< 1
$\mathrm{d}\sigma \,/\, \mathrm{d}m_{34}$	20–82	3–12	1.7	2–3	< 1	1–2	1–8	1–3	< 1
$\mathrm{d}\sigma \,/\, \mathrm{d}\lvert y_H \rvert$	22–81	3–6	1.7	2–3	< 1	< 0.5	1–5	1–3	< 1
$\mathrm{d}\sigma \,/\, \mathrm{d}\lvert \cos\theta^* \rvert$	23–113	3–6	1.7	2–3	< 1	1–2	1–7	1–3	< 0.5
$\mathrm{d}\sigma \,/\, \mathrm{d}\cos\theta_1$	23–44	3–6	1.7	2–3	< 1	< 0.5	1–3	1–2	< 1
$\mathrm{d}\sigma \,/\, \mathrm{d}\cos\theta_2$	22–39	3–6	1.7	2–3	< 1	< 0.5	1–3	1–3	< 1
$\mathrm{d}\sigma \,/\, \mathrm{d}\phi$	20–29	2–5	1.7	2–3	< 1	< 0.5	1–3	1–2	< 0.5
$\mathrm{d}\sigma \,/\, \mathrm{d}\phi_1$	22–33	3–6	1.7	2–3	< 1	< 0.5	1–2	1–3	< 0.5
$\mathrm{d}\sigma \,/\, \mathrm{d}N_{\text{jets}}$	15–37	6–14	1.7	1–3	4–10	< 0.5	1–4	3–7	1–4
$\mathrm{d}\sigma \,/\, \mathrm{d}N_{b-\text{jets}}$	15–67	6–15	1.7	1–3	4–5	1–3	1–2	3–9	1–4
$\mathrm{d}\sigma \,/\, \mathrm{d}p_{\mathrm{T}}^{\text{lead.jet}}$	15–34	3–13	1.7	1–3	4–10	< 0.5	1–2	1–5	< 0.5
$\mathrm{d}\sigma \,/\, \mathrm{d}p_{\mathrm{T}}^{\text{sublead.jet}}$	11–67	5–22	1.7	1–3	2–12	< 1	1–3	2–15	1–5
$\mathrm{d}\sigma \,/\, \mathrm{d}m_{\mathrm{jj}}$	11–50	5–18	1.7	1–3	1–11	< 0.5	1–3	2–15	1–2
$\mathrm{d}\sigma \,/\, \mathrm{d}\eta_{jj}$	11–57	5–17	1.7	1–3	2–10	< 0.5	1–2	2–14	1–4
$\mathrm{d}\sigma \,/\, \mathrm{d}\phi_{jj}$	11–50	4–18	1.7	1–3	2–9	< 0.5	1–3	2–14	1–6
$\mathrm{d}\sigma \,/\, \mathrm{d}m_{4\ell\mathrm{j}}$	15–66	4–19	1.7	1–3	3–9	< 0.5	1–6	3–14	1–8
$\mathrm{d}\sigma \,/\, \mathrm{d}m_{4\ell\mathrm{jj}}$	11–182	5–67	1.7	1–3	4–24	< 0.5	1–5	2–35	1–9
$\mathrm{d}\sigma \,/\, \mathrm{d}p_{\mathrm{T}}^{4\ell\mathrm{j}}$	15–76	6–13	1.7	1–3	2–8	< 1	1–5	3–9	1–3
$\mathrm{d}\sigma \,/\, \mathrm{d}p_{\mathrm{T}}^{4\ell\mathrm{jj}}$	11–76	5–27	1.7	2–3	2–9	1–2	1–4	3–17	1–12
$\mathrm{d}^2\sigma \,/\, \mathrm{d}m_{12}\,\mathrm{d}m_{34}$	16–65	3–11	1.7	2–3	< 1	1–2	1–9	1–3	1–2
$\mathrm{d}^2\sigma \,/\, \mathrm{d}p_{\mathrm{T}}^{H}\,\mathrm{d}\lvert y_H \rvert$	23–63	2–13	1.7	1–3	1–2	< 1	1–6	1–5	1–2
$\mathrm{d}^2\sigma \,/\, \mathrm{d}p_{\mathrm{T}}^{H}\,\mathrm{d}N_{\text{jets}}$	23–93	4–193	1.7	2–14	2–25	1–3	1–7	1–12	1–92
$\mathrm{d}^2\sigma \,/\, \mathrm{d}p_{\mathrm{T}}^{4\ell\mathrm{j}}\,\mathrm{d}m_{4\ell\mathrm{j}}$	15–41	4–12	1.7	1–3	2–8	< 0.5	1–5	2–9	< 1
$\mathrm{d}^2\sigma \,/\, \mathrm{d}p_{\mathrm{T}}^{H}\,\mathrm{d}p_{\mathrm{T}}^{4\ell\mathrm{j}}$	15–53	3–10	1.7	1–3	2–8	< 1	1–2	2–6	1–2
$\mathrm{d}^2\sigma \,/\, \mathrm{d}p_{\mathrm{T}}^{H}\,\mathrm{d}p_{\mathrm{T}}^{\text{lead.jet}}$	15–84	3–21	1.7	1–3	2–18	1–10	1–3	2–9	1–3
$\mathrm{d}^2\sigma \,/\, \mathrm{d}p_{\mathrm{T}}^{\text{lead.jet}}\,\mathrm{d}\lvert y^{\text{lead. jet}} \rvert$	15–38	3–11	1.7	1–3	2–9	< 0.5	1–2	1–4	1–2
$\mathrm{d}^2\sigma \,/\, \mathrm{d}p_{\mathrm{T}}^{\text{lead.jet}}\,\mathrm{d}p_{\mathrm{T}}^{\text{sublead.jet}}$	15–63	5–22	1.7	1–3	4–15	< 0.5	1–4	3–11	1–7

Table 7.2. Fractional uncertainties for the inclusive fiducial and total cross sections, and ranges of systematic uncertainties between bins of the differential observables. The columns e/μ and *jets* represent the experimental uncertainties in lepton and jet reconstruction and identification, respectively. The Z + jets, $t\bar{t}$, tXX (Other Bkg.) column includes uncertainties related to the estimation of these background sources. The ZZ^* theory (ZZ^* th.) uncertainties include the PDF and scale variations. Signal theory (Sig th.) uncertainties include PDF choice, QCD scale, and shower modelling. Finally, the column labelled 'Comp.' contains uncertainties related to production mode composition and unfolding bias which affect the response matrices.

of each NP on the final fitted value of the POI in a particular bin of a given observable, the fit to data is performed $2N$ times, where N is the number of NPs. With each fit, a given NP, θ, is fixed to its post fit value, $\hat{\theta}$, shifted up or down by 1σ of its postfit uncertainty, while all other NPs are left floating. The impact of the considered NP on the fitted value of the POI is depicted by the horizontal bands in Figure 7.2, which correspond to the upper axis. The black dots depict the pull, or the change in the NP between the fitted value, $\hat{\theta}$, and the nominal, θ_0, expressed in standard deviations. The error bars provide the post-fit uncertainties. These points correspond to the lower axis.

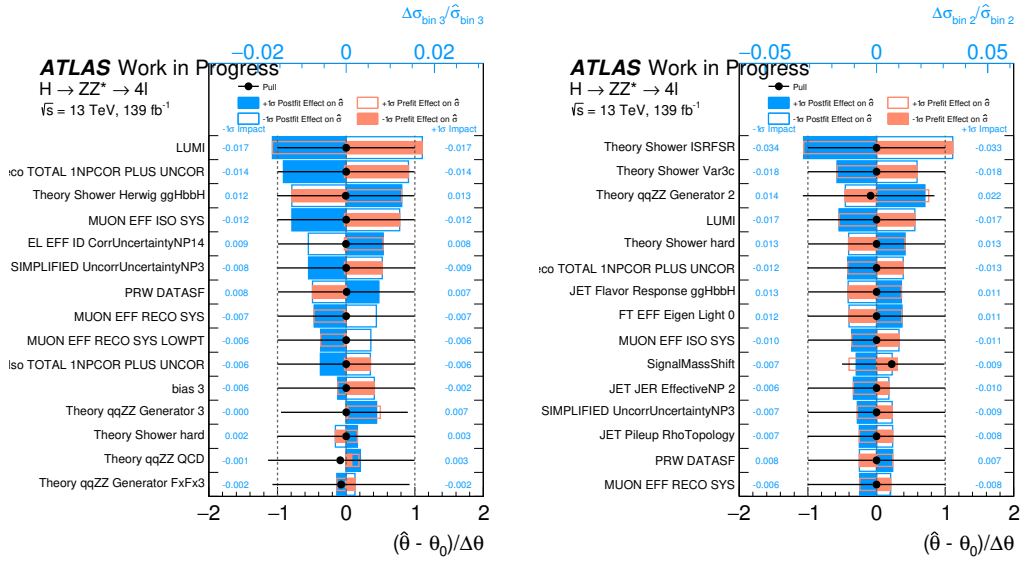

(a) $p_{\mathrm{T}}^{4\ell}$- bin 3

(b) $p_{\mathrm{T}}^{\mathrm{lead.jet}}$- bin 2

Figure 7.2. Ranking plots of the impact of individual nuisance parameters (NPs) on the measured cross sections, σ in bin 3 of the $p_{\mathrm{T}}^{4\ell}$ distribution and bin 2 of the $p_{\mathrm{T}}^{\mathrm{lead.jet}}$ distribution. The NPs are presented in descending order with respect to their impact on the fitted value of σ. The bands correspond to the upper axis and depict the variations on σ when each NP is shifted by its postfit uncertainty either up ($+1\sigma$) or down (-1σ), and held fixed to this value while the fit is performed, with all other parameters allowed to float. The black dots labelled 'pull' correspond to the lower axis, and depict the variations of the fitted NPs, $\hat{\theta}$, from their nominal values.

CHAPTER 8

Results

In this chapter, results of the measurements are presented. Pre-fit distributions, where reconstructed data events passing the selection cuts are overlayed onto signal and background expectation distributions, are presented in Section 8.1. Results of the extracted fidicual cross sections are provided in Section 8.2, while the differential cross section results are given in Section 8.3. Select differential distributions are used to set limits in theoretical interpretations in the next chapter, Chapter 9.

8.1. Yields

In Table 8.1, the observed event yields in each of the four final states of the Higgs boson decay, 4μ, $2e2\mu$, $2\mu2e$, and $4e$, are provided. The total event yield in all decay channels is also provided, as are expected signal and backround yields taken from simulation. The 'Other backgrounds' column contains background contributions from tXX and VVV which are estimated using simulation, as well as contributions from the reducible background sources including $Z+\text{jets}$ and $t\bar{t}$, which are estimated using the data-driven methods described in Section 5.4.1. Events in the table are required to have a four lepton invariant mass between 115 and 130 GeV.

Expected and observed four lepton invariant mass distributions are provided in Figures 8.1 and 8.2. The distributions are provided for the inclusive case as well as per final state. The clear $Z \to 4\ell$ peak is visible around 90 GeV along with the Higgs boson signal peak at 125 GeV.

Final state	Signal	ZZ^* background	Other backgrounds	Total expected	Observed
4μ	78 ± 5	38.0 ± 2.1	2.85 ± 0.18	119 ± 5	115
$2e2\mu$	53.0 ± 3.1	26.1 ± 1.4	2.98 ± 0.19	82.0 ± 3.4	96
$2\mu 2e$	40.1 ± 2.9	17.3 ± 1.3	3.6 ± 0.5	61.0 ± 3.2	57
$4e$	35.3 ± 2.6	15.0 ± 1.5	2.91 ± 0.33	53.2 ± 3.1	42
Total	206 ± 13	96 ± 6	12.2 ± 1.0	315 ± 14	310

Table 8.1. Number of expected and observed events in the four decay channels as well as the total. Expected (prefit) signal and background yields are provided and the total expected yields can be compared to the number of events observed in data. Only events within the mass range $115 < m_{4\ell} < 130$ GeV are included. Expected yields include combined statistical and systematic uncertainties as described in Section 7.3.

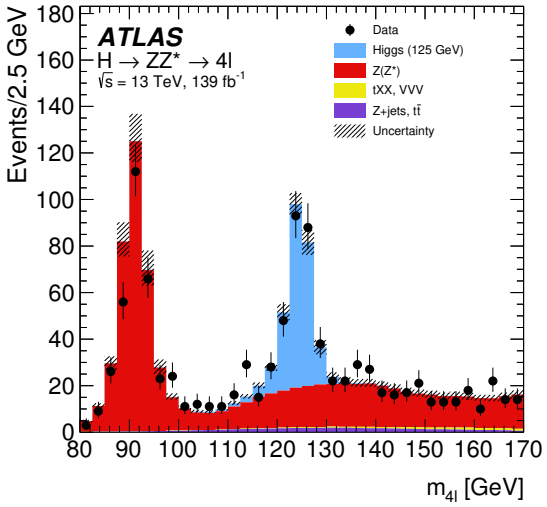

Figure 8.1. Expected and observed four-lepton invariant mass distribution for Higgs boson candidates in all decay channels collected with an integrated luminosity of 139 fb^{-1}at $\sqrt{s} = 13$ TeV. The uncertainty on the prediction is indicated with the hatched error band, evaluated as described in Section 7.3.

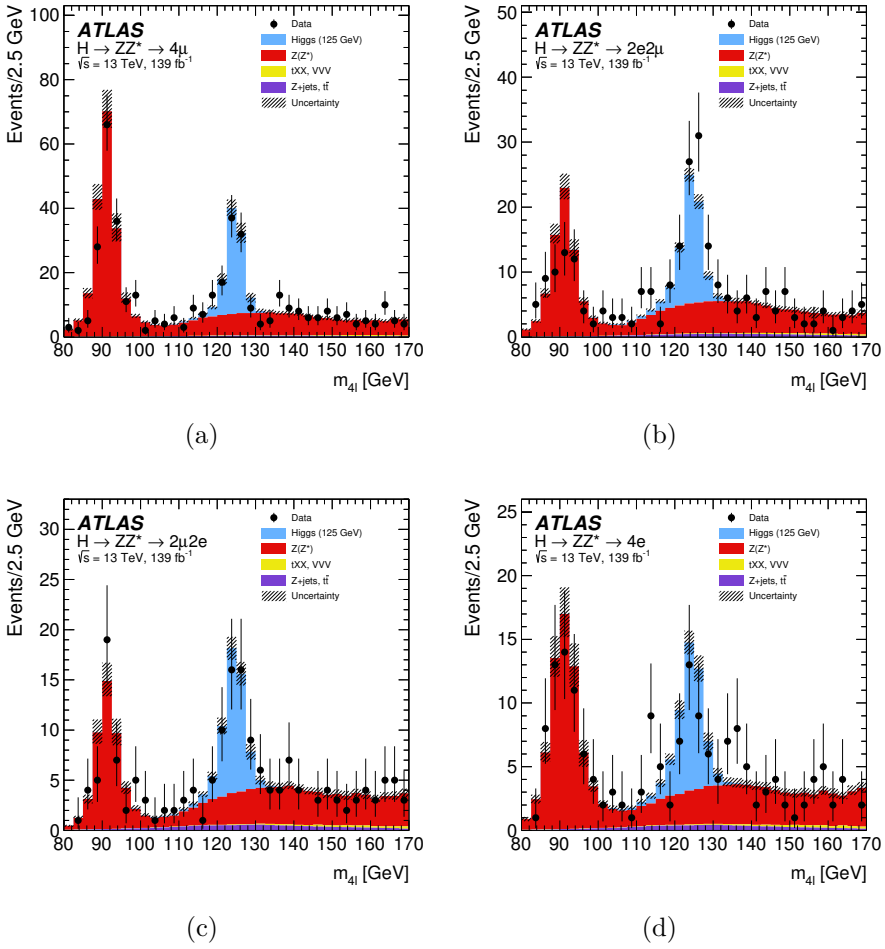

Figure 8.2. Expected and observed four-lepton invariant mass distribution for Higgs boson candidates in the four decay final states, (a) 4μ, (b) $2e2\mu$, (c) $2\mu2e$, and (d) $4e$, collected with an integrated luminosity of 139 fb^{-1}at $\sqrt{s} = 13$ TeV. The uncertainty on the prediction is indicated by the hatched error band, evaluated as described in Section 7.3.

The observed and expected distributions of the one dimensional observables are shown in Figures 8.3-8.8. Following, the observed and expected distribution for the two dimensional observables are shown in Figures 8.9-8.15. These figures include 2D plots that depict the bin boundaries shown in the 1D projections. In all figures, events are selected within an $m_{4\ell}$ mass range between 115 and 130 GeV. More details on the compatibility of the data with the Standard Model are provided in the next section; however, good agreement between observation and prediction is generally observed within the total uncertainties.

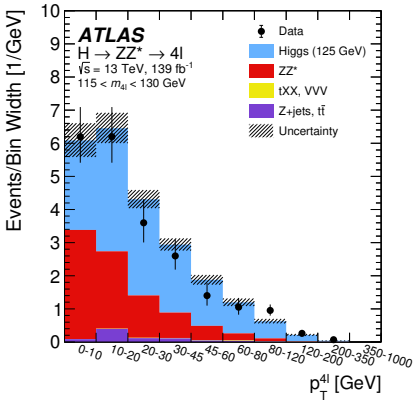

(a)

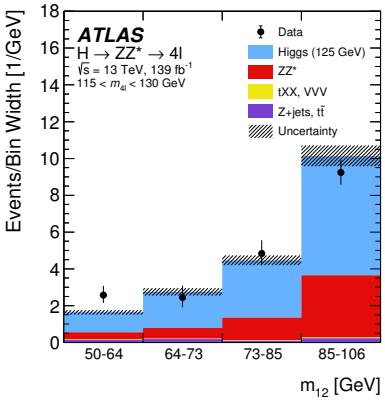

(b)

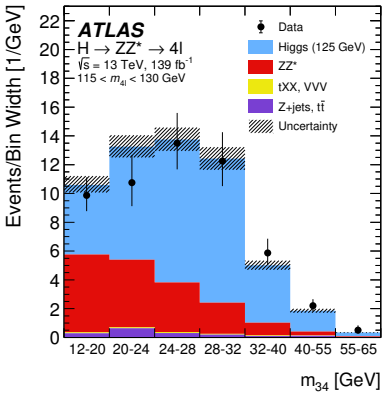

(c)

Figure 8.3. Expected and observed distributions of (a) $p_{\mathrm{T}}^{4\ell}$, (b) m_{12}, and (c) m_{34} in the mass region $115 < m_{4l} < 130$ GeV, for an integrated luminosity of 139 fb^{-1} collected at $\sqrt{s} = 13$ TeV. The uncertainty on the prediction is indicated by the hatched error band, evaluated as described in Section 7.3.

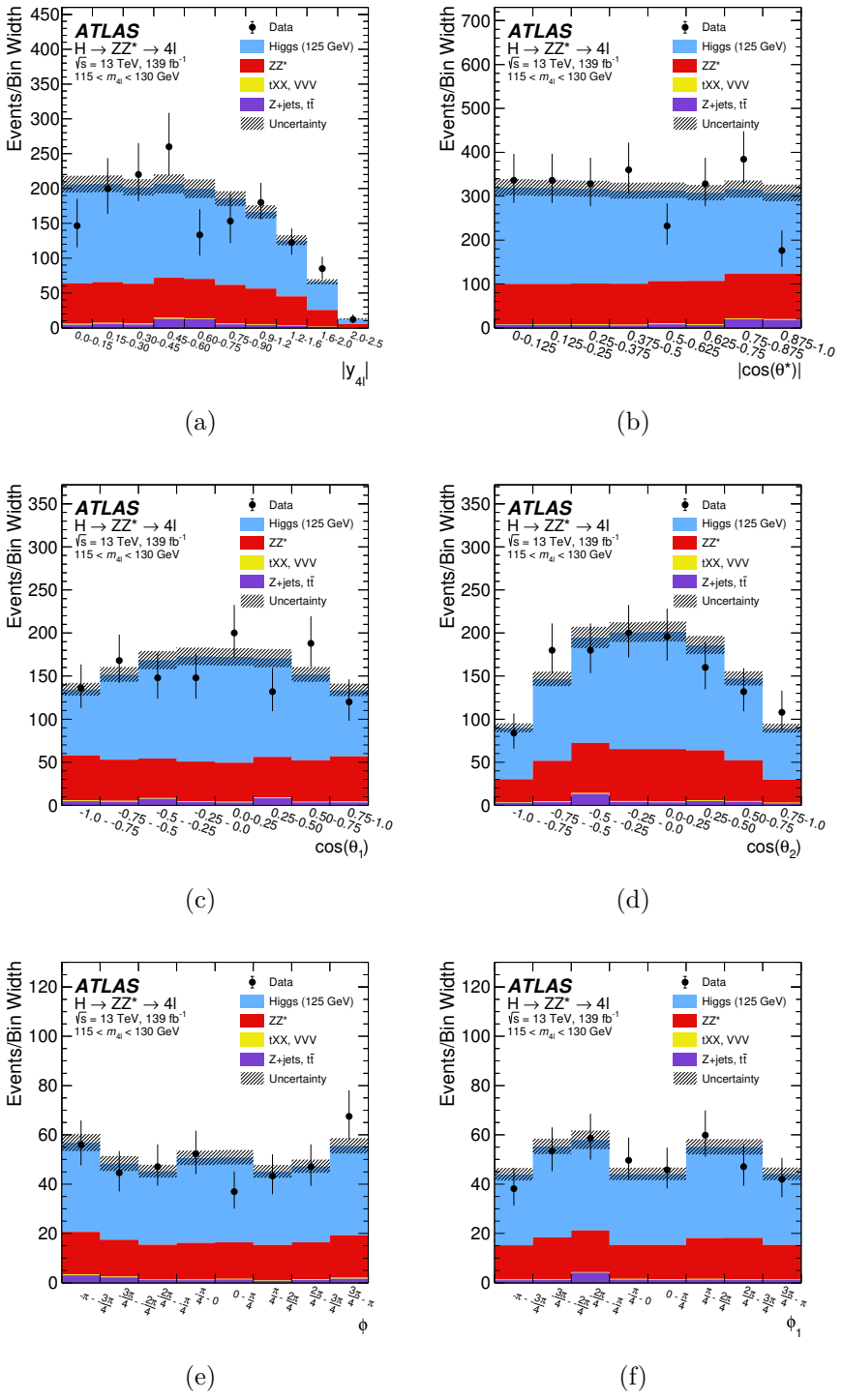

Figure 8.4. Expected and observed distributions of (a) $|y_{4\ell}|$, (b) $|\cos\theta^*|$, (c) $\cos\theta_1$, (d) $\cos\theta_2$, (e) ϕ, and (f) ϕ_1 in the mass region $115 < m_{4l} < 130$ GeV, for an integrated luminosity of 139 fb^{-1} collected at $\sqrt{s} = 13$ TeV. The uncertainty on the prediction is indicated by the hatched error band, evaluated as described in Section 7.3.

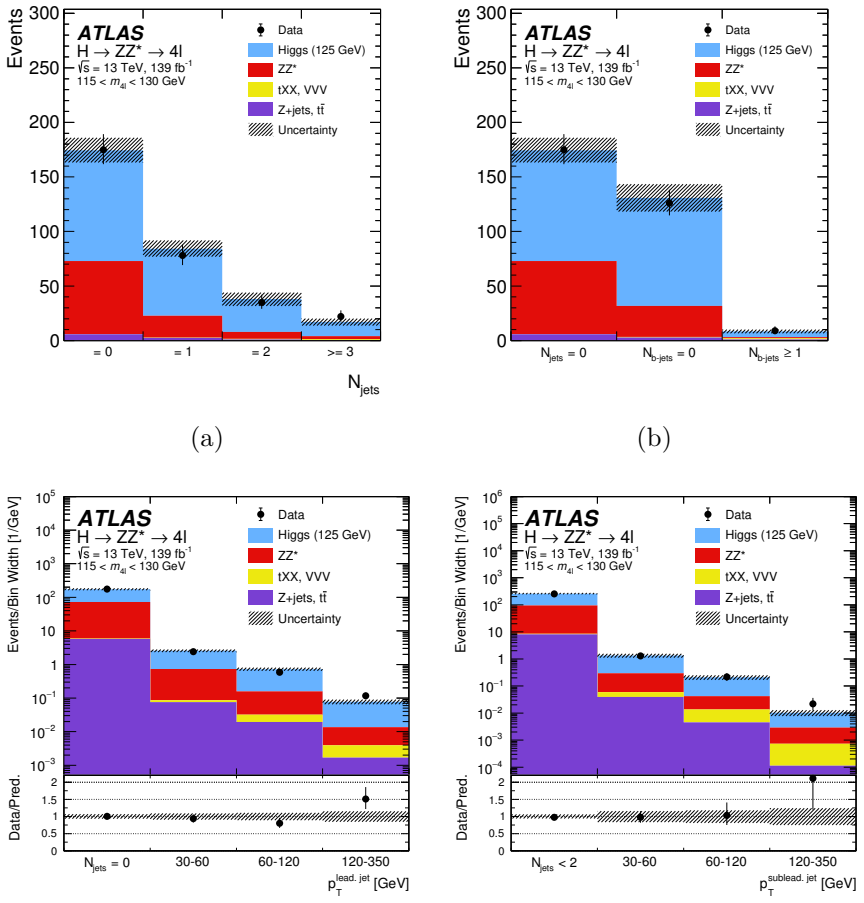

Figure 8.5. Expected and observed distributions of (a) N_{jets}, (b) $N_{b-\text{jets}}$, (c) $p_{\text{T}}^{\text{lead.jet}}$, and (d) $p_{\text{T}}^{\text{sublead.jet}}$ in the mass region $115 < m_{4l} < 130$ GeV, for an integrated luminosity of 139 fb^{-1} collected at $\sqrt{s} = 13$ TeV. The uncertainty on the prediction is indicated by the hatched error band, evaluated as described in Section 7.3.

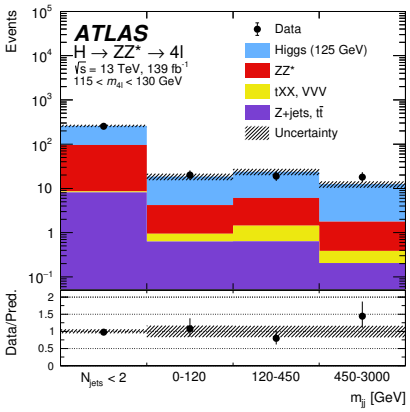

(a)

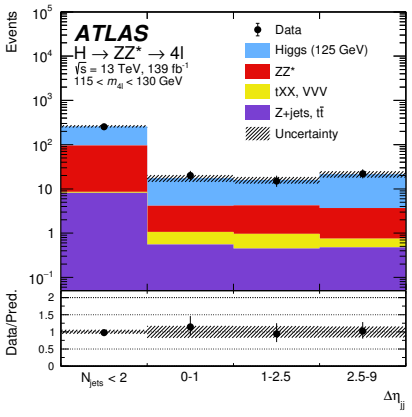

(b)

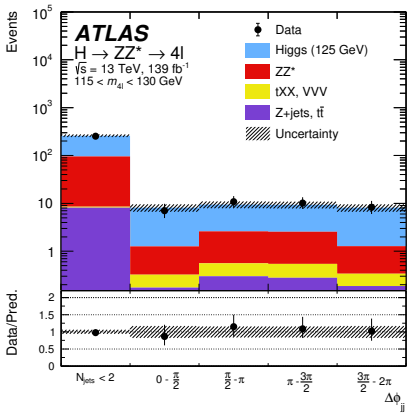

(c)

Figure 8.6. Expected and observed distributions of (a) m_{jj}, (b) $\Delta\eta_{\mathrm{jj}}$, and (c) $\Delta\phi_{\mathrm{jj}}$, in the mass region $115 < m_{4l} < 130$ GeV, for an integrated luminosity of 139 fb^{-1} collected at $\sqrt{\mathrm{s}} = 13$ TeV. The uncertainty on the prediction is indicated by the hatched error band, evaluated as described in Section 7.3.

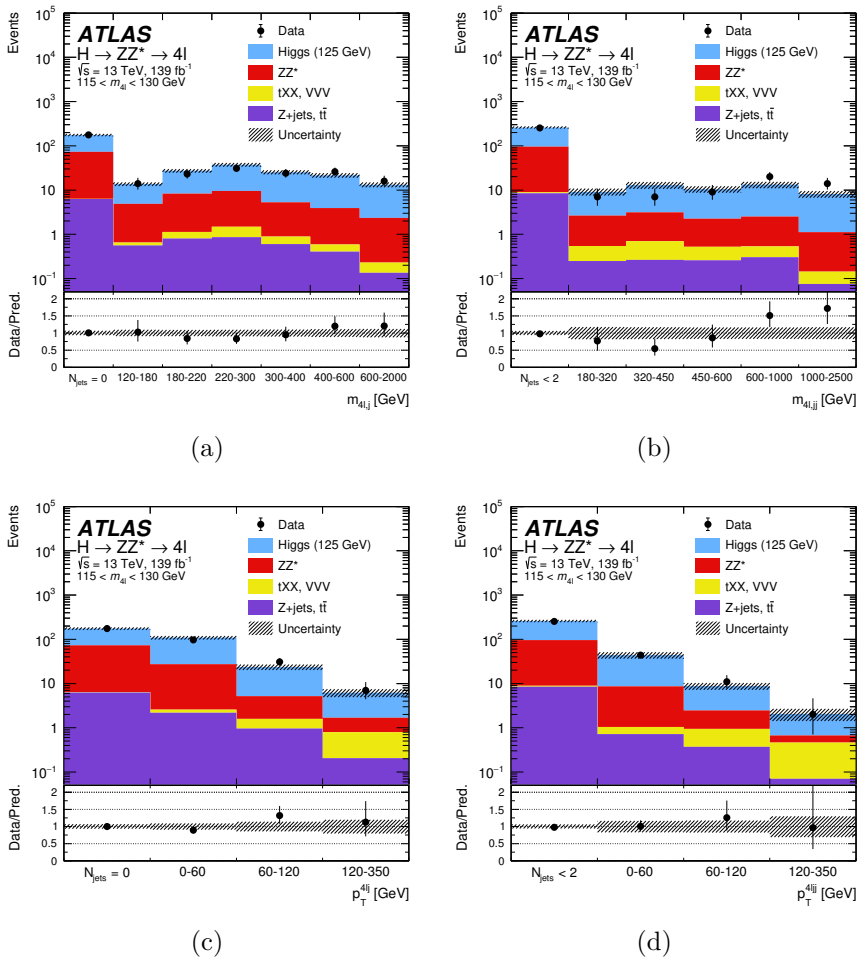

Figure 8.7. Expected and observed distributions of (a) $m_{4\ell\mathrm{j}}$, (b) $m_{4\ell\mathrm{jj}}$, (c) $p_{\mathrm{T}}^{4\ell\mathrm{j}}$, and (d) $p_{\mathrm{T}}^{4\ell\mathrm{jj}}$ in the mass region $115 < m_{4l} < 130$ GeV, for an integrated luminosity of 139 fb^{-1} collected at $\sqrt{\mathrm{s}} = 13$ TeV. The uncertainty on the prediction is indicated by the hatched error band, evaluated as described in Section 7.3.

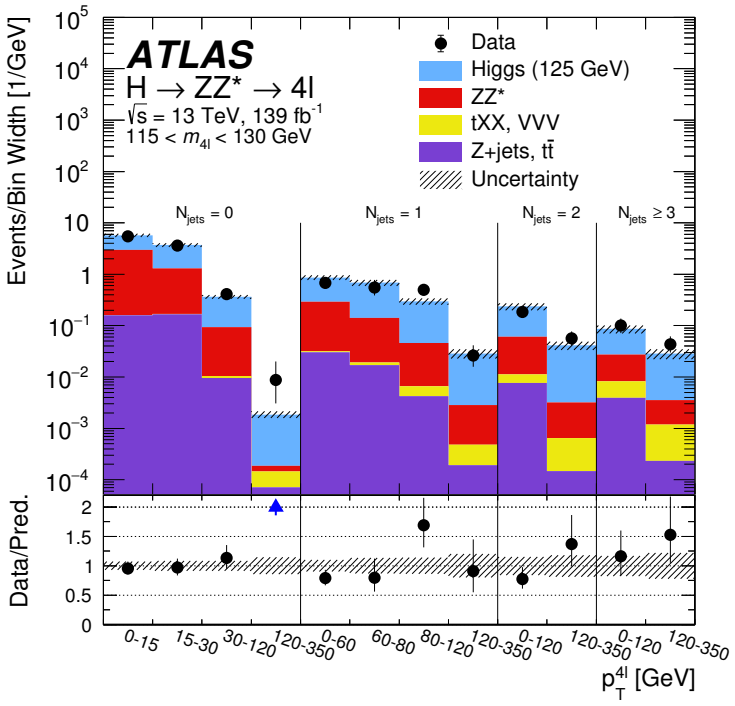

Figure 8.8. Expected and observed distribution of $p_{\mathrm{T}}^{4\ell}$ in N_{jets} bins in the mass region $115 < m_{4l} < 130$ GeV, for an integrated luminosity of 139 fb^{-1} collected at $\sqrt{\mathrm{s}} = 13$ TeV. A SM Higgs boson signal with a mass $m_H = 125$ GeV is assumed. The uncertainty in the prediction is shown by the hatched band, evaluated as described in Section 7.3.

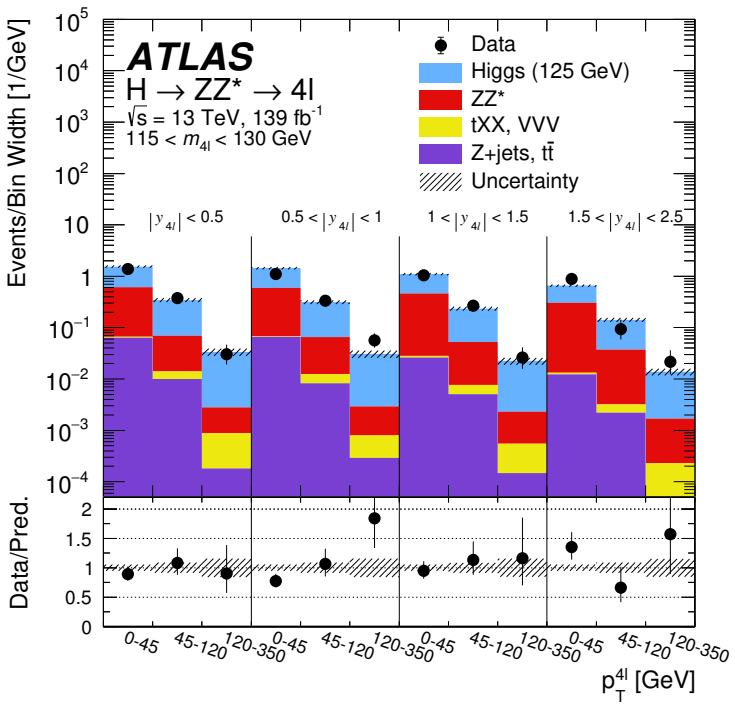

Figure 8.9. Expected and observed distribution of $p_{\mathrm{T}}^{4\ell}$ in $|y_{4\ell}|$ bins in the mass region $115 < m_{4l} < 130$ GeV, for an integrated luminosity of 139 fb^{-1} collected at $\sqrt{\mathrm{s}} = 13$ TeV. A SM Higgs boson signal with a mass $m_H = 125$ GeV is assumed. The uncertainty in the prediction is shown by the hatched band, evaluated as described in Section 7.3.

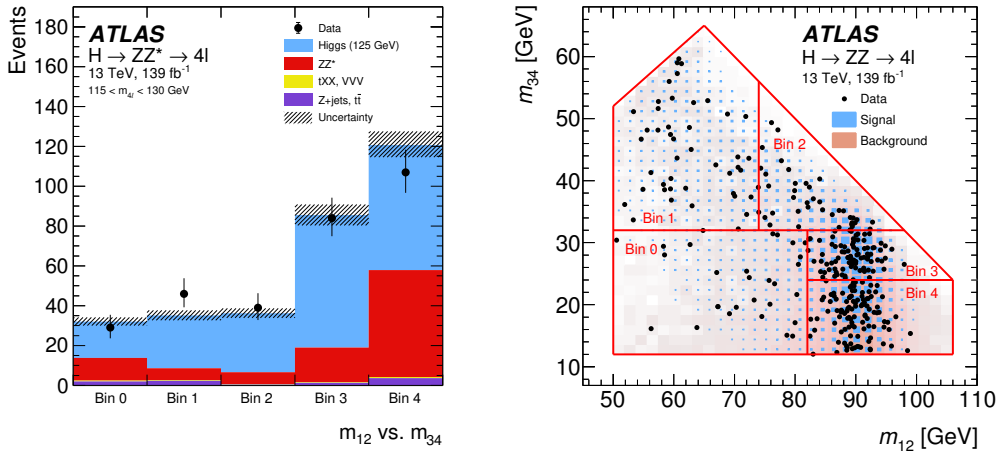

(a) (b)

Figure 8.10. Expected and observed distribution of (a) the leading vs. subleading Z bosons, m_{12} vs. m_{34}, and (b) the same distribution in the 2D plane, where the black dots depict data and the blue and pink shaded areas represent simulated signal and background, respectively. The red lines depict the bin boundaries referenced in (a), chosen as described in Section 6.3.2. These distributions correspond to the mass region $115 < m_{4l} < 130$ GeV, for an integrated luminosity of 139 fb^{-1} collected at $\sqrt{s} = 13$ TeV. The uncertainty on the prediction is indicated by the hatched error band, evaluated as described in Section 7.3.

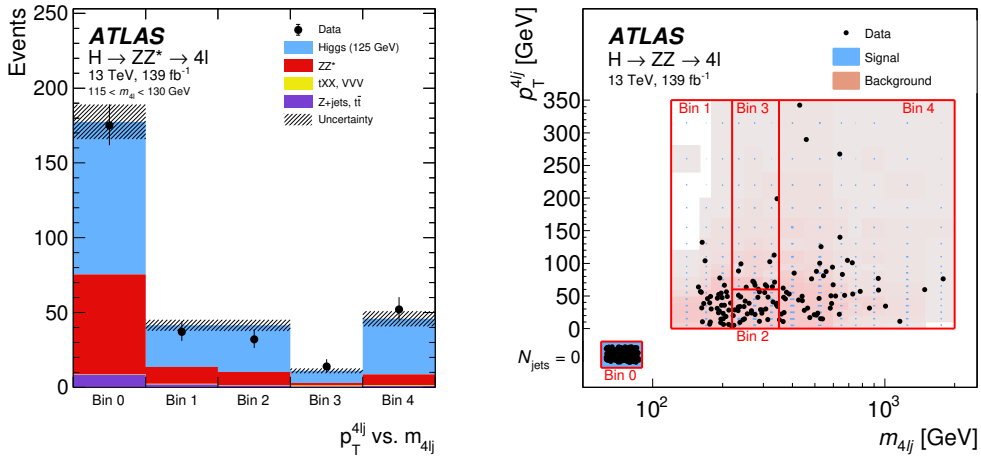

(a) (b)

Figure 8.11. Expected and observed distribution in bins of (a) the transverse momentum of the four lepton plus leading jet system vs. the invariant mass of the four lepton plus leading jet system, $p_{\mathrm{T}}^{4\ell\mathrm{j}}$ vs. $m_{4\ell\mathrm{j}}$, and (b) the same distribution in the 2D plane, where the black dots depict data and the blue and pink shaded areas represent simulated signal and background, respectively. The red lines depict the bin boundaries referenced in (a), chosen as described in Section 6.3.2. These distributions correspond to the mass region $115 < m_{4l} < 130$ GeV, for an integrated luminosity of 139 fb^{-1} collected at $\sqrt{\mathrm{s}} = 13$ TeV. The uncertainty on the prediction is indicated by the hatched error band, evaluated as described in Section 7.3.

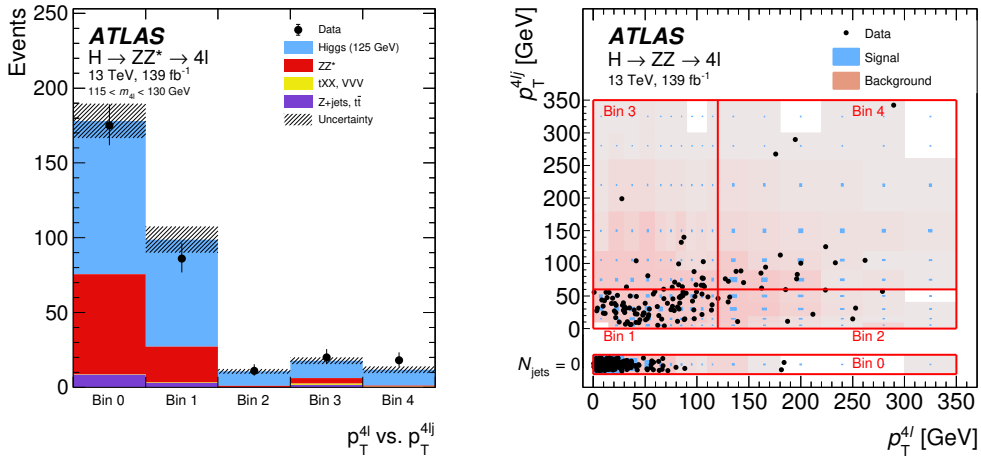

(a) (b)

Figure 8.12. Expected and observed distribution in bins of (a) the transverse momentum of the four lepton system vs. the transverse momentum of the four lepton plus leading jet system, p_{T}^{H} vs. $p_{\mathrm{T}}^{4\ell\mathrm{j}}$ and (b) the same distribution in the 2D plane, where the black dots depict data and the blue and pink shaded areas represent simulated signal and background, respectively. The red lines depict the bin boundaries referenced in (a), chosen as described in Section 6.3.2. These distributions correspond to the mass region $115 < m_{4l} < 130$ GeV, for an integrated luminosity of 139 fb^{-1} collected at $\sqrt{\mathrm{s}} = 13$ TeV. The uncertainty on the prediction is indicated by the hatched error band, evaluated as described in Section 7.3.

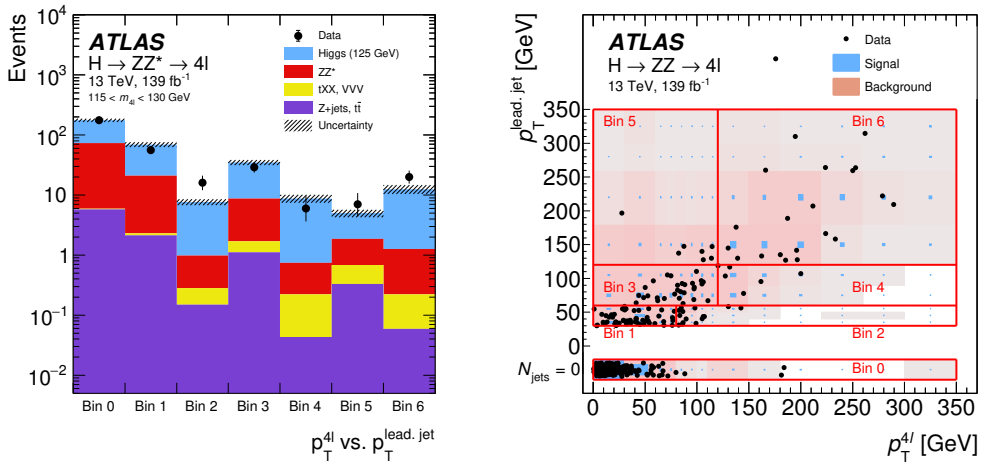

(a) (b)

Figure 8.13. The observed and expected (prefit) distribution in bins of (a) the transverse momentum of the four lepton system vs. the transverse momentum of the leading jet, p_{T}^{H} vs. $p_{\mathrm{T}}^{\mathrm{lead.jet}}$, and (b) the same distribution in the 2D plane, where the black dots depict data and the blue and pink shaded areas represent simulated signal and background, respectively. The red lines depict the bin boundaries referenced in (a), chosen as described in Section 6.3.2. These distributions correspond to the mass region $115 < m_{4l} < 130$ GeV, for an integrated luminosity of 139 fb^{-1} collected at $\sqrt{\mathrm{s}} = 13$ TeV. The uncertainty on the prediction is indicated by the hatched error band, evaluated as described in Section 7.3.

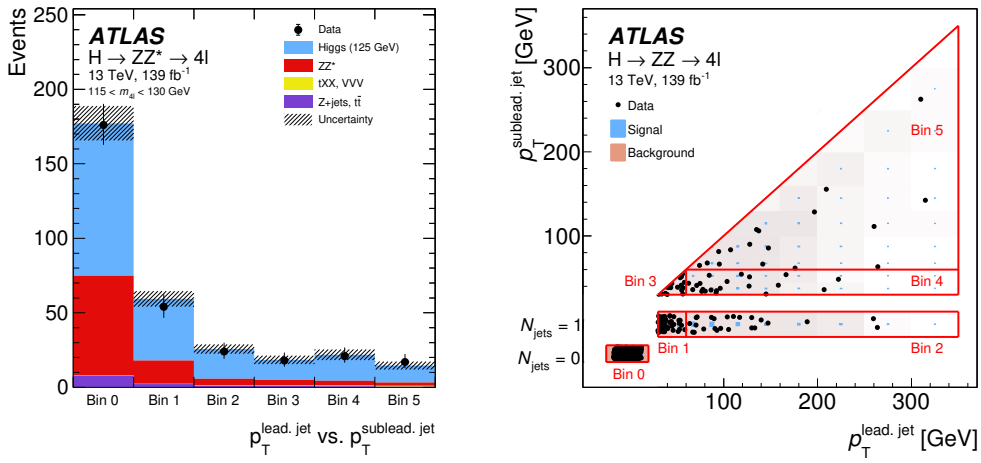

(a) (b)

Figure 8.14. The observed and expected (prefit) distribution in bins of (a) the transverse momentum of the leading vs. subleading jet, $p_{\mathrm{T}}^{\mathrm{lead.jet}}$ vs. $p_{\mathrm{T}}^{\mathrm{sublead.jet}}$, and (b) the same distribution in the 2D plane, where the black dots depict data and the blue and pink shaded areas represent simulated signal and background, respectively. The red lines depict the bin boundaries referenced in (a), chosen as described in Section 6.3.2. These distributions correspond to the mass region $115 < m_{4l} < 130$ GeV, for an integrated luminosity of 139 fb^{-1} collected at $\sqrt{\mathrm{s}} = 13$ TeV. The uncertainty on the prediction is indicated by the hatched error band, evaluated as described in Section 7.3.

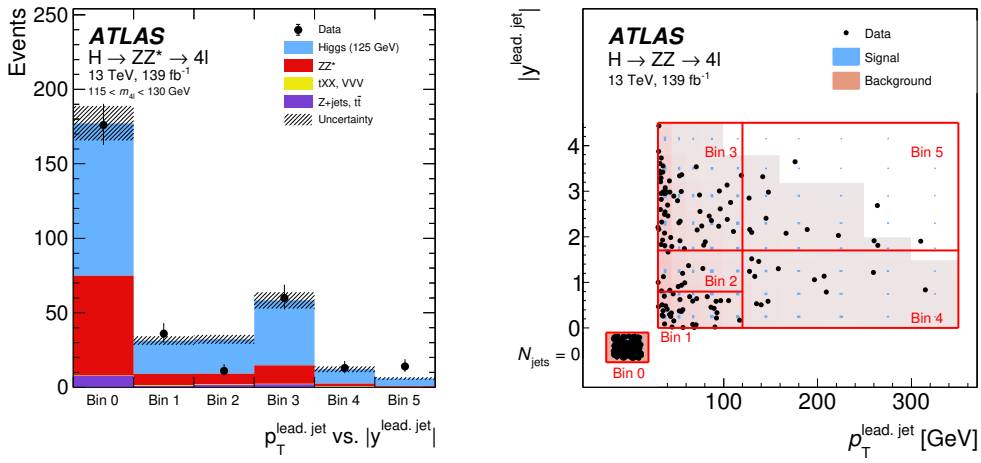

(a) (b)

Figure 8.15. The observed and expected (prefit) distribution in bins of (a) the transverse momentum vs. the rapidity of the leading jet, $p_{\mathrm{T}}^{\mathrm{lead.jet}}$ vs. $|y^{\mathrm{lead.\ jet}}|$, and (b) the same distribution in the 2D plane, where the black dots depict data and the blue and pink shaded areas represent simulated signal and background, respectively. The red lines depict the bin boundaries referenced in (a), chosen as described in Section 6.3.2. These distributions correspond to the mass region $115 < m_{4l} < 130$ GeV, for an integrated luminosity of 139 fb^{-1} collected at $\sqrt{\mathrm{s}} = 13$ TeV. The uncertainty on the prediction is indicated by the hatched error band, evaluated as described in Section 7.3.

8.2. Inclusive fiducial cross sections

Results for the fiducial production cross sections, described in Section 6.2, are presented in Table 8.2 and Figure 8.16. In Figure 8.16, the fiducial cross section measurements for the four decay final states, 4μ, $4e$, $2\mu 2e$, and $2e2\mu$, are provided in the left panel. In the middle panel, the cross sections in the same flavor decay channel, 4μ and $4e$, and the opposite flavor decay channel, $2\mu 2e$ and $2e2\mu$, are provided, along with the inclusive fiducial cross sections obtained by either summing all 4ℓ decay final states, denoted 'sum', or combining them assuming SM relative branching fractions, denoted 'comb'. In all cases, data are compared to the SM prediction. Fiducial acceptances for the predictions are determined using the simulated Higgs boson signal samples described in Section 5.2.

The combined inclusive fiducial cross section is further extrapolated to the total phase space, the result of which is provided in the rightmost panel of Figure 8.16. A set of predictions are provided for comparison here. In all cases, cross section contributions from all Higgs boson signal production modes other than ggF are calculated using the programs listed in Section 5.2. These are denoted in the figure legend as 'XH'. These are then added to various predictions for the ggF cross section. ggF cross section predictions are determined using NNLOPS, MadGraph5_aMC@NLO-FxFx (MG5-FxFx) and Hres 2.3 [121,169]. The p-values, calculated as described in Section 7.2, are provided in Table 8.2. They do not include the systematic uncertainty on the theoretical predictions.

Good compatibility with Standard Model predictions is observed within the measured uncertainties.

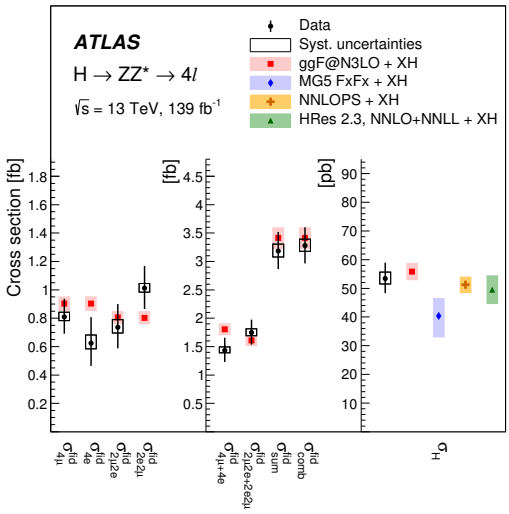

(a)

Figure 8.16. The fiducial cross sections (left two panels) and total cross section (right panel) of Higgs boson production measured in the 4ℓ final state. The fiducial cross sections are shown separately for each decay final state in the left-most panel, and for same- and opposite-flavour decays in the middle panel. The inclusive fiducial cross section is measured as the sum of all final states, as well as by combining the per-final state measurements assuming SM $ZZ^* \to 4\ell$ relative branching ratios. These are provided in the middle panel. The total SM prediction is accurate to N^{3}LO in QCD for the ggF process. The cross sections for all other Higgs boson production modes, denoted XH, are added. For the fiducial cross section predictions, the SM cross sections are multiplied by the acceptances determined using the NNLOPS sample for ggF and the samples discussed in Section 5.2 for the other production modes. For the total cross section, the predictions by the generators NNLOPS, HRES, and MADGRAPH5_aMC@NLO-FxFx are also shown. The error bars on the data points show the total uncertainties, while the systematic uncertainties are indicated by the boxes. The shaded bands around the theoretical predictions indicate the PDF and scale uncertainties, calculated as described in Section 7.3.

Cross section [fb]	Data (± (stat.) ± (syst.))			Standard Model prediction	p-value [%]
$\sigma_{4\mu}$	0.81	±0.12	±0.03	0.90(5)	46
σ_{4e}	0.62	±0.16	±0.05	0.90(5)	14
$\sigma_{2\mu 2e}$	0.74	±0.15	±0.05	0.80(4)	67
$\sigma_{2e2\mu}$	1.01	±0.15	±0.03	0.80(4)	15
$\sigma_{4\mu+4e}$	1.43	±0.21	±0.06	1.81(10)	10
$\sigma_{2\mu 2e+2e2\mu}$	1.75	±0.21	±0.06	1.61(9)	51
σ_{sum}	3.18	±0.31	±0.11	3.41(18)	49
σ_{comb}	3.28	±0.30	±0.11	3.41(18)	67
σ_{tot} [pb]	53.5	±4.9	±2.1	55.8(28)	66

Table 8.2. The fiducial and total cross sections of Higgs boson production measured in the 4ℓ final state. The fiducial cross sections are measured separately for each of the four decay final states, and for same- and opposite-flavor decays. The inclusive fiducial cross section is measured as the sum of all final states (σ_{sum}), as well as by combining the per-final state measurements assuming SM $ZZ^* \to 4\ell$ relative branching ratios (σ_{comb}). In the case of the total cross section (σ_{tot}), the Higgs boson branching ratio at 125 GeV is assumed. The total SM prediction is accurate to N^{3}LO in QCD for the ggF process. For the fiducial cross section predictions, the SM cross sections are multiplied by the acceptances determined using the NNLOPS sample for ggF. For all the other production modes, the cross sections from the samples discussed in Section 5.2 are added. The p-values indicating the compatibility of the measurement and the SM prediction are shown as well. They do not include the systematic uncertainty on the theoretical predictions.

8.3. Differential cross sections

Results of the fiducial differential cross section measurements are provided in this section. For all observables, the distribution of measured cross sections in each differential bin is provided as one sub-figure, paired with a correlation matrix depicting the correlation between cross section parameters of interest as well as the ZZ^* normalization parameters, as discussed in Section 5.4.2, as a second sub-figure.

The measured Higgs boson cross sections in bins of $p_{\mathrm{T}}^{4\ell}$, $\frac{d\sigma}{dp_{\mathrm{T}}^{4\ell}}$, are presented in Figure 8.17. Measured differential cross sections with respect to the invariant masses of the leading and subleading Z bosons, m_{12} and m_{34}, are provided in Figure 8.18. These cross sections are provided as $\frac{d\sigma}{dm_{12}}$ and $\frac{d\sigma}{dm_{34}}$. As these two variables are sensitive to the interference effects from same-flavor lepton decays, results are provided for the same flavor final states, 4μ and 4e, as well as the opposite flavor final states, $2e2\mu$ and $2\mu2e$, in Figures 8.19 and 8.20, respectively. Following, in Figures 8.21- 8.23, the results for the differential cross sections with respect to the angular variables describing the Higgs boson decay are provided. Similarly to m_{12} and m_{34}, results are provided for ϕ, or $\frac{d\sigma}{d\phi}$, split in the same- and opposite-flavor decay channels in Figure 8.24.

Following are the variables that probe the jet activity in events with a Higgs boson. In all jet-related observables, the first differential bin corresponds to either events with zero jets reconstructed and passing the jet selection criteria, or for the variables involving multiple jets, less than two. Differential cross sections in bins of the jet multiplicity, N_{jets}, and number of b-tagged jets, $N_{b-\mathrm{jets}}$, are provided in Figures 8.25 and 8.26, respectively. These are $\frac{d\sigma}{dN_{\mathrm{jets}}}$ and $\frac{d\sigma}{dN_{b-\mathrm{jets}}}$. Following are results for the differential cross sections with respect to to the leading and subleading jet transverse momentum, $\frac{d\sigma}{dp_{\mathrm{T}}^{\mathrm{lead.jet}}}$ and $\frac{d\sigma}{dp_{\mathrm{T}}^{\mathrm{sublead.jet}}}$, in Figure 8.27. In Figures 8.28 and 8.29, cross section measurements in bins of $\frac{d\sigma}{dm_{\mathrm{jj}}}$, $\frac{d\sigma}{d\Delta\eta_{\mathrm{jj}}}$, and $\frac{d\sigma}{d\Delta\phi_{\mathrm{jj}}}$ are provided. Concluding the set of one dimensional observables are results for $m_{4\ell\mathrm{j}}$ and $m_{4\ell\mathrm{jj}}$ in Figure 8.31 and $p_{\mathrm{T}}^{4\ell\mathrm{j}}$ and $p_{\mathrm{T}}^{4\ell\mathrm{jj}}$ in Figure 8.30. The cross sections provided are $\frac{d\sigma}{dm_{4\ell\mathrm{j}}}$, $\frac{d\sigma}{dm_{4\ell\mathrm{jj}}}$, $\frac{d\sigma}{dp_{\mathrm{T}}^{4\ell\mathrm{j}}}$, and $\frac{d\sigma}{dp_{\mathrm{T}}^{4\ell\mathrm{jj}}}$, respectively.

Results of the measured cross sections with respect to the two dimensional variables follow in Figures 8.32- 8.41. The results for $\frac{d^2\sigma}{dm_{12}dm_{34}}$ are provided in both the same- and opposite- flavor decay channels in Figure 8.34, as well as in the $\ell\ell\mu\mu$ and $\ell\ell ee$ final states in Figure 8.33. The latter is used in an interpretation which will be discussed in Section 9.1.

For all observables considered, data is compared with SM predictions described in Section 5.2. As in the case of the fiducial cross section results, all production modes excluding ggF use the nominal set of simulations mentioned in Section 5.2, and are denoted in the figures together as 'XH'. Various predictions are provided for the ggF production mode. Predictions from MadGraph5_aMC@NLO-FxFx and NNLOPS are provided for all variables. p-values are provided to quantify agreement between measured results and the various predictions. As in the inclusive fiducial cases, the p-values do not include systematic uncertainties on the theoretical predictions. Their calculation is described in Section 7.2.

For variables sensitive to the modelling of the Higgs boson decay, specifically m_{12}, m_{34}, ϕ, and m_{12} vs. m_{34}, predictions using alternatives to PYTHIA 8 for modelling the Higgs decay are provided. These are Hto4l and PROPHECY4F, described in Section 5.2.

Jet-related variables include predictions calculated using NNLOJET in all bins with at least one jet. For a subset of these variables, predictions calculated using RadISH are provided as well. RadISH provides resummation at N^{3}LL+NNLO, while NNLOJET provides predictions at N^{2}LO.

Again, citations for all predictions are provided in Section 5.2.

For all measurements, good agreement is seen between the measured cross sections and Standard Model predictions. There are some small deviations in several bins of the angular observables as well as in bins of $m_{4\ell jj}$ and several differential distributions. As an example, the p-values calculated for the $p_{\mathrm{T}}^{\mathrm{lead.jet}}$ vs. $|y^{\mathrm{lead.\ jet}}|$ distribution are particularly low. This can be attributed to the downward fluctuation in the second bin; however, when considering the uncertainties on the measurements, the deviations are not significant. For bins in which no events are observed, an upper limit is set on the cross section. In the highest bin in $p_{\mathrm{T}}^{4\ell}$,

an upper limit of 27 ab at 95% CL_s is set. In the last bin in $p_{\mathrm{T}}^{4\ell\mathrm{jj}}$, an upper limit of $\sigma < 38$ ab at 95% CL_s is set.

A summary of the compatibility observed between measured and Standard Model predicted cross sections for each observable, quanitified by the p-values, is provided in Table 8.3.

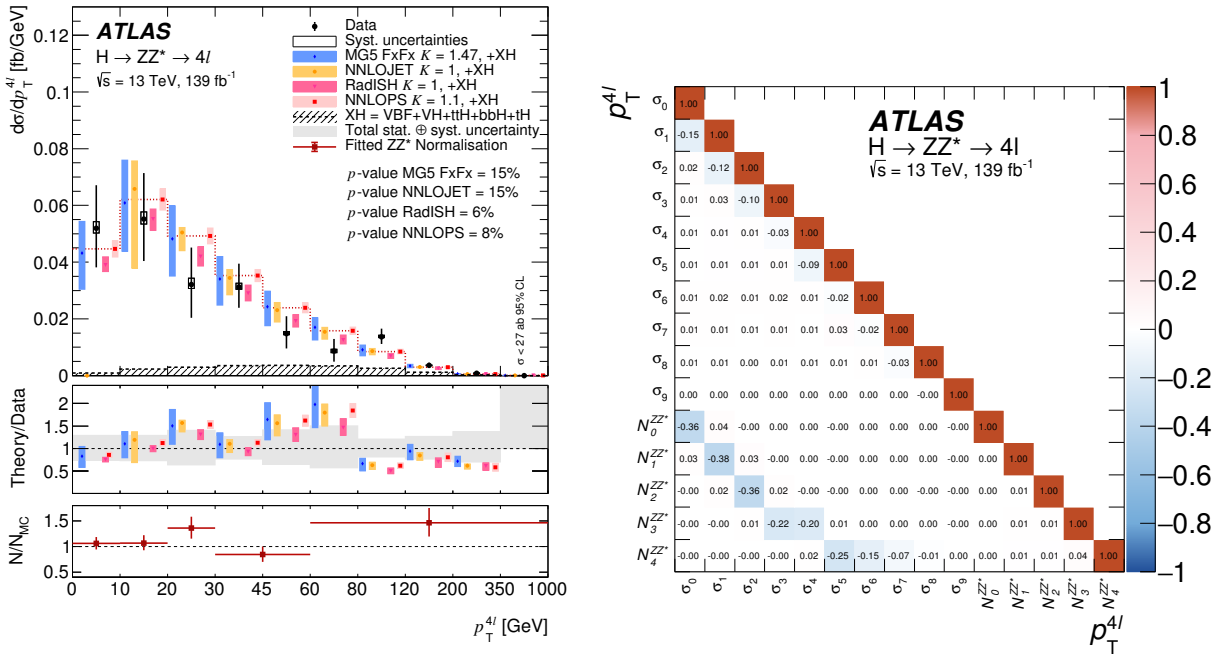

(a) (b)

Figure 8.17. (a) Differential fiducial cross section for the transverse momentum p_{T}^{H} of the Higgs boson, along with (b) the corresponding correlation matrix between the measured cross sections and the ZZ^* background normalization factors. The measured cross sections are compared to ggF predictions by MadGraph5_aMC@NLO-FxFx, NNLOJET, RadISH, and NNLOPS, where MadGraph5_aMC@NLO-FxFx and NNLOPS are normalised to the N^{3}LO total cross section with the listed K-factors while the normalizations for NNLOJET and RadISH are to their respective predicted cross sections. MC-based predictions for all other Higgs boson production modes XH are normalised to the SM predictions. The error bars on the data points show the total uncertainties, while the systematic uncertainties are indicated by the boxes. The shaded bands on the expected cross sections indicate the PDF and scale systematic uncertainties, calculated as described in Section 7.3. The p-values indicating the compatibility of the measurement and the SM predictions, calculated as described in Section 7.2, are shown as well. They do not include the systematic uncertainty in the theoretical predictions. predictions. The central panel of (a) shows the ratio of different predictions to the data, the grey area represents the total uncertainty of the measurement. The bottom panel of (a) shows the ratios of the fitted values of the ZZ^* normalization factors to the predictions from MC discussed in Section 5.4.2. As indicated by the horizontal error bars, the ZZ^* normalization is estimated in each of the first three p_{T}^{H} bins separately, while the next two bins share a common estimation factor, as do the last five bins.

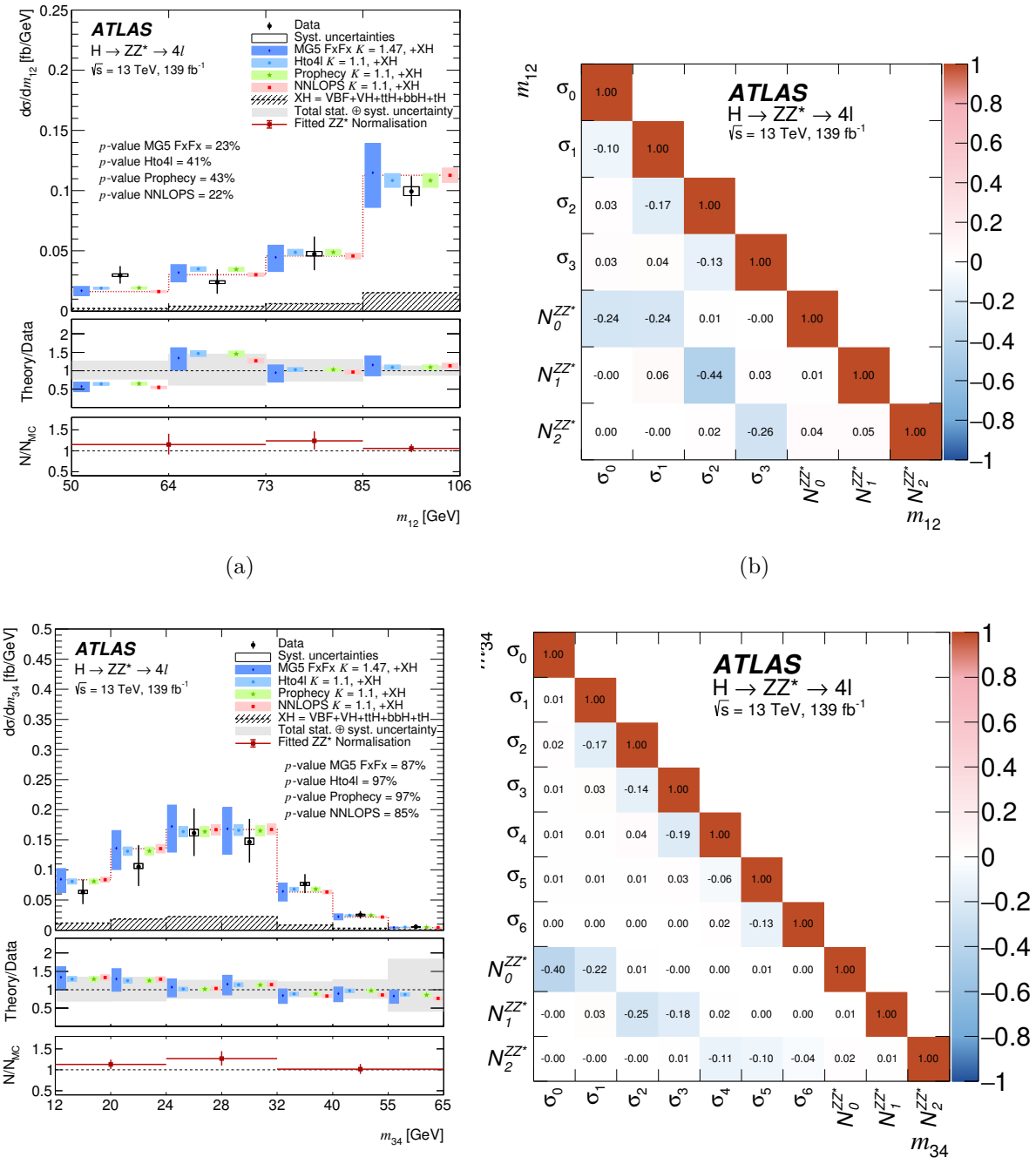

Figure 8.18. Differential fiducial cross sections for (a) the invariant mass m_{12} of the leading Z boson and (c) the invariant mass m_{34} of the subleading Z boson, along with the corresponding correlation matrices between the measured cross sections and the ZZ^* background normalization factors ((b) and (d)).

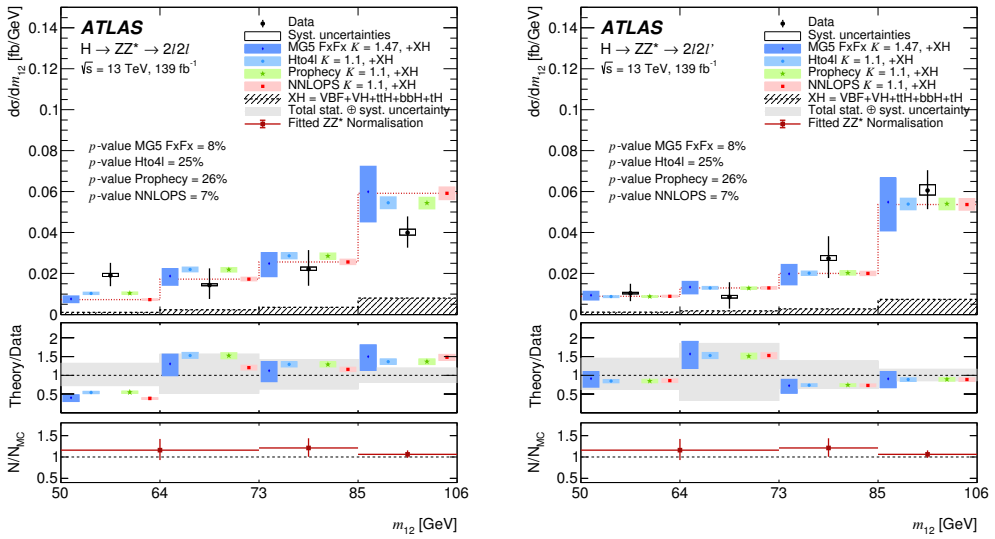

(a) (b)

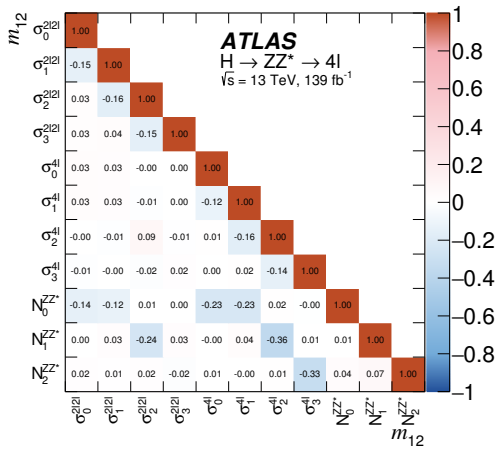

(c)

Figure 8.19. Differential fiducial cross sections for the invariant mass m_{12} of the leading Z boson in (a) the 4μ and $4e$ decay channels and (b) the $2e2\mu$ and $2\mu2e$ decay channels. The corresponding correlation matrix is shown in (c).

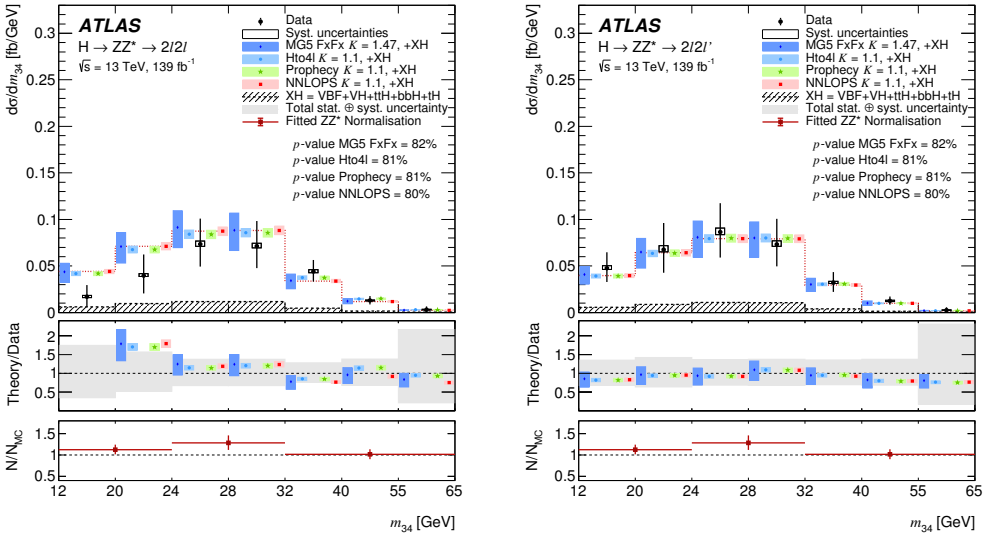

(a) (b)

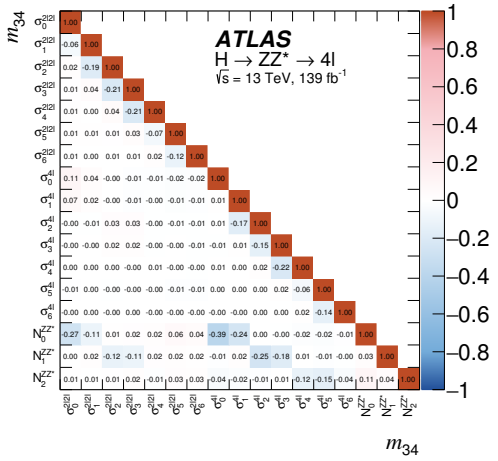

(c)

Figure 8.20. Differential fiducial cross sections for the invariant mass m_{34} of the subleading Z boson in (a) the 4μ and $4e$ decay channels and (b) the $2e2\mu$ and $2\mu2e$ decay channels. The corresponding correlation matrix is shown in (c).

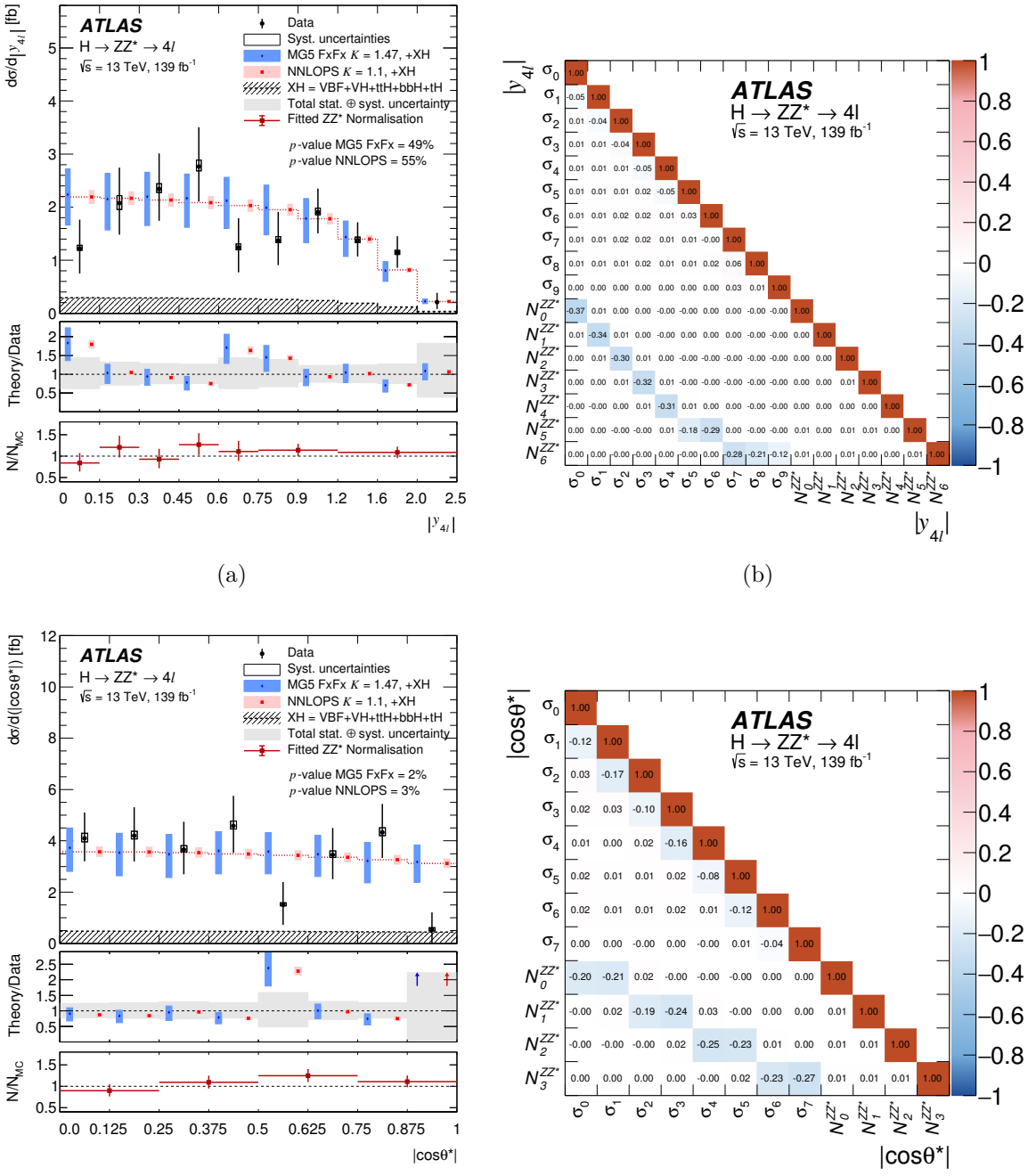

Figure 8.21. Differential fiducial cross sections for (a) the rapidity, $|y_H|$, of the Higgs boson and (c) the production angle, $|\cos\theta^*|$, of the leading Z boson. The corresponding correlation matrices between the measured cross sections and the ZZ^* background normalization factors are also shown ((b) and (d)).

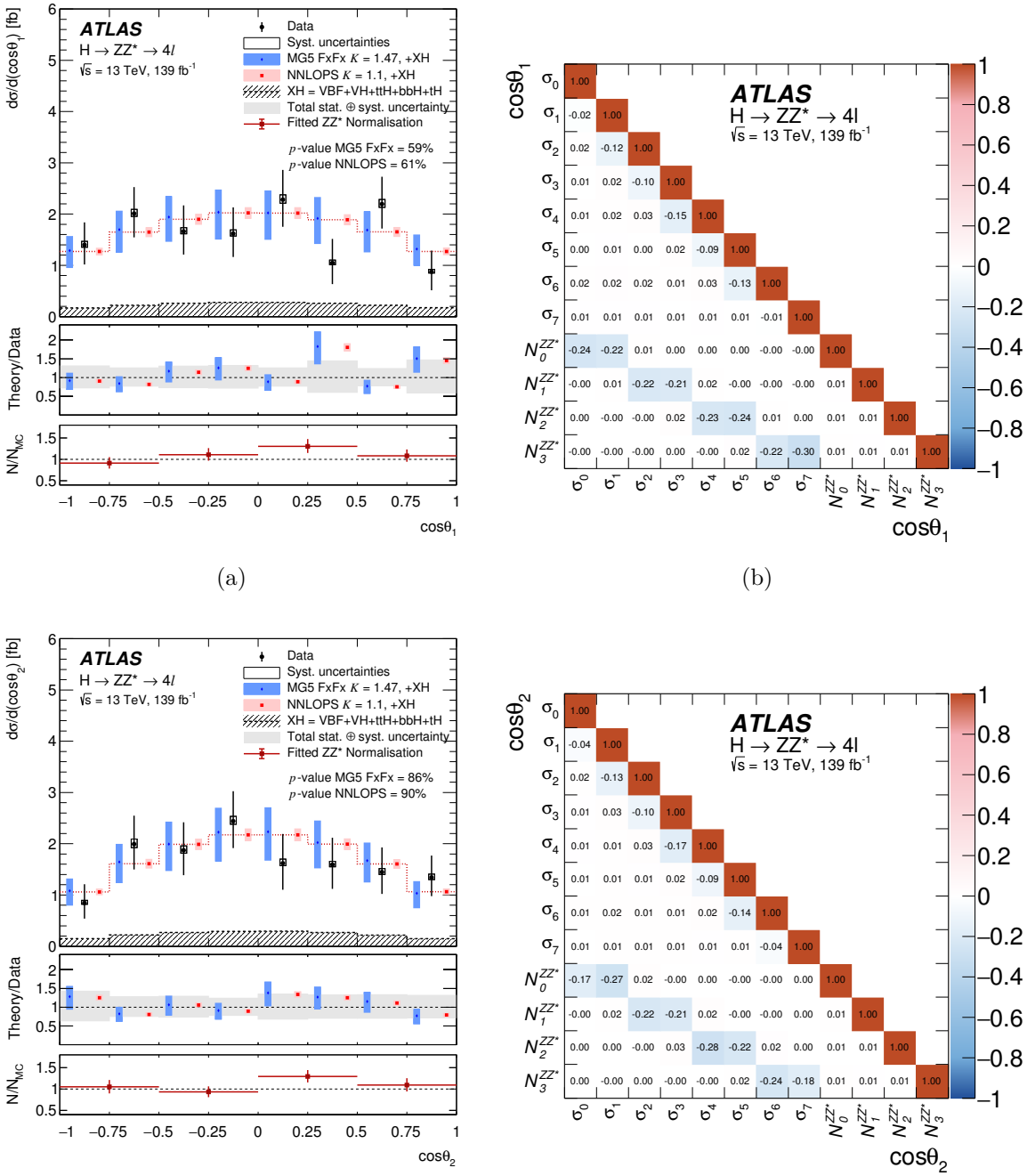

(a) (b)

(c) (d)

Figure 8.22. Differential fiducial cross sections for (a) production angle, $\cos\theta_1$, of anti-lepton from the leading Z boson and (c) the production angle, $\cos\theta_2$, of the anti-lepton from the subleading Z boson. The corresponding correlation matrices between the measured cross sections and the ZZ^* background normalization factors are also shown ((b) and (d)).

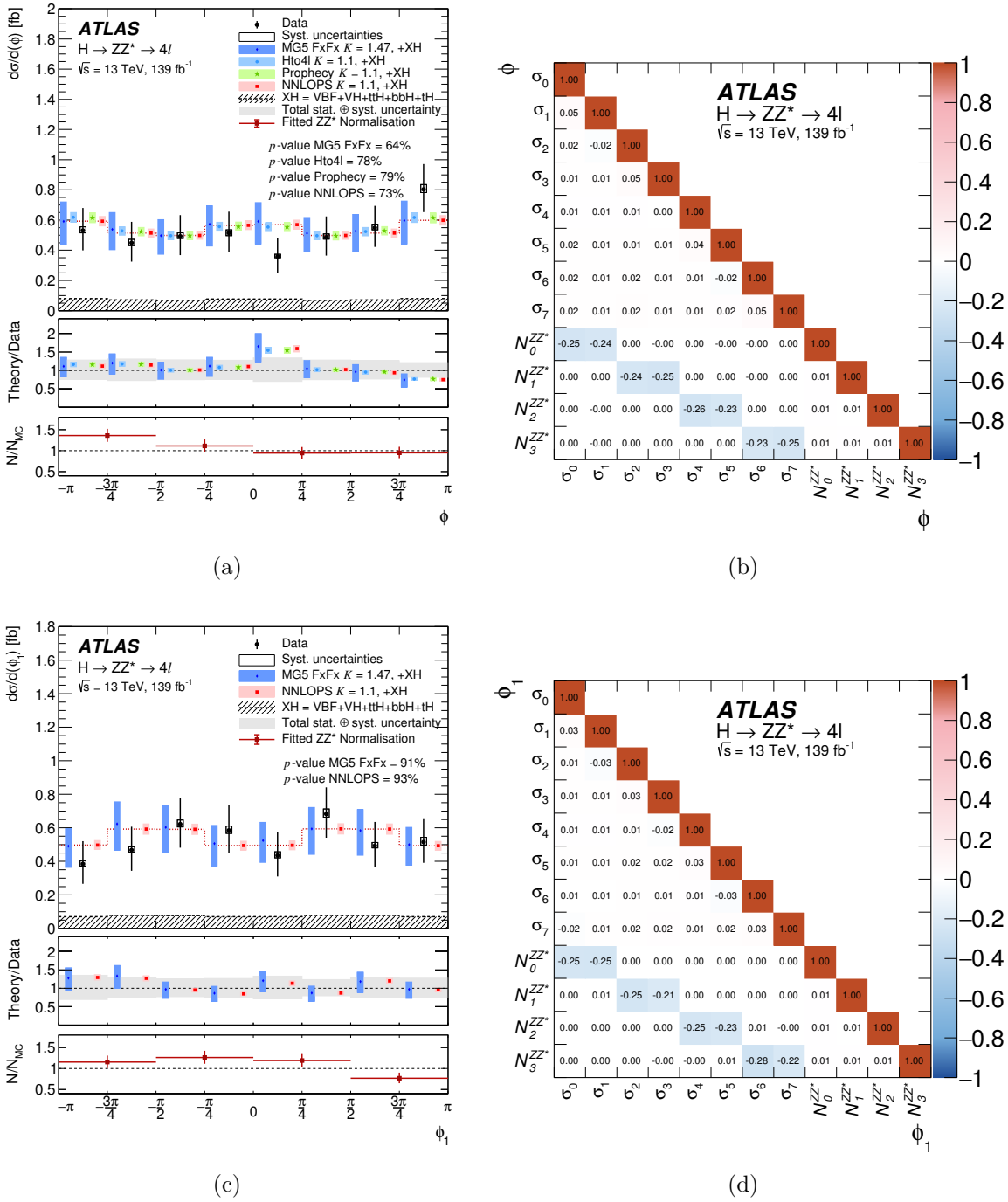

Figure 8.23. Differential fiducial cross sections for (a) the azimuthal angle, ϕ, of the decay planes of the two reconstructed Z bosons and (c) the azimuthal angle, ϕ_1, of the decay plane of the leading Z boson and the plane formed between its four-momentum and the z-axis. The corresponding correlation matrices between the measured cross sections and the ZZ^* background normalization factors are also shown ((b) and (d)).

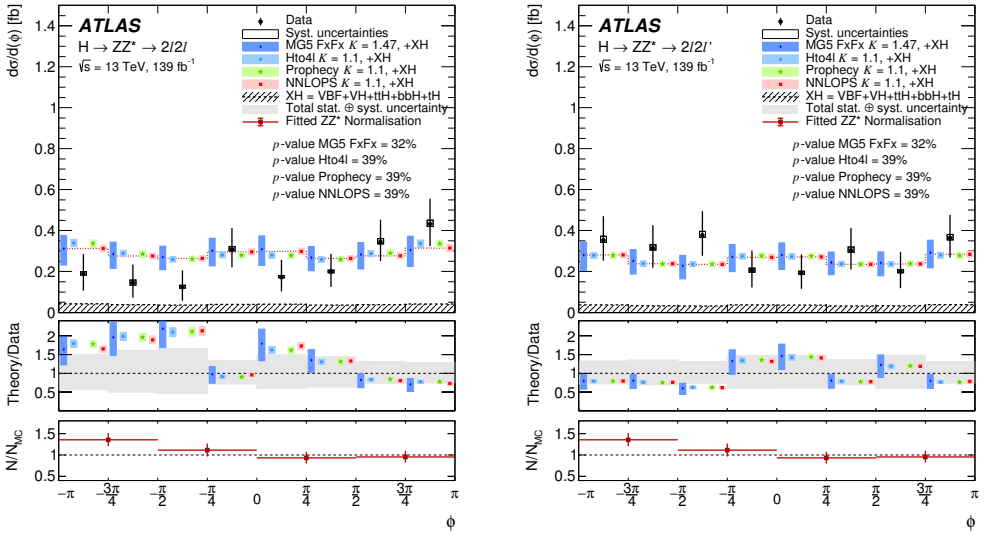

(a)

(b)

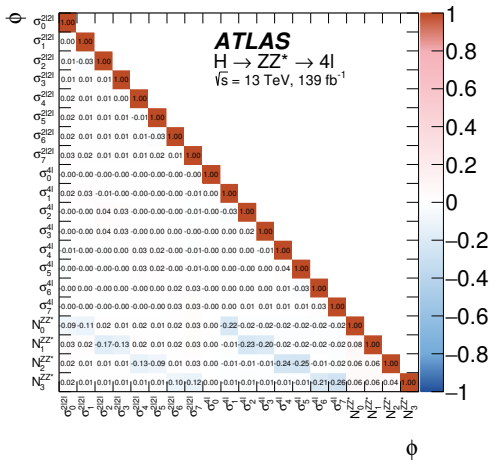

(c)

Figure 8.24. Differential fiducial cross sections for the azimuthal angle, ϕ, of the decay planes of the two reconstructed Z bosons in (a) the 4μ and $4e$ decay channels and (b) the $2e2\mu$ and $2\mu2e$ decay channels. The corresponding correlation matrix is shown in (c).

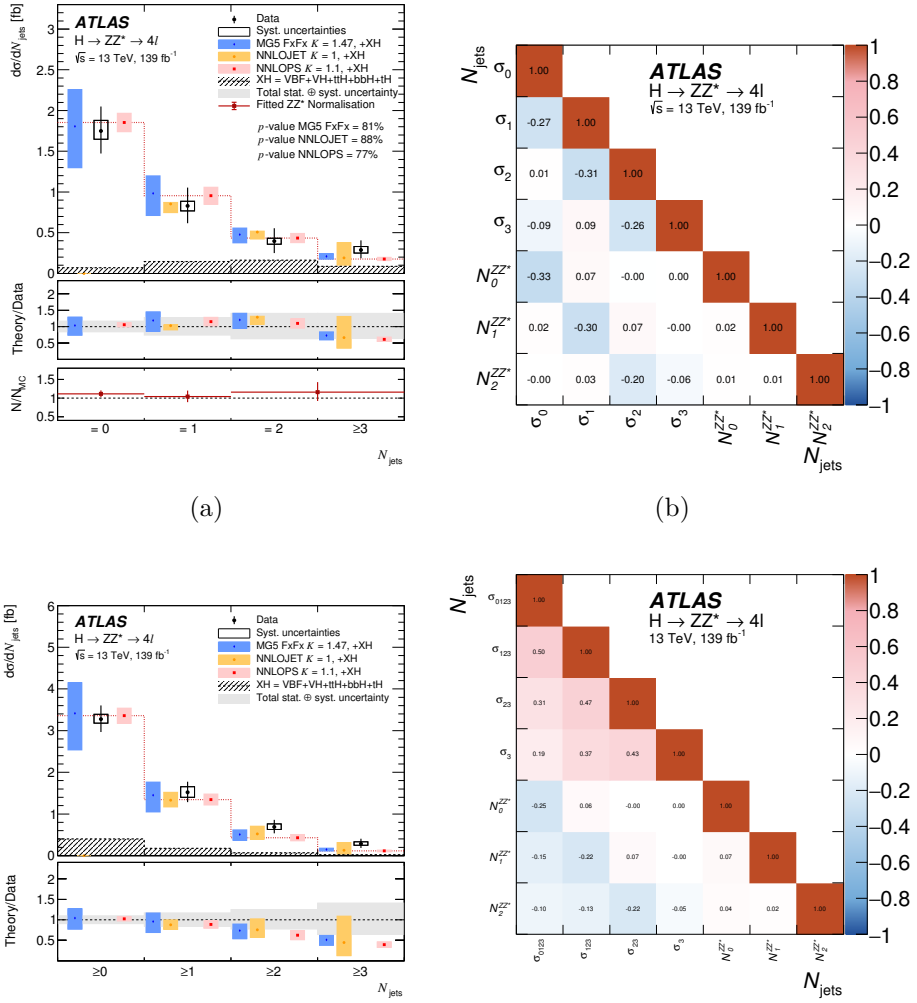

(a) (b)

(c) (d)

Figure 8.25. Differential fiducial cross sections for (a) the jet multiplicity, N_{jets}, in the selected events, and (c), the inclusive jet multiplicity. In the N_{jets} distribution in (a), the first three bins are exclusive in number of jets, while the fourth is inclusive. In the N_{jets} distribution in (c), all bins are inclusive, with the first bin including all events, the second including all events with at least one jet, and so on. The corresponding correlation matrices between the measured cross sections and the ZZ^* background normalization factors are also shown ((b) and (d)).

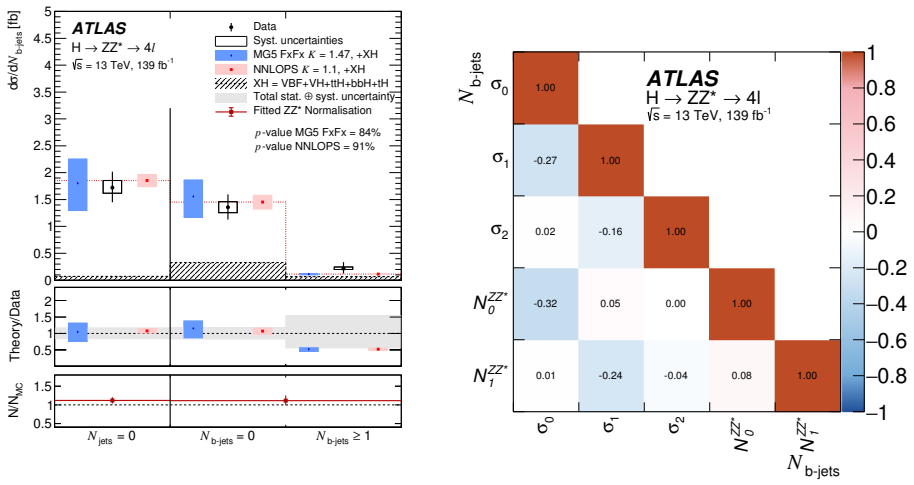

(a) (b)

Figure 8.26. Differential fiducial cross sections for (a) the number of b-quark initiated jets, $N_{b-\text{jets}}$. Three bins are considered. The first bin is filled with events which do not have any jets, the second is filled with events with at least one jet but no b-tagged jets, while the third includes all events with at least one b-tagged jet. The corresponding correlation matrices between the measured cross sections and the ZZ^* background normalization factors are also shown in (b)).

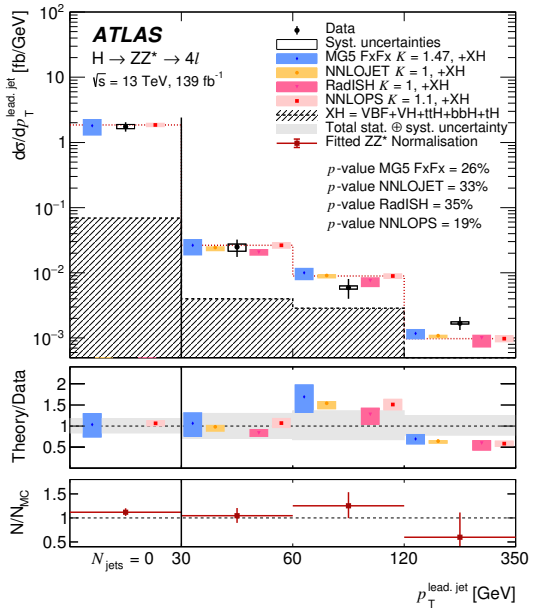

(a)

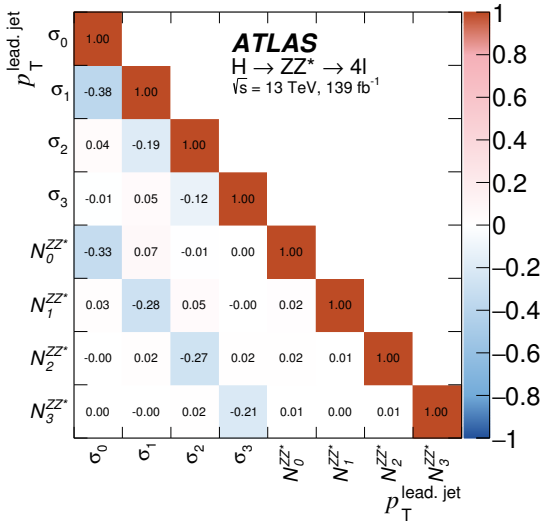

(b)

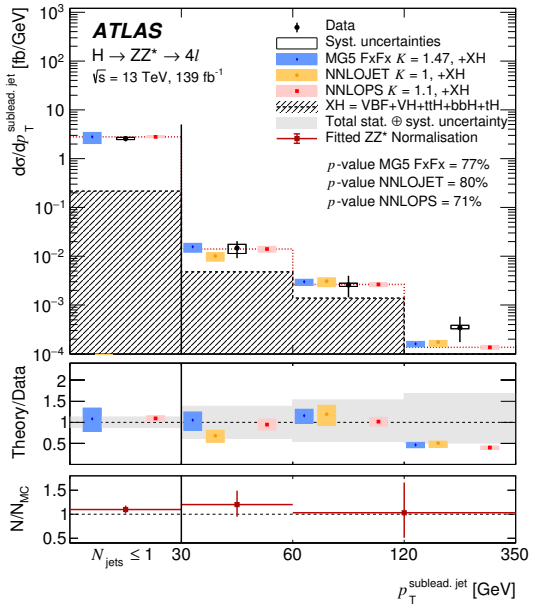

(c)

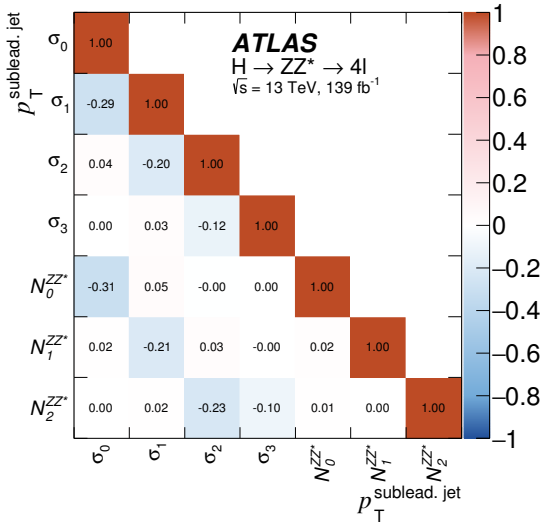

(d)

Figure 8.27. Differential fiducial cross sections for (a) the transverse momentum of the leading jet, $p_{\mathrm{T}}^{\mathrm{lead.jet}}$, in events with at least one jet, and (c) the transverse momentum of the subleading jet, $p_{\mathrm{T}}^{\mathrm{sublead.jet}}$, in events with at least two jets. Leading and subleading jets refer to the jets with the highest and second highest transverse momenta. The first bin contains events which do not pass the jet requirements. The corresponding correlation matrices between the measured cross sections and the ZZ^* background normalization factors are also shown ((b) and (d)).

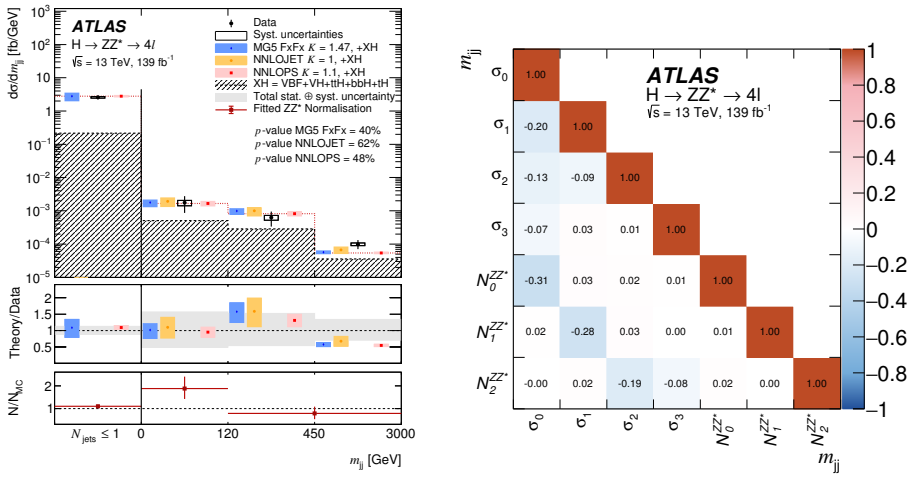

(a) (b)

Figure 8.28. Differential fiducial cross sections for (a) the invariant mass of the two highest-p_T jets, m_{jj}, in events with at least two jets. The corresponding correlation matrix between the measured cross sections and the ZZ^* background normalization factors is also provided ((b)).

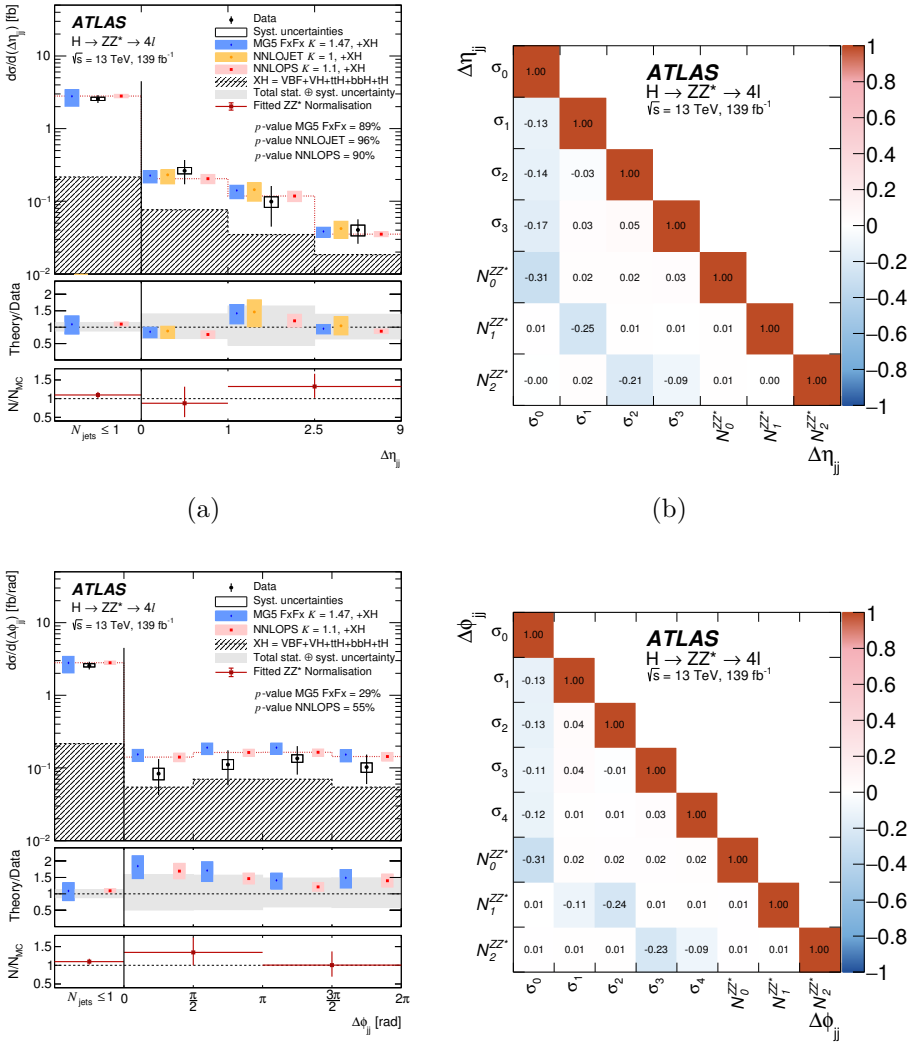

Figure 8.29. Differential fiducial cross sections for (a) the distance between these two jets in pseudorapidity, $\Delta\eta_{\mathrm{jj}}$, and (c) the distance between the two jets in ϕ, $\Delta\phi_{\mathrm{jj}}$. The first bin contains events with fewer than two jets that pass the jet selection requirements. Finally, the corresponding correlation matrices between the measured cross sections and the ZZ^* background normalization factors are provided ((b) and (d)).

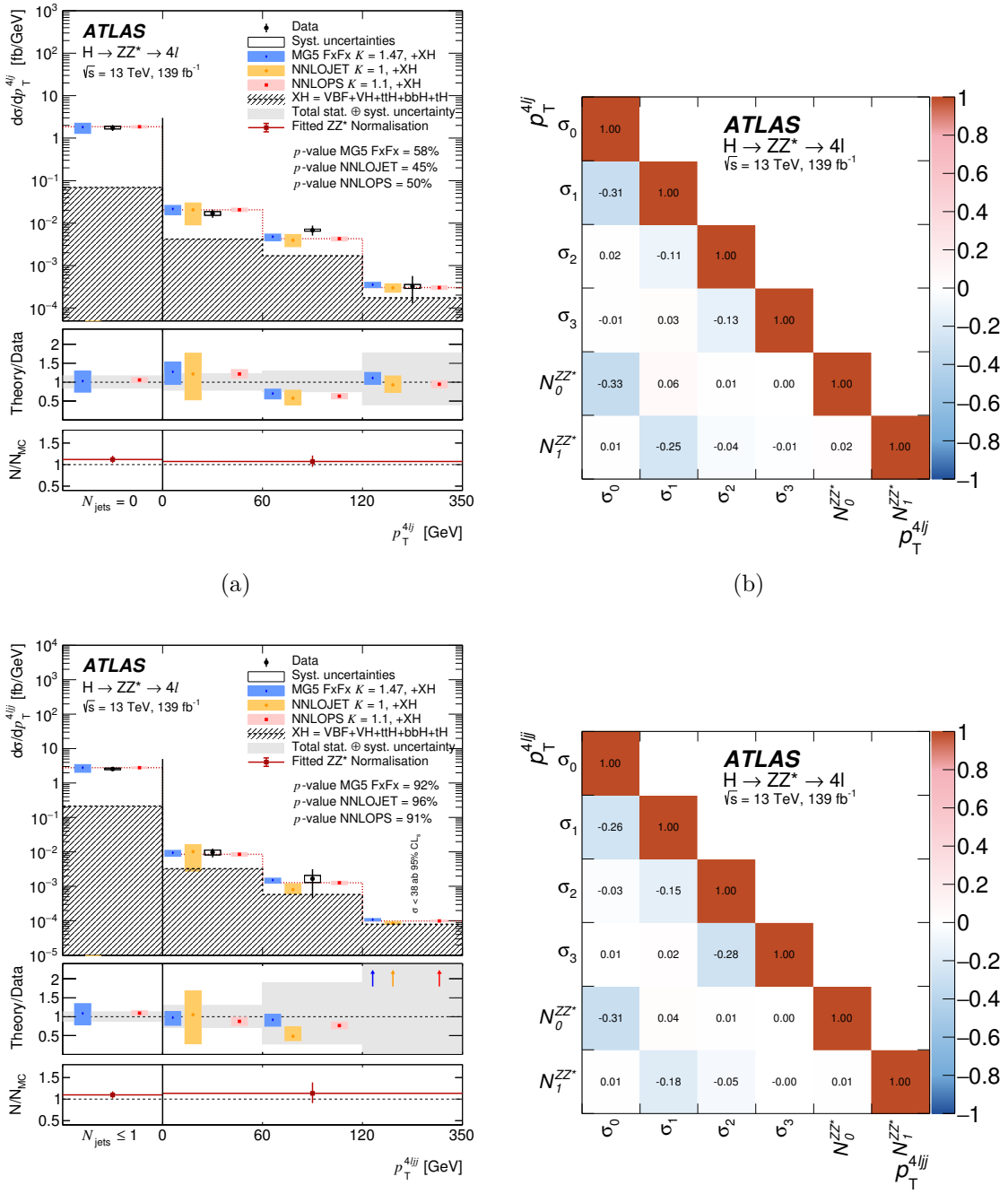

Figure 8.30. Differential fiducial cross sections for (a) the transverse momentum of the four lepton plus jet system, in events with at least one jet, and (c) the transverse momentum of the four lepton plus di-jet system, in events with at least two jets. The corresponding correlation matrices between the measured cross sections and the ZZ^* background normalization factors are also shown ((b) and (d)).

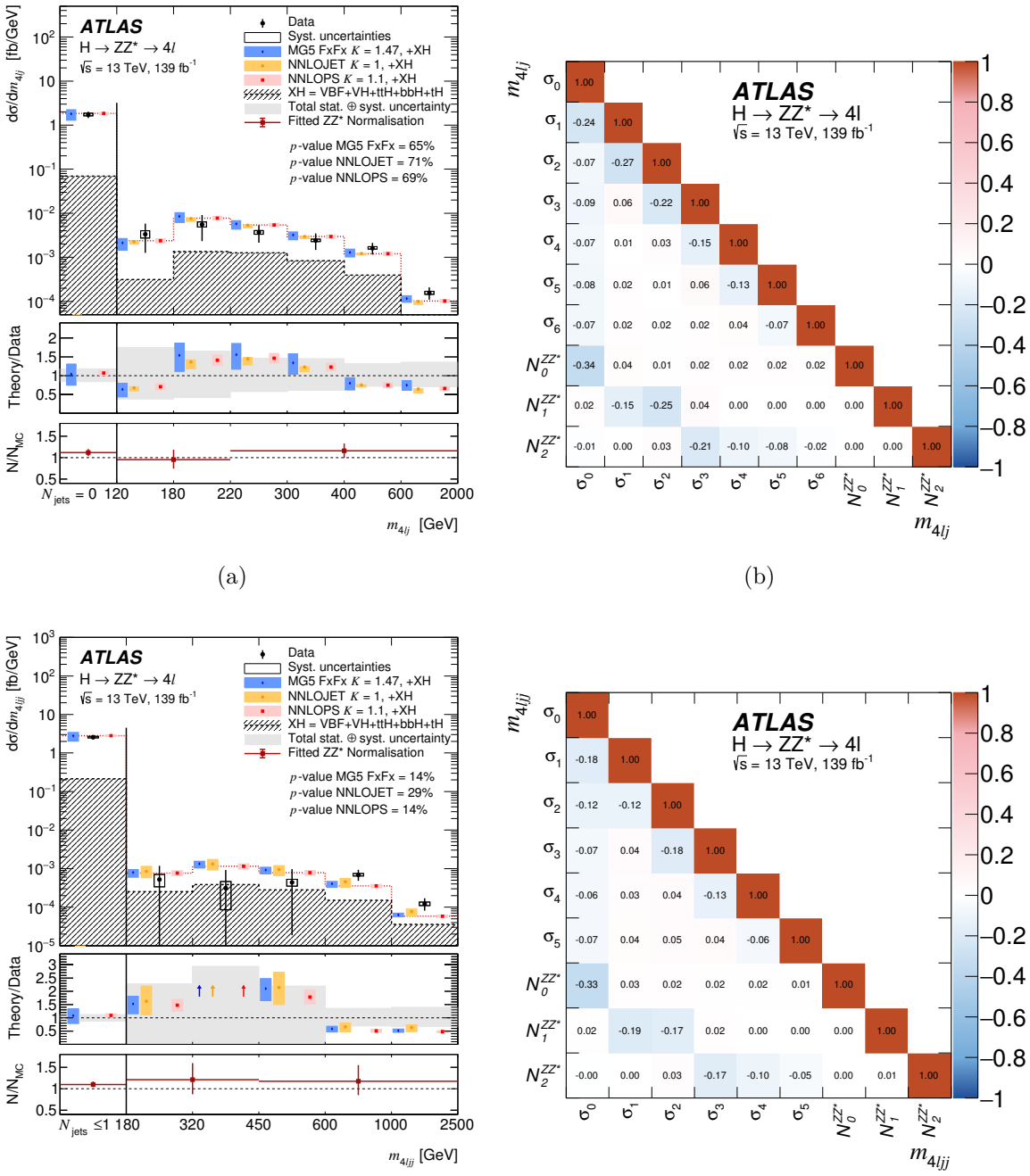

Figure 8.31. Differential fiducial cross sections for (a) the invariant mass of the four lepton plus jet system, in events with at least one jet, and (c) the invariant mass of the four lepton plus di-jet system, in events with at least two jets. The corresponding correlation matrices between the measured cross sections and the ZZ^* background normalization factors are also shown ((b) and (d)).

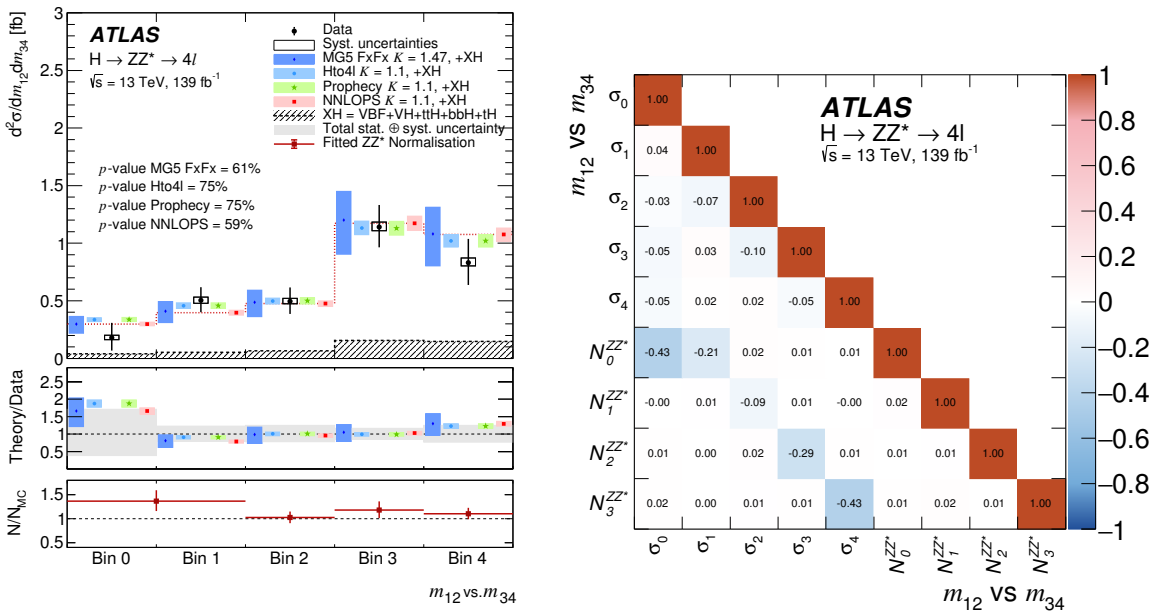

(a) (b)

Figure 8.32. (a) Differential fiducial cross section for the leading vs. subleading Z boson mass, m_{12} vs. m_{34}, and (b) the corresponding correlation matrix between the measured cross sections and the ZZ^* background normalization factors.

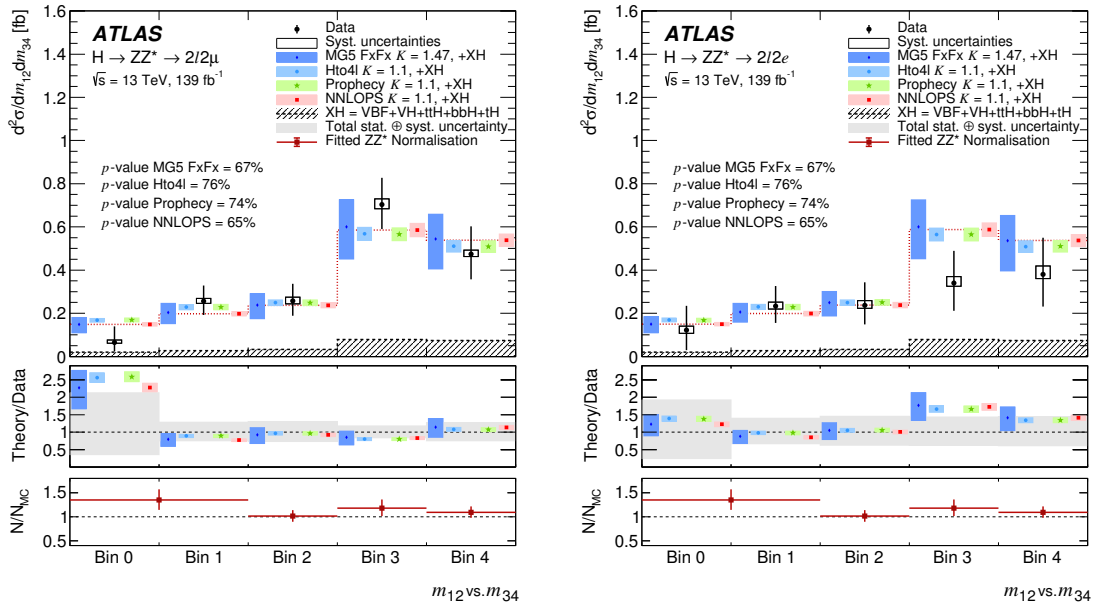

(a) (b)

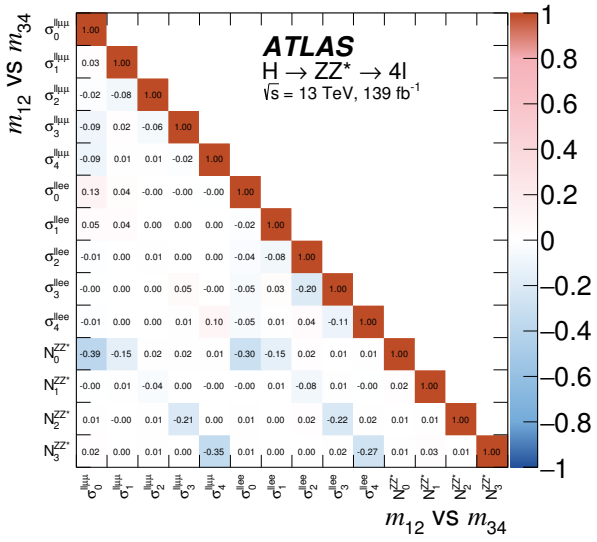

(c)

Figure 8.33. Differential fiducial cross sections for the leading vs. subleading Z boson mass, m_{12} vs. m_{34}, in (a) $\ell\ell\mu\mu$ and (b) $\ell\ell ee$ final states, along with (c) their corresponding correlation matrix between the measured cross sections and the ZZ^* background normalization factors.

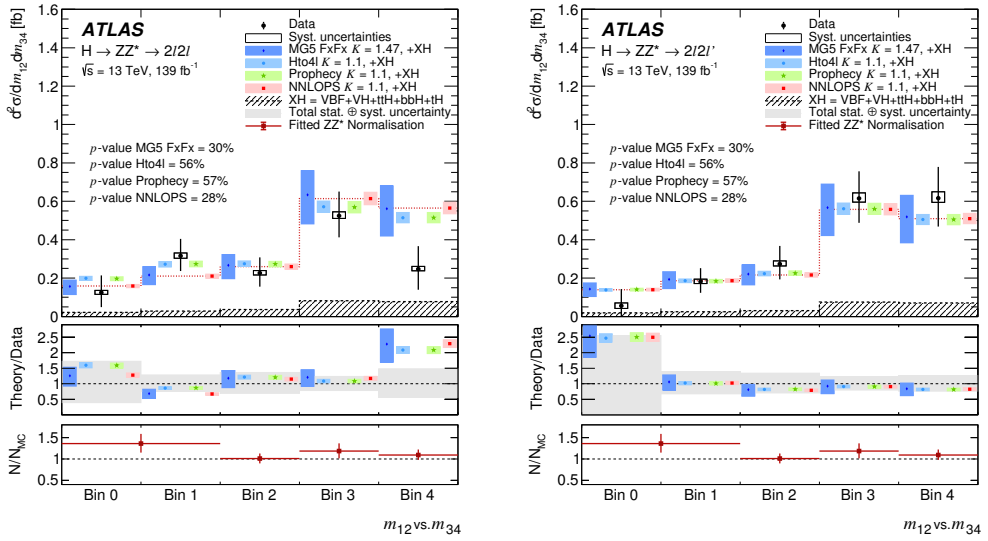

(a) (b)

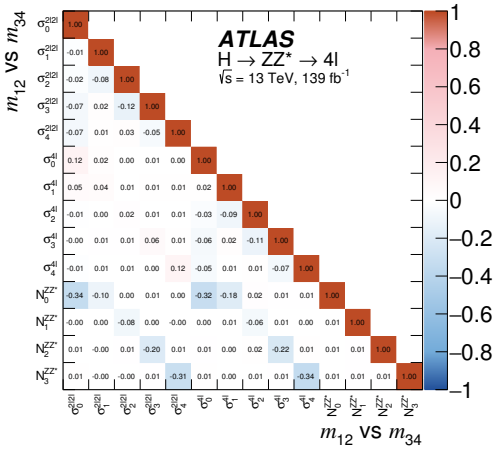

(c)

Figure 8.34. Differential fiducial cross sections for the invariant mass of the leading vs. subleading Z bosons, m_{12} vs. m_{34} and in **??** the 4μ and $4e$ decay channels and**??** the $2e2\mu$ and $2\mu2e$ decay channels. The corresponding correlation matrix is shown in **??**.

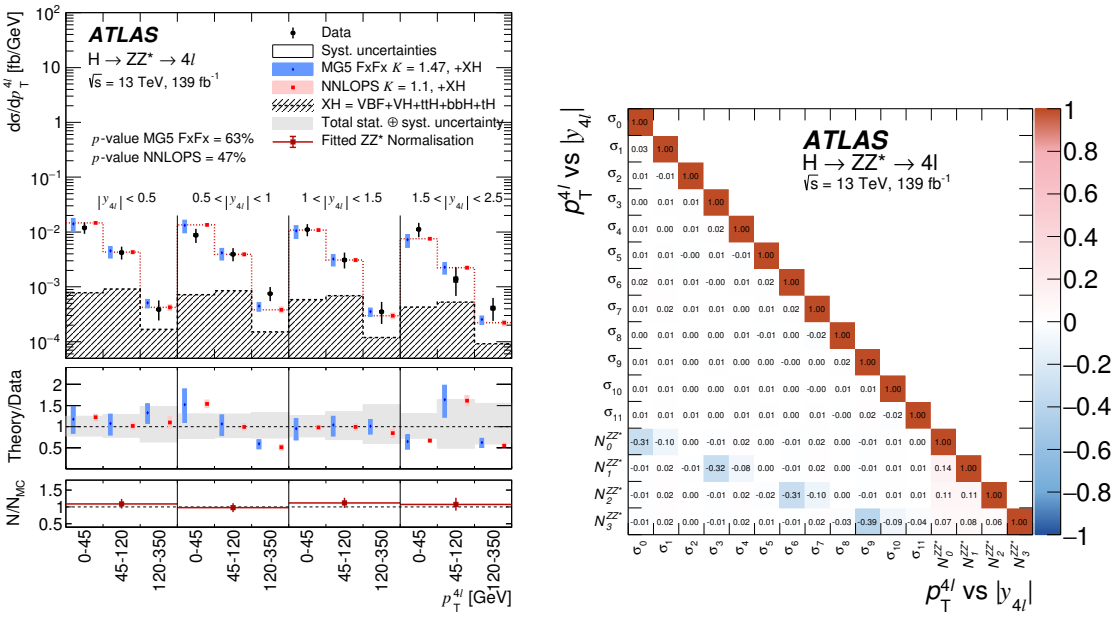

(a) (b)

Figure 8.35. (a) Double differential fiducial cross sections of the p_{T}^{H} distribution in $|y_H|$ bins. The corresponding correlation matrix between the measured cross sections and the ZZ^* background normalization factors is shown in (b). The p-values shown are calculated for all bins across both p_{T}^{H} and $|y_H|$ simultaneously.

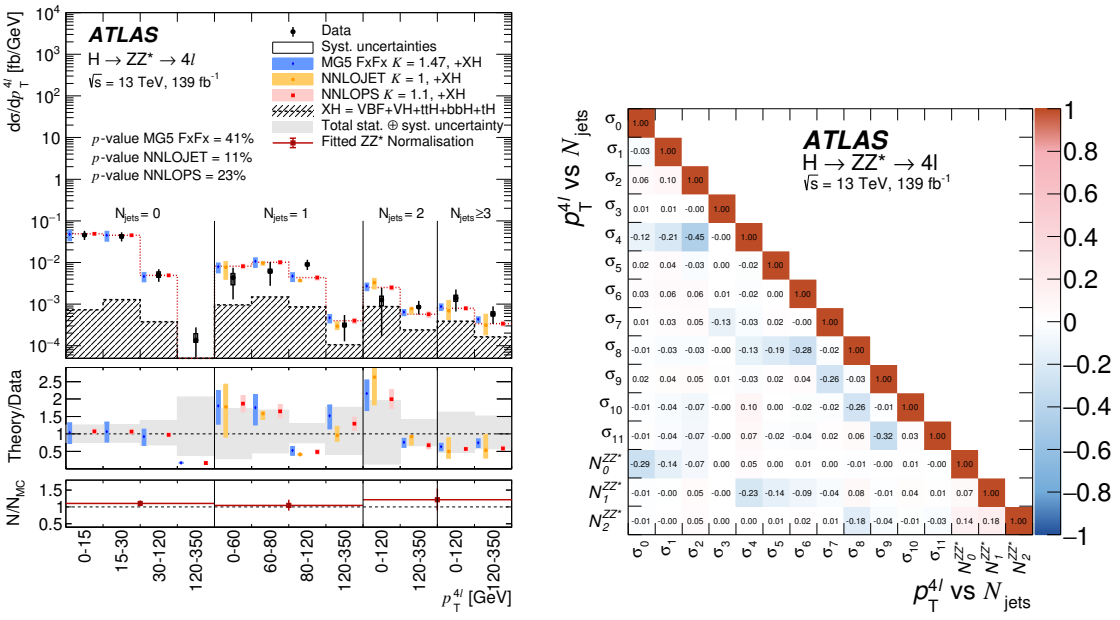

(a) (b)

Figure 8.36. (a) Double differential fiducial cross sections of the p_{T}^{H} distribution in N_{jets} bins. The corresponding correlation matrix between the measured cross sections and the ZZ^* background normalization factors is shown in (b). The p-values shown are calculated for all bins across both p_{T}^{H} and N_{jets} simultaneously.

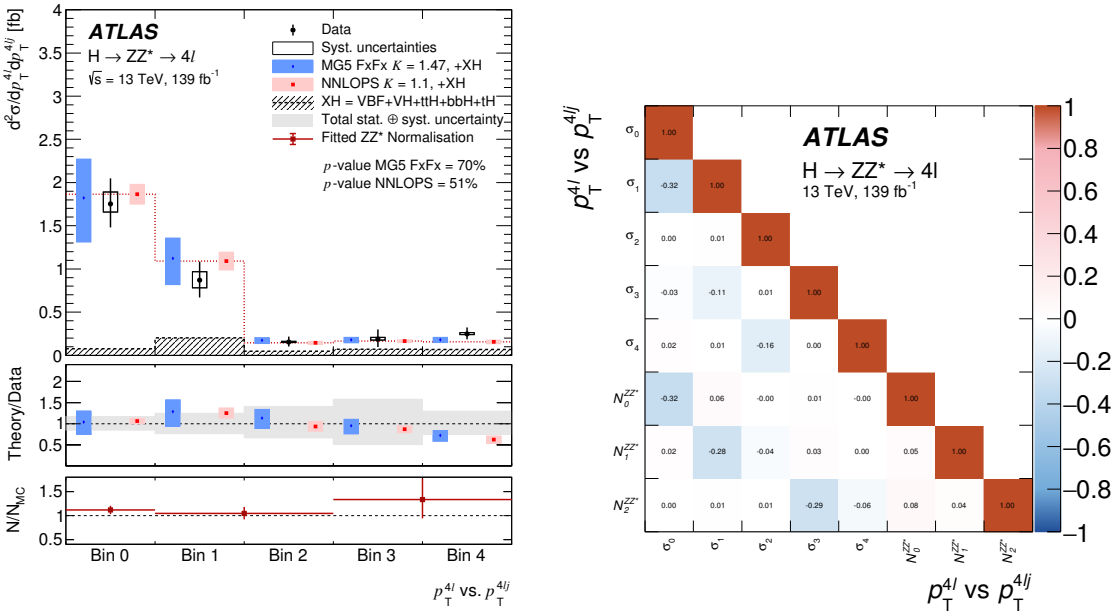

(a) (b)

Figure 8.37. (a) Differential fiducial cross section for the transverse momentum of the four lepton system vs. the transverse momentum of the four lepton plus jet system, p_{T}^{H} vs. $p_{\mathrm{T}}^{4\ell\mathrm{j}}$ and (b) the corresponding correlation matrix between the measured cross sections and the ZZ^* background normalization factors.

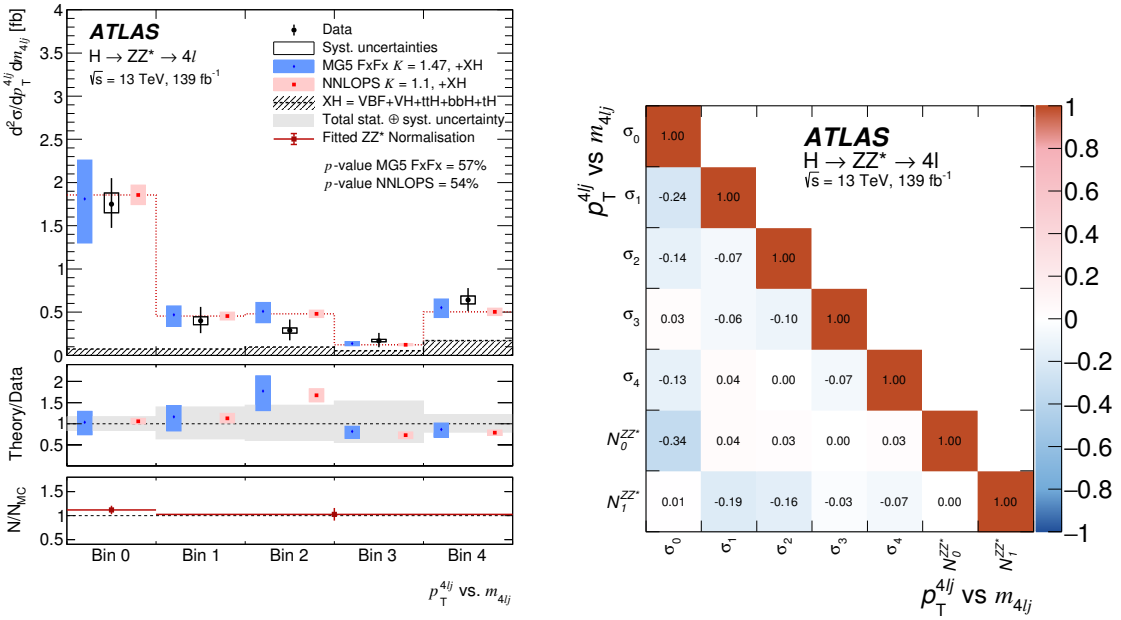

(a) (b)

Figure 8.38. (a) Double differential fiducial cross section for the transverse momentum of the four lepton plus jet system vs. the invariant mass of the four lepton plus jet system, $p_{\mathrm{T}}^{4\ell\mathrm{j}}$ vs. $m_{4\ell\mathrm{j}}$ and (b) the corresponding correlation matrix between the measured cross sections and the ZZ^* background normalization factors.

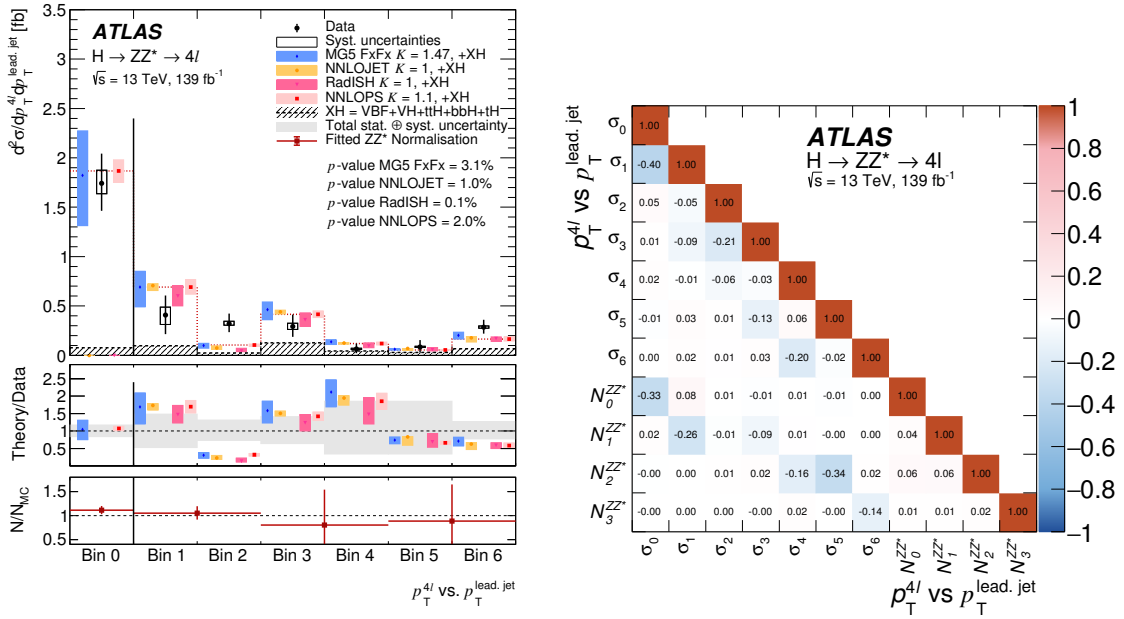

(a) (b)

Figure 8.39. (a) Double differential fiducial cross section for the transverse momentum of the four lepton system vs. the transverse momentum of the leading jet, p_{T}^{H} vs. $p_{\mathrm{T}}^{\mathrm{lead.jet}}$, and (b) the corresponding correlation matrix between the measured cross sections and the ZZ^{*} background normalization factors.

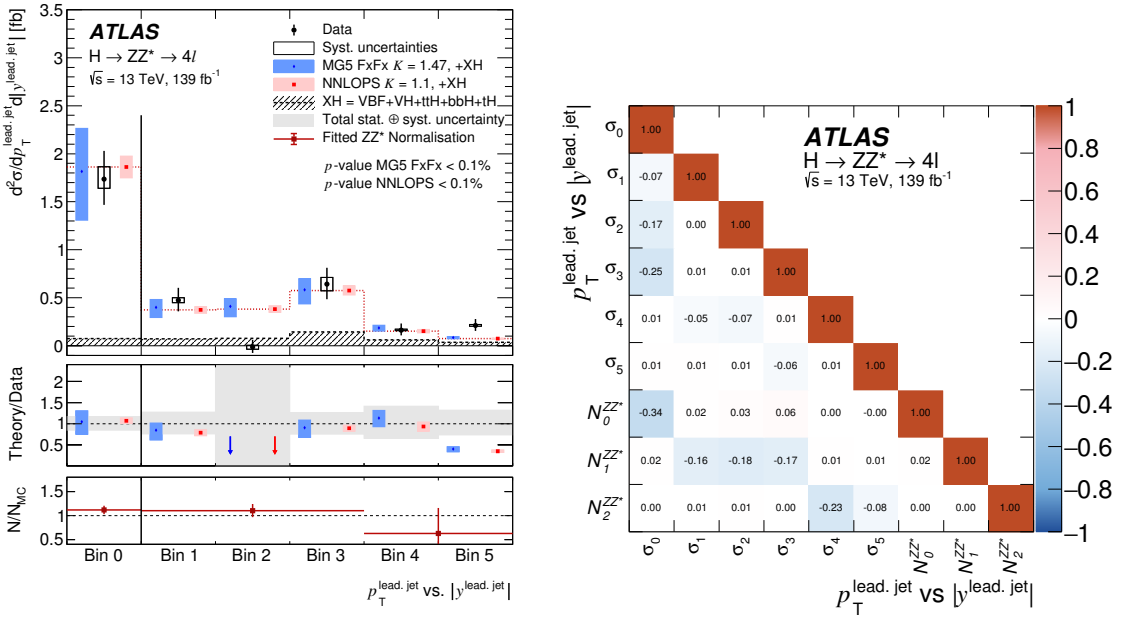

(a) (b)

Figure 8.40. (a) Double differential fiducial cross section for the transverse momentum of the leading jet vs. the rapidity of the leading jet, $p_{\mathrm{T}}^{\mathrm{lead.jet}}$ vs. $|y^{\mathrm{lead.\ jet}}|$, and (b) the corresponding correlation matrix between the measured cross sections and the ZZ^* background normalization factors.

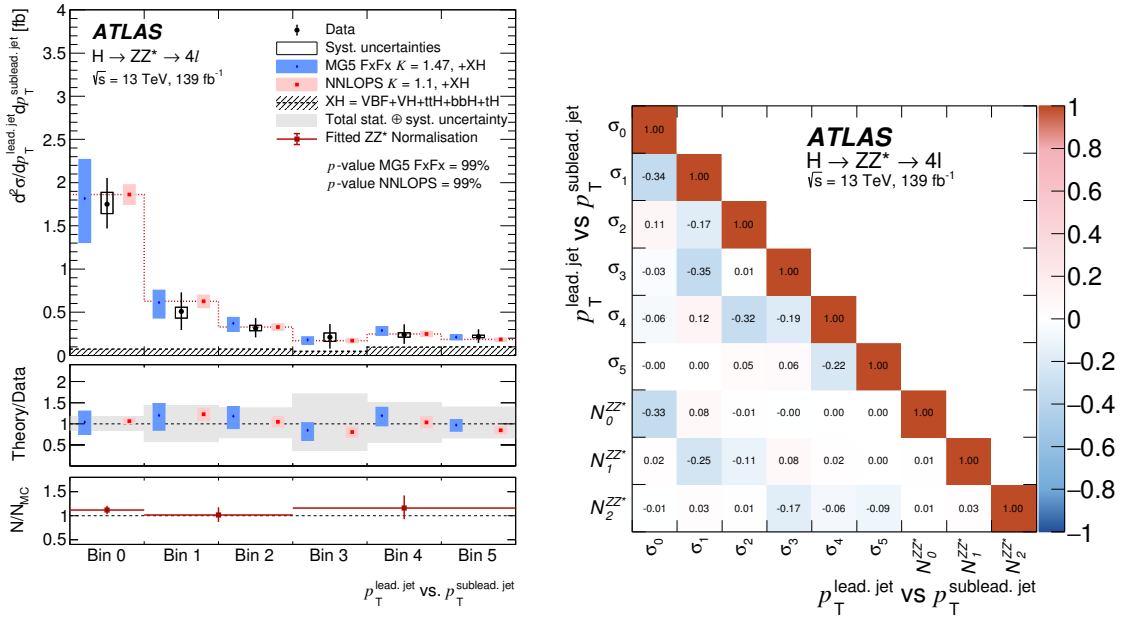

(a) (b)

Figure 8.41. (a) Double differential fiducial cross section for the transverse momentum of leading vs. subleading jet, $p_{\mathrm{T}}^{\mathrm{lead.jet}}$ vs. $p_{\mathrm{T}}^{\mathrm{sublead.jet}}$, and (b) the corresponding correlation matrix between the measured cross sections and the ZZ^* background normalization factor.

Observable	NNLOPS	MG5	RadISH	NNLOJET	Prophecy	Hto4l
$\mathrm{d}\sigma$ / $\mathrm{d}p_{\mathrm{T}}^{H}$	8	15	6	15	–	–
$\mathrm{d}\sigma$ / $\mathrm{d}m_{12}$	22	23	–	–	43	41
$\mathrm{d}\sigma$ / $\mathrm{d}m_{34}$	85	87	–	–	97	97
$\mathrm{d}\sigma$ / $\mathrm{d}m_{12}$ 2l2l	7	8	–	–	26	25
$\mathrm{d}\sigma$ / $\mathrm{d}m_{12}$ 4l	7	8	–	–	26	25
$\mathrm{d}\sigma$ / $\mathrm{d}m_{34}$ 2l2l	80	81	–	–	81	81
$\mathrm{d}\sigma$ / $\mathrm{d}m_{34}$ 4l	80	81	–	–	81	81
$\mathrm{d}\sigma$ / $\mathrm{d}\lvert y_H\rvert$	55	49	–	–	–	–
$\mathrm{d}\sigma$ / $\mathrm{d}\lvert\cos\theta^*\rvert$	3	2	–	–	–	–
$\mathrm{d}\sigma$ / $\mathrm{d}\cos\theta_1$	61	59	–	–	–	–
$\mathrm{d}\sigma$ / $\mathrm{d}\cos\theta_2$	90	86	–	–	–	–
$\mathrm{d}\sigma$ / $\mathrm{d}\phi$	73	64	–	–	79	78
$\mathrm{d}\sigma$ / $\mathrm{d}\phi$ - 2l2l	39	32	–	–	39	39
$\mathrm{d}\sigma$ / $\mathrm{d}\phi$ - 4l	39	32	–	–	39	39
$\mathrm{d}\sigma$ / $\mathrm{d}\phi_1$	93	91	–	–	–	–
$\mathrm{d}\sigma$ / $\mathrm{d}N_{\mathrm{jets}}$	77	81	–	88	–	–
$\mathrm{d}\sigma$ / $\mathrm{d}N_{b-\mathrm{jets}}$	91	84	–	–	–	–
$\mathrm{d}\sigma$ / $\mathrm{d}p_{\mathrm{T}}^{\mathrm{lead.jet}}$	19	26	35	33	–	–
$\mathrm{d}\sigma$ / $\mathrm{d}p_{\mathrm{T}}^{\mathrm{sublead.jet}}$	71	77	–	80	–	–
$\mathrm{d}\sigma$ / $\mathrm{d}m_{\mathrm{jj}}$	48	40	–	62	–	–
$\mathrm{d}\sigma$ / $\mathrm{d}\eta_{jj}$	90	89	–	96	–	–
$\mathrm{d}\sigma$ / $\mathrm{d}\phi_{jj}$	55	29	–	–	–	–
$\mathrm{d}\sigma$ / $\mathrm{d}m_{4\ell\mathrm{j}}$	69	65	–	71	–	–
$\mathrm{d}\sigma$ / $\mathrm{d}m_{4\ell\mathrm{jj}}$	14	14	–	29	–	–
$\mathrm{d}\sigma$ / $\mathrm{d}p_{\mathrm{T}}^{4\ell\mathrm{j}}$	50	58	–	45	–	–
$\mathrm{d}\sigma$ / $\mathrm{d}p_{\mathrm{T}}^{4\ell\mathrm{jj}}$	91	92	–	96	–	–
$\mathrm{d}\sigma$ / $\mathrm{d}m_{12}$ m_{34}	59	61	–	–	75	75
$\mathrm{d}\sigma$ / $\mathrm{d}m_{12}$ m_{34} 2l2e	65	67	–	–	74	76
$\mathrm{d}\sigma$ / $\mathrm{d}m_{12}$ m_{34} 2l2l	28	30	–	–	57	56
$\mathrm{d}\sigma$ / $\mathrm{d}m_{12}$ m_{34} 2l2mu	65	67	–	–	74	76
$\mathrm{d}\sigma$ / $\mathrm{d}m_{12}$ m_{34} 4l	28	30	–	–	57	56
$\mathrm{d}^2\sigma$ / $\mathrm{d}p_{\mathrm{T}}^{H}$ $\mathrm{d}\lvert y_H\rvert$	63	47	–	–	–	–
$\mathrm{d}^2\sigma$ / $\mathrm{d}p_{\mathrm{T}}^{H}$ $\mathrm{d}N_{\mathrm{jets}}$	11	41	–	23	–	–
$\mathrm{d}^2\sigma$ / $\mathrm{d}p_{\mathrm{T}}^{4\ell\mathrm{j}}$ $\mathrm{d}m_{4\ell\mathrm{j}}$	54	57	–	–	–	–
$\mathrm{d}^2\sigma$ / $\mathrm{d}p_{\mathrm{T}}^{H}$ $\mathrm{d}p_{\mathrm{T}}^{4\ell\mathrm{j}}$	51	70	–	–	–	–
$\mathrm{d}^2\sigma$ / $\mathrm{d}p_{\mathrm{T}}^{H}$ $\mathrm{d}p_{\mathrm{T}}^{\mathrm{lead.jet}}$	2	3.1	0.1	1	–	–
$\mathrm{d}^2\sigma$ / $\mathrm{d}p_{\mathrm{T}}^{\mathrm{lead.jet}}$ $\mathrm{d}\lvert y^{\mathrm{lead.\ jet}}\rvert$	<0.1	<0.1	–	–	–	–
$\mathrm{d}^2\sigma$ / $\mathrm{d}p_{\mathrm{T}}^{\mathrm{lead.jet}}$ $\mathrm{d}p_{\mathrm{T}}^{\mathrm{sublead.jet}}$	99	99	–	–	–	–

Table 8.3. Summary of the compatibility with the Standard Model for all differential cross section measurements.

CHAPTER 9

Interpretations

One of the main motivations for making precision measurements of differential distributions is the sensitivity of particular distributions to potential beyond the Standard Model (BSM) effects. As described in Section 6.3.1, the m_{12} vs. m_{34} and $p_{\mathrm{T}}^{4\ell}$ distributions are particularly sensitive to BSM effects, and the unfolded results are used here in two interpretations. In Section 9.1, the m_{12} vs. m_{34} double differential cross section results are used within the Pseudo-Observables framework [155] to probe several BSM modifications of the Higgs decay to four leptons. Following, in Section 9.2, the $p_{\mathrm{T}}^{4\ell}$ differential cross section measurement is used to constrain the Yukawa couplings between the Higgs boson and b- and c-quarks [154].

9.1. Pseudo-Observables interpretation

Many BSM models predict modified couplings between the Higgs boson and other SM particles. Parameterizations of these couplings in a particluar BSM model are needed in order to evaluate the compatibility between experimental results and predictions within the model.

The Pseudo-Observables framework [155] provides a parameterization using on-shell Higgs boson decay amplitudes. In the decay channel to four leptons, couplings that modify the contact terms between the Higgs boson, the Z boson, and the left- or right-handed leptons, $\epsilon_{Z\ell,L}$ and $\epsilon_{Z\ell,R}$, are considered [170].

Various symmetries can be imposed that target different BSM scenarios. Four scenarios are considered here [170], with two independent pseudo-observables associated with each. In all cases, parameters associated with pseudo-observables that affect angular distributions, including $\epsilon_{ZZ}^{(CP)}$, $\epsilon_{Z\gamma}^{(CP)}$, $\epsilon_{\gamma\gamma}^{(CP)}$, are set to zero. The scenarios are:

1. **Linear EFT-inspired**, in which the Higgs boson is assumed to be part of an $\mathrm{SU}(2)_L$ doublet. Lepton flavor universality is imposed, and the parameters of interest are κ_{ZZ} vs. $\epsilon_{Z\ell_R}$. The requirements are made that $\epsilon_{Ze_{L,R}} = \epsilon_{Z\mu_{L,R}}$, $\epsilon_{Z\ell_L} = 2\epsilon_{Z\ell_L}$, and all other $\epsilon \to 0$.

2. **Flavor universal contact terms**, where the parameters of interest are $\epsilon_{Z\ell_L}$ vs. $\epsilon_{Z\ell_R}$, under the requirements that $\epsilon_{Ze_{L,R}} = \epsilon_{Z\mu_{L,R}}$, $\kappa_{ZZ} = 1$, and all other $\epsilon \to 0$. The first requirement implies that the interactions described by these contact terms have the same strength for electrons and muons.

3. **Flavor non-universal vector contact terms**, in which the parameters of interest are ϵ_{Ze_R} vs. $\epsilon_{Z\mu_R}$, and $\epsilon_{Ze_L} = \epsilon_{Ze_R}$, $\epsilon_{Z\mu_L} = \epsilon_{Z\mu_R}$, $\kappa_{ZZ} = 1$, and all other $\epsilon \to 0$ are required. The first two requirements impose that the helicity structure of the couplings is vector. Furthermore, lepton flavor universality can be violated in this scenario.

4. **Flavor non-universal axial contact terms**, where the parameters of interest are again ϵ_{Ze_R} vs. $\epsilon_{Z\mu_R}$. Here, the requirement is made that $\epsilon_{\ell_L} = -\epsilon_{\ell_R}$, while also requiring $\kappa_{ZZ} = 1$, and all other $\epsilon \to 0$. Here, the helicity structure of the couplings is axial. Again, lepton flavor universality violation is allowed.

In each of the bins of the m_{12} vs. m_{34} double differential distribution, the relative variation of the fiducial cross section as a function of the BSM couplings with respect to the SM couplings is calculated using MadGraph5_aMC@NLO. This is done for a grid of points in the BSM parameter space, for each of the four scenarios considered. The relative variations are fit to a 2D quadratic function in each case, which is then included in the likelihood used to set limits on the values of the couplings. The values are fit in the inclusive decay channel for the linear EFT-inspired and flavor universal scenarios, and in the $\ell\ell ee$ and $\ell\ell\mu\mu$ final states for the flavor non-universal scenarios.

The results are shown in Figure 9.1 and Table 9.1. In Figure 9.1, the observed 68% and 95% confidence intervals are provided on the modified couplings values for all four scenarios. The Standard Model predictions are shown, as are the observed best fit values. The corresponding 95% confidence intervals for the various parameters are provided in Table 9.1.

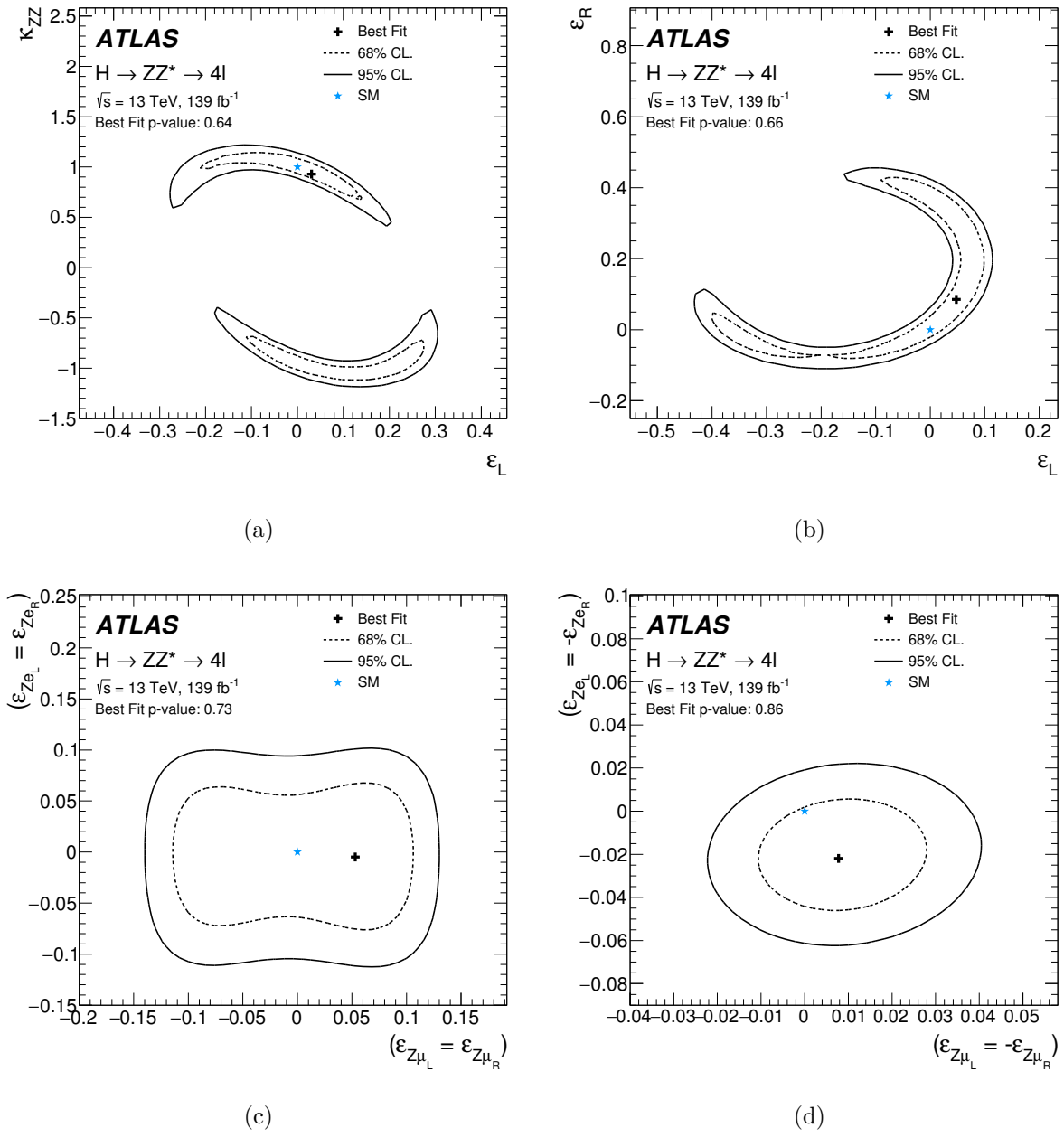

Figure 9.1. Observed limits at 68% (dashed lines) and 95% (solid lines) CL on modified Higgs boson decays in the Pseudo-Observables framework for the four scenarios considered: (a) linear EFT-inspired, (b) flavor universal contact terms, (c) flavor non-universal vector contact terms, and (d) flavor non-universal axial contact terms. For each scenario, the Standard Model predictions are indicated by the blue stars, while the Observed best fit values are indicated by the black plus signs. The p-values shown quantify the compatibility between the data and the m_{12} vs. m_{34} prediction that corresponds to the best fit value for the parameters of interest in each of the four scenarios considered.

Interpretation	Parameter best fit value	95% Confidence Interval
EFT-inspired	$\epsilon_L = 0.03$	$[-0.26, 0.18]$
	$\kappa_{ZZ} = 0.93$	$[0.50, 1.16]$
Flavour Non-Universal Vector	$\epsilon_{Ze} = 0.005$	$[-0.099, 0.083]$
	$\epsilon_{Z\mu} = 0.053$	$[-0.132, 0.115]$
Flavour Non-Universal Axial	$\epsilon_{Ze} = -0.021$	$[-0.056, 0.013]$
	$\epsilon_{Z\mu} = -0.008$	$[-0.016, 0.034]$

Table 9.1. Confidence intervals for three the Linear EFT-inspired, Flavour Non-Universal Vector and Flavour Non-Universal Axial scenarios from the Pseudo-Observables framework described previously. 1D exclusion intervals based on the observed 2D exclusion contours shown in Figure 9.1 are provided, where the observed limits for each parameter of interest are calculated while profiling the other parameters of interest. In the EFT-inspired scenario, limits are derived assuming $\kappa_{ZZ} \geq 0$.

9.2. Constraints on b- and c-quark Yukawa couplings

With the recent observations of the ttH production mode and the decay of the Higgs boson to two b-quarks [171–174], the Yukawa couplings of the Higgs to third generation quarks have been measured and found to be in agreement with SM prediction.

Following the establishment of the Yukawa couplings of third generation quarks to the Higgs boson are attempts to measure the Yukawa coupling of second generation quarks, specifically that of the heavier charm quark. Direct searches for $VH, H \to c\bar{c}$ face challenges of low branching ratios, for example in the $H \to J/\psi\gamma \to \mu^+\mu^-\gamma$ decay, and high QCD backgrounds, as in the case of $H \to c\bar{c}$ decay channel. It has been shown however, that it is possible to use the p_{T}^{H} spectrum to indirectly constrain quark Yukawa couplings to the Higgs boson [154].

Here, the results of the $p_{\mathrm{T}}^{4\ell}$ differential cross section measurements are used to constrain deviations in the couplings modifiers of the Higgs boson to b- and c-quarks, κ_b and κ_c, respectively, caused by potential BSM effects. This is done separately for three cases defined below, listed in order of increasing model dependence.

1. Modified fiducial cross sections in each bin of the $p_{\mathrm{T}}^{4\ell}$ distribution as well as a global normalization factor are fit to data.

2. Only modified fiducial cross sections in each bin of the $p_{\mathrm{T}}^{4\ell}$ distribution are fit to data, without the inclusion of the normalization factor in the likelihood. Here, the total cross section is fixed to the SM prediction, and only modifications of the $p_{\mathrm{T}}^{4\ell}$ shape induced by non-SM values of κ_b and κ_c are probed.

3. Modifications of the total width, and thus the branching ratio (BR), are encoded in the likelihood in addition to modifications of the total cross section and the differential $p_{\mathrm{T}}^{4\ell}$ shape.

In each case, the fiducial cross section in each $p_{\mathrm{T}}^{4\ell}$ bin is parameterized as a function of κ_b and κ_c, similarly to the method used in the Pseudo-Observables interpretation described previously in Section 9.1. Gluon-initiated process predictions were provided by the authors of

Ref. [154] and calculated using RadISH, while predictions for quark-initiated processes were generated using MadGraph5 and LHAPDF. Modified p_{T}^{H} distributions from gluon- and quark-initiated process are provided for modified values of κ_b and κ_c are shown in Figure 9.2. Theoretical uncertainties were evaluated by varying the renormalization and factorization scales by a factor of two up and down in the eight-point variation scheme. The configuration with the largest variation across $p_{\mathrm{T}}^{4\ell}$ bins is used to define the uncertainty, with an impact of roughly 20%.

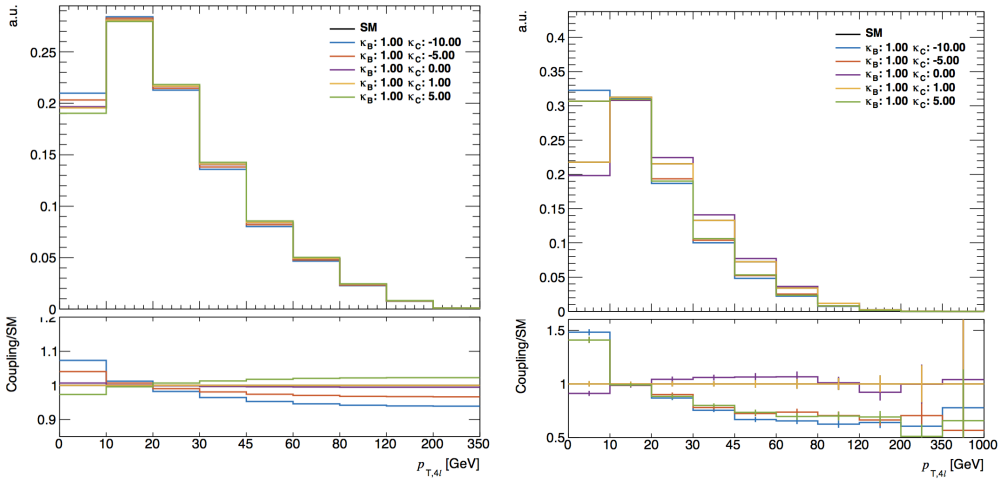

Figure 9.2. Predicted modifications to the p_{T}^{H} shape from gluon- (left) and quark- (right) initiated processes, for various modified values of κ_b and κ_c [157].

Results are provided in Figure 9.3 and Table 9.2 below, with limits on κ_c competetive with those from direct searches [175, 176]. All best fit values are in agreement with SM prediction.

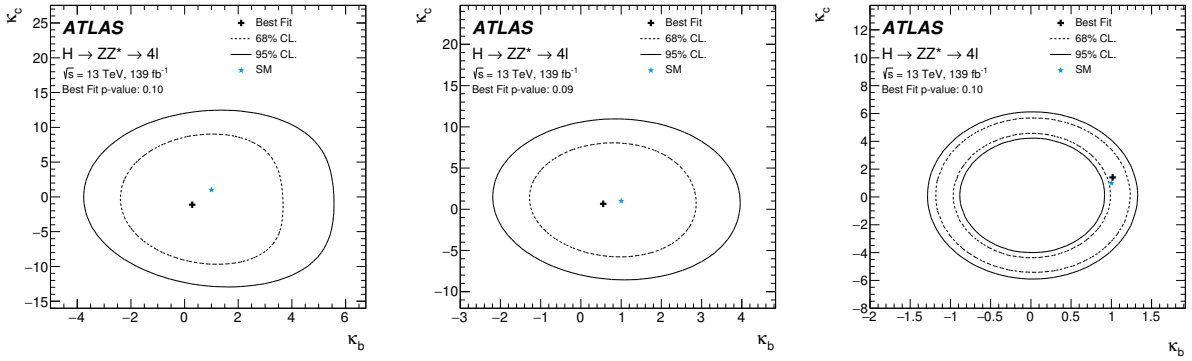

(a) (b) (c)

Figure 9.3. Observed limits at 95% CL on Yukawa the couplings modifiers κ_c and κ_b for the three scenarios considered: (a) only the p_{T}^H shape information is used to constrain the values of the couplings modifiers; (b) the predicted p_{T}^H differential cross section is used to constrain the values assuming the SM value of the total cross section; (c) both the prediction of the p_{T}^H differential cross section and the modification to the branching ratio due to the κ_c and κ_b values are used. The $p-$values provided quantify the compatibility between the data and the predictions that correspond to the best fit values of the couplings modifiers. The SM predictions are depicted by the blue stars while the observed best fit values are depicted by the black plus signs.

Interpretation	Parameter best fit value	95% Confidence Interval
Modifications to only p_{T}^H shape	$\kappa_c = -1.1$	$[-11.9, 10.6]$
	$\kappa_b = 0.29$	$[-3.26, 4.58]$
Modifications to p_{T}^H predictions	$\kappa_c = 0.66$	$[-7.58, 9.39]$
	$\kappa_b = 0.55$	$[-1.86, 3.40]$

Table 9.2. Confidence intervals for κ_c and κ_b. 1D exclusion intervalues are provided based on the 2D exclusion contours for interpretations where modification to the p_{T}^H shape and predictions are considered. The observed limits are calculated while profiling the other parameter of interest.

CHAPTER 10

Conclusions

Measurements of the inclusive and differential fiducial cross sections of the Higgs boson in the $H \to ZZ^* \to 4\ell$ decay channel have been presented. The measurements were performed using proton−proton collision data from the LHC, collected between 2015 and 2018, corresponding to an integrated luminosity of 139 fb^{-1}. Despite the low branching ratio, the $H \to ZZ^* \to 4\ell$ decay has a fully reconstructable final state and low backgrounds, making it an excellent channel in which to perform Higgs precision measurements to test our understanding of the Standard Model.

In this thesis, cross section measurements were made within the fiducial region of the ATLAS detector. These were done both inclusively, as well as differentially, in bins of observables that probe both the Higgs boson production and decay.

The Higgs boson inclusive fiducial cross sections include σ_{comb}, the combination of the four individual decay channels assuming Standard Model relative branching fractions, measured to be 3.28 ± 0.30 (stat.) ± 0.11 (syst.) fb, as well as σ_{sum}, the sum of the four decay channels, measured to be 3.18 ± 0.31 (stat.) ± 0.11 (syst.) fb. Both are in agreement with the Standard Model prediction of 3.41 ± 0.18 fb. The total cross section has also been measured, extrapolating to the full phase space, which introduces additional model dependency arising from the acceptance factors used in the extrapolation. This cross section, σ_{tot}, was measured to be 53.5 ± 4.9 (stat.) ± 2.1 (syst.), also in agreement with the Standard Model prediction of 55.8 ± 2.8 fb, within the uncertainties.

Fiducial cross sections in the four individual decay channels, 4μ, $4e$, $2e2\mu$, and $2\mu2e$ were also measured, as were the same- and opposite-flavor decays, 4μ+$4e$ and $2e2\mu$+$2\mu2e$, and were also found to be in good agreement with Standard Model predictions.

The differential cross sections were generally found to be in good agreement with Standard Model predictions as well, though some fluctuations were observed causing measured p-values to show poor compatibility in a couple of measurements. In the last bin of the $\frac{d\sigma}{dp_{\mathrm{T}}^{4\ell}}$ distribution there were zero events observed, and an upper limit of 27 ab at 95% CL_s was set. The $\frac{d\sigma}{dp_{\mathrm{T}}^{4\ell}}$ distribution is sensitive to deviations caused by potential particles beyond the Standard Model as well as possible anomolous couplings of Standard Model particles to the Higgs boson. As no significant deviation from the Standard Model prediction was observed, measured cross sections in $p_{\mathrm{T}}^{4\ell}$ bins were used to set limits on Yukawa couplings modifiers between b- and c-quarks and the Higgs boson. The most stringent limits place κ_b between -1.85 and 3.40, and κ_c between -7.58 and 9.39 at the 95% confidence level, competitive with current direct $H \to c\bar{c}$ searches [175,176]. The Standard Model prediction for each couplings modifier is 1.

The $\frac{d^2\sigma}{dm_{12}dm_{34}}$ cross section measurement is also used to set limits in a beyond the Standard Model interpretation, using the framework of Pseudo-Observables [155]. Limits are set on contact terms between the Higgs boson and the intermediate Z bosons and four leptons. Best-fit values for all four scenarios considered were found to be compatible with Standard Model predictions.

Looking to the future, the expected increases in data will be useful in studying distributions that are still lacking in statistics. For example, many BSM models predict deviations in the high p_{T}^{H} phase space region; however, in the Run 2 dataset, zero events were observed in the last bin in $p_{\mathrm{T}}^{4\ell}$. Many other differential distributions will also benefit from an increase in events. The four lepton decay channel is still limited by statistics rather than systematic effects, and will continue to be so until the end of Run 3. The addition of data in future LHC runs will be invaluable in measuring these observables with higher precision, and gaining an even better understanding of the Standard Model and potential physics beyond its scope.

Appendix A

Liquid Argon Calibration Infrastructure

As mentioned in Section 3.2.3.2, regular calibrations of the Liquid Argon (LAr) sub-detector system are taken in order to determine parameters used in the determination of optimal filtering coefficients used for the energy calculations on the digital signal processors. My work in the LAr online software group was on development and maintenance of the infrastructured used to take these calibrations.

Calibrations can are run using a Java-based graphical user interface, referred to as the 'Calibration Panel', to send signals to configure the Calibration boards (housed in the Front End Crates, or FECs). These boards are configured using text files that specify which calibration lines will be pulsed. Based on these, signals are sent from the Calibration boards directly to the Front End Boards, or FEBs, in order to determine calibration constants needed for calculating optimal filtering coefficients, as described in Section 3.2.3.1.

These patterns typically pulse entire Trigger Towers, as defined in Section 3.2.3.1, at a time. In preparation for the Phase-I upgrades for the LHC Run 3, I developed new calibration patterns aimed at pulsing Super Cells. Super Cells are finer granularity groups of calorimeter cells that will send information to the Level-1 trigger during Run 3, allowing for better discrimination between calorimeter objects at the lowest level trigger.

Calibrations that are done frequently are performed using a Python-based user interface that runs the Java-based code behind-the-scenes. The tool, takeCalib, was developed by Murrough Landon, from the Level 1 Calorimeter group. Much of my work on LAr was in modifying this tool to work with the calibrations that are taken frequently by LAr experts. I added additional calibrations to this tool, improved the functionality, and ported the tool to work outside of the ATLAS Point 1 network on the Testbed Network. Here, the tool was

able to be used by experts working at the LAr Electronics Maintenance Facility, or EMF, where LAr mainains a Half Front End Crate along with the full readout system for doing tests and validation studies. A screenshot of the takeCalib tool is shown in Figure A.1.

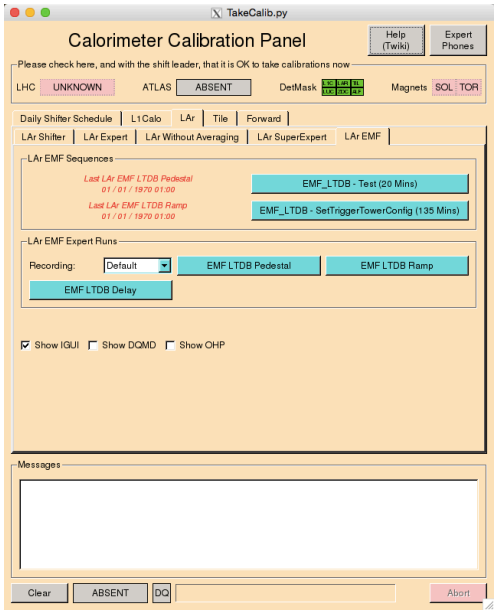

Figure A.1. Screen shot of the takeCalib tool used for taking calibrations with the Liquid Argon Calorimeter subdetector system.

Appendix B

LAr operations work

During the running periods of the LHC, the ATLAS control room (ACR) is staffed by eight 'ACR shifters' who monitor the detector status and operations during an eight hour shift, notifying on-call experts of any issues that arise during data-taking. Of the eight shifters in the ACR at a given time, the 'Calo/FWD' shifter is responsible for monitoring the status of the calorimeters and foward detectors. This person is responsible for verifying that the run parameters for these subsystems are properly set for each run, that there are no hardware or data-taking issues with any of the subsystems, and that calibrations are taken at regular intervals between runs. When I first joined the ATLAS collaboration, I took a series of shifts at the Calo/FWD desk in the ACR. These were blocks of three or four consecutive days, with an eight hour shift in the ACR each day.

After taking several of these shift blocks, I was promoted to a Super Shifter. This is a position particular to the Calo/FWD desk that involves overseeing the group of people qualified to sign up for Calo/FWD desk shifts. The Super Shifters train desk shifters, are available to cover shifts if needed, and generally provide support. I was given this position at a time when the training course and associated documentation and slides needed to be updated, so in addition, I overhauled the training course, rewrote the shifter exams, and updated the documentation. I trained roughly 30 people who took shifts at the Calo/FWD desk.

After working as a Super Shifter for some time as well as working with the LAr online software group, as discussed in Appendix A, I began to take software expert on-call shifts for the LAr Calorimeters (referred to henceforth as simply 'LAr'). This position is a position related to data acquisition and software issuses related to LAr that might arise during data

taking. These are week-long, 24/7 on-call shifts where any issues with data-taking that come from LAr are investigated and diagnosed as quickly as possible in order to minimize lost data. In addition, I provided support for any special tests to be done related to LAr and any special calibrations that were needed.

After gaining experience as a software on-call expert, I began taking LAr Run Coordinator (RC) shifts. The RC oversees LAr operations and is responsible for making the final decision when there is any issue with data taking. The RC represents the LAr operations team in the daily and weekly ATLAS operations meetings, and organizes the LAr operations plans for the week, including scheduling special runs, tests, or calibrations, as needed.

Appendix C

Bias Studies

For each unfolding method - bin-by-bin and matrix - the biases associated with the unfolding uncertainty were studied.

The signal composition bias tests described in the following section were used to test extreme cases of variation in the ggF and VBF signal cross sections, or XS. Because of the extreme and unrealistic scenarios, no uncertainties were assigned from these studies.

Results for the $p_{\mathrm{T}}^{4\ell}$ and N_{jets} differential variables are shown here, where $p_{\mathrm{T}}^{4\ell}$ represents a variable which has a diagonal response matrix and therefore should behave quite well. Meanwhile, N_{jets} has considerably larger migrations and so should be more sensitive to potential biases introduced by the unfolding method.

C.1. Signal Composition Bias Tests

The aim of the signal composition bias tests was to study the effects that assumptions on the signal composition have on the unfolding procedure. What is called the nominal case here assumes production mode cross section predictions provided by the LHC Cross Section Working Group (LHCXSWG) [30]. Response matrices and correction factors are evaluated using simulation with these assumptions built in. Subsequently, the response matrices and correction factors were again evaluated in variations, by scaling either the ggF and VBF cross sections. The ggH cross section was scaled up to $\pm 10\%$ in steps of 2%, while the VBF cross section was scaled up to $\pm 50\%$ in steps of 10%. In addition to these points, the cross sections were also scaled by the theoretical unceratinty on the cross sections, which are -7.4% and $+5.6\%$, and $\pm 2.1\%$, for ggF and VBF, respectively.

Asimov data [1] (with the nominal composition) was unfolded using correction factors and response matrices which were calculated using the scaled cross sections, and the resulting fits were compared to the nominal Asimov results. The nominal migration matrices as well as the migration matrices for the most extreme scaling cases (ggF scaled up by +10% of the expected cross section and VBF scaled up by +50%) are shown in Figures C.1 and C.4 for N_{jets} and $p_{\text{T}}^{4\ell}$, respectively. The corresponding response matrices are shown in Figures C.2 and C.5.

Results of the tests are shown in Figures C.3-C.8, where the correction factor unfolding is show on the top and matrix is shown on the bottom. On the left are the ratios of the fit values obtained using the scaled XS unfolding inputs to the fit value obtained using the nominal unfolding inputs, and on the right are the percent errors on these fits compared to the percent error on the nominal.

[1] The Asimov dataset is a single representative dataset that can be used to replace an ensemble **??**.

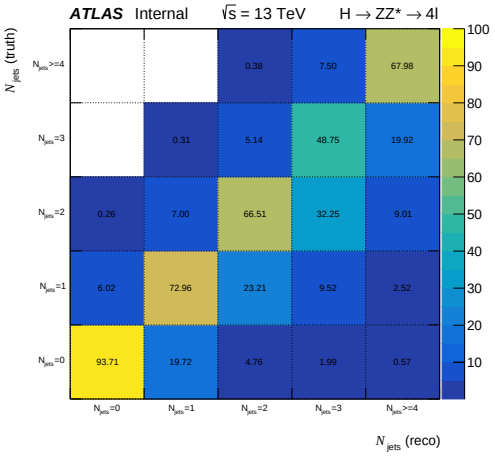

(a) Nominal response matrix

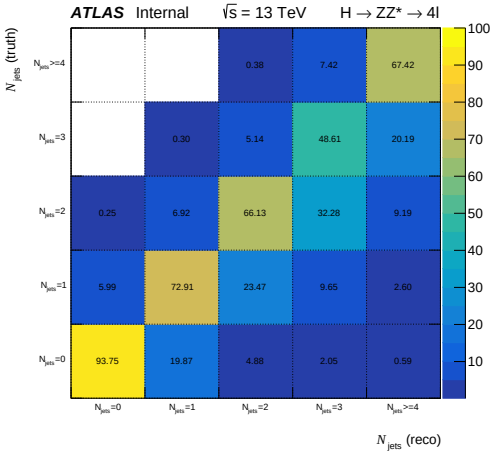

(b) ggF XS scaled by +10%

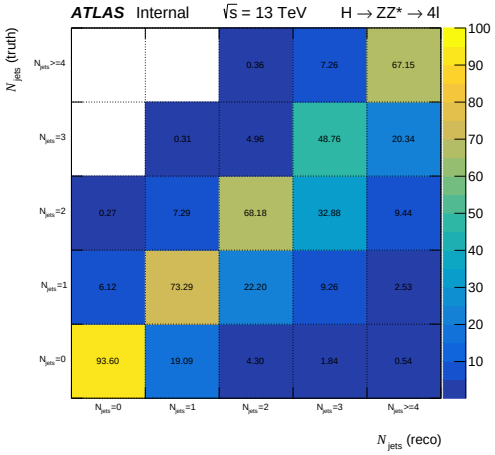

(c) VBF XS scaled by +50%

Figure C.1. Migration matrices for N_{jets} for the nominal cross sections as well as the two most extreme cases of scaled cross sections - ggF scaled up by +10% of the expected cross section and VBF scaled up by +50%.

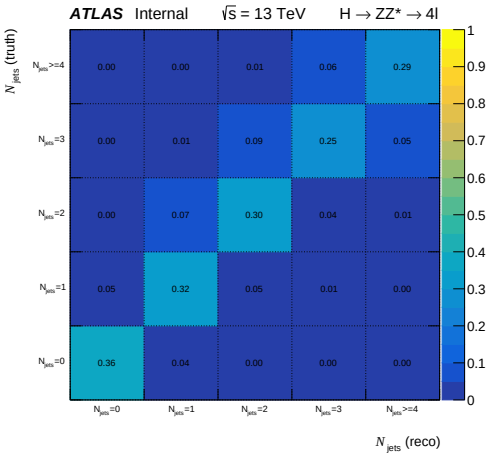

(a) Nominal response matrix

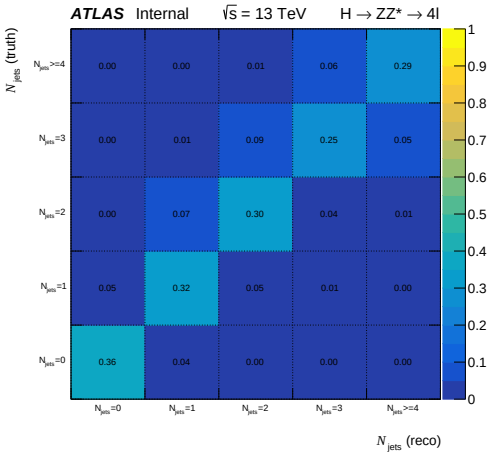

(b) ggF XS scaled by +10%

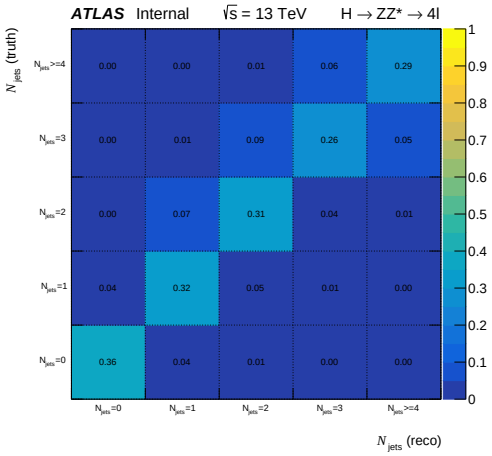

(c) VBF XS scaled by +50%

Figure C.2. Response matrices for N_{jets} for the nominal cross sections as well as the two most extreme cases of scaled cross sections - ggF scaled up by +10% of the expected cross section and VBF scaled up by +50%.

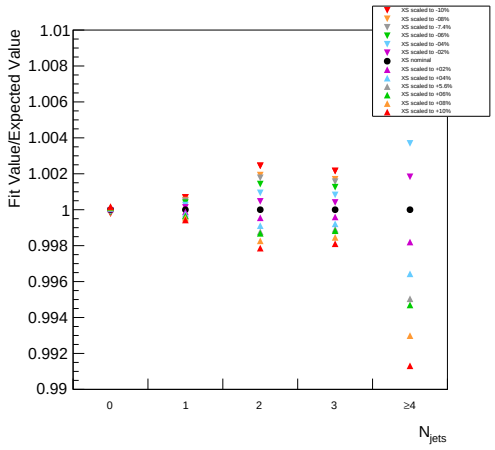

(a) Fit/Nominal Fit - c_F unfolding

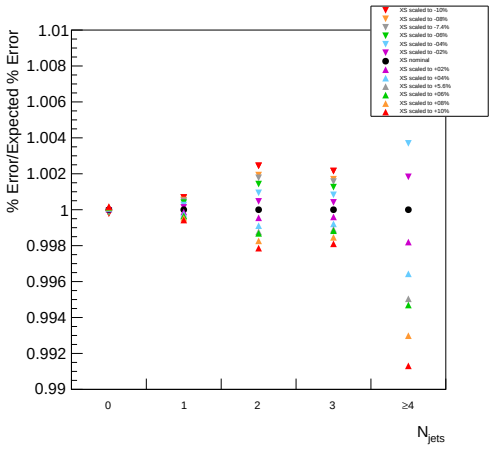

(b) % Error/Nominal % Error - c_F unfolding

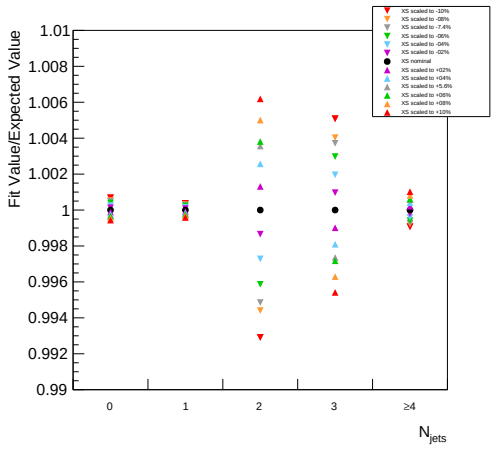

(c) Fit/Nominal Fit - matrix unfolding

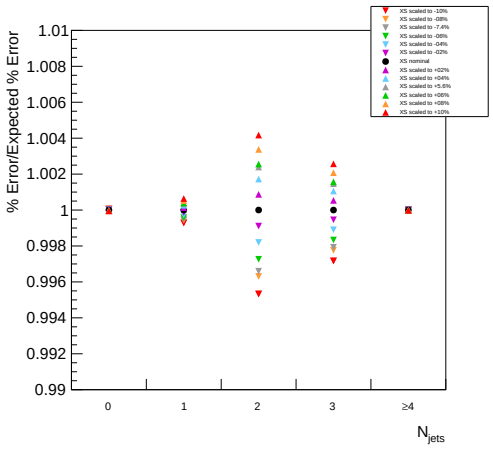

(d) % Error/Nominal % Error - matrix unfolding

Figure C.3. Cross sections fit from nominal Asimov data fit using bin-by-bin correction factor unfolding where the correction factors are calculated for various scalings of the ggF XS, divided by XS fit from nominal Asimov data fit using the LHCXS working group XS for all production modes when calculating correction factors (top left). Percent errors on the fits using scaled ggF XS inputs divided by the percent error on the nominal fit (top right). Similarily, the bottom two plots show the same distibutions using the matrix unfolding method rather than correction factor.

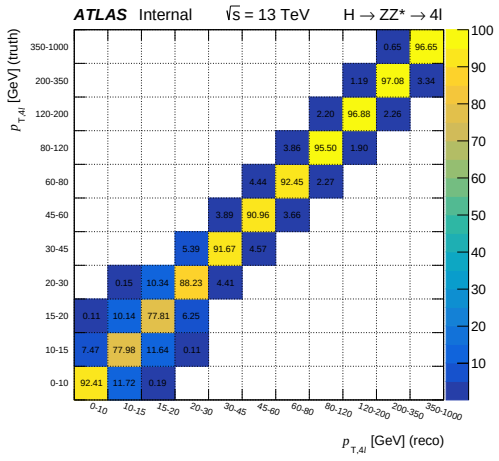

(a) Nominal response matrix

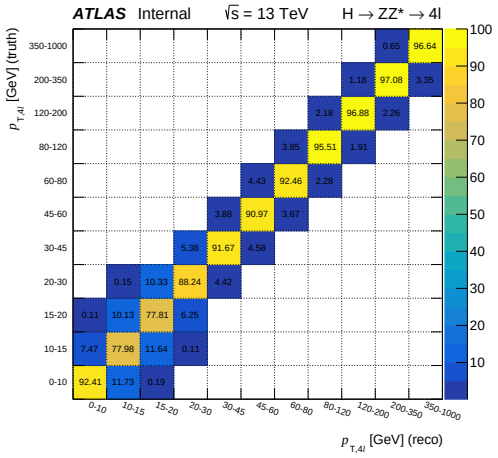

(b) ggF XS scaled by +10%

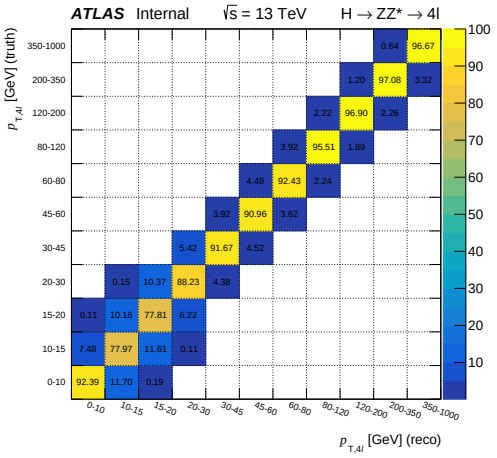

(c) VBF XS scaled by +50%

Figure C.4. Migration matrices for $p_{\mathrm{T}}^{4\ell}$ for the nominal cross sections as well as the two most extreme cases of scaled XS - ggF scaled up by +10% of the expected cross section and VBF scaled up by +50%.

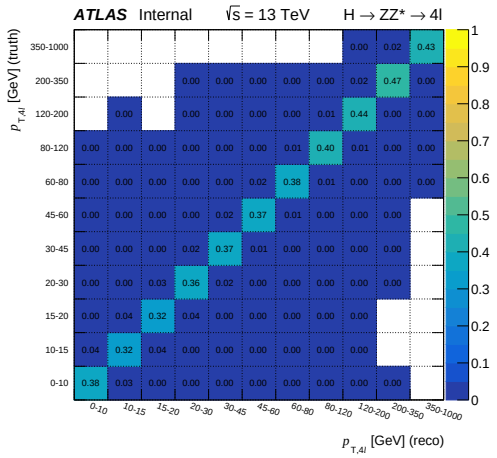

(a) Nominal response matrix

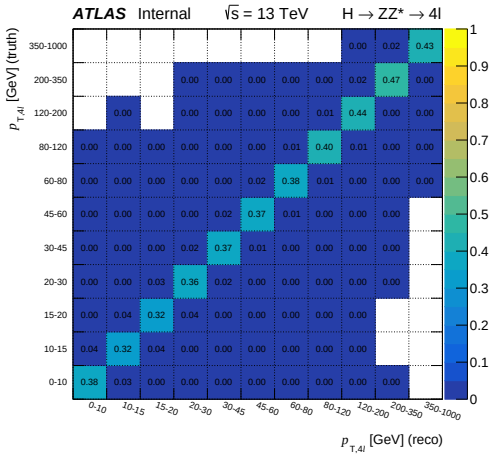

(b) ggH XS scaled by +10%

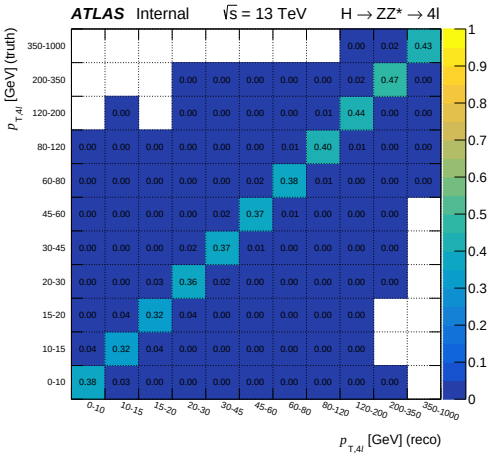

(c) VBF XS scaled by +50%

Figure C.5. Response matrices for $p_{\mathrm{T}}^{4\ell}$ for the nominal cross sections as well as the two most extreme cases of scaled XS - ggF scaled up by +10% of the expected cross section and VBF scaled up by +50%.

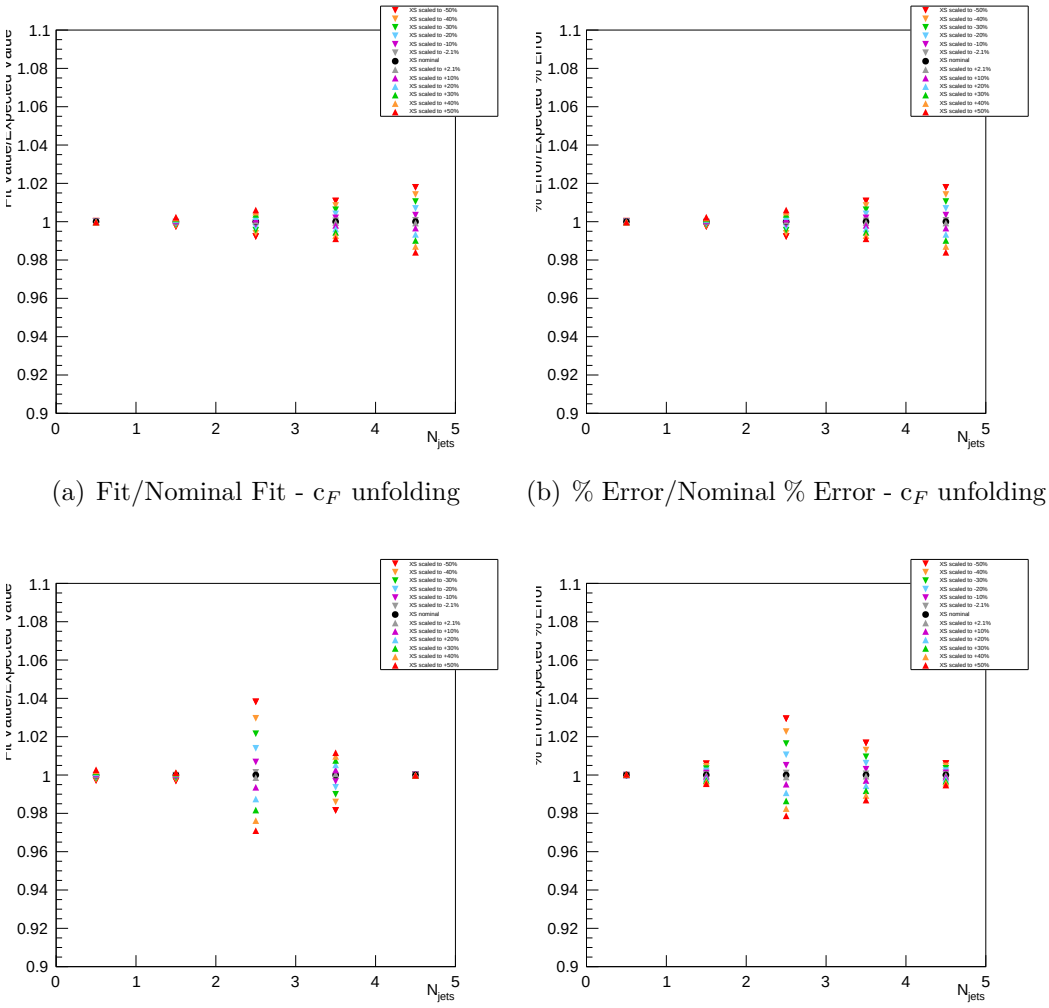

(a) Fit/Nominal Fit - c_F unfolding

(b) % Error/Nominal % Error - c_F unfolding

(c) Fit/Nominal Fit - matrix unfolding

(d) % Error/Nominal % Error - matrix unfolding

Figure C.6. Cross sections fit from nominal Asimov data fit using bin-by-bin correction factor unfolding where the correction factors are calculated for various scalings of the VBF XS, divided by XS fit from nominal Asimov data fit using the LHCXS working group XS for all production modes when calculating correction factors (top left). Percent errors on the fits using scaled VBF XS inputs divided by the percent error on the nominal fit (top right). Similarily, the bottom two plots show the same distibutions using the matrix unfolding method rather than correction factor.

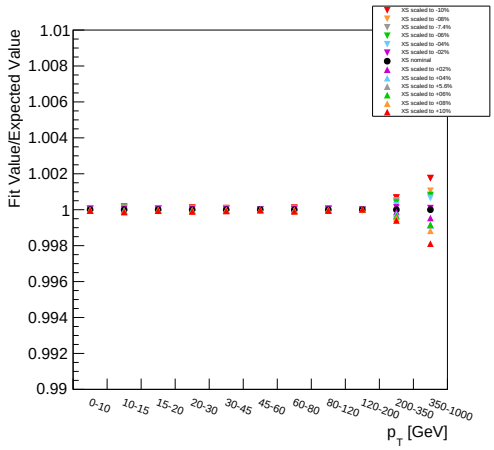

(a) Fit/Nominal Fit - c_F unfolding

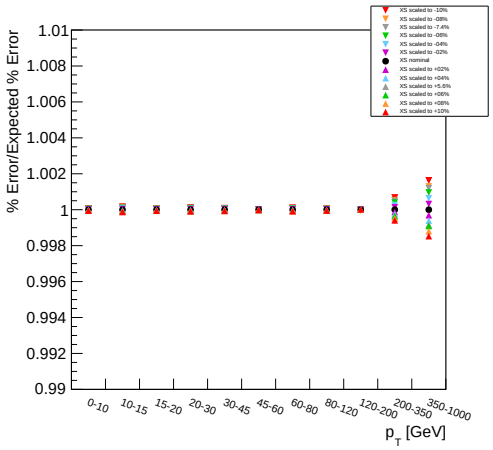

(b) % Error/Nominal % Error - c_F unfolding

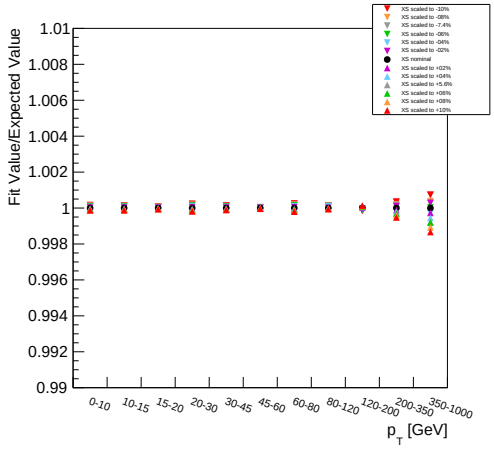

(c) Fit/Nominal Fit - matrix unfolding

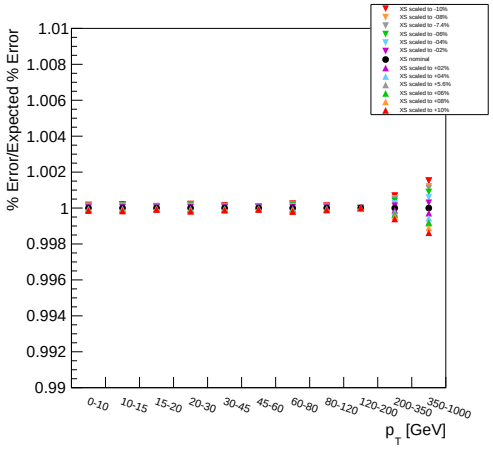

(d) % Error/Nominal % Error - matrix unfolding

Figure C.7. Cross sections fit from nominal Asimov data fit using bin-by-bin correction factor unfolding where the correction factors are calculated for various scalings of the ggF XS, divided by XS fit from nominal Asimov data fit using the LHCXS working group XS for all production modes when calculating correction factors (top left). Percent errors on the fits using scaled ggF XS inputs divided by the percent error on the nominal fit (top right). Similarily, the bottom two plots show the same distibutions using the matrix unfolding method rather than correction factor.

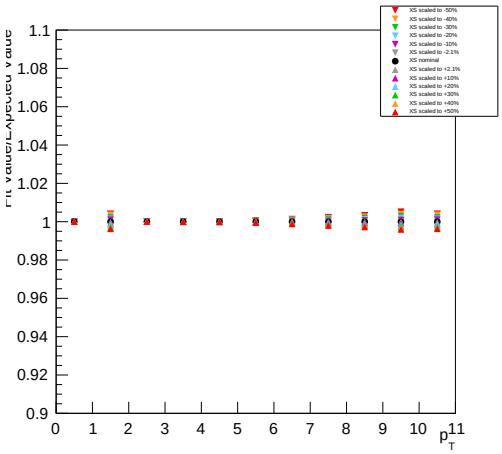

(a) Fit/Nominal Fit - c_F unfolding

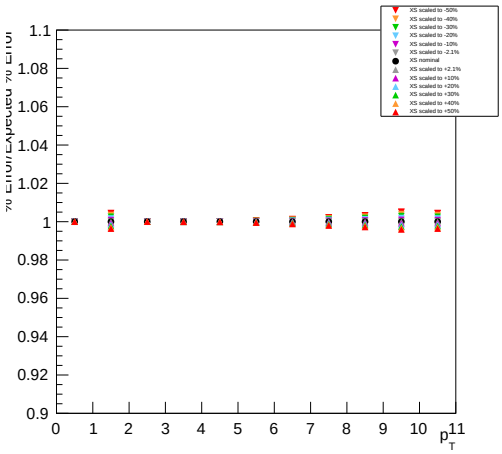

(b) % Error/Nominal % Error - c_F unfolding

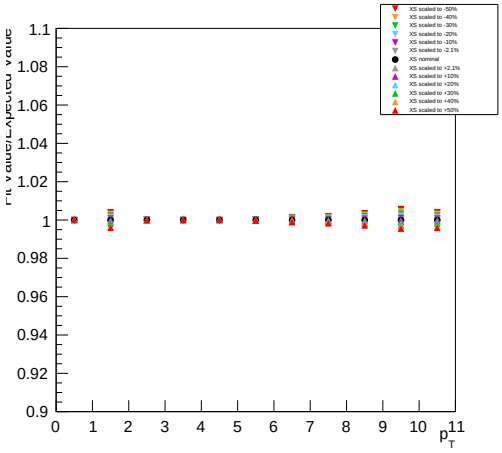

(c) Fit/Nominal Fit - matrix unfolding

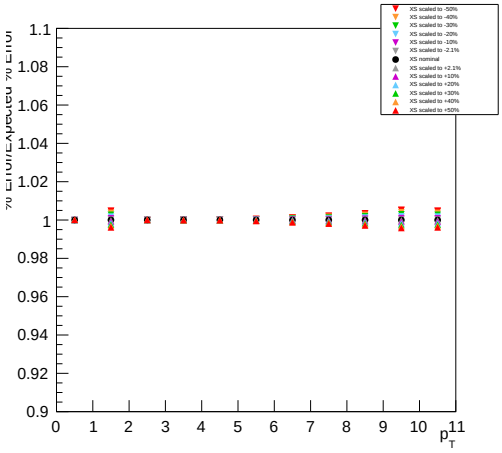

(d) % Error/Nominal % Error - matrix unfolding

Figure C.8. Cross sections fit from nominal Asimov data fit using bin-by-bin correction factor unfolding where the correction factors are calculated for various scalings of the VBF XS, divided by XS fit from nominal Asimov data fit using the LHCXS working group XS for all production modes when calculating correction factors (top left). Percent errors on the fits using scaled VBF XS inputs divided by the percent error on the nominal fit (top right). Similarily, the bottom two plots show the same distibutions using the matrix unfolding method rather than correction factor.

It can be seen that the response matrix unfolding is more sensitive to changes in the production mode dependent event topology in bins with higher migrations, such as the 2-jet bin in N_{jets}, while the correction factor unfolding is more sensitive in bins with lower numbers of expected events. In both cases, the variation in fitted cross sections are small, particularly compared to the production mode cross section uncertainties and the overall expected uncertainty on the measurement. Furthermore, in the p_T distribution where the matrices are largely diagonal, the variation in fitted cross sections are completely negligible. Therefore it was decided that the production mode uncertainty could be added as a systematic and would cover any potential bias introduced by the unfolding method due to composition.

BIBLIOGRAPHY

[1] T. S. Kuhn, *The structure of scientific revolutions*. University of Chicago Press, Chicago, 1970.

[2] P. W. Higgs, *Broken Symmetries, Massless Particles and Gauge Fields*, *Phys. Lett.* **12** (1964) 132–133.

[3] P. W. Higgs, *Broken symmetries and the masses of gauge bosons*, *Phys. Rev. Lett.* **13** (Oct, 1964) 508–509.

[4] F. Englert and R. Brout, *Broken symmetry and the mass of gauge vector mesons*, *Phys. Rev. Lett.* **13** (Aug, 1964) 321–323.

[5] ATLAS Collaboration, *Observation of a new particle in the search for the standard model higgs boson with the atlas detector at the lhc*, *Physics Letters B* **716** (2012) 1 – 29.

[6] CMS Collaboration, *Observation of a new boson at a mass of 125 gev with the cms experiment at the lhc*, *Physics Letters B* **716** (2012) 30 – 61.

[7] P. A. Dirac, *The Quantum Theory of the Emission and Absorption of Radiation*, *Proceedings of the Royal Society of London. Series A* **114** (1927) 243–265.

[8] E. Fermi, *Tentativo di una teoria dei raggi β*, *Il Nuovo Cimento (1924-1942)* **11** (Sep, 2008) 1.

[9] S. Weinberg, *A model of leptons*, *Phys. Rev. Lett.* **19** (Nov, 1967) .

[10] S. L. Glashow, *The renormalizability of vector meson interactions*, *Nucl. Phys.* **10** (1959) .

[11] A. Salam and J. C. Ward, *Weak and electromagnetic interactions*, *Il Nuovo Cimento (1955-1965)* **11** (Feb, 1959) .

[12] O. W. Greenberg, *Spin and Unitary Spin Independence in a Paraquark Model of Baryons and Mesons*, *Phys. Rev. Lett.* **13** (1964) .

[13] M. Y. Han and Y. Nambu, *Three Triplet Model with Double SU(3) Symmetry*, *Phys. Rev.* **139** (1965) .

[14] M. B. Robinson, K. R. Bland, G. B. Cleaver and J. R. Dittmann, *A Simple Introduction to Particle Physics. Part I - Foundations and the Standard Model*, 0810.3328.

[15] H. J. Lipkin, *Lie groups for pedestrians*. Dover books on physics. Dover, New York, NY, 2002.

[16] I. J. R. Aitchison and A. J. G. Hey, *Gauge theories in particle physics*. Institute of Physics Pub., 4 ed., 2003.

[17] M. E. Peskin and D. V. Schroeder, *An Introduction to quantum field theory*. Addison-Wesley, Reading, USA, 1995.

[18] K. G. Wilson, *Confinement of quarks*, *Phys. Rev. D* **10** (Oct, 1974) 2445–2459.

[19] U. . C. LHC, *The standard model and beyond*, 2016.

[20] D. J. Gross, *The role of symmetry in fundamental physics*, *Proceedings of the National Academy of Sciences* **93** (1996) 14256–14259, [https://www.pnas.org/content/93/25/14256.full.pdf].

[21] I. Kleiner, *A History of Abstract Algebra*. Dover books on physics. Birkhauser Boston, 2007, https://doi.org/10.1007/978-0-8176-4685-1.

[22] E. Noether, *Invariant variation problems*, 1918. 10.1080/00411457108231446.

[23] A. Djouadi, *The Anatomy of electro-weak symmetry breaking. I: The Higgs boson in the standard model*, 2008. 10.1016/j.physrep.2007.10.004.

[24] J. Goldstone, *Field Theories with Superconductor Solutions*, *Nuovo Cim.* **19** (1961) 154–164.

[25] H. Yukawa, *On the Interaction of Elementary Particles. I*, *Progress of Theoretical Physics Supplement* **1** (01, 1955) 1–10, [http://oup.prod.sis.lan/ptps/article-pdf/doi/10.1143/PTPS.1.1/5310694/1-1.pdf].

[26] S. Höche, *Introduction to parton-shower event generators*, in *Proceedings, Theoretical Advanced Study Institute in Elementary Particle Physics: Journeys Through the Precision Frontier: Amplitudes for Colliders (TASI 2014): Boulder, Colorado, June 2-27, 2014*, pp. 235–295, 2015. 1411.4085. DOI.

[27] ATLAS Collaboration collaboration, *Standard Model Summary Plots Summer 2019*, Tech. Rep. ATL-PHYS-PUB-2019-024, CERN, Geneva, Jul, 2019.

[28] U. of Zurich, *Higgs boson production feynman diagrams*, 2019.

[29] *The higgs boson's shadow*, May, 2017.

[30] LHC Higgs Cross Section Working Group collaboration, J. R. Andersen et al., *Handbook of LHC Higgs Cross Sections: 3. Higgs Properties*, 1307.1347.

[31] Particle Data Group collaboration, M. T. et al. (Particle Data Group)*Phys. Rev. D* **98** (Aug, 2018) 030001.

[32] LHC Higgs Cross Section Working Group collaboration, D. de Florian, C. Grojean, F. Maltoni, C. Mariotti, A. Nikitenko, M. Pieri et al., *Handbook of LHC Higgs Cross Sections: 4. Deciphering the Nature of the Higgs Sector*. CERN Yellow Reports: Monographs. Oct, 2016, 10.23731/CYRM-2017-002.

[33] CERN, *LHC description*, 2019.

[34] B.Salvachua, *Accelerators*, 2019.

[35] R. Bruce, N. Fuster-Martínez, A. Mereghetti, D. Mirarchi and S. Redaelli, *Review of LHC Run 2 Machine Configurations*, 2019.

[36] ATLAS Collaboration, "Luminosity Public Results Run 2."

[37] *ATLAS Experiment at CERN, Detector and Technology*, August, 2017.

[38] ATLAS Collaboration, *The ATLAS Experiment at the CERN Large Hadron Collider*, *JINST* **3** (2008) S08003. 437 p.

[39] G. e. a. Aad, *ATLAS Pixel Detector Electronics and Sensors*, tech. rep., 2008. 10.1088/1748-0221/3/07/P07007.

[40] ATLAS Collaboration collaboration, M. Capeans, G. Darbo, K. Einsweiller, M. Elsing, T. Flick, M. Garcia-Sciveres et al., *ATLAS Insertable B-Layer Technical Design Report*, Tech. Rep. CERN-LHCC-2010-013. ATLAS-TDR-19, Sep, 2010.

[41] ATLAS Collaboration collaboration, *ATLAS inner detector: Technical Design Report, 1*. Technical Design Report ATLAS. CERN, Geneva, 1997.

[42] ATLAS collaboration collaboration, A. La Rosa, *ATLAS Pixel Detector: Operational Experience and Run-1 to Run-2 Transition*, Tech. Rep. arXiv:1410.6347. ATL-INDET-PROC-2014-007, CERN, Geneva, Oct, 2014. 10.22323/1.227.0001.

[43] ATLAS collaboration, G. Aad et al., *Operation and performance of the ATLAS semiconductor tracker*, *JINST* **9** (2014) P08009, [1404.7473].

[44] A. Vogel, *ATLAS Transition Radiation Tracker (TRT): Straw Tube Gaseous Detectors at High Rates*, Tech. Rep. ATL-INDET-PROC-2013-005, CERN, Geneva, Apr, 2013.

[45] ATLAS Collaboration, "Public TRT Plots for Collision Data."

[46] R. Schaffer, *From LAr Calorimeter to Higgs Mass*, 2014.

[47] P. Krieger, *The atlas liquid argon calorimeter: construction, integration, commissioning and performance from selected particle beam test results*, in *IEEE Nuclear Science Symposium Conference Record, 2005*, vol. 2, pp. 1029–1033, Oct, 2005. DOI.

[48] ATLAS Collaboration, "LAr Public Results Run 2."

[49] ATLAS Collaboration collaboration, *ATLAS liquid-argon calorimeter: Technical Design Report*. Technical Design Report ATLAS. CERN, Geneva, 1996.

[50] ATLAS collaboration, N. Nikiforou, *Performance of the ATLAS Liquid Argon Calorimeter after three years of LHC operation and plans for a future upgrade*, in *Proceedings, 3rd International Conference on Advancements in Nuclear Instrumentation Measurement Methods and their Applications (ANIMMA 2013): Marseille, France, June 23-27, 2013*, 2013. 1306.6756. DOI.

[51] ATLAS Collaboration collaboration, *ATLAS tile calorimeter: Technical Design Report*. Technical Design Report ATLAS. CERN, Geneva, 1996.

[52] ATLAS Collaboration collaboration, ATLAS Collaboration, *Performance of the ATLAS muon trigger in pp collisions at $\sqrt{s}$ =8 TeV. Performance of the ATLAS muon trigger in pp collisions at $\sqrt{s} = 8$ TeV*, *Eur. Phys. J. C* **C75** (Aug, 2014) 120. 19 p.

[53] ATLAS collaboration, ATLAS Collaboration, *Commissioning of the ATLAS Muon Spectrometer with Cosmic Rays*, *Eur. Phys. J.* **C70** (2010) 875–916, [1006.4384].

[54] ATLAS Collaboration collaboration, *ATLAS muon spectrometer: Technical Design Report*. Technical Design Report ATLAS. CERN, Geneva, 1997.

[55] ATLAS Collaboration, "Public Muon Spectrometer Plots for Collision Data."

[56] ATLAS Collaboration, *The level-1 trigger muon barrel system of the atlas experiment at cern*, *JINST* **4** (2009) P04010.

[57] ATLAS Collaboration, "L1Muon Trigger Public Results Run 2."

[58] ATLAS Collaboration collaboration, D. Zanzi, *The ATLAS Trigger in 2017 and 2018: Developments and Performance*, Tech. Rep. ATL-DAQ-PROC-2018-031, CERN, Geneva, Nov, 2018.

[59] R. Fruhwirth, *Application of kalman filtering to track and vertex fitting*, *Nuclear Instruments and Methods in Physics Research Section A: Accelerators, Spectrometers, Detectors and Associated Equipment* **262** (1987) 444 – 450.

[60] ATLAS Collaboration collaboration, *Performance of the ATLAS Inner Detector Track and Vertex Reconstruction in the High Pile-Up LHC Environment*, Tech. Rep. ATLAS-CONF-2012-042, CERN, Geneva, Mar, 2012.

[61] ATLAS Collaboration, *Electron efficiency measurements in 2017 data and electron identification discriminating variables from 2016 data*, 2019.

[62] ATLAS collaboration, ATLAS Collaboration, *Electron reconstruction and identification in the ATLAS experiment using the 2015 and 2016 LHC proton-proton collision data at $\sqrt{s}$ = 13 TeV*, *Eur. Phys. J.* **C79** (2019) 639, [1902.04655].

[63] ATLAS collaboration, G. Aad et al., *Electron and photon performance measurements with the ATLAS detector using the 2015–2017 LHC proton-proton collision data*, *JINST* **14** (2019) P12006, [1908.00005].

[64] ATLAS Collaboration, *Muon identification and reconstruction efficiencies in full run-2 dataset*, 2019.

[65] S. D. Ellis and D. E. Soper, *Successive combination jet algorithm for hadron collisions*, *Phys. Rev.* **D48** (1993) 3160–3166, [hep-ph/9305266].

[66] ATLAS collaboration, M. Aaboud et al., *Jet reconstruction and performance using particle flow with the ATLAS Detector*, *Eur. Phys. J.* **C77** (2017) 466, [1703.10485].

[67] *Monte Carlo Calibration and Combination of In-situ Measurements of Jet Energy Scale, Jet Energy Resolution and Jet Mass in ATLAS*, Tech. Rep. ATLAS-CONF-2015-037, CERN, Geneva, Aug, 2015.

[68] ATLAS Collaboration, "Flavour Tagging Performance."

[69] GEANT4 collaboration, S. Agostinelli et al., *GEANT4: A Simulation toolkit*, *Nucl. Instrum. Meth. A* **506** (2003) 250.

[70] S. Alioli, P. Nason, C. Oleari and E. Re, *A general framework for implementing NLO calculations in shower Monte Carlo programs: the POWHEG BOX*, *JHEP* **06** (2010) 043, [1002.2581].

[71] S. Frixione, P. Nason and C. Oleari, *Matching NLO QCD computations with parton shower simulations: the POWHEG method*, *JHEP* **11** (2007) 070, [0709.2092].

[72] P. Nason, *A new method for combining NLO QCD with shower Monte Carlo algorithms*, *JHEP* **11** (2004) 040, [hep-ph/0409146].

[73] E. Bagnaschi, G. Degrassi, P. Slavich and A. Vicini, *Higgs production via gluon fusion in the POWHEG approach in the SM and in the MSSM*, *JHEP* **02** (2012) 088, [1111.2854].

[74] U. Aglietti, R. Bonciani, G. Degrassi and A. Vicini, *Two loop light fermion contribution to Higgs production and decays*, *Phys. Lett. B* **595** (2004) 432–441, [hep-ph/0404071].

[75] P. Nason and C. Oleari, *NLO Higgs boson production via vector-boson fusion matched with shower in POWHEG*, *JHEP* **02** (2010) 037, [0911.5299].

[76] G. Luisoni, P. Nason, C. Oleari and F. Tramontano, *$HW^{\pm}/HZ$ + 0 and 1 jet at NLO with the POWHEG BOX interfaced to GoSam and their merging within MiNLO*, *JHEP* **10** (2013) 083, [1306.2542].

[77] J. Butterworth et al., *PDF4LHC recommendations for LHC Run II*, *J. Phys. G* **43** (2016) 023001, [1510.03865].

[78] K. Hamilton, P. Nason and G. Zanderighi, *MINLO: Multi-Scale Improved NLO*, *JHEP* **10** (2012) 155, [1206.3572].

[79] K. Hamilton, P. Nason, E. Re and G. Zanderighi, *NNLOPS simulation of Higgs boson production*, *JHEP* **10** (2013) 222, [1309.0017].

[80] S. Catani and M. Grazzini, *An NNLO subtraction formalism in hadron collisions and its application to Higgs boson production at the LHC*, *Phys. Rev. Lett.* **98** (2007) 222002, [hep-ph/0703012].

[81] M. Grazzini, *NNLO predictions for the Higgs boson signal in the $H \to WW \to l\nu l\nu$ and $H \to ZZ \to 4l$ decay channels*, *JHEP* **02** (2008) 043, [0801.3232].

[82] M. Wiesemann, R. Frederix, S. Frixione, V. Hirschi, F. Maltoni and P. Torrielli, *Higgs production in association with bottom quarks*, *JHEP* **02** (2015) 132, [1409.5301].

[83] H.-L. Lai et al., *New parton distributions for collider physics*, *Phys. Rev. D* **82** (2010) 074024, [1007.2241].

[84] NNPDF collaboration, R. D. Ball et al., *Parton distributions for the LHC Run II*, *JHEP* **04** (2015) 040, [1410.8849].

[85] ATLAS Collaboration, "ATLAS Pythia 8 tunes to 7 TeV data." ATL-PHYS-PUB-2014-021, 2014.

[86] D. J. Lange, *The EvtGen particle decay simulation package*, *Nucl. Instrum. Meth.* **A462** (2001) 152–155.

[87] J. Alwall, R. Frederix, S. Frixione, V. Hirschi, F. Maltoni, O. Mattelaer et al., *The automated computation of tree-level and next-to-leading order differential cross sections, and their matching to parton shower simulations*, *JHEP* **07** (2014) 079, [1405.0301].

[88] R. Frederix, S. Frixione, E. Vryonidou and M. Wiesemann, *Heavy-quark mass effects in Higgs plus jets production*, *JHEP* **08** (2016) 006, [1604.03017].

[89] H. Mantler and M. Wiesemann, *Hadronic Higgs production through NLO + PS in the SM, the 2HDM and the MSSM*, *Eur. Phys. J.* **C75** (2015) 257, [1504.06625].

[90] H. Mantler and M. Wiesemann, *Top- and bottom-mass effects in hadronic Higgs production at small transverse momenta through LO+NLL*, *Eur. Phys. J.* **C73** (2013) 2467, [1210.8263].

[91] X. Chen, T. Gehrmann, E. W. N. Glover and M. Jaquier, *Precise QCD predictions for the production of Higgs + jet final states*, *Phys. Lett.* **B740** (2015) 147–150, [1408.5325].

[92] X. Chen, J. Cruz-Martinez, T. Gehrmann, E. W. N. Glover and M. Jaquier, *NNLO QCD corrections to Higgs boson production at large transverse momentum*, *JHEP* **10** (2016) 066, [1607.08817].

[93] X. Chen, T. Gehrmann, E. W. N. Glover and A. Huss, *Fiducial cross sections for the four-lepton decay mode in Higgs-plus-jet production up to NNLO QCD*, *JHEP* **07** (2019) 052, [1905.13738].

[94] A. Banfi, P. F. Monni, G. P. Salam and G. Zanderighi, *Higgs and Z-boson production with a jet veto*, *Phys. Rev. Lett.* **109** (2012) 202001, [1206.4998].

[95] A. Banfi, F. Caola, F. A. Dreyer, P. F. Monni, G. P. Salam, G. Zanderighi et al., *Jet-vetoed Higgs cross section in gluon fusion at N^3LO+NNLL with small-R resummation*, *JHEP* **04** (2016) 049, [1511.02886].

[96] P. F. Monni, E. Re and P. Torrielli, *Higgs Transverse-Momentum Resummation in Direct Space*, *Phys. Rev. Lett.* **116** (2016) 242001, [1604.02191].

[97] W. Bizon, P. F. Monni, E. Re, L. Rottoli and P. Torrielli, *Momentum-space resummation for transverse observables and the Higgs $p_\perp$ at N^3LL+NNLO*, *JHEP* **02** (2018) 108, [1705.09127].

[98] P. F. Monni, L. Rottoli and P. Torrielli, *Higgs transverse momentum with a jet veto: a double-differential resummation*, 1909.04704.

[99] M. Grazzini, S. Kallweit and M. Wiesemann, *Fully differential NNLO computations with MATRIX*, *Eur. Phys. J.* **C78** (2018) 537, [1711.06631].

[100] M. Grazzini, S. Kallweit, D. Rathlev and M. Wiesemann, *Transverse-momentum resummation for vector-boson pair production at NNLL+NNLO*, *JHEP* **08** (2015) 154, [1507.02565].

[101] S. Boselli, C. M. Carloni Calame, G. Montagna, O. Nicrosini and F. Piccinini, *Higgs boson decay into four leptons at NLOPS electroweak accuracy*, *JHEP* **06** (2015) 023, [1503.07394].

[102] S. Boselli, C. M. Carloni Calame, G. Montagna, O. Nicrosini, F. Piccinini and A. Shivaji, *Higgs decay into four charged leptons in the presence of dimension-six operators*, *JHEP* **01** (2018) 096, [1703.06667].

[103] A. Bredenstein, A. Denner, S. Dittmaier and M. Weber, *Precise predictions for the Higgs-boson decay $H \to WW/ZZ \to 4$ leptons*, *Phys. Rev. D* **74** (2006) 013004, [hep-ph/0604011].

[104] A. Bredenstein, A. Denner, S. Dittmaier and M. M. Weber, *Precision calculations for the Higgs decays $H \to ZZ/WW \to 4$ leptons*, *Nucl. Phys. Proc. Suppl.* **160** (2006) 131–135, [0607060].

[105] A. Bredenstein, A. Denner, S. Dittmaier and M. Weber, *Radiative corrections to the semileptonic and hadronic Higgs-boson decays $H \to WW/ZZ \to 4$ fermions*, *JHEP* **02** (2007) 080, [hep-ph/0611234].

[106] L. Altenkamp, S. Dittmaier and H. Rzehak, *Renormalization schemes for the Two-Higgs-Doublet Model and applications to $h \to WW/ZZ \to 4$ fermions*, *JHEP* **09** (2017) 134, [1704.02645].

[107] L. Altenkamp, S. Dittmaier and H. Rzehak, *Precision calculations for $h \to WW/ZZ \to 4$ fermions in the Two-Higgs-Doublet Model with Prophecy4f*, *JHEP* **03** (2018) 110, [1710.07598].

[108] L. Altenkamp, M. Boggia and S. Dittmaier, *Precision calculations for $h \to WW/ZZ \to 4$ fermions in a singlet extension of the Standard Model with PROPHECY4F*, *JHEP* **04** (2018) 062, [1801.07291].

[109] A. Denner, S. Dittmaier and J.-N. Lang, *Renormalization of mixing angles*, *JHEP* **11** (2018) 104, [1808.03466].

[110] LHC Higgs Cross Section Working Group, S. Dittmaier, C. Mariotti, G. Passarino, R. Tanaka (Eds), *Handbook of LHC Higgs Cross Sections: 1. Inclusive Observables*, *CERN-2011-002* (2011) , [1101.0593].

[111] LHC Higgs Cross Section Working Group, S. Dittmaier, C. Mariotti, G. Passarino, R. Tanaka (Eds), *Handbook of LHC Higgs Cross Sections: 2. Differential Distributions*, *CERN-2012-002* (2012) , [1201.3084].

[112] LHC Higgs Cross Section Working Group, S. Heinemeyer, C. Mariotti, G. Passarino, R. Tanaka (Eds), *Handbook of LHC Higgs Cross Sections: 3. Higgs Properties*, *CERN-2013-004* (2013) , [1307.1347].

[113] A. Djouadi, J. Kalinowski and M. Spira, *HDECAY: A Program for Higgs boson decays in the Standard Model and its supersymmetric extension*, *Comput. Phys. Commun.* **108** (1998) 56–74, [hep-ph/9704448].

[114] A. Djouadi, M. M. Mühlleitner and M. Spira, *Decays of supersymmetric particles: The Program SUSY-HIT (SUspect-SdecaY-Hdecay-InTerface)*, *Acta Phys. Polon. B* **38** (2007) 635–644, [hep-ph/0609292].

[115] S. Dulat, T.-J. Hou, J. Gao, M. Guzzi, J. Huston, P. Nadolsky et al., *New parton distribution functions from a global analysis of quantum chromodynamics*, *Phys. Rev. D* **93** (2016) 033006, [1506.07443].

[116] L. A. Harland-Lang, A. D. Martin, P. Motylinski and R. S. Thorne, *Parton distributions in the LHC era: MMHT 2014 PDFs*, *Eur. Phys. J. C* **75** (2015) 204, [1412.3989].

[117] C. Anastasiou, C. Duhr, F. Dulat, F. Herzog and B. Mistlberger, *Higgs Boson Gluon-Fusion Production in QCD at Three Loops*, *Phys. Rev. Lett.* **114** (2015) 212001, [1503.06056].

[118] C. Anastasiou et al., *High precision determination of the gluon fusion Higgs boson cross-section at the LHC*, *JHEP* **05** (2016) 058, [1602.00695].

[119] S. Actis, G. Passarino, C. Sturm and S. Uccirati, *NLO electroweak corrections to Higgs boson production at hadron colliders*, *Phys. Lett. B* **670** (2008) 12–17, [0809.1301].

[120] C. Anastasiou, R. Boughezal and F. Petriello, *Mixed QCD-electroweak corrections to Higgs boson production in gluon fusion*, *JHEP* **04** (2009) 003, [0811.3458].

[121] M. Grazzini and H. Sargsyan, *Heavy-quark mass effects in Higgs boson production at the LHC*, *JHEP* **09** (2013) 129, [1306.4581].

[122] I. W. Stewart and F. J. Tackmann, *Theory uncertainties for Higgs and other searches using jet bins*, *Phys. Rev. D* **85** (2012) 034011, [1107.2117].

[123] M. Ciccolini, A. Denner and S. Dittmaier, *Strong and electroweak corrections to the production of Higgs + 2-jets via weak interactions at the LHC*, *Phys. Rev. Lett.* **99** (2007) 161803, [0707.0381].

[124] M. Ciccolini, A. Denner and S. Dittmaier, *Electroweak and QCD corrections to Higgs production via vector-boson fusion at the LHC*, *Phys. Rev. D* **77** (2008) 013002, [0710.4749].

[125] P. Bolzoni, F. Maltoni, S.-O. Moch and M. Zaro, *Higgs production via vector-boson fusion at NNLO in QCD*, *Phys. Rev. Lett.* **105** (2010) 011801, [1003.4451].

[126] O. Brein, A. Djouadi and R. Harlander, *NNLO QCD corrections to the Higgs-strahlung processes at hadron colliders*, *Phys. Lett. B* **579** (2004) 149–156, [hep-ph/0307206].

[127] A. Denner, S. Dittmaier, S. Kallweit and A. Mück, *Electroweak corrections to Higgs-strahlung off W/Z bosons at the Tevatron and the LHC with HAWK*, *JHEP* **03** (2012) 075, [1112.5142].

[128] L. Altenkamp, S. Dittmaier, R. V. Harlander, H. Rzehak and T. J. E. Zirke, *Gluon-induced Higgs-strahlung at next-to-leading order QCD*, *JHEP* **02** (2013) 078, [1211.5015].

[129] W. Beenakker et al., *NLO QCD corrections to $t\bar{t}H$ production in hadron collisions*, *Nucl. Phys. B* **653** (2003) 151–203, [hep-ph/0211352].

[130] S. Dawson, C. Jackson, L. Orr, L. Reina and D. Wackeroth, *Associated Higgs production with top quarks at the large hadron collider: NLO QCD corrections*, *Phys. Rev. D* **68** (2003) 034022, [hep-ph/0305087].

[131] Y. Zhang, W.-G. Ma, R.-Y. Zhang, C. Chen and L. Guo, *QCD NLO and EW NLO corrections to $t\bar{t}H$ production with top quark decays at hadron collider*, *Phys. Lett. B* **738** (2014) 1–5, [1407.1110].

[132] S. Frixione, V. Hirschi, D. Pagani, H.-S. Shao and M. Zaro, *Electroweak and QCD corrections to top-pair hadroproduction in association with heavy bosons*, *JHEP* **06** (2015) 184, [1504.03446].

[133] S. Dawson, C. Jackson, L. Reina and D. Wackeroth, *Exclusive Higgs boson production with bottom quarks at hadron colliders*, *Phys. Rev. D* **69** (2004) 074027, [hep-ph/0311067].

[134] S. Dittmaier, M. Krämer and M. Spira, *Higgs radiation off bottom quarks at the Tevatron and the CERN LHC*, *Phys. Rev. D* **70** (2004) 074010, [hep-ph/0309204].

[135] R. V. Harlander and W. B. Kilgore, *Higgs boson production in bottom quark fusion at next-to-next-to leading order*, *Phys. Rev. D* **68** (2003) 013001, [hep-ph/0304035].

[136] T. Gleisberg, S. Höche, F. Krauss, M. Schönherr, S. Schumann et al., *Event generation with SHERPA 1.1*, *JHEP* **02** (2009) 007, [0811.4622].

[137] T. Gleisberg and S. Höche, *Comix, a new matrix element generator*, *JHEP* **12** (2008) 039, [0808.3674].

[138] F. Cascioli, P. Maierhofer and S. Pozzorini, *Scattering Amplitudes with Open Loops*, *Phys. Rev. Lett.* **108** (2012) 111601, [1111.5206].

[139] F. Caola, K. Melnikov, R. Röntsch and L. Tancredi, *QCD corrections to ZZ production in gluon fusion at the LHC*, *Phys. Rev. D* **92** (2015) 094028, [1509.06734].

[140] F. Caola, K. Melnikov, R. Röntsch and L. Tancredi, *QCD corrections to W^+W^- production through gluon fusion*, *Phys. Lett. B* **754** (2016) 275–280, [1511.08617].

[141] J. M. Campbell, R. K. Ellis, M. Czakon and S. Kirchner, *Two Loop Correction to Interference in $gg \to ZZ$*, *JHEP* **08** (2016) 011, [1605.01380].

[142] K. Melnikov and M. Dowling, *Production of two Z-bosons in gluon fusion in the heavy top quark approximation*, *Phys. Lett.* **B744** (2015) 43–47, [1503.01274].

[143] S. Schumann and F. Krauss, *A Parton shower algorithm based on Catani-Seymour dipole factorisation*, *JHEP* **03** (2008) 038, [0709.1027].

[144] S. Höche, F. Krauss, M. Schönherr and F. Siegert, *QCD matrix elements + parton showers: The NLO case*, *JHEP* **04** (2013) 027, [1207.5030].

[145] ATLAS Collaboration, "Studies on top-quark Monte Carlo modelling for Top2016." ATL-PHYS-PUB-2016-020, 2016.

[146] ATLAS Collaboration, *The ATLAS Simulation Infrastructure*, *Eur. Phys. J. C* **70** (2010) 823, [1005.4568].

[147] T. Sjöstrand, S. Mrenna and P. Z. Skands, *A brief introduction to PYTHIA 8.1*, *Comput. Phys. Commun.* **178** (2008) 852–867, [0710.3820].

[148] R. D. Ball et al., *Parton distributions with LHC data*, *Nucl. Phys. B* **867** (2013) 244–289, [1207.1303].

[149] ATLAS Collaboration, "The Pythia 8 A3 tune description of ATLAS minimum bias and inelastic measurements incorporating the Donnachie–Landshoff diffractive model." ATL-PHYS-PUB-2016-017, 2016.

[150] ATLAS Collaboration, *Measurement of the Inelastic Proton–Proton Cross Section at $\sqrt{s} = 13$ TeV with the ATLAS Detector at the LHC*, *Phys. Rev. Lett.* **117** (2016) 182002, [1606.02625].

[151] S. H. Abidi, G. Barone, P. Bechtle, P. Bellos, B. M. Ciungu, R. Di Nardo et al., *Event selection and background estimation in the H→ZZ→4l channel at $\sqrt{s}$=13TeV - Final Run 2 Analysis*, Tech. Rep. ATL-COM-PHYS-2018-1710, CERN, Geneva, Dec, 2018.

[152] M. Pivk and F. R. Le Diberder, *SPlot: A Statistical tool to unfold data distributions*, *Nucl. Instrum. Meth.* **A555** (2005) 356–369, [physics/0402083].

[153] S. Bolognesi, Y. Gao, A. V. Gritsan, K. Melnikov, M. Schulze, N. V. Tran et al., *Spin and parity of a single-produced resonance at the LHC*, 1208.4018.

[154] F. Bishara, U. Haisch, P. F. Monni and E. Re, *Constraining Light-Quark Yukawa Couplings from Higgs Distributions*, *Physical Review Letters* **118** (Mar., 2017) 121801, [1606.09253].

[155] M. González-Alonso, A. Greljo, G. Isidori and D. Marzocca, *Pseudo-observables in Higgs decays*, *European Physical Journal C* **75** (Mar., 2015) 128, [1412.6038].

[156] G. Cowan, *A survey of unfolding methods for particle physics*, in *Prepared for Conference on Advanced Statistical Techniques in Particle Physics, Durham, England*, pp. 18–22, 2002.

[157] S. H. Abidi, C. Arcangeletti, G. Barone, B. M. Ciungu, R. Di Nardo, A. Gabrielli et al., *Measurement of the fiducial, differential and total Higgs production cross sections in the $H \to ZZ^* \to \ell^+\ell^-\ell^+\ell^-$ final state from proton–proton collisions at $\sqrt{s} = 13$ TeV with 2015-2018 data*, Tech. Rep. ATL-COM-PHYS-2019-930, CERN, Geneva, Jul, 2019.

[158] W. Verkerke and D. Kirkby, *The RooFit toolkit for data modeling*, *ArXiv Physics e-prints* (June, 2003) , [physics/0306116].

[159] L. Moneta, K. Cranmer, G. Schott and W. Verkerke, *The RooStats project*, in *Proceedings of the 13th International Workshop on Advanced Computing and Analysis Techniques in Physics Research. February 22-27, 2010, Jaipur, India. http://acat2010.cern.ch/. Published online at <A href="http://pos.sissa.it/cgi-bin/reader/conf.cgi?confid=93">http://pos.sissa.it/cgi-bin/reader/conf.cgi?confid=93</A>, id.57*, p. 57, 2010. 1009.1003.

[160] ATLAS Collaboration, *Luminosity determination in pp collisions at $\sqrt{s} = 7$ TeV using the ATLAS detector at the LHC*, *Eur. Phys. J. C* **71** (2011) 1630, [1101.2185].

[161] ATLAS collaboration, M. Aaboud et al., *Measurements of b-jet tagging efficiency with the ATLAS detector using $t\bar{t}$ events at $\sqrt{s} = 13$ TeV*, *JHEP* **08** (2018) 089, [1805.01845].

[162] I. W. Stewart, F. J. Tackmann, J. R. Walsh and S. Zuberi, *Jet p_T resummation in Higgs production at $NNLL' + NNLO$*, *Phys. Rev.* **D89** (2014) 054001, [1307.1808].

[163] X. Liu and F. Petriello, *Reducing theoretical uncertainties for exclusive Higgs-boson plus one-jet production at the LHC*, *Phys. Rev.* **D87** (2013) 094027, [1303.4405].

[164] R. Boughezal, X. Liu, F. Petriello, F. J. Tackmann and J. R. Walsh, *Combining Resummed Higgs Predictions Across Jet Bins*, *Phys. Rev.* **D89** (2014) 074044, [1312.4535].

[165] S. Gangal and F. J. Tackmann, *Next-to-leading-order uncertainties in Higgs+2 jets from gluon fusion*, *Phys. Rev.* **D87** (2013) 093008, [1302.5437].

[166] LHC Higgs Cross Section Working Group, D. de Florian et al. (Eds), *Handbook of LHC Higgs Cross Sections: 4. Deciphering the Nature of the Higgs Sector*, *CERN-2017-002* (2017) , [1610.07922].

[167] *Les Houches 2017: Physics at TeV Colliders Standard Model Working Group Report*, 2018.

[168] ATLAS collaboration, M. Aaboud et al., *Measurement of the Higgs boson coupling properties in the $H \to ZZ^* \to 4\ell$ decay channel at $\sqrt{s} = 13$ TeV with the ATLAS detector*, *JHEP* **03** (2018) 095, [1712.02304].

[169] D. de Florian, G. Ferrera, M. Grazzini and D. Tommasini, *Higgs boson production at the LHC: transverse momentum resummation effects in the $H \to \gamma\gamma$, $H \to WW \to \ell\nu\ell\nu$ and $H \to ZZ \to 4\ell$ decay modes*, *JHEP* **06** (2012) 132, [1203.6321].

[170] J. S. Gainer et al., *Adding pseudo-observables to the four-lepton experimentalist's toolbox*, *JHEP* **10** (2018) 073, [1808.00965].

[171] ATLAS Collaboration, *Observation of Higgs boson production in association with a top quark pair at the LHC with the ATLAS detector*, *Phys. Lett. B* **784** (2018) 173, [1806.00425].

[172] CMS Collaboration, *Observation of $t\bar{t}H$ Production*, *Phys. Rev. Lett.* **120** (2018) 231801, [1804.02610].

[173] ATLAS Collaboration, *Observation of $H \to b\bar{b}$ decays and VH production with the ATLAS detector*, *Phys. Lett. B* **786** (2018) 59, [1808.08238].

[174] CMS collaboration, A. M. Sirunyan et al., *Observation of Higgs boson decay to bottom quarks*, *Phys. Rev. Lett.* **121** (2018) 121801, [1808.08242].

[175] ATLAS collaboration, M. Aaboud et al., *Search for the Decay of the Higgs Boson to Charm Quarks with the ATLAS Experiment*, *Phys. Rev. Lett.* **120** (2018) 211802, [1802.04329].

[176] CMS collaboration, A. M. Sirunyan et al., *A search for the standard model Higgs boson decaying to charm quarks*, 1912.01662.

[177] ATLAS collaboration, M. Aaboud et al., *Measurement of the Inelastic Proton-Proton Cross Section at $\sqrt{s} = 13$ TeV with the ATLAS Detector at the LHC*, *Phys. Rev. Lett.* **117** (2016) 182002, [1606.02625].

[178] O. S. Brüning, P. Collier, P. Lebrun, S. Myers, R. Ostojic, J. Poole et al., *LHC Design Report*. CERN Yellow Reports: Monographs. CERN, Geneva, 2004.

[179] P. W. Higgs, *Broken symmetries, massless particles and gauge fields*, *Phys. Lett.* **12** (1964) 132–133.

[180] VUS CERN LHC, *The standard model and beyond*, 2016.

[181] O. Greenberg, *Spin and unitary-spin independence in a paraquark model of baryons and mesons*, *Phys. Rev. Lett.* **13** (Nov, 1964) 598–602.

[182] Wikimedia Commons, *Scatteringdiagram*, 2007.

[183] ATLAS and CMS Collaborations, *Combined Measurement of the Higgs Boson Mass in pp Collisions at $\sqrt{s} = 7$ and 8 TeV with the ATLAS and CMS Experiments*, *Phys. Rev. Lett.* **114** (2015) 191803, [1503.07589].

[184] ATLAS Collaboration, *The ATLAS Experiment at the CERN Large Hadron Collider*, *JINST* **3** (2008) S08003.

[185] *ATLAS Experiment at CERN, The Collaboration*, August, 2019.

[186] ATLAS Collaboration, "L1Calo Public Results Run 2."

[187] ATLAS Collaboration collaboration, *ATLAS level-1 trigger: Technical Design Report*. Technical Design Report ATLAS. CERN, Geneva, 1998.

[188] ATLAS Collaboration collaboration, P. Jenni, M. Nessi, M. Nordberg and K. Smith, *ATLAS high-level trigger, data-acquisition and controls: Technical Design Report*. Technical Design Report ATLAS. CERN, Geneva, 2003.

[189] D. J. Griffiths, *Introduction to elementary particles; 2nd rev. version*. Physics textbook. Wiley, New York, NY, 2008.

[190] G. Cowan, K. Cranmer, E. Gross and O. Vitells, *Asymptotic formulae for likelihood-based tests of new physics*, *Eur. Phys. J.* **C71** (2011) 1554, [1007.1727].

[191] K. Cranmer, *Practical Statistics for the LHC*, in *Proceedings, 2011 European School of High-Energy Physics (ESHEP 2011): Cheile Gradistei, Romania, September 7-20, 2011*, pp. 267–308, 2015. 1503.07622. DOI.

[192] ATLAS Collaboration, *Jet energy measurement with the ATLAS detector in proton–proton collisions at $\sqrt{s} = 7$ TeV*, *Eur. Phys. J. C* **73** (2013) 2304, [1112.6426].

[193] ATLAS Collaboration, *Jet energy resolution in proton–proton collisions at $\sqrt{s} = 7$ TeV recorded in 2010 with the ATLAS detector*, Eur. Phys. J. C **73** (2013) 2306, [1210.6210].

[194] ATLAS Collaboration, *Measurements of b-jet tagging efficiency with the ATLAS detector using $t\bar{t}$ events at $\sqrt{s} = 13$ TeV*, JHEP **08** (2018) 089, [1805.01845].

[195] W. Lampl, S. Laplace, D. Lelas, P. Loch, H. Ma, S. Menke et al., *Calorimeter Clustering Algorithms: Description and Performance*, Tech. Rep. ATL-LARG-PUB-2008-002. ATL-COM-LARG-2008-003, CERN, Geneva, Apr, 2008.

[196] ATLAS Collaboration collaboration, ATLAS Collaboration, *Improved electron reconstruction in ATLAS using the Gaussian Sum Filter-based model for bremsstrahlung*, Tech. Rep. ATLAS-CONF-2012-047, CERN, Geneva, May, 2012.

[197] ATLAS collaboration, ATLAS Collaboration, *Muon reconstruction performance of the ATLAS detector in proton–proton collision data at $\sqrt{s}$ =13 TeV*, Eur. Phys. J. **C76** (2016) 292, [1603.05598].

[198] ATLAS Collaboration collaboration, S. Schramm, *ATLAS Jet Reconstruction, Calibration, and Tagging of Lorentz-boosted Objects*, Tech. Rep. ATL-PHYS-PROC-2017-236, CERN, Geneva, Nov, 2017.

[199] ATLAS collaboration, M. Aaboud et al., *Measurement of inclusive and differential cross sections in the $H \to ZZ^* \to 4\ell$ decay channel in pp collisions at $\sqrt{s} = 13$ TeV with the ATLAS detector*, JHEP **10** (2017) 132, [1708.02810].

[200] S. Mrenna and P. Skands, *Automated Parton-Shower Variations in Pythia 8*, Phys. Rev. **D94** (2016) 074005, [1605.08352].

[201] F. Maltoni, K. Mawatari and M. Zaro, *Higgs characterisation via vector-boson fusion and associated production: NLO and parton-shower effects*, Eur. Phys. J. **C74** (2014) 2710, [1311.1829].

[202] ATLAS collaboration, G. Aad et al., *Study of the spin and parity of the Higgs boson in diboson decays with the ATLAS detector*, Eur. Phys. J. **C75** (2015) 476, [1506.05669].

[203] J. Alwall, R. Frederix, S. Frixione, V. Hirschi, F. Maltoni et al., *The automated computation of tree-level and next-to-leading order differential cross sections, and their matching to parton shower simulations*, JHEP **1407** (2014) 079, [1405.0301].

[204] Y. e. a. Gao, *Spin determination of single-produced resonances at hadron colliders*, Phys. Rev. **D 81** (2010) , [1001.3396].

[205] Particle Data Group collaboration, K. A. Olive et al., *Review of particle physics*, Chin. Phys. C **38** (2014) 090001.

[206] M. Dobbs and J. B. Hansen, *The HepMC C++ Monte Carlo event record for high energy physics*, *Comput. Phys. Commun.* **134** (2001) 41–46, [10.1016/S0010-4655(00)00189-2].

[207] T. Carli et al., *Draft proposal for truth particle definitions used in ATLAS*, Tech. Rep. ATL-COM-PHYS-2014-439, CERN, Geneva, 2014.

[208] ATLAS collaboration, G. Aad et al., *Fiducial and differential cross sections of Higgs boson production measured in the four-lepton decay channel in pp collisions at* $\sqrt{s} = 8\,\text{TeV}$ *with the ATLAS detector*, *Phys. Lett.* **B738** (2014) 234–253, [1408.3226].

[209] LHC Higgs Cross Section Working Group, S. Dittmaier, C. Mariotti, G. Passarino and R. Tanaka (Eds.), *Handbook of lhc higgs cross sections: 1. inclusive observables*, *CERN-2011-002* (2011) , [1101.0593].

[210] D. de Florian et al., *Transverse-momentum resummation: Higgs boson production at the Tevatron and the LHC*, *JHEP* **064** (2011) 1111.

[211] D. de Florian, G. Ferrera, M. Grazzini and D. Tommasini, *Higgs boson production at the LHC: transverse momentum resummation effects in the H->2gamma, H->WW->lnu lnu and H->ZZ->4l decay modes*, *JHEP* **1206** (2012) 132, [1203.6321].

[212] M. Grazzini and H. Sargsyan, *Heavy-quark mass effects in Higgs boson production at the LHC*, *JHEP* **1309** (2013) 129, [1306.4581].

[213] G. Cowan, "Discovery sensitivity for a counting experiment with background uncertainty."

[214] P. Nason, *A New method for combining NLO QCD with shower Monte Carlo algorithms*, *JHEP* **11** (2004) 040, [hep-ph/0409146].

[215] S. Frixione, P. Nason and C. Oleari, *Matching NLO QCD computations with parton shower simulations: the POWHEG method*, *JHEP* **11** (2007) 070, [0709.2092].

[216] S. Alioli, P. Nason, C. Oleari and E. Re, *A general framework for implementing NLO calculations in shower Monte Carlo programs: the POWHEG BOX*, *JHEP* **06** (2010) 043, [1002.2581].

[217] J. M. Campbell, R. K. Ellis, R. Frederix, P. Nason, C. Oleari and C. Williams, *NLO Higgs Boson Production Plus One and Two Jets Using the POWHEG BOX, MadGraph4 and MCFM*, *JHEP* **07** (2012) 092, [1202.5475].

[218] T. Sjöstrand, S. Mrenna and P. Z. Skands, *PYTHIA 6.4 physics and manual*, *JHEP* **05** (2006) 026, [hep-ph/0603175].

[219] M. Bahr et al., *Herwig++ physics and manual*, *Eur. Phys. J. C* **58** (2008) 639–707, [0803.0883].

[220] J. Bellm et al., *Herwig++ 2.7 Release Note*, 1310.6877.

[221] G. Bozzi, S. Catani, D. de Florian and M. Grazzini, *Transverse-momentum resummation and the spectrum of the Higgs boson at the LHC*, *Nucl. Phys.* **B737** (2006) 73–120, [hep-ph/0508068].

[222] D. de Florian, G. Ferrera, M. Grazzini and D. Tommasini, *Transverse-momentum resummation: Higgs boson production at the Tevatron and the LHC*, *JHEP* **11** (2011) 064, [1109.2109].

[223] A. Alloul, N. D. Christensen, C. Degrande, C. Duhr and B. Fuks, *FeynRules 2.0 - A complete toolbox for tree-level phenomenology*, *Comput. Phys. Commun.* **185** (2014) 2250–2300, [1310.1921].

[224] C. Degrande, C. Duhr, B. Fuks, D. Grellscheid, O. Mattelaer and T. Reiter, *UFO - The Universal FeynRules Output*, *Comput. Phys. Commun.* **183** (2012) 1201–1214, [1108.2040].

[225] A. Djouadi, M. Spira and P. Zerwas, *Production of Higgs bosons in proton colliders: QCD corrections*, *Phys. Lett. B* **264** (1991) 440–446.

[226] S. Dawson, *Radiative corrections to Higgs boson production*, *Nucl. Phys. B* **359** (1991) 283–300.

[227] M. Spira, A. Djouadi, D. Graudenz and P. Zerwas, *Higgs boson production at the LHC*, *Nucl. Phys. B* **453** (1995) 17–82, [hep-ph/9504378].

[228] R. V. Harlander and W. B. Kilgore, *Next-to-next-to-leading order Higgs production at hadron colliders*, *Phys. Rev. Lett.* **88** (2002) 201801, [hep-ph/0201206].

[229] C. Anastasiou and K. Melnikov, *Higgs boson production at hadron colliders in NNLO QCD*, *Nucl. Phys. B* **646** (2002) 220–256, [hep-ph/0207004].

[230] V. Ravindran, J. Smith and W. L. van Neerven, *NNLO corrections to the total cross-section for Higgs boson production in hadron hadron collisions*, *Nucl. Phys. B* **665** (2003) 325–366, [hep-ph/0302135].

[231] C. Anastasiou et al., *Higgs boson gluon-fusion production at threshold in N^3LO QCD*, *Phys. Lett. B* **737** (2014) 325–328, [1403.4616].

[232] C. Anastasiou et al., *Higgs boson gluon-fusion production beyond threshold in N^3LO QCD*, *JHEP* **03** (2015) 091, [1411.3584].

[233] C. Anastasiou, S. Buehler, F. Herzog and A. Lazopoulos, *Inclusive Higgs boson cross-section for the LHC at 8 TeV*, *JHEP* **04** (2012) 004, [1202.3638].

[234] D. de Florian and M. Grazzini, *Higgs production at the LHC: updated cross sections at $\sqrt{s}$=8 TeV*, *Phys. Lett. B* **718** (2012) 117–120, [1206.4133].

[235] J. Baglio and A. Djouadi, *Higgs production at the LHC*, *JHEP* **03** (2011) 055, [1012.0530].

[236] K. Arnold et al., *VBFNLO: A parton level Monte Carlo for processes with electroweak bosons*, *Comput. Phys. Commun.* **180** (2009) 1661–1670, [0811.4559].

[237] T. Han and S. Willenbrock, *QCD correction to the $pp \to WH$ and ZH total cross-sections*, *Phys. Lett. B* **273** (1991) 167–172.

[238] M.L. Ciccolini, S. Dittmaier and M. Krämer, *Electroweak radiative corrections to associated WH and ZH production at hadron colliders*, *Phys. Rev. D* **68** (2003) 073003, [hep-ph/0306234].

[239] W. Beenakker et al., *Higgs radiation off top quarks at the Tevatron and the LHC*, *Phys. Rev. Lett.* **87** (2001) 201805, [hep-ph/0107081].

[240] S. Dawson, L. Orr, L. Reina and D. Wackeroth, *Next-to-leading order QCD corrections to $pp \to t\bar{t}h$ at the CERN Large Hadron Collider*, *Phys. Rev. D* **67** (2003) 071503, [hep-ph/0211438].

[241] R. Harlander, M. Krämer and M. Schumacher, *Bottom-quark associated Higgs-boson production: Reconciling the four- and five-flavour scheme approach*, 1112.3478.

[242] G. Cowan, K. Cranmer, E. Gross and O. Vitells, *Asymptotic formulae for likelihood-based tests of new physics*, *Eur. Phys. J.* **C71** (2011) 1554, [1007.1727v2].

[243] H. Team, *Event selection and background estimation in the $H \to ZZ^{(*)} \to 4\ell$ channel at $\sqrt{s} = 13TeV$ - Moriond 2017 Analysis*, Nov, 2016.

[244] ATLAS collaboration, G. Aad et al., *Measurements of four-lepton production in pp collisions at $\sqrt{s} = 8$ TeV with the ATLAS detector*, *Phys. Lett.* **B753** (2016) 552–572, [1509.07844].

[245] J. Meyer, S. Heim, R. Di Nardo, E. Mountricha and A. Schaffer, *Theoretical uncertainties and inputs occurring in H→ZZ analyses*, Tech. Rep. ATL-COM-PHYS-2015-1278, CERN, Geneva, Oct, 2015.

[246] The ATLAS Collaboration, The CMS Collaboration, The LHC Higgs Combination Group collaboration, *Procedure for the LHC Higgs boson search combination in Summer 2011*, Tech. Rep. CMS-NOTE-2011-005. ATL-PHYS-PUB-2011-11, CERN, Geneva, Aug, 2011.

[247] S. Forte, D. Gillberg, C. Hays, G. Petrucciani, A. Massironi, G. Zanderighi et al., *Gluon-gluon fusion*, .

[248] S. Hoeche, F. Krauss, S. Schumann and F. Siegert, *QCD matrix elements and truncated showers*, *JHEP* **05** (2009) 053, [0903.1219].

[249] M. Cacciari, F. A. Dreyer, A. Karlberg, G. P. Salam and G. Zanderighi, *Fully Differential Vector-Boson-Fusion Higgs Production at Next-to-Next-to-Leading Order*, *Phys. Rev. Lett.* **115** (2015) 082002, [1506.02660].

[250] A. Hocker and V. Kartvelishvili, *SVD approach to data unfolding*, *Nucl. Instrum. Meth.* **A372** (1996) 469–481, [hep-ph/9509307].

[251] R. V. Harlander and W. B. Kilgore, *Production of a pseudoscalar Higgs boson at hadron colliders at next-to-next-to leading order*, *JHEP* **10** (2002) 017, [hep-ph/0208096].

[252] C. Anastasiou and K. Melnikov, *Pseudoscalar Higgs boson production at hadron colliders in NNLO QCD*, *Phys. Rev.* **D67** (2003) 037501, [hep-ph/0208115].

[253] S. Dawson, C. B. Jackson, L. Reina and D. Wackeroth, *Higgs production in association with bottom quarks at hadron colliders*, *Mod. Phys. Lett.* **A21** (2006) 89–110, [hep-ph/0508293].

[254] D. Dicus, T. Stelzer, Z. Sullivan and S. Willenbrock, *Higgs boson production in association with bottom quarks at next-to-leading order*, *Phys. Rev.* **D59** (1999) 094016, [hep-ph/9811492].

[255] C. Balazs, H.-J. He and C. P. Yuan, *QCD corrections to scalar production via heavy quark fusion at hadron colliders*, *Phys. Rev.* **D60** (1999) 114001, [hep-ph/9812263].

[256] F. Maltoni, Z. Sullivan and S. Willenbrock, *Higgs-boson production via bottom-quark fusion*, *Phys. Rev.* **D67** (2003) 093005, [hep-ph/0301033].

[257] S. Bühler, F. Herzog, A. Lazopoulos and R. Müller, *The fully differential hadronic production of a Higgs boson via bottom quark fusion at NNLO*, *JHEP* **07** (2012) 115, [1204.4415].

[258] R. V. Harlander, A. Tripathi and M. Wiesemann, *Higgs production in bottom quark annihilation: Transverse momentum distribution at NNLO+NNLL*, *Phys. Rev.* **D90** (2014) 015017, [1403.7196].

[259] F. Demartin, F. Maltoni, K. Mawatari and M. Zaro, *Higgs production in association with a single top quark at the LHC*, *Eur. Phys. J. C* **75** (2015) 267, [1504.00611].

[260] F. Demartin, B. Maier, F. Maltoni, K. Mawatari and M. Zaro, *tWH associated production at the LHC*, 1607.05862.

[261] B. Biedermann, A. Denner, S. Dittmaier, L. Hofer and B. Jäger, *Electroweak corrections to $pp \to \mu^+\mu^-e^+e^- + X$ at the LHC: a Higgs background study*, *Phys. Rev. Lett.* **116** (2016) 161803, [1601.07787].

[262] B. Biedermann, M. Billoni, A. Denner, S. Dittmaier, L. Hofer, B. Jäger et al., *Next-to-leading-order electroweak corrections to $pp \to W^+W^- \to 4$ leptons at the LHC*, *JHEP* **06** (2016) 065, [1605.03419].

[263] B. Biedermann, A. Denner, S. Dittmaier, L. Hofer and B. Jager, *Next-to-leading-order electroweak corrections to the production of four charged leptons at the LHC*, *JHEP* **01** (2017) 033, [1611.05338].

[264] M. Bonvini, F. Caola, S. Forte, K. Melnikov and G. Ridolfi, *Signal-background interference effects for $ggHW^+W^-$ beyond leading order*, *Phys. Rev.* **D88** (2013) 034032, [1304.3053].

[265] C. S. Li, H. T. Li, D. Y. Shao and J. Wang, *Soft gluon resummation in the signal-background interference process of $gg(\to h) \to ZZ$*, *JHEP* **08** (2015) 065, [1504.02388].